Unlocking the Aquatic Ballet of Sea Turtles: Harnessing Sea Turtle Biomechanics for the Evolution of Marine Technologies

By:

Nicholas James John van der Geest

School of Engineering, Computer and Mathematical Sciences

A research component submitted to Auckland University of Technology in fulfilment of the requirements of the degree of Doctor of Philosophy in Mechanical Engineering

Auckland, New Zealand, 2023

Supervisors: Dr Lorenzo Garcia and Associate Professor Roy Nates

Abstract

Sea turtles are marvels of marine navigation, employing sophisticated biomechanical strategies that enable them to traverse thousands of kilometres across oceans. Despite their importance in oceanic ecosystems, all sea turtle species face the risk of extinction, largely due to human activities. This doctoral thesis provides an in-depth analysis of the biomechanics and hydrodynamics involved in sea turtle movement. It emphasises creating non-intrusive techniques for examining and mimicking their swimming behaviours. The study aims to enhance biological and biomechanical understanding and inspire technological innovations drawing from nature's design.

This research first introduces a novel, non-invasive procedure for studying the biomechanics of wild sea turtles by utilising underwater drones to film them in their natural habitat, the Great Barrier Reef. Through this approach, distinctive swimming patterns were observed, deviating from those recorded in captive juveniles. Our findings show that the flipper goes through a closed-loop trajectory with extended sweeping of the flipper tip towards the centre of the carapace to create a clapping motion. We have named this the "sweep stroke", and in contrast to previously described four-stage models, it creates a five-stage cycle swimming locomotion model.

Delving into the migratory prowess of sea turtles, the thesis then examines the biomechanical and hydrodynamic aspects of long-distance travel. Sea turtles achieve this remarkable feat despite a diet consisting primarily of low-energy foods. A model based on the green sea turtle (Chelonia mydas) and a custom testing rig was developed to investigate only the upstroke phase of their swimming. It was found that sea turtles likely utilise a passive upstroke, significantly reducing their drag coefficient and allowing them to maintain swim speed without generating thrust, thereby conserving energy.

The thesis further investigates the green sea turtle's incredible ability to swim up to 50 km per day on a diet of seagrass or microalgae. By factoring in the newly described five-stage swimming cycle, a soft-robotic sea turtle named Cornelia, capable of mimicking the real animal's form and function, was developed to provide biomechanical insights without invasive experimentation. The study reveals that the green sea turtle may only produce propulsion for about 30% of the limb beat cycle, with the rest of the time spent in a low-drag glide, minimising speed loss due to their large mass and low drag coefficient. These insights can potentially revolutionise oceanic exploration through a new generation of robotic systems that harness sea turtle-inspired propulsion strategies.

Furthermore, this work utilised Cornelia, to investigate the flow manipulation during the sea turtle's propulsive phase. By analysing the relationship between swim speed, flipper angle of attack, power consumption, and the production of thrust and lift, this research hypothesises how flow features contribute to the sea turtle's propulsive efforts and cost of transport. The findings indicate that sea turtles achieve exceptionally low cost of transport values, affirming the efficiency of their swimming technique and providing valuable data that could inform the design of high-efficiency underwater drones for extended missions.

Lastly, the thesis explores the development of prosthetic flippers for sea turtles that have lost a limb. Robotic testing demonstrated that a prosthetic could effectively mimic the sea turtle's downstroke and upstroke, allowing for regained manoeuvrability. Swim tests with the

prosthetic attached to the robotic model yielded promising results, nearly matching the average swim speeds of wild sea turtles. This work aspires to lay the groundwork for open-source prosthetic designs that could empower veterinary professionals worldwide to assist injured turtles. The broader ambition is to inspire further animal-based robotic designs, advancing technologies geared towards ecological conservation and rehabilitation.

In conclusion, this thesis presents a multifaceted investigation into the locomotion of sea turtles, yielding significant original insights that bridge biology, robotics, conservation, and bioinspired engineering. The findings have profound implications for understanding the biomechanical efficiency of these endangered species and offer a pathway toward developing sustainable technologies that could benefit both wildlife conservation and human engineering pursuits.

Contents

List of Figures

List of Tables

Attestation of Authorship

I hereby declare that this submission is my own work and that, to the best of my knowledge and belief, it contains no material previously published or written by another person (except where explicitly defined in the acknowledgements), nor material to which a substantial extent has already been submitted for the award of any other degree or diploma of a university or other institution of higher learning.

……

Nicholas James John van der Geest

Co-Author contributions

Chapter 3: New insight into the swimming kinematics of wild Green sea turtles (*Chelonia mydas*)

Nick van der Geest: Conducted the research, designed the experiments, data acquisition, modelling, data analysis, interpretation, writing and editing

Lorenzo Garcia: Supervision, Conducted the research, designed the experiments, writing and editing

Roy Nates: Supervision, writing and editing

Daniel A. Godoy: Data acquisition, project management, writing and editing

Chapter 4: Sea Turtles Employ Drag-Reducing Techniques to Conserve Energy

Nick van der Geest: Conducted the research, designed the experiments, data acquisition, modelling, data analysis, interpretation, writing and editing

Lorenzo Garcia: Supervision, Conducted the research, designed the experiments, writing and editing

Roy Nates: Supervision, writing and editing

Alberto Gonzalez-Vazquez: Designed the experiments, writing and editing

Chapter 5: Soft-robotic green sea turtle (*Chelonia mydas*) developed to replace animal experimentation provides new insight into their propulsive strategies

Nick van der Geest: Conducted the research, designed the experiments, data acquisition, modelling, data analysis, interpretation, writing and editing

Lorenzo Garcia: Supervision, Conducted the research, designed the experiments, writing and editing

Fraser Borrett: designed the experiments, modelling, writing and editing

Roy Nates: Supervision, writing and editing

Alberto Gonzalez-Vazquez: Designed the experiments, writing and editing

Chapter 6: New insights into sea turtle propulsion and their cost of transport point to a potential new generation of high-efficient underwater drones for ocean exploration.

Nick van der Geest: Conducted the research, designed the experiments, data acquisition, modelling, data analysis, interpretation, writing and editing

Lorenzo Garcia: Supervision, Conducted the research, designed the experiments, writing and editing

Roy Nates: Supervision, writing and editing

Fraser Borrett: designed the experiments, modelling, writing and editing

Chapter 7: Employing Robotics for the Biomechanical Validation of a Prosthetic Flipper for Sea Turtles as a Substitute for Animal Clinical Trials

Nick van der Geest: Conducted the research, designed the experiments, data acquisition, modelling, data analysis, interpretation, writing and editing

Lorenzo Garcia: Supervision, Conducted the research, designed the experiments, writing and editing

Co-Author Agreement

Nick van der Geest:

Lorenzo Garcia:

Roy Nates:

Daniel A. Godoy:

Alberto Gonzalez:

Fraser Borrett:

List of Publications Arising from Doctoral Thesis

van der Geest, N., Garcia, L., Nates, R., Godoy, D. New insight into the swimming kinematics of wild Green sea turtles (*Chelonia mydas*). *Sci Rep*, **2022**.
https://doi.org/10.1038/s41598-022-21459-y

van der Geest, N., Garcia, L., Nates, R., Gonzalez-Vazquez, A. Sea Turtles Employ Drag-Reducing Techniques to Conserve Energy. *J. Mar. Sci. Eng.* **2022**.
https://doi.org/10.3390/jmse10111770

van der Geest, N., Garcia, L., Borrett, F., Nates, R., Gonzalez-Vazquez, A. Soft-robotic green sea turtle (*Chelonia mydas*) developed to replace animal experimentation provides new insight into their propulsive strategies. *Sci Rep*, **2023**.
https://doi.org/10.1038/s41598-023-37904-5

van der Geest, N., Garcia, L., Nates, R., Borrett, F. New Insights into Sea Turtle Propulsion and Their Cost of Transport Point to a Potential New Generation of High-Efficient Underwater Drones for Ocean Exploration. *J. Mar. Sci. Eng.* **2023**.
https://doi.org/10.3390/jmse11101944

van der Geest, N., Garcia, L. Employing Robotics for the Biomechanical Validation of a Prosthetic Flipper for Sea Turtles as a Substitute for Animal Clinical Trials. *Biomechanics* **2023**.
https://doi.org/10.3390/biomechanics3030033

Acknowledgements

First and foremost, I extend my deepest gratitude to my parents, Gary and Bronwyn, for their unwavering support and dedication to my research, making what seemed like an insurmountable task manageable. My siblings Anton, Corry, Trystan, and Keegan also deserve special thanks for their generous donation of time, often on weekends, to assist with extensive testing, even sometimes sacrificing their own commitments to help.

I am profoundly thankful to my supervisors, Dr Lorenzo Garcia and Associate Professor Roy Nates, for their invaluable guidance and keen attention to detail in enhancing my work.

A heartfelt appreciation goes out to my co-authors Lorenzo, Roy, Dan, Alberto, and Fraser for their diligent efforts in producing five outstanding publications in top-tier journals.

I owe a significant debt of gratitude to Associate Professor David White and the Bio Design Lab for their comprehensive support, both financially and physically, right from the start of this project.

Special thanks to Catherine Crofts for imparting her knowledge on thesis formatting to us engineers and for the time she dedicated to refining my thesis.

I am immensely grateful to Blue Planet Marine for entrusting Dr Dan Godoy to lead our expedition in Australia's Great Barrier Reef.

Acknowledgement is also due to Gowing's Whale Trust and Gowing Bros for their role in organising our expedition and connecting us with key partners.

A warm thank you to Gennie Gilbert from the Cairns Turtle Rehabilitation Centre for their assistance during our expedition.

Additionally, a huge thank you to MAG Assembly and PSP LTD for their role in the manufacturing of robotic parts and the provision of materials.

Gratitude is extended to Zenith Technica for crafting our first sea turtle prosthesis.

Finally, the most profound thanks to my wonderful wife Lena, for her patience and understanding through the countless hours I dedicated to this research.

Ethics Approval

Approval to conduct filming of wild sea turtles in Australia's Great Barrier Reef was granted by the Great Barrier Reef Marine Park Authority and the Queensland Government on the 30th of June 2022 under permit number G21/45637.1. The permit can be viewed in Appendix E on page 165 of this thesis.

Chapter 1: Introduction

The boundless wonders of nature and its resultant biodiversity have perpetually captivated the scientific community. Among the myriad species that inhabit our planet, sea turtles stand out due to their exceptional swimming abilities and tenacity, navigating oceans for over a hundred million years. Nevertheless, although the biology of sea turtles dominates the literature, very little work has been produced to understand their intricate swimming dynamics, which masterfully meld power with elegance, remains elusive. This research journey, articulated across five sequential publications, endeavours to illuminate the lesser-known facets of sea turtle locomotion. To fill the prevailing knowledge void and unearth potential technological innovations inspired by the sea turtle's propulsion technique.

This thesis centres around four pivotal research questions chosen for their potential to augment understanding in biological science, mechanical engineering, and marine exploration. In the subsequent sections, we shall delve into these research questions, embarking on a journey to uncover the secrets hidden within the fluid strokes of the sea turtle's flippers. These questions are:

1. What characterises the aquatic locomotion of Sea turtles in their natural habitat, and how do they differ from those observed in juvenile individuals in captive environments?
2. Through what biomechanical and physiological mechanisms do Sea turtles generate efficient thrust for propulsion in their aquatic environments?
3. How does the morphology and movement of Sea turtle flippers manipulate surrounding hydrodynamic fields to influence their locomotion?
4. Can insights drawn from understanding the propulsion mechanisms of Sea turtles contribute to practical applications and the advancement of marine technologies?

As we navigate the depth of this thesis, each question serves as a beacon, guiding us deeper into the multifaceted world of sea turtle locomotion and its profound implications for both biology and technology.

The first research question aims to delineate the swimming kinematics of wild sea turtles and discern whether they differ from captive juveniles. Understanding the natural locomotion of these marine creatures in their native habitats would illuminate how environmental factors, evolutionary pressures, and physical maturity influence their swimming mechanics. Additionally, such an understanding can aid in developing husbandry practices and rehabilitation programs for captive and injured sea turtles. The comparison between the wild and captive individuals could offer insight into the potential behavioural and mechanical changes induced by captivity and how it influences the biomechanics of the animal.

The second research question probes into sea turtle locomotion's biomechanical and physiological aspects, specifically how these creatures produce efficient propulsion. Unravelling the intricacies of their swimming mechanism could pave the way for bio-inspired design principles in hydrodynamics and naval engineering. Moreover, understanding the energetic expenditure and efficiency of propulsion can shed light on the life history traits of these species, like migration patterns and foraging behaviours.

The third question seeks to dissect how sea turtles manipulate the flow fields around their flippers. This aspect of their swimming mechanism contributes to their agility and efficiency in water. Further exploration of this phenomenon could elucidate how the fluid-structure interactions facilitate the locomotion of marine creatures. From a broader perspective, understanding these interactions could revolutionise the designs of aquatic robots and submarines, optimising them for enhanced manoeuvrability and reduced energy consumption. Coupled with this, the focus on quantifying sea turtle locomotion in terms of the dimensionless values of the Reynolds and Strouhal numbers. The Reynolds number characterises the flow regime, signifying the role of viscous forces relative to inertial forces. The Strouhal number signifies the propulsive efficiency associated with the oscillatory motion of the flippers. Deciphering these dimensionless numbers' range and ideal values for sea turtles can provide a solid mathematical foundation for understanding their locomotion, contributing to comparative biomechanics and fluid dynamics. Moreover, it can help engineers design efficient marine vehicles and propulsion systems.

Finally, the fourth research question explores the potential of translating the insights gained from studying sea turtle propulsion to practical applications that may help advance ocean exploration technologies. Through millions of years of evolution, sea turtles have achieved an optimal balance between power and efficiency in their locomotion, which man-made technologies strive to emulate. By investigating these natural mechanisms and extracting bio-inspired principles, we could revolutionise the design and functionality of aquatic exploration equipment, enabling them to operate efficiently in challenging oceanic environments.

These research questions are relevant to the scientific community as they lie at the intersection of biology, physics, and engineering. The proposed research not only contributes to a deeper understanding of marine animal locomotion but also paves the way for innovations and inspiration in naval engineering and oceanic exploration. Furthermore, these inquiries are congruent with the growing field of biomimicry, wherein solutions to complex human problems are sought in nature's time-tested patterns and strategies.

The implications of this research extend beyond academia. Conservation efforts for sea turtles could greatly benefit from understanding the locomotive characteristics of these creatures. Additionally, advancements in ocean exploration technologies, guided by the principles of sea turtle propulsion, could catalyse a new era of marine research and resource utilisation.

Overall, the proposed research seeks to unravel the science behind the grace of sea turtle swimming, bridging the gap between nature's ingenuity and human innovation. By illuminating the potential for biomimetic applications in technology, this work advocates for a symbiotic relationship between scientific progress and natural preservation. By enhancing our understanding of the natural world, we can better appreciate its value, fostering a deeper commitment to its preservation for future generations.

1.0 Delimitations of the Study

This section delineates the specific boundaries and decisions that define the scope of this research.

1- Focus on a Specific Species and Habitat

The study concentrated on the green sea turtle, Chelonia mydas, within the Great Barrier Reef ecosystem. This specialised focus allowed for a detailed examination of this species in this habitat but limited the extrapolation of the findings to other species or environments.

2- Methodological Constraints

The research was characterised by the exclusive use of non-invasive techniques for data collection. This ethical choice, aimed at minimising disturbance to these endangered creatures, consequently limited the depth and breadth of biological data that could be obtained compared to more invasive research methods.

3- Budgetary and Equipment Constraints

Operating under a tight budget of $7000 NZD, the research faced constraints in terms of the quality and diversity of available equipment. This affected the construction of the robotic sea turtle 'Cornelia' and other research tools, potentially influencing the precision and complexity of the experiments conducted.

4- Time Constraints

The study's duration posed another limitation. The time-restricted nature of the research meant that long-term trends and developments in the behaviour and habitats of sea turtles could not be extensively explored.

5- Theoretical Framework Scope

The theoretical lens of the thesis was focused on specific areas within marine biology and biomechanics, emphasising propulsion mechanisms and physical movements. Consequently, other relevant areas of sea turtle biology were not within the purview of this research.

6- Use of a Robotic Model

Employing 'Cornelia' as a robotic model for sea turtle swimming provided valuable insights but also introduced limitations. The extent to which this robot accurately replicated the nuanced, organic movements of actual sea turtles may affect the generalisability of the results.

1.1 Thesis overview

1.2 Thesis organisation

This thesis is arranged as a methodical assortment of published peer-reviewed studies, methodically organised into a sequence of chapters, each building upon the findings of the last. As such, repetition of information may occur, with supplementary information found in the Appendices and Movies found by following the links provided. An instructive roadmap of this structured layout is depicted in Figure 1. Chapter 2 initiates a comprehensive review of the existing scholarly literature on sea turtles' kinematics and propulsion techniques, setting the academic foundation for the following studies.

Chapter 3 marks the beginning of my published research, detailing an extensive data collection initiative within the vibrant ecosystem of Australia's Great Barrier Reef. This pivotal chapter hones in on the green sea turtle species, Chelonia mydas, and examines their flipper movements during routine swimming activities, offering critical insights that respond directly to the first posed research question.

Moving forward, Chapter 4 presents an in-depth analysis of the upstroke movement of the sea turtle's flipper. It carefully interprets the data obtained from the naturalistic observations detailed in Chapter 3, advancing our understanding and partially unravelling the intricacies of the second and third research questions.

Chapters 5 and 6 represent an integrative phase of the thesis, where the separate strands of data from the preceding chapters are woven together to assess the sea turtles' complete swimming cycle. This is achieved through innovative experimental procedures involving our robotic sea turtle surrogate, 'Cornelia.' These experiments are critical in providing a holistic view of the swimming dynamics, directly addressing research questions two and three while also intersecting with the fourth question, which concerns the practical applications of our findings.

In Chapter 7, the narrative shifts towards the translational impact of the research, exploring the feasibility and design considerations of a prosthetic flipper that could assist sea turtles who have lost limbs. This chapter is devoted to the pragmatic application of the accumulated knowledge from the thesis and endeavours to provide a solution to the final research question.

Chapter 8 concludes the thesis, offering an extensive discussion synthesising the insights gleaned from the entire body of work. It critically analyses the conclusions drawn from the research and extrapolates them to envisage prospective directions for future scientific inquiries. This concluding chapter not only situates the entire thesis within the more comprehensive scholarly conversation but also highlights potential pathways for future research, signalling ongoing advancements in the field of marine biology and bionics.

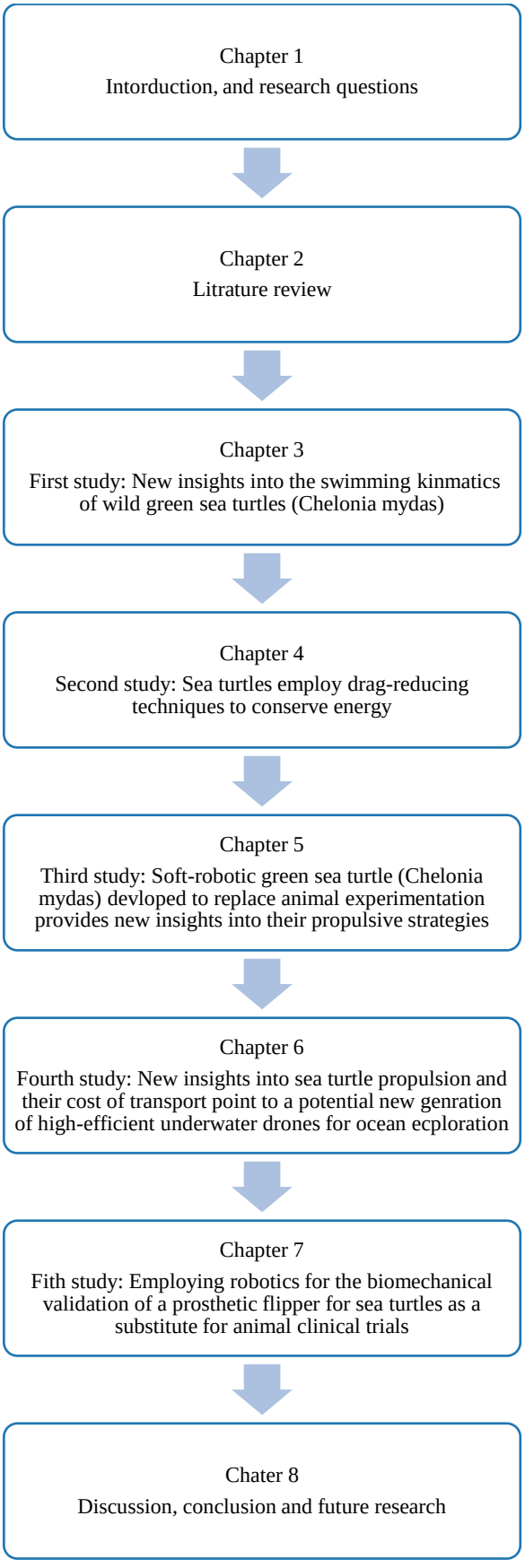

Figure 1: Thesis structure

1.3 Thesis methodology

The methodological foundation of this thesis is defined by its commitment to non-invasive research techniques, a decision that presents both a significant advantage and a limitation. The choice to employ only non-invasive methods was rooted in an ethical commitment to the welfare of the sea turtle species, which face the threat of endangerment. This ethical stance reflects respect for the biological subjects of the study but also aligns with the increasing global advocacy for humane research practices.

One of the primary justifications for this approach is facilitating a more streamlined data collection process. By eliminating the need for invasive procedures, the study sidestepped the protracted and often unpredictable animal ethics approval process, which can introduce substantial delays to research timelines. This efficiency is particularly valuable in conservation biology, where time-sensitive data influences policy and intervention strategies.

Moreover, non-invasive observation allowed for capturing sea turtles' behaviour within their natural habitats, a crucial aspect considering that behaviour in the wild often differs from that observed in captivity. Such authenticity in behavioural data is indispensable for understanding the true nature of these creatures in their ecological context, which is the bedrock of ecological and ethological research. While this method precludes the acquisition of certain types of biological data that would require physical interaction with the animals, it also eliminates the variable of human interference, which can often skew natural behaviours.

Financial constraints further shaped the methodology. With only $7,000 NZD available, the project required innovative approaches to both the development of research tools and the execution of the study. The construction of 'Cornelia,' the robotic sea turtle, serves as a testament to the resourcefulness necessitated by the budget. The robotic model provided a controlled means to study sea turtle locomotion without incurring the ethical and financial costs of using live animals in a laboratory setting.

The budget also mandated that all testing equipment be designed and built in-house. This self-reliance fostered a deep understanding of the research tools, enabling customisation and adaptation to the study's specific needs, which off-the-shelf solutions could not provide. While acknowledging that these custom-built tools may not align with established industry benchmarks, it is crucial to recognise that innovation often arises from working within limitations. The equipment was meticulously tested and calibrated to ensure that, despite its unconventional genesis, it would yield data of the highest integrity.

In conclusion, the methodological choices made in this thesis are justified by the ethical imperative to conduct humane research, the need for ecological validity in behavioural observations, and the innovative spirit engendered by financial limitations. The results presented are the culmination of a research process that was as much about overcoming challenges as it was about studying sea turtle locomotion, and they stand as a robust contribution to the field, achieved with integrity and a commitment to professional standards.

Chapter 2: Literature Review

The study of sea turtle biomechanics reveals an extraordinary resemblance to the mechanics of bird flight. These aquatic reptiles utilise a blend of gliding and flapping motions with their forelimbs, not unlike birds, to produce the forces necessary for aquatic flight. Moreover, phylogenomic analysis has recently placed turtles as the sister group to birds, suggesting a shared evolutionary path[1]. However, there is a significant distinction in their mechanics. Birds are entirely dependent on lift generation to sustain flight, whereas sea turtles have the ability to modulate their buoyancy, achieving near-neutral buoyancy[2], which negates the absolute necessity for lift.

The propulsion of sea turtles is mainly attributed to the downstroke of their forelimbs, where their uniquely shaped flippers reminiscent of the cambered aerofoil found in aircraft come into play[3-5]. This motion, which is characteristically more vigorous during the downstroke than the upstroke, has been typically described to produce a figure-of-eight trajectory[3,5-7]. A pivotal role in sea turtle underwater flight is the angle of attack (AOA) that sea turtles use on their pectoral flippers. The AOA is of particular interest because it is essential for creating the hydrodynamic forces necessary for swimming. This AOA has typically only been portrayed for the wing tip[3-5]. However, sea turtles do not rotate their flippers with a constant value but twist them to generate a gradient of values across the wing span. This gradient could be a critical factor in the efficiency and manoeuvrability of their swimming[8-13].

The ability to vary the AOA offers a potential explanation for the sea turtle's exceptional swimming proficiency. By adjusting the twist of their flippers, they might fine-tune their propulsion to suit different swimming speeds or manoeuvring requirements. This could be particularly advantageous during long migratory passages where energy conservation is vital, or when navigating through complex environments such as coral reefs or coastal shallows.

Given the potential importance of the flipper's twist, a critical question arises: How does this variability in the flipper's twist contribute to the sea turtle's overall swimming mechanics, and why is understanding this twist crucial for our broader comprehension of sea turtle biomechanics and hydrodynamics? Unravelling the specifics of this mechanism may not only answer questions about the sea turtle's migratory efficiency but could also inform the design of aquatic robots and propulsion systems that mimic biological entities, enhancing their performance and energy efficiency.

The migratory behaviour of sea turtles, with journeys extending thousands of kilometres[14-16], is one of nature's marvels. A quantitative model of their swimming could shed light on whether their locomotion contributes to their migratory success. While previous studies have used two-dimensional models to represent turtle-inspired swimming styles[17-19], these models may not fully capture the three-dimensional hydrodynamic features that are essential for accurate propulsion, which are heavily influenced by kinematic factors[20-22].

The natural swimming patterns of sea turtles have been studied[3,5,23-27], yet these studies often rely on observations of young turtles in captivity, which may not accurately represent the behaviours of wild, adult sea turtles. This is evident when comparing works by Davenport et al.[3] and Yasuda et al.[28], with Davenport et al. [3] reporting on flapping frequencies of juveniles around 1Hz and Yasuda al. [28] reporting flapping frequencies of approximately 0.23Hz in wild adults. Thus, if the flapping frequency has such a sparse difference, what other features in

terms of flipper motion differ between captive juveniles and wild adults? As such, the comprehensive mathematical characterisation of the locomotion of wild sea turtles remains incomplete. There is a particular gap in understanding how these patterns might differ between a juvenile in captivity and an adult in the wild. Filling this knowledge gap could provide deeper insights into the biomechanical strategies that underpin the sea turtle's long-distance navigation and its evolutionary success.

The phenomenon of sea turtle migration presents an intriguing biological puzzle, especially considering their diet is predominantly composed of low-energy foods[29-33]. These foods include jellyfish, sponges, and algae, which provide minimal caloric intake compared to the high-energy demands of long-distance travel. Despite this apparent contradiction, sea turtles embark on epic journeys across the oceans. The exact mechanisms that enable them to achieve such remarkable migratory feats remain something of a mystery, but their unique swimming strategies may play a significant role in their ability to travel vast distances[34].

Research into the flipper motion patterns of sea turtles has frequently observed that the downward motion of their stroke, or the downstroke, occurs at a rate nearly double that of the upward motion, or the upstroke[3-5]. This difference in speed suggests distinct functions for each phase of the stroke cycle in sea turtle locomotion. The role of the upstroke in sea turtle swimming has been a subject of debate among marine biologists and biomechanics researchers[3-5,27]. Some suggest that the upstroke serves as a feathering stroke a recovery phase that positions the flippers for the next downstroke with minimal resistance against the water. Others argue that the upstroke contributes to thrust production, albeit in a more subtle manner than the downstroke. The upstroke may not be as visibly powerful, but it could play a critical role in maintaining the turtle's forward momentum by generating lift and controlling the animal's pitch and position in the water.

This debate is not merely academic; it has practical implications for our understanding of sea turtle physiology and the conservation strategies that might be employed to protect these animals. If the upstroke is indeed used for thrust production, it would indicate a higher overall energy expenditure for swimming, which must be accounted for in the turtles' energy budgets. This, in turn, affects how we interpret their feeding habits, migratory patterns, and the potential impacts of environmental changes on their well-being.

Moreover, resolving this debate could enhance the development of bio-inspired robotic designs. If engineers can accurately replicate the mechanics of sea turtle swimming, they could create more efficient underwater vehicles for research and exploration. Thus, a clear understanding of the upstroke's function in sea turtle locomotion remains a valuable pursuit for both biological and technological advancements.

The mechanics of locomotion in both aerial and aquatic animals often involve the creation of complex vortex patterns in their wake, which is critical for effective propulsion. A particularly intriguing phenomenon observed is the generation of a reverse von Karman vortex street. This pattern arises from the strategic shedding of counter-rotating vortices at the outermost points of an animal's stroke cycle, whether it be from the flapping of wings in birds or the undulation of caudal fins in fish[35-40]. The precise timing and interaction of these vortices are what allow high-momentum jet flows to form, cleverly converting what would be drag into additional thrust, thereby enhancing the animal's propulsion efficiency[35].

Sea turtles, however, exhibit a distinctive asymmetry in their flipper oscillations[3-5]. This asymmetry in stroke could suggest a deviation from the typical vortex shedding patterns seen in other species. It raises questions about the extent to which sea turtles can harness the reverse von Karman vortex street to their advantage. Given this potential deviation, the intriguing question emerges: What evolutionary adaptations have sea turtles developed that allow them to maintain efficient propulsion despite this apparent mechanical divergence?

Further investigation into the hydrodynamic implications of the sea turtles' asymmetric flipper oscillation is essential. These studies could reveal whether sea turtles have developed unique methods of vortex manipulation or if they employ entirely different mechanisms to achieve their graceful and enduring swimming ability. The exploration of these evolutionary techniques is crucial not only for the field of biomechanics but also for the broader understanding of adaptation and survival in the marine environment.

A hypothesis by David T. Booth[4] suggests that the downstroke of a sea turtle's flipper may serve a dual purpose, generating both lift-based and drag-based propulsion contingent on the flipper's angle of attack. Lift-based propulsion is akin to an aeroplane's wing, creating an upward force that can be tilted to drive the animal forward, while drag-based propulsion is generated by pushing against the water directly. However, a detailed understanding of what these types of propulsion look like in sea turtles and the accuracy of this hypothesis remains a gap in the current research.

To date, no comprehensive studies have illustrated the flow features and fluid dynamics that sea turtles exploit during their downstroke, incorporating authentic sea turtle kinematics. Although there have been analyses on simplified 2-dimensional turtle-inspired models[17,18], these studies cannot capture the complexities of 3-dimensional effects. These effects include spanwise flow and Coriolis forces, which are pivotal in biological flapping mechanisms[21,41].

For over two decades, it has been recognised that the leading edge vortex (LEV) is a cornerstone of high-performance force generation in biological flapping wings[41-43]. This phenomenon has been observed across various animal species, both flying and swimming[42-45], with insect flight a conundrum until the LEV's role was discovered[42]. The LEV, a spiral of air or water that forms at the leading edge of a moving flipper or wing, significantly enhances lift and thrust by delaying stall and reattaching flow to the wing or flipper's low-pressure side[43,46-48].

Despite the extensive research on LEVs in the context of flapping wings, there seems to be a significant lack of such studies focused on LEVs during the downstroke of sea turtles using accurate sea turtle kinematics. This gap highlights a need for research that could explain how sea turtles, with their unique flapping kinematics, might produce or utilise LEVs for efficient propulsion. Understanding this could clarify Booth's hypothesis[4] and contribute to biomimetic designs in underwater vehicle propulsion, where replicating such natural hydrodynamic strategies could lead to breakthroughs in efficiency and manoeuvrability.

The investigation into the existence and function of LEVs in sea turtles' downstrokes necessitates intricate, multidimensional modelling and empirical research that can accurately replicate the flippers' movement in three-dimensional space. Such work could revolutionise our understanding of marine locomotion and inform conservation strategies for these ancient mariners by providing insights into how they perform their prodigious migrations with apparent ease. Given the ecological importance and endangered status of many sea turtle

species, filling this research void is not only scientifically significant but also crucial for the preservation efforts of these remarkable creatures.

Navigating the ethical landscape of research involving endangered species like sea turtles presents significant hurdles, primarily due to the stringent requirements for obtaining necessary approvals. Such considerations are crucial, as the well-being of these animals must be at the forefront of any scientific inquiry. Once ethical clearances are granted, further complications arise; sea turtles may not exhibit their natural swimming behaviours within the constraints of captivity, leading to potential biases in data collection.

To sidestep these ethical and practical challenges, researchers have turned to bio-inspired robotics, creating mechanical analogues to study biological phenomena[49-54]. These robotic models aim to shed light on the intricacies of their movement and energy efficiency. Robotic sea turtles have been produced before[55-61] however, despite these efforts, fully capturing the complexity of sea turtle locomotion has proven difficult. Previous robotic models were restricted to two degrees of freedom[56,59,62], falling short of emulating the full range of motion seen in living sea turtles. Although more advanced robots with three degrees of freedom have been introduced[55,58,60,63], the primary intention behind these creations was to demonstrate innovative technologies rather than to mimic sea turtle locomotion accurately in every detail.

Crafting a robotic sea turtle that authentically replicates the behaviour of its living counterpart presents two substantial engineering challenges. The first is the design of soft robotic flippers capable of dynamic shape adaptation, essential for achieving the optimal wing twist that living sea turtles use to navigate their watery realm. These flippers must also withstand significant flexural stresses from hydrodynamic forces, a task that rigid robots with complex jointed mechanisms find challenging. To address this, researchers have explored soft robotics, where simple material deformations can emulate the nuanced movements of biological entities[64-66].

The current landscape of soft wing-twisting technology generally follows two paths. One involves actuators such as shape memory alloys (SMA) or ionic polymer-metal composites (IPMC)[60,67,68], which, while innovative, at this point in time do not suffice to generate substantial hydrodynamic forces required for effective flapping motion that sea turtles can produce. The other integrates soft materials into a fundamentally rigid structure[49,52,69,70], enhancing the robot's ability to perform complex movements while bearing higher hydrodynamic loads. This approach, however, necessitates a more intricate design and manufacturing process.

The second challenge is to package the necessary mechanical components within the robot's limbs without compromising the authentic form factor of the sea turtle. This is a complex endeavour, as the robotic replica must be a near-perfect physical match to the actual animal to study its locomotion accurately. Yan et al.'s[61] recent work presents a turtle-like robot equipped with variable stiffness hydrofoils, which can adjust the rigidity along the flippers' span through a series of small interconnected rigid segments. Despite its innovative approach, this design has yet to capture a crucial characteristic of sea turtle flippers: the ability to smoothly twist along the span in a single, continuous motion. This feature is vital for maintaining the correct angle of attack across the entire flipper, a potential key to the animal's efficient swimming prowess.

Creating a robotic sea turtle that accurately mirrors the species' authentic movements and physical characteristics is not merely an academic exercise; it holds the potential to revolutionise our understanding and capabilities in marine engineering and biomechanics. The novelty of a realistic robotic sea turtle lies in its ability to provide insights into the complex locomotion strategies of these animals, which have evolved over millions of years to optimise energy efficiency for long-distance travel in the ocean.

A robot that can adjust its flipper stiffness and mimic the natural twisting motion could allow researchers to study the intricate hydrodynamics of sea turtle swimming without the ethical and practical challenges of working with live, endangered animals. It could serve as a dynamic model to test hypotheses about marine propulsion and energy efficiency, offering a window into the fluid-structure interactions that occur during the turtle's stroke cycle.

Moreover, by closely replicating the sea turtle's movements, such a robot could lead to the development of new underwater vehicles with unprecedented levels of efficiency and manoeuvrability. These bio-inspired designs could be used in various applications, from oceanographic research to environmental monitoring, search and rescue missions, and even military operations, all while minimising energy consumption.

The implications for conservation and ecological studies are also significant. Robotic sea turtles could be deployed to track real turtle migrations, gather data on ocean conditions, and monitor marine ecosystems with minimal disturbance, providing a sustainable option for long-term ecological monitoring.

In summary, a realistic robotic sea turtle could be a transformative tool for marine research and technology, offering a blend of ecological fidelity and engineering innovation. Its development would not only represent a leap forward in soft robotics and bio-inspired engineering but could also pave the way for sustainable solutions to explore and conserve our oceans.

Chapter 3: New insight into the swimming kinematics of wild Green sea turtles (*Chelonia mydas*)

3.0 Preface

The exquisite intricacies of movement exhibited by animals have always been a compelling research frontier. Among these, the locomotion of sea turtles, animals that elegantly traverse their aquatic habitats much like avian species do in the skies stands as a fascinating paradigm. While the biomechanics of captive juvenile sea turtles are well-documented, there is limited knowledge about how wild sea turtles navigate and move through the water.

Unravelling the biomechanics of these submerged sea-bound "birds" is an overwhelming task. As an endangered species, the ethical and technical complications of studying sea turtles make it a complex challenge to approach without causing a disturbance. This predicament leads us to a crucial research question: What characterises the aquatic locomotion kinematics of wild Sea turtles in their natural habitat, and how do they differ from those observed in juvenile individuals in captive environments?

To answer this, chapter 3 offers an innovative, non-invasive procedure to develop a comprehensive three-dimensional model of the kinematics of sea turtles. Utilising advanced underwater drone technology, we ventured into the heart of their natural environment Australia's Great Barrier Reef and studied these magnificent creatures with minimal intrusion.

3.1 Abstract

Biomechanically, sea turtles could be perceived as birds of the ocean as they glide and flap their forelimbs to produce the necessary forces required for locomotion, making sea turtles an interesting animal to study. However, being an endangered species makes studying the sea turtle's biomechanics a complex problem to solve, both technically and ethically, without causing disturbance. This work develops a novel, non-invasive procedure to develop full three-dimensional kinematics for wild sea turtles by filming the animals in Australia's Great Barrier Reef using underwater drones without disturbing them. We found that the wild animals had very different swimming patterns than previous studies on juveniles in captivity. Our findings show that the flipper goes through a closed-loop trajectory with extended sweeping of the flipper tip towards the centre of the carapace to create a clapping motion. We have named this the “sweep stroke” and in contrast to previously described four-stage models, it creates a five-stage cycle swimming locomotion model. The model presented here could lead to a better comprehension of the sea turtle propulsion methods and their fluid-structure interaction.

3.2 Introduction

The locomotory biomechanics of sea turtles share similarities with birds, given that they glide and flap their forelimbs to produce the necessary forces required for locomotion. In fact, in recent studies, phylogenomic analyses has shown turtles as the sister group of birds[1]. However, unlike birds who require lift generation to remain in the air, sea turtles can adjust their buoyancy to become almost entirely neutrally buoyant [2]. Thus, lift generation is not wholly required as their buoyant force may be sufficient. The forward thrust generated by turtles to swim has been shown to almost entirely occur during the downstroke, using their cambered aerofoil-shaped flippers [3,5]. The downstroke has been previously described as twice as fast as the upstroke, typically producing a figure-of-eight pattern [3,5-7]. Prior research has typically illustrated that sea turtles apply an angle of attack (AOA) of their pectoral flippers [3,5] so the animal can generate the necessary hydrodynamic loads for swimming. However, this is not entirely accurate as the flipper generates a variable AOA across their wingspan via twisting of the forelimb.

Sea turtles are migratory species with end-to-end journeys of thousands of kilometres [14-16]. Having a mathematical representation of their swimming locomotion would greatly help answer whether or not the sea turtle's swimming style is a factor in their migratory success. Previous studies have applied simplified two-dimensional models of turtle inspired swimming styles [17-19]. However, hydrodynamic features that influence propulsion are highly dependent on the kinematics[20-22], which suggests that while the research done to date provides a rudimentary approach to help describe the propulsion mechanism, it does not contain all the related factors. Various studies have illustrated the natural sea turtle locomotion [3,5,23-27]. However, these studies often collected data on young juveniles held in captivity without describing the patterns in a mathematical form. Therefore, the natural swimming description of wild sea turtles is still unknown, along with understanding if it differs from a juvenile in captivity.

Developing a mathematical model to describe the turtle's natural flipper patterns is tremendously complex for several reasons. Among the difficulties, the most complex issue comes from producing a data collection from within their natural habitat to ensure their surroundings do not enforce an abnormal swimming pattern. The current state of the art techniques, such as X-ray Reconstruction of Moving Morphology (XROMM) [71,72], requires a unique set up that would be impractical to impossible to set up in a marine environment. Not only are techniques like this impractical, but receiving animal ethics approval to put an endangered species into a lab to study its biomechanics creates further hurdles.

This paper describes a non-invasive process to film sea turtle swimming patterns and forelimb twist through a video camera attached to a remotely operated underwater vehicle (ROV). The films formed the basis for generating 3D mathematical biomechanical pattern reconstruction. Filming sea turtles with an ROV has been done before [73,74]. However, to the best of our knowledge, this work is the first report of collecting and analysing turtle flipper kinematics using an underwater ROV. This paper also includes developing and applying an original data processing method to uncover the full 3D kinematics of the turtle flipper movement.

3.3 Methods

3.4 Data collection

3.5 Filming procedure and locations

To collect detailed data on the kinematics of wild turtles, it was decided to film them in their natural environment. Filming occurred over a three-week program at Australia's Great Barrier Reef, with the approach slightly altering depending on location. All permits and animal ethics approvals were obtained from the Australian Government Marine Park Authority (reference number G21/45637.1), with all methods performed in accordance with guidelines and protocols approved. Only green sea turtles (*Chelonia mydas*) were observed during this time. The first half of the data collection was accomplished at Fitzroy Island, Cairns, Australia, using an ROV shown in Fig. 1a deployed from the shoreline over shallow fringing reef. On average, four dives were made per day, each lasting approximately 30 minutes, recording the entire dive duration. The camera used was programmed to save the footage at 2 GB segments to minimise the chances of a total data loss. The ROV, on average, would travel 25-75m from the beach until turtles were observed.

A second location was established at Heron Island, Queensland, Australia, and the filming procedure was assisted with a rigid inflatable vessel to launch the ROV seen in Fig. 2a. Data collection follows the same routine described for the first location. However, the vessel was the launch platform enabling a higher degree of habitat and depth options to ensure a full suite of natural swimming behaviours were captured.

At all times, during the approach to a turtle, a distance was kept of approximately 5m to ensure the animal was undisturbed and continued with its usual swimming pattern. In general, the turtles showed no interest in the ROV and would continue the locomotion as usual. On rare occasions, we found that some turtles even showed interest in the ROV and approached it for closer inspection out of curiosity. The ROV was set in hover mode to allow the animal to interact when this occurred. Therefore, the recording was only made if the turtle was observed swimming in its general swimming pattern. This pattern was identified with the turtle producing complete oscillations of its pectoral fins with its hind flippers tucked in and pointing back to lower its pressure drag, captured in Fig. 2b. Filming was done from the side, front and rear viewpoints with the ROV following the turtle, matching its swim speed to keep the turtle centred on the camera lens. This process proved to work well for filming from the sides; however, the turtles would often adjust their swim patterns when attempting to film from the front or rear. Turtle swim speeds were estimated using a surface snorkeler holding a camera with GPS by following the turtles from the surface, as illustrated in Fig 2c. Swimming speeds of approximately 0.2 to 1m/s were observed and correlate well with previous research values [34,75-78].

Figure 2: Data collection. (a) ROV with external camera launched from the rigid inflatable vessel. (b), ROV user interface showing sea turtle applying general swimming routine, (c) Sea turtle swim speeds from GoPro GPS, with snorkelling assistance from the top. The photograph was taken at Fitzroy Island using the DJI fly IOS application with a DJI mini 2. https://www.dji.com/nz/downloads/djiapp/dji-fly .

3.6 Equipment specification and settings

The ROV used, (Chasing M2) was equipped with a 200m long tether connected to a handheld transmitter. The camera on the ROV was never used to film and only used for feedback to the operator. The system has a maximum dive depth of 100m, however, it was only used to 2-30m. The system is equipped with 8 EDF thrusters to allow 6 DOF allowing the ROV to manage ocean currents with speeds up to 1.5 m/s. A 3D printed adaptor was manufactured to enable an extra camera to be mounted to the ROV chassis. The camera (Paralenz, Vaquita) was set up to film at full HD 1080P, 240 frames per second, allowing smooth slow-motion footage. The footage was stored to a 128GB SanDisk extreme pro micro SD card. The camera was selected as the best option available because its slim rugged aluminium body did not require a waterproof case. Additionally, it is equipped with a distortion-free lens and higher frame rate compatibility compared to other cameras available at the time.

3.7 Data processing

3.8 Data preparation

The challenge in this work was to extract the absolute motion of the flipper with respect to the straight carapace length (SCL). The SCL illustrated in Fig. 3a was used as the reference frame of motion due to it being a rigid body and thus not changing in size. Side view footage was prioritised due to its more accessible collection, and additionally, this orientation allowed for a clear sight of the turtle's flipper tip for all values of time. The film footage was edited in software (VideoPad Professional, NCH Software). This process involved snipping and exporting the content into individual images that matched the film frame rates. Thus allowing detailed photos of the flipper position with respect to time. Using a CAD system (Solidworks 2019 SP5), the photos were imported using the "sketch picture" feature and sorted in the design space at 0.1 second time intervals shown in Fig. 3b. A single image was selected for creating a 2D spline around the turtle carapace. This 2D spline was then placed over each image to ensure each image was not distorted and suitable for data collection seen in Fig. 3c. This process also gave a reference coordinate system to ensure the data could be accurately knitted together. After confirmation that each frame was appropriate, a data point could be placed on the turtle's flipper tip for every image as per Fig. 3d. An assembly could then be made off each flipper tip point using the 2D spline of the carapace as a reference geometry observed in Fig. 3e. This process ensured the flipper tip position was accurately positioned with respect to the turtle's carapace and time. After completion, a CAD part file was produced containing the data assembly. The process was repeated from seven separate sets of film ,

five sets from Fitzroy Island and the remainder from Heron Island, Australia. A similar process was applied to the front view film however, only four specimens were successfully obtained.

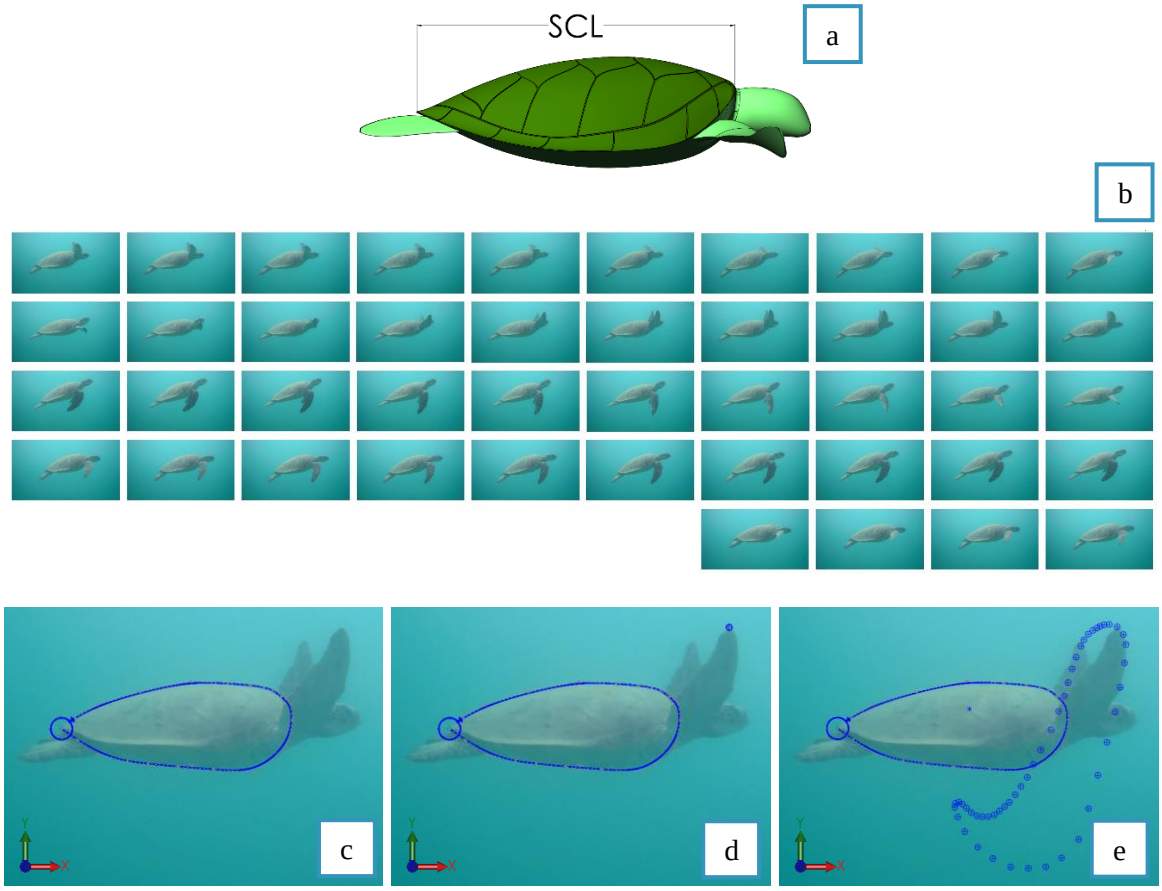

Figure 3: Data preparation illustration. (a) Sea turtle straight carapace length measurement (b), photos of turtle at 0.1-second intervals; (c), 2D spline around turtle carapace to serve as reference geometry; (d), Datapoint placed at flipper tip; (e), Assembly of data points with reference to carapace and time.

3.9 Data 3D conversion

Turning the 2D flipper paths into a 3D example required an iterative and repetitive process of assembling links representing the turtles' humerus (shoulder to elbow) and forearm (elbow to flipper tip) displayed in Fig. 4a. The links were modelled in Solidworks as individual part files ".SLDPRT". The size of each link was determined by identifying the position of the turtle's shoulder, elbow, and flipper tip from the side and frontal film with film images imported into CAD scaled to SCL of approximately 610mm. To ensure the links modelled in CAD representing the humerus and forearm were anatomically correct in length, comparisons were made with a real sea turtle's skeletal anatomy, as seen in Fig. 5b. A Solidworks assembly was then created ".SLDASM." to assemble the links into a simplified 3D limb (Fig. 4a). The assembled limb could then be rotated in a SolidWorks assembly from the turtle's shoulder and elbow joints into position by simultaneously using the 2-dimensional data and the correspondent interval of the video footage from the side and front views to constrain the

possible limb movement seen in Fig. 4b. This process was followed for each data point creating a full 3D representation of the turtle's stroke, as illustrated in Fig. 4c. From here, a new "SLDPRT" file could be generated consisting of the 3D data point with respect to time represented in Fig. 4d. These points consisted of the flipper tip, elbow and shoulder and were created by starting a "3D sketch" and mating each point concentrically to the joints and rotation point of interest from Fig. 4c.

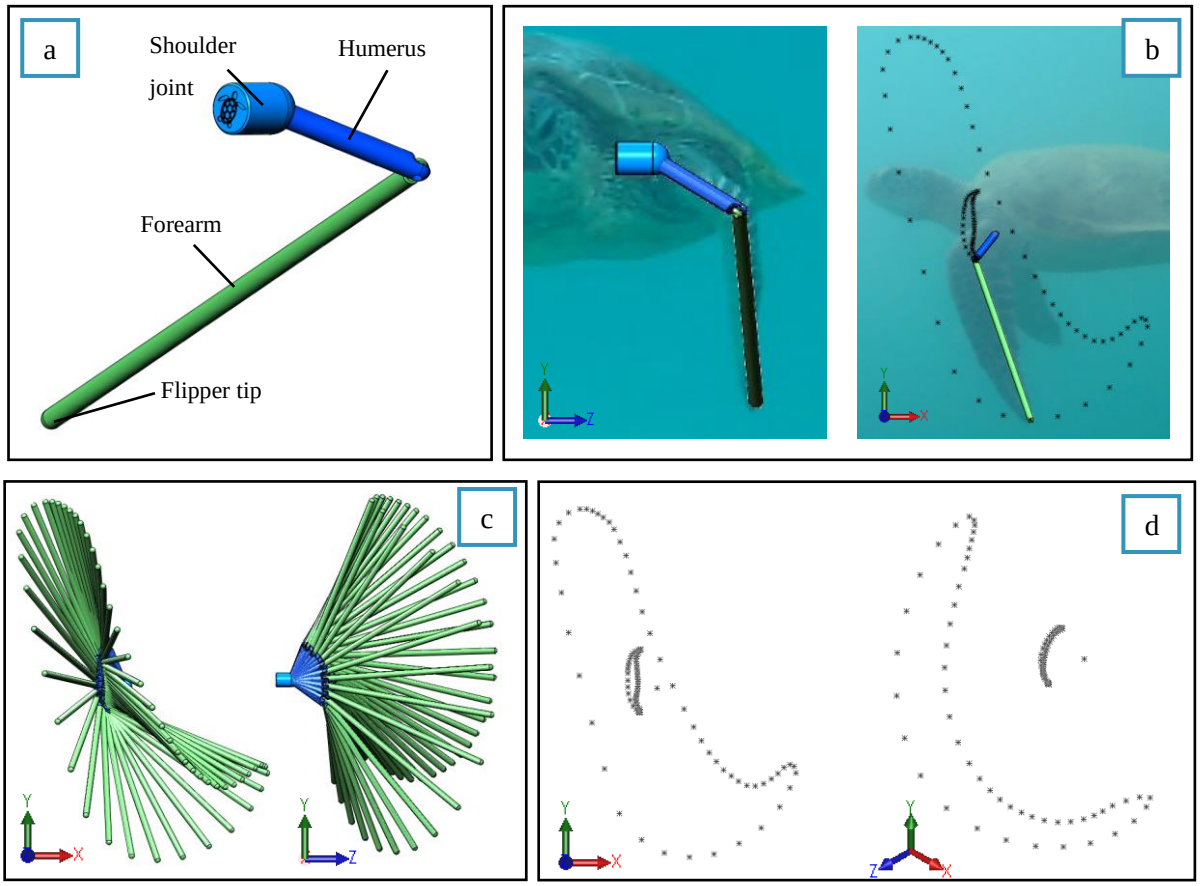

Figure 4: Data preparation. (a), Simplified sea turtle limb; (b), Rotation of limb in CAD, into 3D positions using 2-dimensional front and side data for reference; (c), Complete limb motion assembly viewed from xy and zy planes; (d), Conversion of limb motion into x,y,z data points of the flipper tip, elbow and shoulder rotation point, viewed from xy plane and an isometric viewpoint.

3.10 Data postprocessing

The "SLDPRT" file containing all the data points along the x,y,z axis were exported as a ".igs" file type. This file type allows the data to be viewed and cleaned up in a simple text processing software (Notepad). The data was then imported into a numeric computing suite (Matlab) to have a "Fourier series" fitted with the x, y and z data represented by “equation (1-3)”:

$$x(t) = s_f(a_x + \sum_{i=1}^{n} a_{ix}\, cos(iw_x t) + b_{ix}\, sin(iw_x t)) \quad \textbf{(1)}$$

$$y(t) = s_f(a_y + \sum_{i=1}^{n} a_{iy}\, cos(iw_y t) + b_{iy}\, sin(iw_y t)) \quad \textbf{(2)}$$

$$z(t) = s_f(a_z + \sum_{i=1}^{n} a_{iz}\, cos(iw_z t) + b_{iz}\, sin(iw_z t)) \quad \textbf{(3)}$$

The Fourier coefficients were solved with the Matlab function "fourier8" to give the functions eight terms with the time variable defined as the frame rate used to collect the original data. A variable "s_f" was added to the functions to allow a scaling factor to be applied to modify the functions to suit various sized turtles. Appling a "s_f" equal to one was representative of a turtle with SCL equal to 610mm and was defined as:

$$s_f = \frac{s_d}{610} \quad \textbf{(4)}$$

Where s_d is the desired SCL in mm if scaling should be required. To understand the flipper rate of change in position and velocity, the position functions were differentiated with respect to time to create the flipper velocity, “equation (5-7)” and acceleration expressed as "equation (8-10)”:

$$\dot{x}(t) = s_f(\sum_{i=1}^{n} -iw_x a_{ix} \sin(iw_x t) + iw_x b_{ix} \cos(iw_x t)) \quad \textbf{(5)}$$

$$\dot{y}(t) = s_f(\sum_{i=1}^{n} -iw_y a_{iy} \sin(iw_y t) + iw_y b_{iy} \cos(iw_y t)) \quad \textbf{(6)}$$

$$\dot{z}(t) = s_f(\sum_{i=1}^{n} -iw_z a_{iz} \sin(iw_z t) + iw_z b_{iz} \cos(iw_z t)) \quad \textbf{(7)}$$

$$\ddot{x}(t) = s_f(\sum_{i=1}^{n} -(iw_x)^2 a_{ix} \cos(iw_x t) - (iw_x)^2 b_{ix} \sin(iw_x t)) \quad \textbf{(8)}$$

$$\ddot{y}(t) = s_f(\sum_{i=1}^{n} -(iw_y)^2 a_{iy} \cos(iw_y t) - (iw_y)^2 b_{iy} \sin(iw_y t)) \quad \textbf{(9)}$$

$$\ddot{z}(t) = s_f(\sum_{i=1}^{n} -(iw_z)^2 a_{iz} \cos(iw_z t) - (iw_z)^2 b_{iz} \sin(iw_z t)) \quad \textbf{(10)}$$

3.11 Flipper twist model

The skeletal structure that supports the motion of the sea turtle flipper from a mechanical viewpoint is homologous to the human arm skeleton seen in Fig. 5a-b. For example, in Fig. 5c, it can be observed that the human forearm can create a twist from the elbow to the fingertips without any rotation of the humerus. Based on this assumption and from evidence observed in our video footage, we hypothesise that the flipper twist can be modelled to take place between the turtle elbow joint and flipper tip.

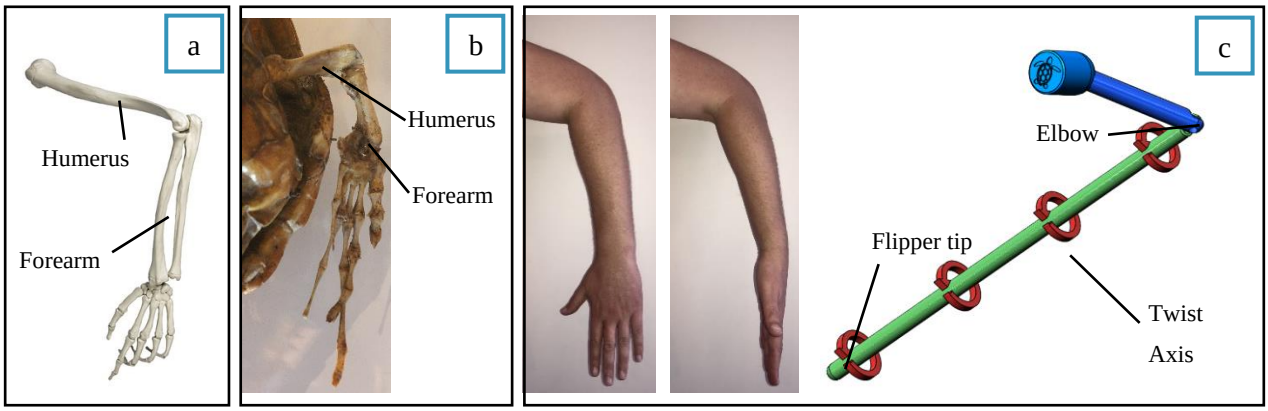

Figure 5: Human and Sea turtle skeleton. (a), Human arm skeleton (created by Henri et George/Shutterstock.com); (b), Hawksbill Sea turtle flipper skeleton. (c) Forearm rotation example.

The twist angle $\theta(t)$ shown in Fig. 6c was defined using the right-hand rule based on the plane that intercepts the humerus and forearm with zero degrees in line with the horizontal x-axis of that plane. The amount of twist produced by the turtles was identified by comparing a detailed CAD geometry with the film images at various points along the upstroke and downstroke, as seen in Fig. 6a-b. The CAD geometry was twisted, keeping constant mass and volume until it closely matched the turtle's flipper in the film. The twisting of the CAD model was achieved using the Solidworks tool "Flex" by twisting the flipper geometry between a plane from the elbow to the flipper tip illustrated in Fig. 5c. The twist angle used was then numerically stored with respect to time for the postprocessing operations. Matlab was used in the same process as the previous section, fitting a function of flipper twist with respect to time. However, a piecewise function based on a Fourier series was used as "equation (11)":

$$\theta(t) = \begin{cases} -72.4, & 0 \le t < 0.84 \\ \sum_{n=i}^{n} a_{dsi}\, sin(b_{dsi}t + c_{dsi}), & 0.84 \le t < 2.436 \\ 27.9, & 2.436 \le t < 3.612 \\ \sum_{n=i}^{n} a_{usi}\, sin(b_{usi}t + c_{usi}), & 3.612 \le t < 4.2 \end{cases} \quad \textbf{(11)}$$

$$\theta(x) = \frac{\theta(t)}{s}x \quad \textbf{(12)}$$

Where $\theta(t)$ represents the angle of twist in degrees, the coefficients a, b and c are solved using the Matlab functions, "sin5" and "sin6" to give five and six terms to each function. The exact amount of flex on any point of the turtle's flipper could then be found applying "equation (12)", where x is the position of interest on the turtle wingspan (s).

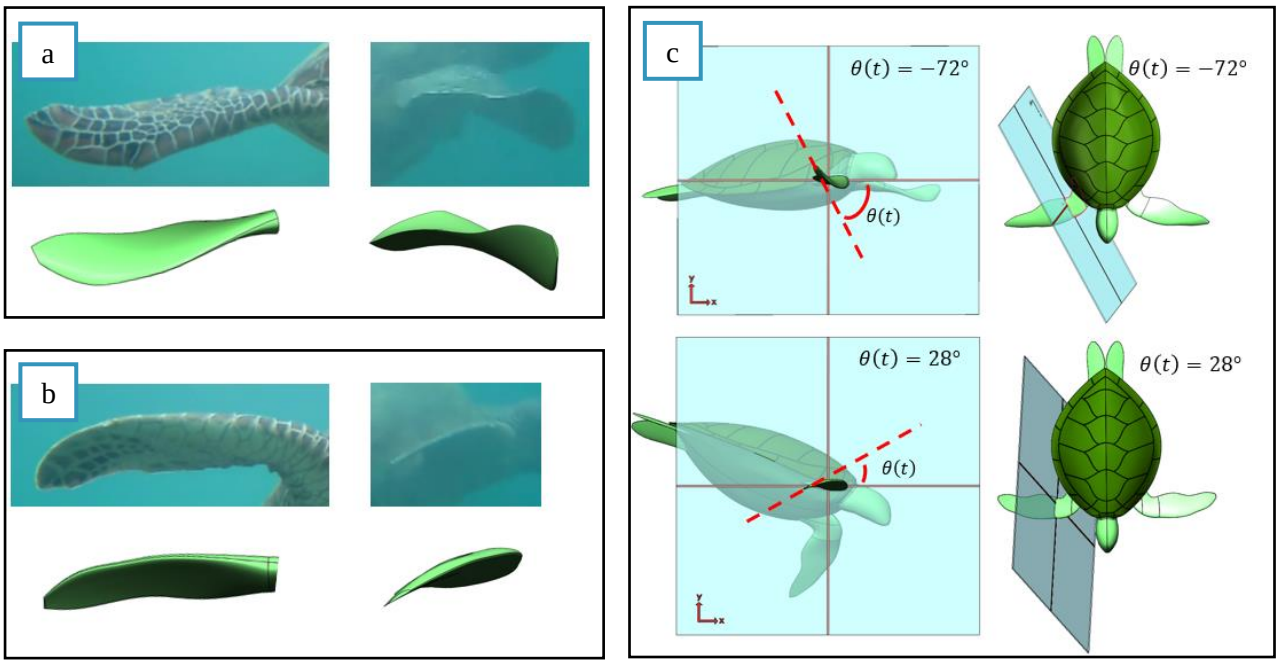

Figure 6: Flipper twist. (a), Downstroke twist of -72˚; (b), Upstroke twist of 28˚; (c), Reference plane with **0°** *being inline with the horizontal x-axis of the elbow cross-section, additionally showing how the plane moves with the turtle flipper to remain normal to the rotation axis.*

3.12 Results and Discussion

3.13 Swimming pattern characteristics

Approximately one terabyte of film was collected during the period of observation. The suitable film sets were identified by sea turtles producing full locomotion pattern of the forelimb, as earlier described. Therefore, from the total amount of footage collected, we found only seven film sets were appropriate for side views, while four film sets were appropriated for front views. This selection process reduced the data from approximately one terabyte to two gigabytes and a total of eleven sets of film.

Observations showed that all turtles filmed (meaning the eleven above-mentioned selected sets) swam with the same general pattern as shown in Fig. 7, which resembles a closed loop with extended sweeping of the flipper tip towards the centre of the carapace from the Sagittal plane. At no time was the figure-of-eight pattern observed in the Sagittal plane previously reported by others [3,5-7]. However, the complete figure-of-eight pattern is evident from the Transverse and Coronal planes. The average limb beat cycle was 4.2 ± 0.32 seconds, closely matching observations from past research [34,79]. As observed in Fig. 7, we have broken down the flipper motion into five stages, "Downstroke (DS)", "Sweep stroke (SS)", "recovery stroke one (RS1)", "upstroke (US)", and "recovery stroke two (RS2)". The stages are defined based on the flipper tip position in the Sagittal plane, as this was the only viewpoint that gave a clear line of sight to the flipper tip for all values of time. To help simplify comparing each of the turtle's swim patterns, the percentage of time spent in each of the five stages was compared. Table 1 outlines the time spent in each of the five stages from observed swimming patterns in wild animals. Our findings show that regardless of the turtle observed, limb beat

frequency and ocean current, the flipper's percentage of time spent in each of the five motion stages was very similar.

Table 1: Amount of time the flipper tip spends in each of the five stages. Data from the Sagittal plane. Refer to supplementary Fig. S1 for swimming patterns.

Sea turtle film sets and location	DS (s)	SS (s)	RS1 (s)	US (s)	RS2 (s)	Limb beat cycle (s)
1 (Fitzroy Island)	0.9	0.8	0.9	1.1	0.6	4.3
2 (Fitzroy Island)	0.9	0.7	0.8	1.2	0.6	4.2
3 (Fitzroy Island)	1	1	1	1.3	0.7	5
4 (Fitzroy Island)	0.8	0.8	0.7	1.1	0.5	3.9
5 (Fitzroy Island)	0.7	0.7	0.8	1.1	0.4	3.7
6 (Heron Island)	0.7	0.9	0.7	1.2	0.9	4.4
7 (Heron Island)	0.8	0.7	0.7	1.2	0.5	3.9

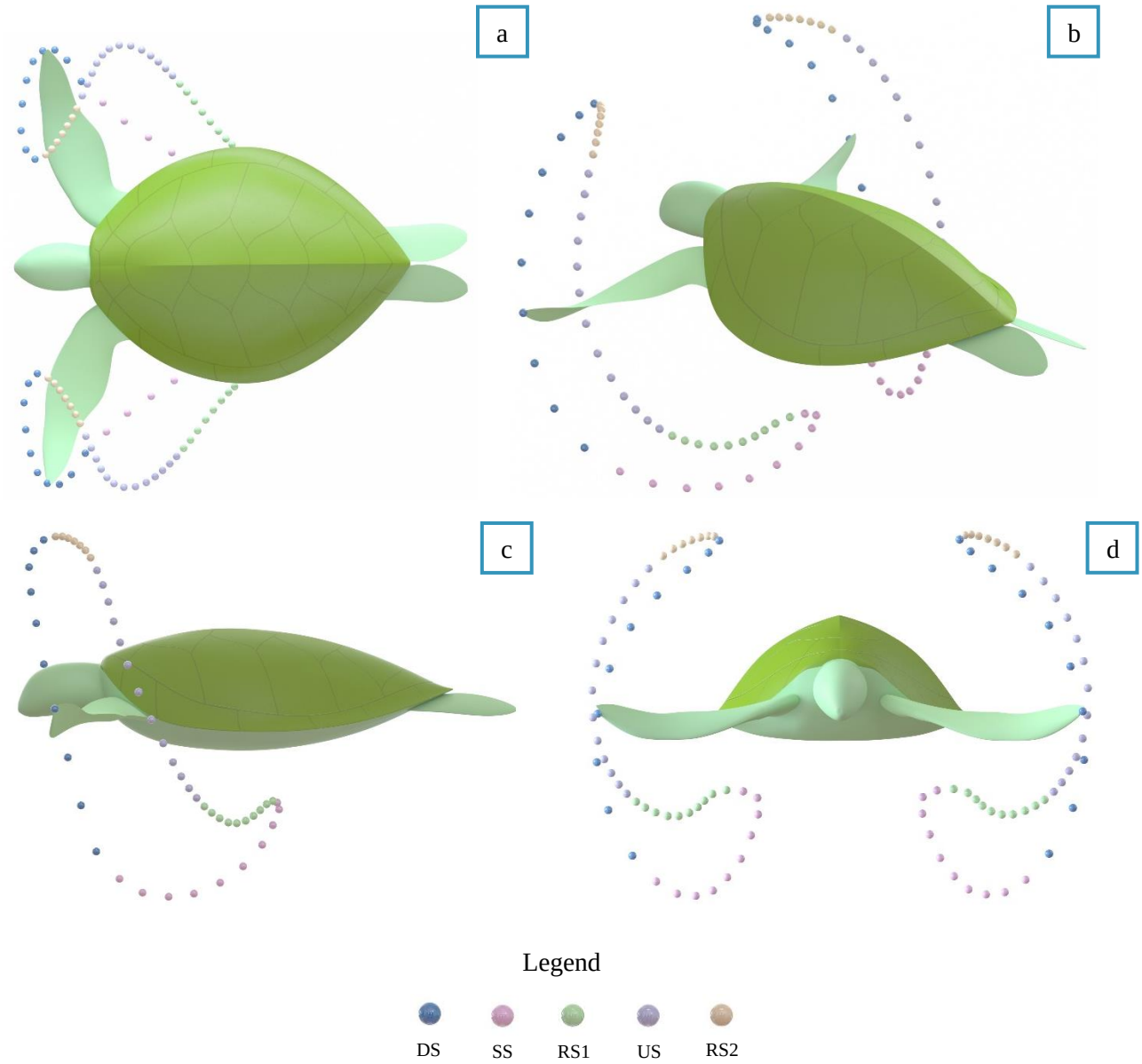

Figure 7: Complete 3D reconstruction of flipper tip motion from observational video.Data spheres represent 0.084 second time increments. When viewing from the Sagittal plane, the five stages can be characterised as follows: The downstroke (DS) is characterised by the fastest flipper motion with a slight reward motion. Sweep stroke (SS) is characterised by substantial horizontal displacement towards the centre of the carapace. Recovery stroke one (RS1) is characterised by slow-moving and modest horizontal displacement to recover the flipper into position for the upstroke. The upstroke (US) is characterised by a slow, predominantly straight path with slight forward motion. And finally, recovery stroke two (RS2) is characterised by the slowest moving section of the stroke to ready the flipper for the fast-moving downstroke. (a), View from Coronal plane. (b), 3D View, (c), View from Sagittal plane. (d), View from Transverse plane.

3.14 General swimming model

This section will continuously refer to Fig. 8-9, which details the flippers five stages of motion. All plots are representative of a turtle with SCL equal to 610mm and "s_f" equal to one. During the “DS”, the flipper tip and elbow roll down together, creating the fastest part of the limb beat. The flipper twist during the DS is at its most aggressive average angle of -72.4 ± 2.5º, with the elbow going through its most significant displacement during this time. As viewed from the Sagittal plane, the flipper tip takes a mostly straight path, making up 19.7% ± 1.4% of the limb cycle. The “SS” movement starts when the humerus begins to slow, and the elbow accelerates the forelimb in a curved sweeping motion until the flipper tip reaches approximately half the carapace length. During this stroke section, the flipper twist rotates to 0º, bringing the two flippers parallel beneath the carapace. It can be observed that the elbow begins to rise before the forelimb reaches the end of the SS, creating a clapping motion similar to sea lions [50]. Overall the SS made up 19% ± 1.1% of the limb cycle. “RS1” is a slow-moving motion of the humerus and forelimb to allow the turtle to get itself ready for the upstroke by flexing the forelimb to an average value of 27.9 ± 4.8º. Overall the RS1 made up 19% ± 1.5% of the overall limb cycle. The “US” occurred at approximately 50% of the downstroke speed, matching previous findings [3]. During the entire US, a steady flipper average twist of 27.9 ± 4.8º was observed. Overall, the US made up 28% ± 1.4% of the limb cycle and looked entirely passive in motion. The final section, "RS2", is the slowest moving of the limb beat cycle. During this process, the flipper twist travels through its most extensive Rotation from 27.9 ± 4.8º to -72.4 ± 2.5º, making up 14% ± 2.2% of the overall limb cycle. The possible reason for the slow movement of RS2 is to help reduce turbulence during the aggressive change in flipper twist, thus potentially lowering the drag coefficient.

3.15 Result verification

As the combination of separate sets of two-dimensional data creates uncertainty in the model, we help verify the results by graphically comparing our three-dimensional model with various footage sets of swimming turtles. Such verification shows a good visual correlation between all footage sets (Fig. 10a) and our model (Fig. 10b). As displayed in Fig. 10a, in four different specimens (Fig. 10a.1-a.4), though the flipper paths slightly differed from one turtle to the other, excellent correlations were observed between the five flipper stages, with the general swimming pattern evident in all specimens that produced complete wing oscillations. For instance, the blue spheres representing the downstroke, it can be observed this produces the fastest section of the limb cycle, with each sphere representing 0.1-second time intervals for Fig. 10a. Additionally, the downstroke can be seen producing a small reward horizontal motion. The pink spheres producing the sweep stroke can be observed in all specimens to produce large amounts of horizontal displacement in Fig. 10 a1-2, with a clapping motion as seen in Fig. 10a3-4. Recovery stroke one shown in green spheres can be observed in all specimens with considerable slow-moving horizontal displacement to recover the flipper into a position suitable for the upstroke. The upstroke shown in purple spheres can be seen in all specimens to produce a slow vertical motion with low levels of forwards motion. As seen in Fig. 10a3-a4, the upstroke crosses paths with the downstroke to create a figure-of-eight path before finally arriving at recovery stroke two, where the flipper travels at low speed into a position suitable for the aggressive downstroke. Additionally, a “MATLAB” program available in Appendix A: turtle_flipper.m with precompiled animations available at:

https://www.nature.com/articles/s41598-022-21459-y#Sec17 was created to verify the flipper's motion. The program solves the three-dimensional model to produce a live three-dimensional animation of the flipper motion giving illustrative graphical feedback, where the model presented in this work is visually compared with the flipper motion of wild green sea turtles.

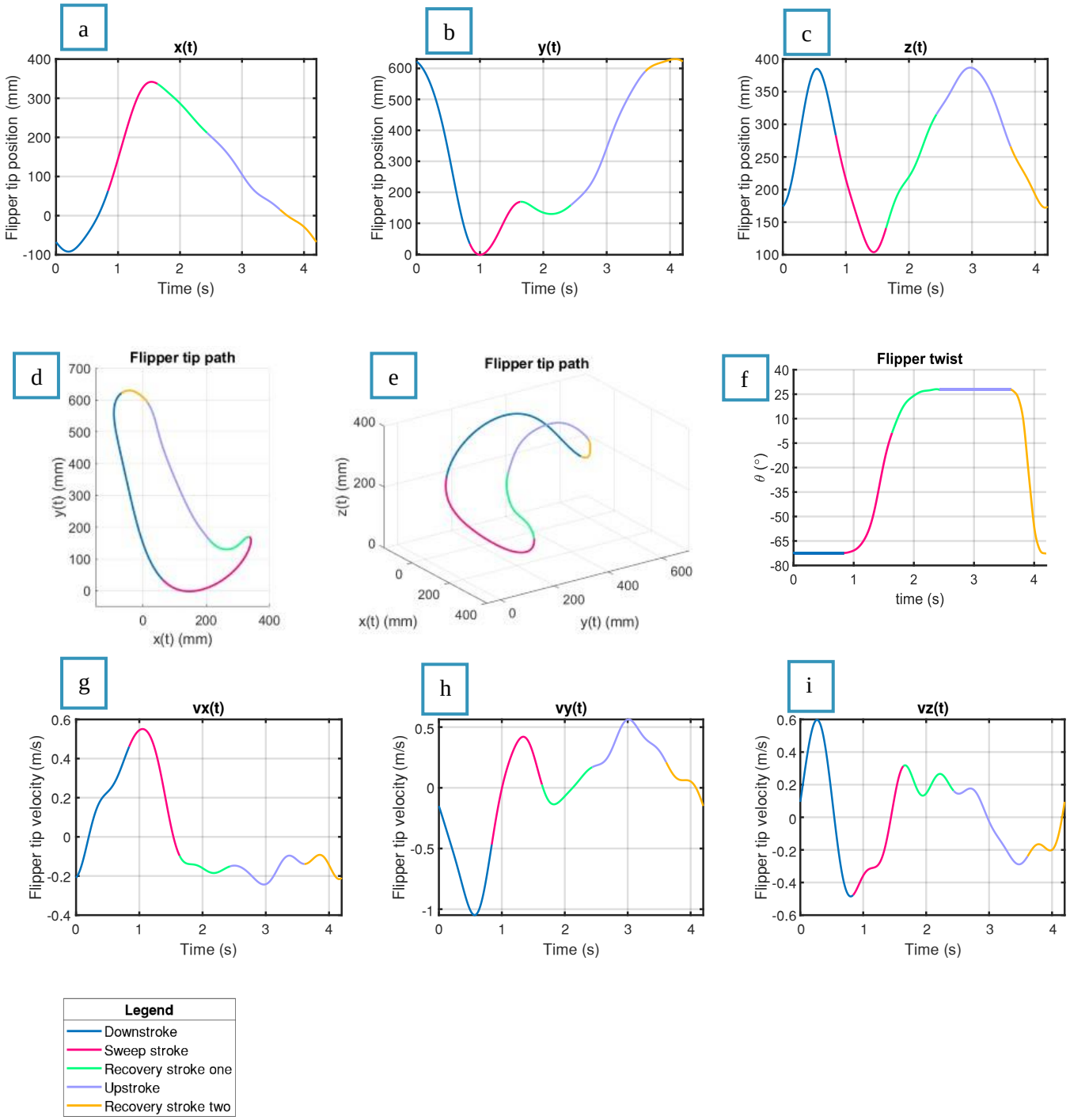

Figure 8: Forelimb flipper kinematics plotted against time. Shoulder rotation point located at (92.5, 305, 27.6)(mm). All plots represent a turtle of SCL equal to 610mm. (a), Flipper tip position in x, (b), Flipper tip position in y, (c), Flipper tip position in z, (d), Flipper tip path in x,y plane. (e), Flipper tip path 3D. (f), Flipper twist. (g), Flipper tip velocity in x, (h), Flipper tip velocity in y, (i), Flipper tip velocity in z.

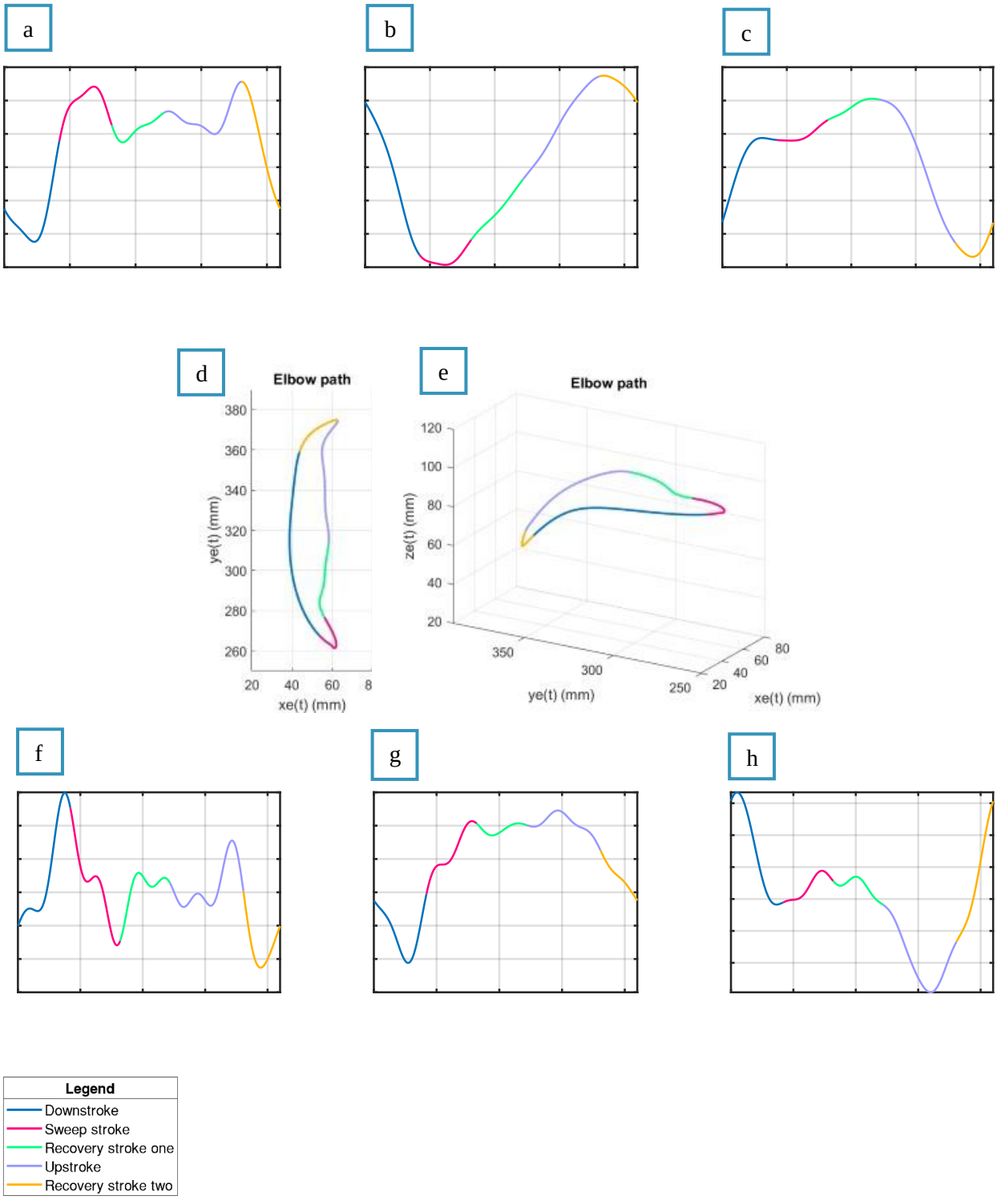

Figure 9: Elbow kinematics plotted against time. Shoulder rotation point located at (92.5, 305, 27.6)(mm). All plots represent a turtle of SCL equal to 610mm. (a), Flipper elbow position in x, (b), Flipper elbow position in y, (c), Flipper elbow position in z, (d), Flipper elbow path in x,y plane. (e), Flipper elbow path 3D. (f), Flipper elbow velocity in x, (g), Flipper elbow velocity in y, (h), Flipper elbow velocity in z.

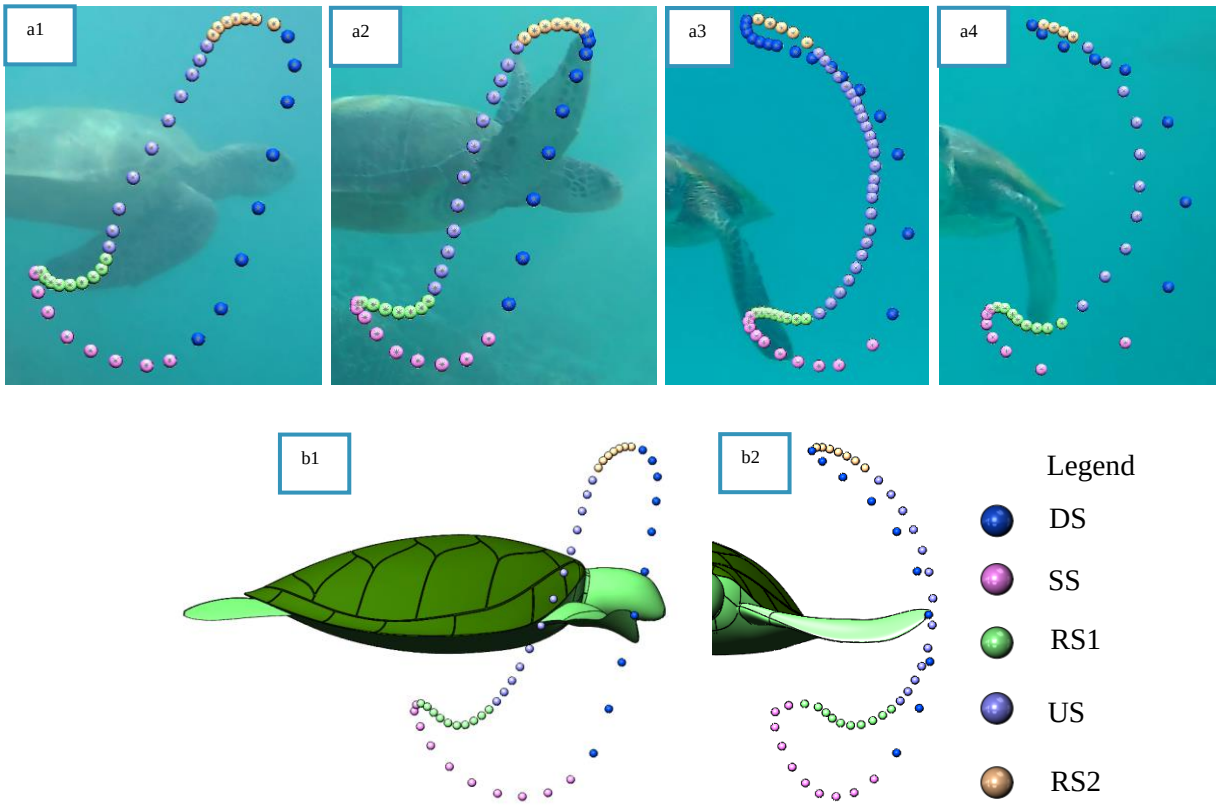

Figure 10: Comparison of various sea turtles filmed at different locations and times compared with the proposed three-dimensional model. (a), Observed Flipper paths from four different sea turtle specimens spheres within the figure representing the position of the flipper tip at 0.1-second increments. (b), The proposed 3D model flipper path with spheres within the figure represents the flipper tip's position at 0.084-second increments.

3.16 Conclusion and Future Work

We present a five-stage cycle swimming locomotion model, in contrast to the previous four-stage ones [6,7], adding a new finding we have named the sweep stroke. Based on findings from previous work, this model could also potentially represent the swimming of the Hawksbill [5] and Loggerhead turtle [26]. Our results provided no evidence of a figure-of-eight pattern in the sagittal plane previously reported [3,5-7]. Instead, it showed a closed-loop with extended sweeping of the flipper tip towards the centre of the carapace to create a swept clapping motion. However, a figure-of-eight pattern is evident in the transverse and coronal planes. Although our methods for creating the three-dimensional models have been generated from two-dimensional data, thus creating what could be called the best guess, we have illustrated an excellent correlation between the model compared with natural swimming footage. Additionally, the advantages of this process of collecting the data from the animal's natural habitat without disturbing the animal far outweigh any disadvantages compared to more traditional data collection methods. This could potentially lead to other animals being analysed by filming with non-invasive underwater drone technologies. The model presented here could lead to a better comprehension of the sea turtle propulsion methods and their fluid-structure interaction.

Chapter 4: Sea Turtles Employ Drag-Reducing Techniques to Conserve Energy

4.0 Preface

Navigating the biomechanical and physiological mechanisms that underpin sea turtles' efficient propulsion in their aquatic environments is a core area of this research. In an attempt to unravel these complex phenomena, we have employed a variety of methodologies and models, producing intriguing findings that contribute significantly to our understanding of these marine creatures' locomotion.

The first piece of this work in chapter 3 offers a non-invasive method to study sea turtle locomotion, resulting in a comprehensive three-dimensional kinematic model. Using underwater drones, we observed these creatures in their natural habitat, Australia's Great Barrier Reef and discovered a unique swimming pattern. This pattern notably expands on previous four-stage locomotion models, suggesting a more nuanced five-stage cycle.

Chapter 4 advances the understanding gained from the initial investigation into the aquatic movement of sea turtles, honing in specifically on the upstroke action in their swimming pattern. This detailed study is directed towards unraveling the biomechanical efficiency that enables these marine animals to embark on lengthy migrations, despite relying largely on a diet consisting mainly of low-energy food. By delving into this aspect, this chapter seeks to provide a comprehensive explanation of the remarkable endurance and resilience exhibited by sea turtles in their natural long-distance journeys.

4.1 Abstract

Sea turtles are recognised as one of the ocean's most remarkable migratory species, accomplishing journeys that cover thousands of kilometres. This fact is made even more extraordinary when considering sea turtles consume mostly low energy foods. The biology of sea turtles dominates the literature, however, the swimming strategies they employ to achieve their migratory success from a biomechanical and hydrodynamic viewpoint is relatively unexplored. In past research, the sea turtle's upstroke has been debated among researchers as to whether it is passive or for thrust production. In this work, we recreate a model based on the green sea turtle (*Chelonia mydas*) and develop an ad-hoc testing rig to uncover the secrets behind the sea turtle's upstroke. Our findings suggest sea turtles utilise a passive upstroke that can substantially lower the animal's drag coefficient to levels that cause insignificant losses in swim speed despite not developing any thrust force. This can conceivably save the animal a notable amount of energy as the upstroke is responsible for a large percentage of the overall limb beat cycle. These findings could potentially pave a path towards developing high-efficiency bio-inspired underwater drone technologies.

4.2 Introduction

Sea turtles are well known to be one of the ocean's most fascinating migratory species, with migrations across oceans covering thousands of kilometres [14,16,80]. These migrations are even more interesting when considering their diet of low-energy foods [29,31-33]. Understanding how sea turtles accomplish such enormous migrations is not thoroughly understood but could be partly due to their swimming strategies [34]. Unlike flying animals [81,82] and some swimming animals [83] that require lift forces to stay in the air or remain afloat, sea turtles can regulate their buoyancy to become almost entirely neutrally buoyant [2]. Because of this, the turtle can likely adapt their swimming style to maximise efficient propulsion.

Efficient propulsion in flying and swimming animals has been shown to occur as the animal flawlessly sheds interacting vortices into their wake. The interacting vortices referred to as the reverse von Karman vortex street, occur due to perfectly timed counterrotating vortices shed at the extreme limits of the animal's control surface (pectoral flippers/wings or caudal fin) stroke. The interaction of the vortices produces high-momentum, high-velocity jet flows, helping the animal replace some drag for thrust [35]. Sea turtles apply highly asymmetric oscillations of their wings [3,5,17-19,84]. The asymmetric stroke pattern may indicate that sea turtles cannot take full advantage of the reverse von Karman vortex. If so, what evolutionary techniques have sea turtles adopted to produce efficient propulsion?

Work has been produced to replicate 2-dimensional asymmetric swimming patterns in sea turtles [17-19] by simplifying the analysis into a single plane and wing cross-section. However, vortex shedding and wake signatures depend on the kinematics, so although these 2D studies give insight, they fall short of fully uncovering the turtle propulsion methods. This leaves a substantial shortcoming in our understanding of how this animal produces efficient propulsion. Studies into the kinematics of sea turtles have often described the downstroke as two times faster than the upstroke. However, there has been much debate about whether the upstroke is a feathering stroke or for thrust production 3,5,84, with most studies taking data from young juveniles, sometimes even hatchlings [3,4,27]. In a recent study by van der Geest et al. [84], the swimming patterns of wild green sea turtles (*Chelonia mydas*) are detailed three-dimensionally. They describe the upstroke as appearing passive, taking on average 1.2 seconds to complete with a relatively constant wing twist of 28˚ (Fig. 11). They also describe the wing twist as linearly increasing from the turtle's elbow to the wing tip (wingspan (s)) with the exact amount of twist at any point along the span calculated by: $\theta(x) = \frac{\theta}{s}x$ .Where θ is the maximum amount of twist at the wing tip measured from the horizontal plane and x is the location of interest along the turtle's wingspan (s).

In this paper we take advantage of the recent findings from van der Geest et al. [84] and apply them to uncover how the green sea turtle (*Chelonia mydas*) uses its pectoral wings (Fig. 11) during the upstroke. To accomplish this, we design and build a full-scale turtle model based on wild green sea turtles (*Chelonia mydas*) (Fig. 11) that can reproduce the animal's upstroke through various testing procedures.

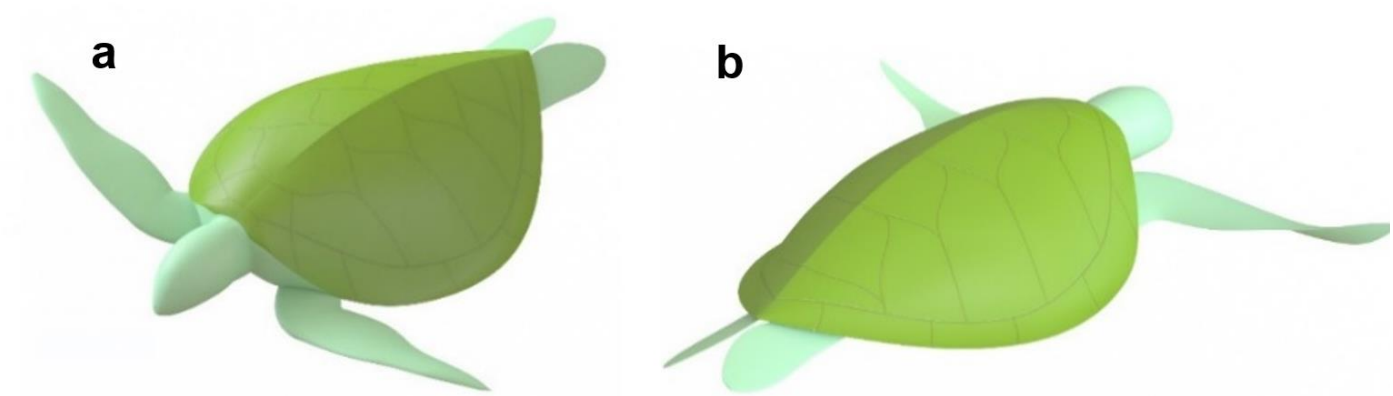

Figure 11: Three-dimensional model of a green sea turtle (Chelonia mydas) displaying various levels of wing twist of the pectoral wing. a, model showing upstroke with 28˚ degrees of wing twist. b, model showing downstroke with -72˚ of wing twist[84].

Our findings suggest that during the sea turtle's general swimming routine, they employ a drag-reducing passive upstroke to conserve energy. This potentially supports how sea turtles produce efficient propulsion to achieve their migratory success, as the upstroke is responsible for a substantial amount of the overall limb beat cycle. Additionally, the passive upstroke can lower the turtle's drag coefficient to levels that cause minor losses in velocity during the upstroke period despite not generating any thrust force. To the best of our knowledge, this is the first study that focuses on the upstroke in wild adult sea turtles and the first report of the upstroke not only being passive but drag-reducing. Furthermore, these findings could be applied and optimised to enhance the efficiency of underwater robots and drone technologies.

4.3 Methods

4.4 Overview of methods

To create the proposed model in Fig.11, we take full advantage of modern additive manufacturing equipment to produce the model to a straight carapace length (SCL) of 490mm. Using a custom-designed and built tow rig shown in Fig. 12, we measure the drag forces and upstroke based on the swim speed of sea turtles of 0.6 m/s [76,77]. To streamline experimental testing, the model is designed with quick exchange wing geometries shown in Fig. 12b. Each wing geometry was created with various degrees of wing twist as produced by wild sea turtles [3,5,84] (Fig. 12b). The test rig (Fig. 12a) was installed into a commercial freshwater pool of dimensions 4m long by 2m wide and 1m deep.

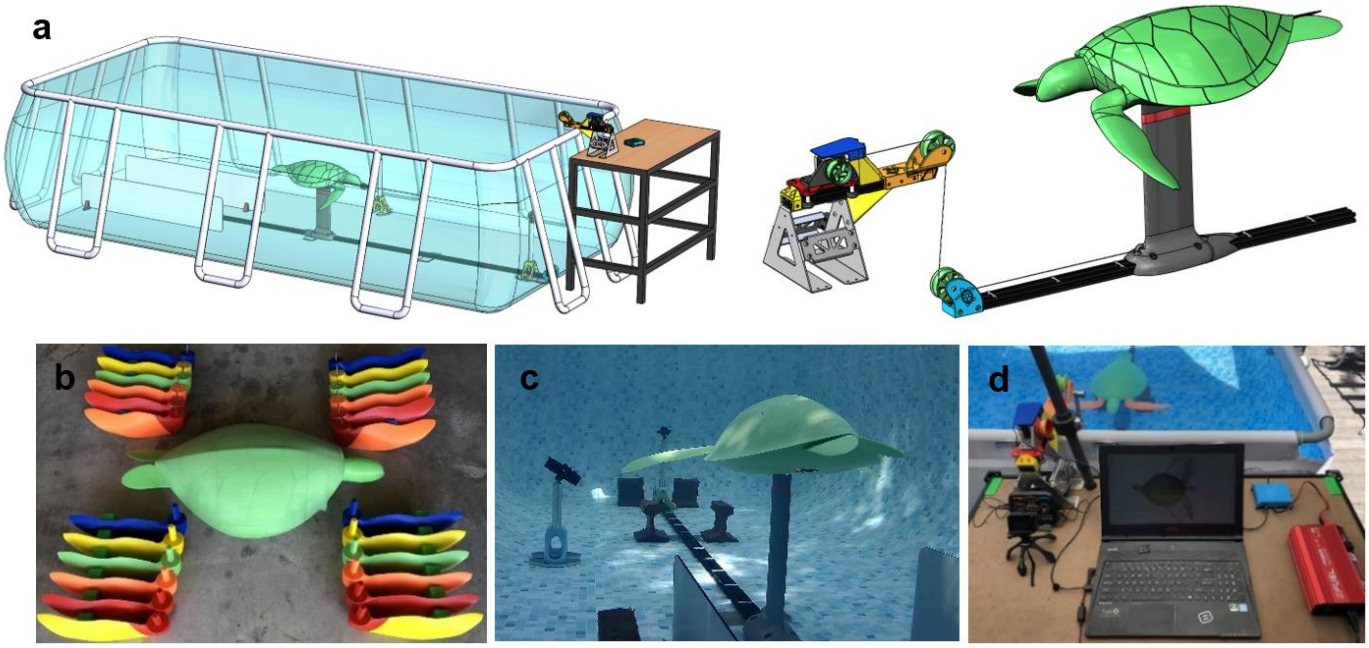

Figure 12: Test rig assembly. a, complete test rig assembly CAD model, with a closeup of pully assembly shown at the top right. b, 3D printed turtle with all wings. Yellow/red and orange/red = 35˚ twist, red = 28˚, orange = 22˚, green = 18˚, yellow = 15˚ and blue = 10˚. Passive wings are shown above turtle with rigid wings below. All wings are manufactured to the same volume and mass of 226.5 cubic centimetres and 230 grams. c, Image showing a typical test. d, workstation setup.

4.5 Sea Turtle Geometry

The sea turtle geometry (Fig. 11) was created from video footage of wild green sea turtles in Australia's Great Barrier Reef obtained from work done by van der Geest et al. [84]. This process involved filming from the top, side and front of three different green sea turtles. The video footage was then imported into CAD (SolidWorks, Waltham, Massachusetts, USA) with each clip being placed and scaled onto the appropriate plane using the "sketch picture" tool. Planes were generated within the images for producing 2-dimensional sketches that ran to the limits of each Image. From this, the "Loft" tool is used to loft all 2-dimensional sketches into a finished surface (Fig. 13a). This process was followed approximately four times for the shell, head, front wings and rear fins geometries. The rear fins were modelled tucked in behind the carapace, pointing backwards, as this lowers the turtle's parasitic drag during the regular swimming routine [84].

Wing twist was modelled using the SolidWorks feature "Flex" by twisting the wing geometry linearly from a plane at the wingtip to a plane at the wing root (Fig 13c.). As seen in Fig 13b, the wing twist values are based on findings from van der Geest et al.[84], where they matched their CAD models with footage of freely swimming green sea turtles while keeping the CAD model mass and volume constant. The exact amount of twist at any point on the wing can be found using: $\theta(x) = \frac{\theta}{s}x$. Where θ is the maximum amount of twist measured from the horizontal plane and x is the location of interest along the turtle's wingspan (s).

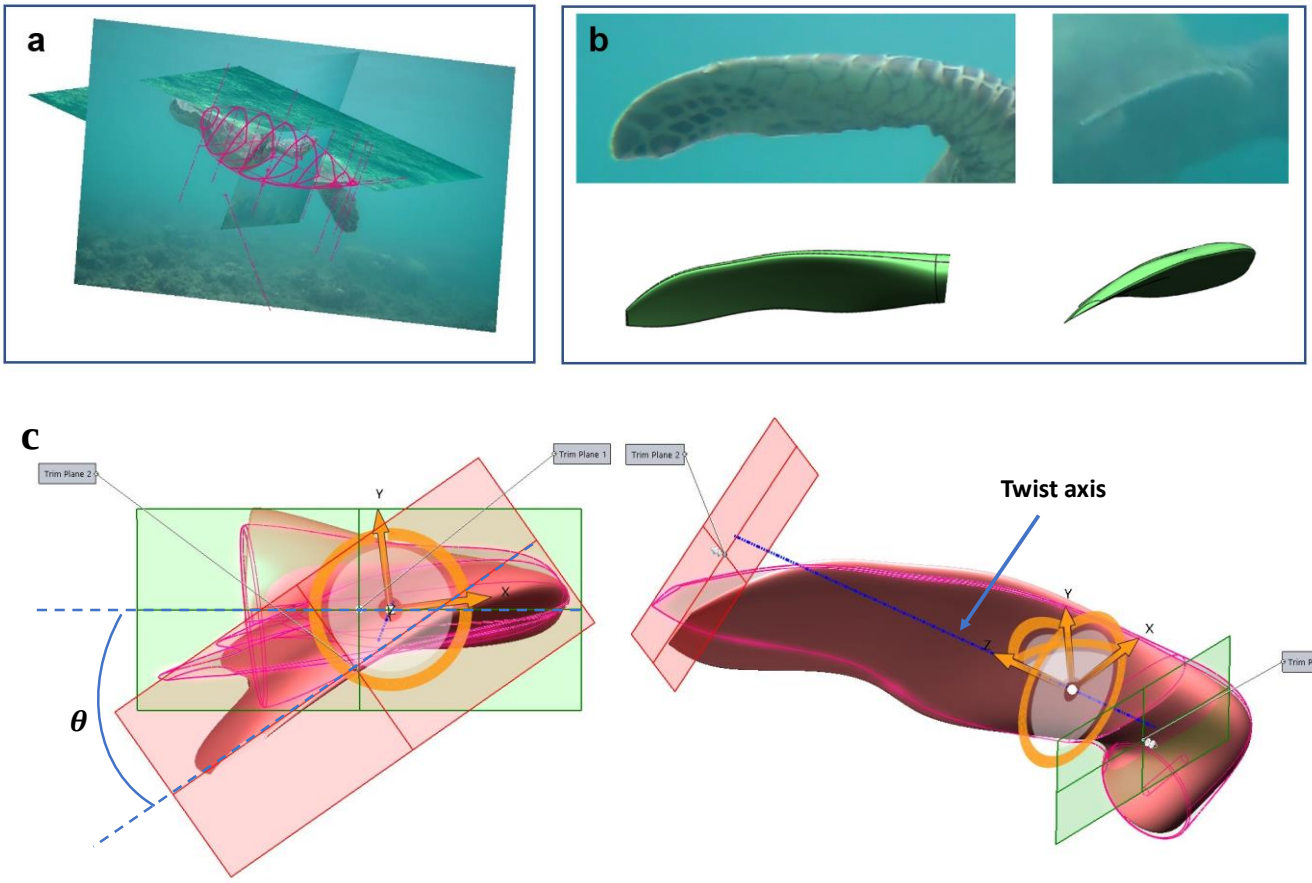

Figure 13: Turtle geometry development. a Side, top and front view footage sets of wild green sea turtles (Chelonia mydas) overlayed in CAD showing the two-dimensional sketches on each generated plane. b, Images from van der Geest et al. [84] showing wing twist compared with CAD models during the upstroke. c, Wing twist generation in CAD using the SolidWorks feature "Flex" to generate a linear varying twist between the plane at the wing tip (red plane) and elbow (green plane).

4.6 Test Rig Design and Manufacture

This section details the design to manufacture of the test rig assembly as displayed in Fig. 12. The turtle chassis (head, carapace and rear flippers) was 3d printed from PLA+ (Esun, Shenzhen, China) in six separate hollow sections (Fig S2). Each section was printed at 215ºC with 0.2mm layer heights with a consistent 1.6mm wall thickness. The part cooling fan was set to 80% flow rate to capture fine details but did not affect layer adhesion. Each part of the chassis was designed to fill with water through filling bungs at the bottom of each section to make the chassis slightly negatively buoyant. The front wings were manufactured in two sections: the wing tip to elbow section and elbow to shoulder section (Fig S2). These used identical temperatures and layer heights as the chassis however, 18 solid top and bottom layers with 9 shells at 35% honeycomb infill were used for the wing tip to the elbow section. The shoulder to elbow section used the identical infill settings however, 26 solid top and bottom layers were used with 13 shells. All parts were sliced with Simplify3D (Simplify3D version 4.1, Cincinnati, Ohio, USA) and printed on a "Caribou 420 MK3s Rel 3" machine (Caribou MK3s, Remagen, Germany).. The printer was set up with a Mosquito hotend, (Slice engineering, Florida, USA) with 0.4mm nozzle and dual gear direct drive extruder (Bondtech, Värnamo, Sweden). Using these print settings, a surface finish of Ra 7µm perpendicular to flow direction and Ra 3µm parallel to flow direction was measured with a stylus profilometer (FORMTALYSURF 50, Taylor Hobson, Leicester, UK)(Fig S3). All fins were manufactured to 230 grams with an identical volume of 226.5 cubic centimetres. The centre of buoyancy

for every fin was 70mm from the fin rotation axis, with the centre of mass located 73mm from the rotation axis. This created a small torque to resist passive operation.

The pulley assembly was primarily 3d printed except for the linear rails, standard hardware and the main aluminium truss frame. All printed parts used Esun PLA+ except for the motor mount that was printed from PETG at 245ºC. PLA+ and PETG were printed with 4 shells 8 top and bottom solid layers with 35% honeycomb infill.

To ensure the absolute lowest friction while running all rotating components used 100% Zirconia Oxide ceramic bearings, this also made sure the bearings that were located underwater did not suffer from corrosion. The motor and pulley assembly was installed onto a linear rail, allowing the motor and pulley to pull against the force sensor. The pulley cable was from Spectra fibre 50lb braided line (Spectra® , Honeywell, North Carolina, USA) due to its high strength to low stretch properties. During towing, the braided line was designed to neatly wind onto the pully to ensure the system had a consistent velocity after the acceleration stage.

The pulley system was controlled by an electric circuit consisting of a stepper motor "NEMA 17", an A4988 stepper motor driver (Allegro Microsystems, Manchester, New Hampshire, USA), a microcontroller (Arduino.cc, Somerville, MA, USA) and a variable DC power supply (SkyRC Technology, Guanlan, Shenzhen, China). The Arduino controlled the angular speed of the motor in revolutions per minute (RPM) using the A4988 driver. The necessary RPM was calculated from the required linear velocity using the following formula: $RPM = \frac{60v}{2\pi r}$, Where "v" is the linear velocity, and "r" is the radius of the pulley (r = 0.0225 m). Furthermore, to ensure a smooth transition at the start of each test and to avoid high acceleration loads, linear velocity was defined as: $v = 0.2t$, Where t the time in seconds was terminated at maximum velocity to keep the system at the desired constant velocity. Moreover, to ensure smooth motor steps during the low initial speeds, micro-stepping of ¼ step was implemented.

4.7 Testing Procedure

Drag force testing consisted of five procedures, all of which were repeated a minimum of five times at 0.6 m/s. The Arduino program that controlled motor speed was tuned to ensure motor speeds were within a 0.5% target. The speed was verified by timing how quickly the pylon passed white markers placed on the linear rail using high-speed video footage at 240 FPS. Additionally, the pully RPM was verified with a digital tachometer to ensure linear velocity was proportional to angular velocity values. All tests performed consisted of towing a pylon of cross-section NACA 0010 on a linear rail, as seen in Fig 12, down a 4m long, 2m wide and 1m deep freshwater swimming pool of temperature 20 to 21ºC. Data was collected for the last second of running to ensure the system was as close as possible to steady-state. Depending on the test, the pylon would have the following items attached consisting of:

- Pylon only (No attachments)
- Pylon with force sensitivity device (To measure system sensitivity to lift forces)
- Pylon with Sea turtle model and rigidly mounted wings (Wings could not rotate)

- Pylon with Sea turtle model and passive wings (Wings are free to rotate)
- Pylon with sea turtle model with wings removed (No wings turtle carapace only)

Running the pylon only without attachments resulted in a resistance of 0.596 ± 0.016N at 0.6 m/s. This value was then subtracted from all force measurements. A sensitivity study was conducted to ensure that any lift forces generated did not affect the drag force due to an increase in load acting normal to the linear rail. This process involved designing the device shown in Fig. 14 that could retain a constant hydrodynamic drag force while controlling a variable force acting normal to the linear rail. Adjusting the normal force was achieved by inserting 100-gram weights internally into the device (Fig. 14b). The device produced a maximum buoyant force of 8.085 N, acting normal to the linear rail with no internal weights. Additionally, this buoyant force was positioned forwards of the bearings to induce a moment to simulate the torque generated by the lift force from the rigid turtle wings. The findings from this exercise showed that the system's sensitivity to forces acting normal to the linear rail could be neglected with changes only up to 0.06N evident in the pull force data (Fig. S4).

The passively mounted wing and rigidly mounted wing both shared identical geometry except for the attachment point with rigid wings using a splined input shaft to prevent rotation and the passive wing using a smooth input shaft running on ceramic bearings. This allowed the passive wing to freely rotate about the turtle's shoulder during a tow tests.

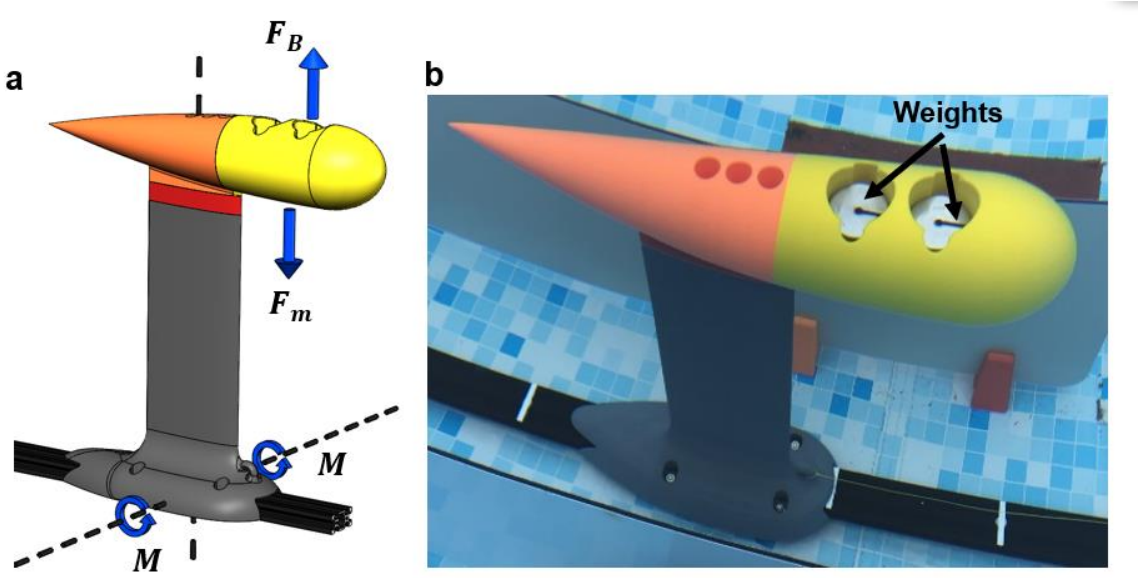

Figure 14: Normal load sensitivity study. a, Calibration device schematic with $F_B = 8.085N$ and $F_m = 0.981n$, where n is equal to the number of 100-gram weights used. b, Calibration device with six 100 gram weights installed.

Upstroke angular displacement data was obtained by filming the turtle during a tow test from the front, as illustrated in Fig. 15. Tests were performed at 0.6 m/s tow speeds. Filming was done with a Paralenz Vaquita camera (Paralenz, Rødovre, Denmark) at Full HD 240 FPS. The video footage was edited in the software "VideoPad Professional" (NCH Software, Canberra, Australia) to find the time taken to complete the upstroke. The test rig was set up to release the fins at approximately 135˚ clockwise from the vertical axis, this was defined

based on findings by van der Geest et al.[84] based on the position of the wing at the start of the upstroke in wild sea turtles. The top of the upstroke was taken as the wings highest point before leaving the camera frame. Based on the time taken for the wings to complete the angular displacement, angular velocity could be calculated for 0.6 m/s swim speeds.

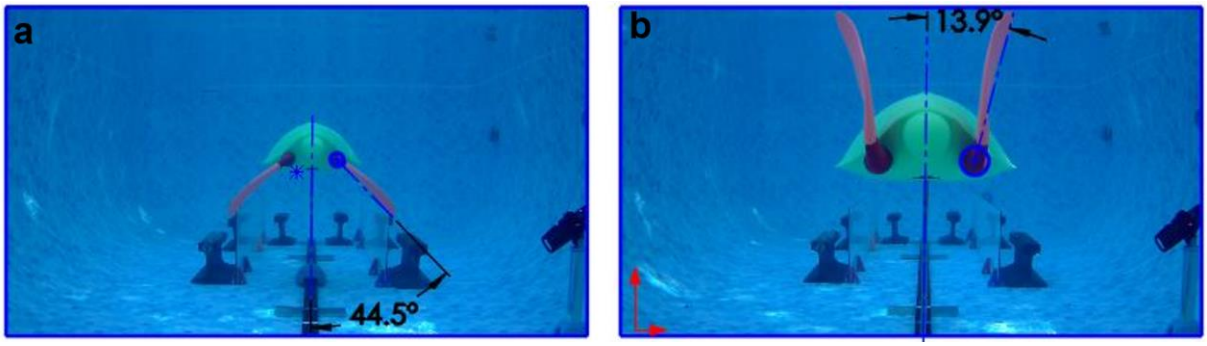

Figure 15: Upstroke data collection showing wings of 35˚ twist during a 0.6 m/s pull test. a, Beginning of upstroke as wings leave the 135˚ constrainer. b, Top of the upstroke measured anticlockwise from the virtical axis.

4.8 Flow Pattern Generation

Dye injection was used to help better understand why the fluid dynamic forces changed for each testing case. Flow patterns generated by the turtle were documented by injecting water-based dye. The water-based dye ensured it remained neutral after injection and did not sink or rise in the water column. Documentation of flow patterns was obtained by filming how the dye mixed with freshwater when the turtle passed through (Fig S5a-d and Video S1, video availble at https://www.mdpi.com/2077-1312/10/11/1770) using two high-speed cameras (Chronos 2.1-HD 32GB, Kron Technologies Inc, Burnaby, Canada) filming at full HD 1000 FPS. Dye testing was utilised for this work due to its ease of application, low cost and has been successfully applied in many high-level applications [85-88].

As no commercial devices were available to purchase for such a test, two devices were designed and built, shown in Fig. 16a-b to allow different methods of dye injection. Device one (Fig. 16a) could inject significant levels of stationary dye with up to two colours. The device made it simple to acquire information on wing tip vortex formation concerning passive and rigid wings. On the other hand, device two (Fig. 16b) was designed to induce streamlines into the turtle's incoming flow to help visualise flow separation and attachment (Fig S5a-d and Video S1 video availble at https://www.mdpi.com/2077-1312/10/11/1770). Both devices utilised medical syringes built into their central bodies and produced dye injection via a hand trigger.

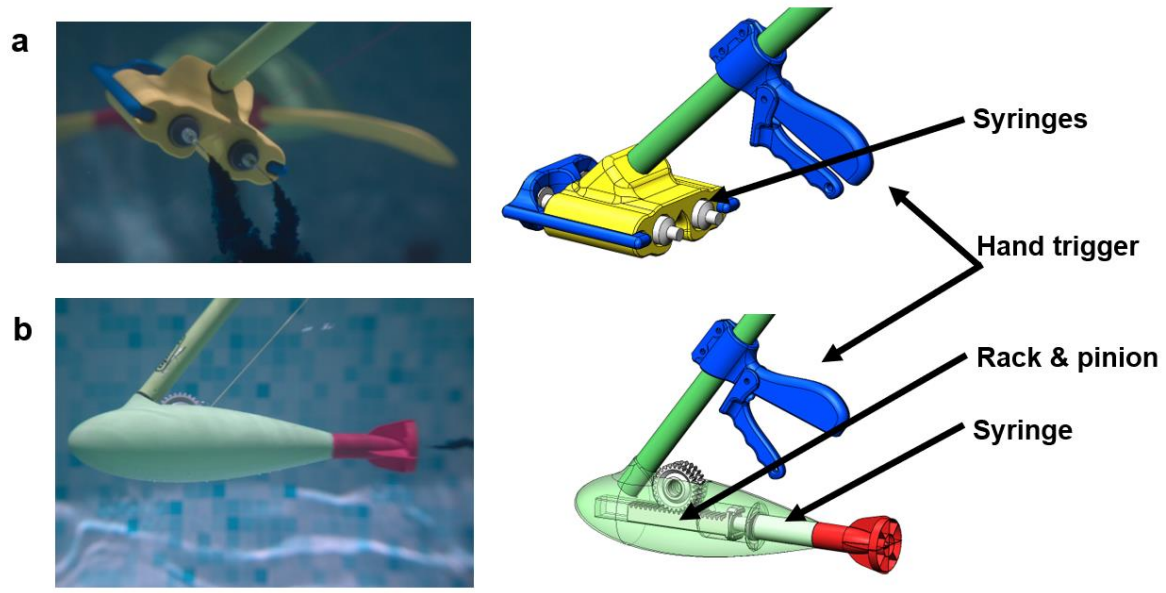

Figure 16: 3D printed flow vis test equipment. a, Dual injection tool for inserting motionless clouds of dye. Actuation via hand trigger attached via a braided line to a sliding plunger b, Streamline injection tool to add streamlines of dye into turtle swim path. Actuation via hand trigger attached via a braided line to a rack and pinion mechanism. (Hand trigger location not in actual position).

4.9 CFD Analysis

CFD simulations were produced with commercial CFD software ANSYS Fluent (ANSYS 2021 R2, Pennsylvania, USA) using the Reynolds Average Navier Stokes (RANS) models. The CFD simulations in this study were only made for rigidly mounted wings. The simulations also served two purposes: firstly, to provide a second solution to the drag coefficients that did not rely on testing results and secondly, to help display the flow features that caused the increase in drag during non-passive wing operation.

The pylon geomerty was subtracted from the computational domain and all surface fasteners to simplify the model thus lowering nodal count. The computational domain (Fig S6a) was set up with a symmetry boundary condition to half the domain and substantially lower computational expense. The curvature of the pool wall was modelled in and set as a zero slip moving wall, with the pool surface modelled as a zero shear/free slip wall. All surfaces of the turtle geometry were set as zero slip smooth walls, with the measured surface roughness not considered in any simulations. Fluents Poly Hexcore mesh was used, containing approximately 12,500,000 nodes and 6,000,000 elements. Each simulation had an initial estimate using the realisable k-epsilon model before switching to the k-omega SST model. The mesh was refined down to an average wall y^+ value of 1.07 to resolve the flow down to the viscous sublayer. Bodies of influence were added at the wingtips, rear of the turtle's body and one zone encasing the entire turtle assembly to refine the mesh in those critical areas. Monitors were set up to observe the scaled residuals, drag force, lift force, wall y^+ and the standard deviation of the velocity at the outlet. Comparing the CFD values with field test values, a close correlation was achieved for the drag coefficient (Fig. S6b). Additionally, when comparing flow patterns from CFD to field testing, corresponding flow feature trends were obtained.

4.10 Results and Discussion

The results section is broken up into three subcategories. The first section describes the effect of a passive wing on the overall turtle drag coefficient (c_d), as well as details the contribution towards changes in c_d. Additionally, our turtles c_d results and frontal area are compared with the same values from literature to ensure geometry correlates with previous works. The second section details the effects of the wing twist on time required to complete the turtle's upstroke. The final section details a numerical process to calculate the drop in swim speed due to the turtle producing a passive drag reducing upstroke.

4.11 Effect of passive wings on the turtles drag coefficient

Testing with the wings held rigidly would increase the drag force almost linearly for all values of wing twists. Contribution to the increase in drag came from an increase in magnitude of the wing tip vortex (Fig. 17a) and increased flow separation due to adverse pressure gradients (Fig. 17b) caused by the increase in wing twist. The passive wings (meaning the wing is free to rotate around its axes, refers to the axes of rotation in Fig. 18d) were able to keep prolonged flow attachment (Video S1 and Fig. S5) owing to the relative angle of attack remaining constant along the wingspan. This was owing to the addition of an increasing vertical component of velocity towards the wingtip. Additionally, the wingtip vortex was cancelled out, likely due to the wing entering a near-equilibrium state, creating near-constant pressure across each surface, preventing any cross-flow due to pressure differences. To quantify these effects, the drag coefficient (c_d) was calculated applying:

$$c_d = \frac{2F_d}{A_p \rho_{h2o} v^2}, \tag{1}$$

Where F_d was the average drag force (obtained from test rig data) acting on the turtle and wing assembly, A_p the projected area perpendicular to the flow direction, ρ_{h2o} the fluid density and v the tow speed. All force measurements were taken at 0.6 m/s with a Reynolds number (Re) of 297,970 based on the straight carapace length (SCL). The Reynolds number was defined by:

$$Re = \frac{v D_{SCL} \rho_{h2o}}{\mu_{h2o}}, \tag{2}$$

Where v is the tow speed, the characteristic length is defined as D_{SCL} with ρ_{h2o} and μ_{h2o} being the fluid density and dynamic viscosity. Referring to Fig. 8a, it can be observed an average c_d for a passive wing was 0.151 ± 0.008 and was obtained for all values of wing twist. Tests without wings produced a c_d of 0.133 ± 0.012, which directly coincides with values obtained by T.Todd Jones et al. [89] of 0.13 ± 0.02 from castings (without front wings) of deceased green sea turtles through wind tunnel testing.

Additionally, the frontal area of our test rig model was between 0.0436 to 0.0482 m^2 (depending on wing twist). This closely correlates with findings by Kinoshita et al. [34] of 0.0416 to 0.0448 m^2 for similar-sized green sea turtles. Based on the mentioned literature, the accuracy of our green sea turtle geometry appears justified.

Based on the c_d values, it can be observed that a passive wing, regardless of wing twist, only contributes to 12% of the overall drag on the turtle, while rigid wings contribute from 21% up to 50% of the overall drag depending on the value of wing twist.

4.12 Passive wing rotation speed based on wing twist

Fig. 18b displays the average angular velocity of a passive wing from testing results at swim speeds of 0.6 m/s. Based on the average upstroke displacement of 79.6º , we found a passive upstroke with a wing twist of 28˚ occurs in 1.25 seconds at a swim speed of 0.6 m/s, closely matching the findings of van der Geest et al. (Fig. 18c) [84] of 28º twist in 1.2 seconds. Moreover, this swim speed aligns neatly with literature for the cruising speeds of sea turtles [76,77]. Unsurprisingly, the 35º wing twist produced the fasted upstroke at just 1.03 seconds, with the lowest wing twist of 10˚ completing the upstroke in 3.07 seconds.

Tests for this work was carried out with a slightly negatively buoyant wing geometry (Fig. 18d). This was based on the body density of a sea turtle being 1046.5 kg/m^3 [90] in saltwater of density 1025 kg/m^3. There was a slight mismatch in the centre buoyancy compared with the centre of mass of the test wings due to manufacturing limitations, however, the position remained constant for all wings manufactured.

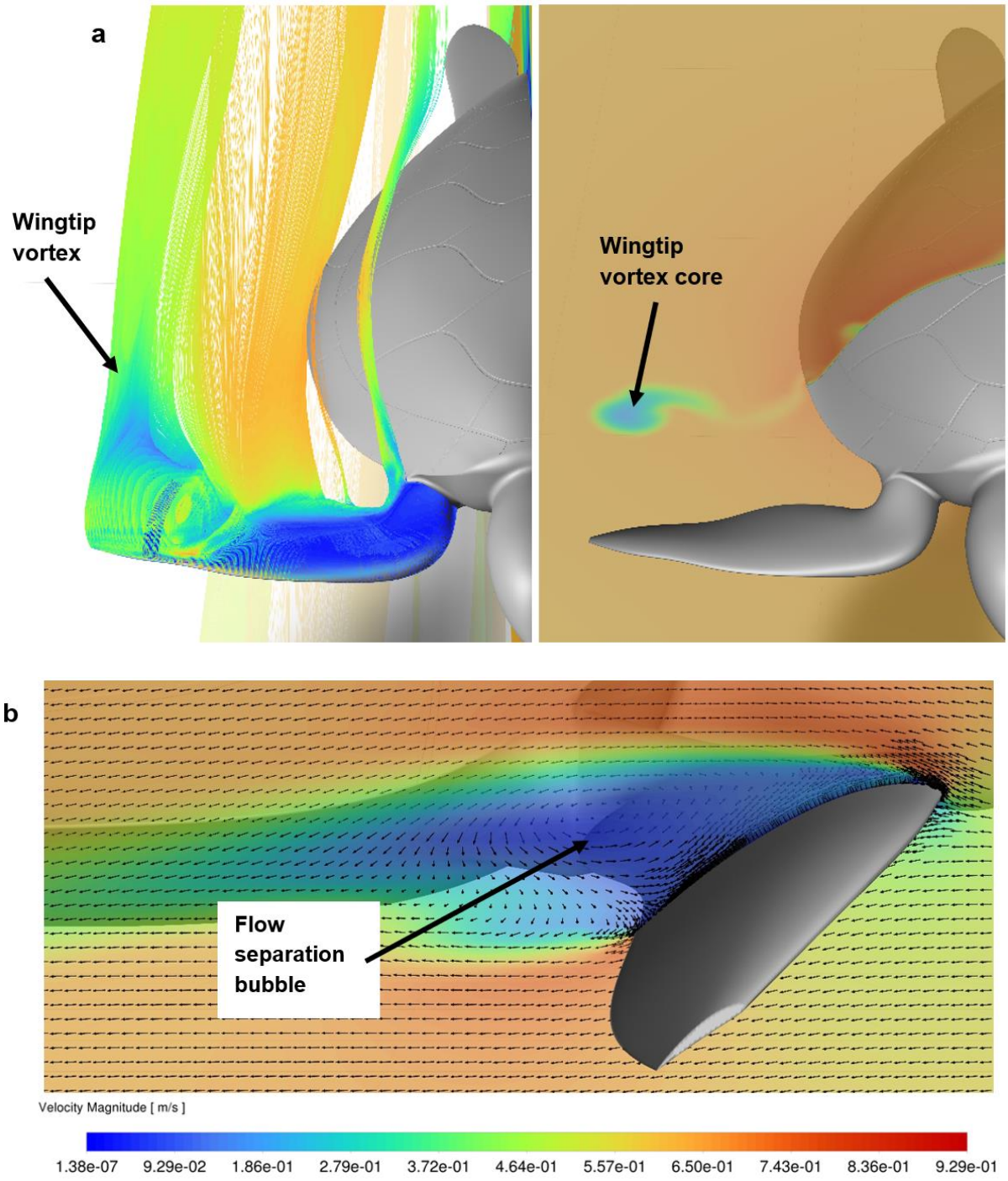

Figure 17: CFD post-processing results of flow field velocity for a rigid wing of flex 35˚. a, Rigid wing generating the wingtip vortex. The Image on the left shows streamlines starting at the turtles wing. The Image on the right shows the vortex core via a transverse plane. b, Longitudinal section plane through turtle wing showing flow separation due to adverse pressure gradients observed on rigid wings.

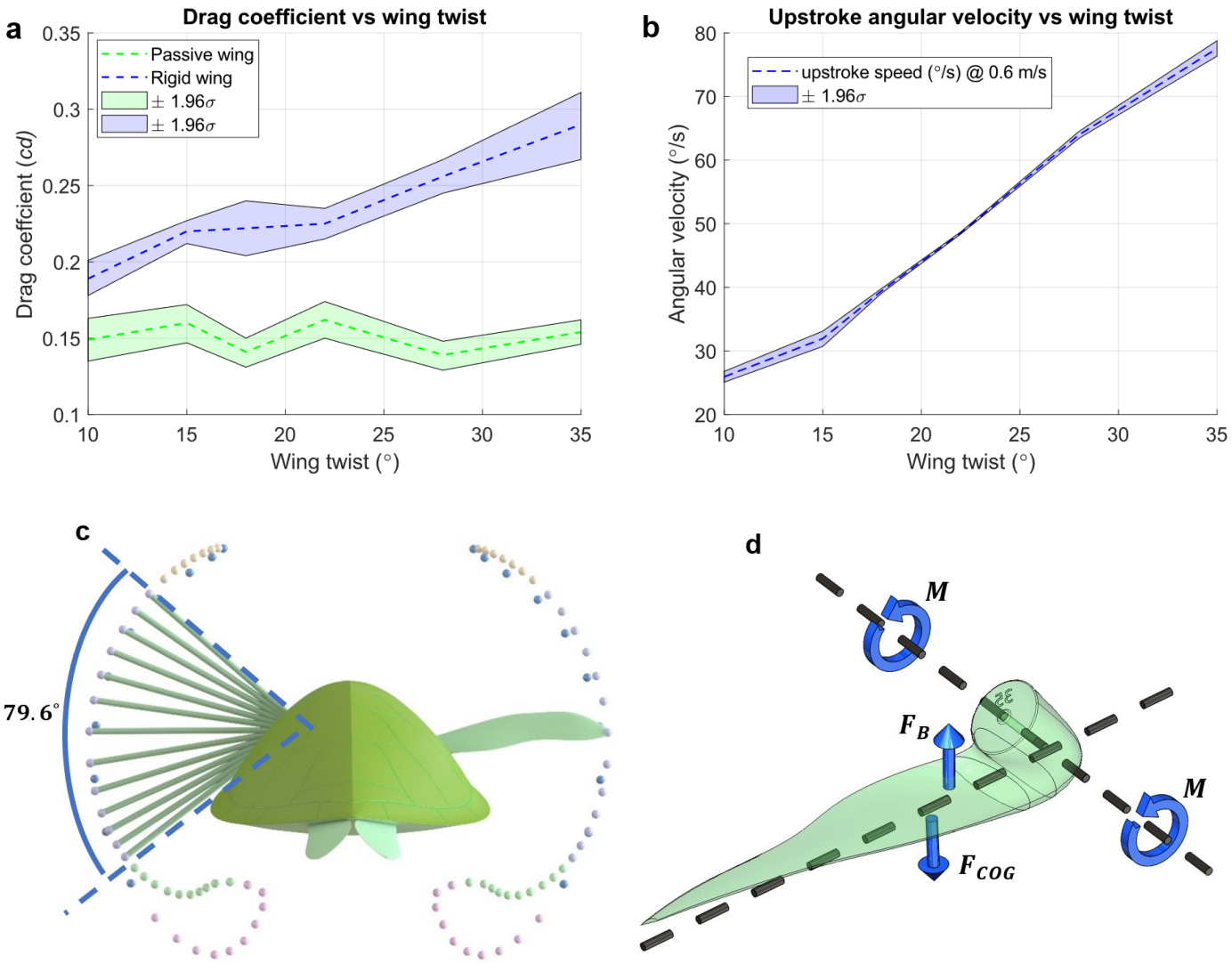

Figure 18: Testing data and parameters. a, Drag coefficient vs wing twist, the blue line represents a rigidly mounted wing with green line representing a passive wing b, Average upstroke angular velocity vs wing twist for passive wings. c, Sea turtle swimming pattern [84] detailing upstroke angular displacement of 79.6˚ for the turtle's wing with solid green links and purple spheres. Blue spheres represent downstroke, pink spheres the sweep stroke, green spheres the recovery stroke one, and orange shears recovery stroke two[84]. d, Free body diagram of test rig fin showing the centre of gravity acting 73mm from the rotation axis and centre of buoyancy acting at 70mm from the rotation axis.

4.13 Velocity drop during the non-propulsive upstroke

Based on the findings, it is reasonable to assume the turtle does not generate any thrust during a passive upstroke and thus must lose swim speed during the upstroke period. To quantify this, the drop in swim speed as a function of time was derived from Newtonian physics as:

$$v_{drop}(t) = \frac{A_p \rho_{h2o} v^2 c_d}{2m} t, \tag{3}$$

Where v is the initial swim speed, c_d the average drag coefficient during the upstroke, ρ_{h2o} the fluid density, t, the time taken for the upstroke to complete with the turtle mass m calculated based on research by Eguchi et al. [91] using their empirical function with respect to the SCL: $m(SCL) = e^{0.96+0.04SCL}$. The frontal area A_p was found by scaling the turtle CAD geometry seen in Fig. 19a, within CAD to varying levels of SCL. At each scale A_p was

measured within CAD as seen in Fig. 19a. The results of A_p with respect to SCL proved to align remarkably well with the past research values obtained by Kinoshita et al.[34].

It can be observed in Fig. 19b that the loss in swim speed for larger turtles is as low as 0.03 m/s. Combining findings from earlier work that relate the mass and size of a turtle to its age [92,93] with findings from this study shows adult sea turtles >80kg are far less affected than juveniles < 80kg for swim speed losses generated by a passive upstroke. This could suggest that adult green sea turtles are naturally more efficient swimmers. From an evolutionary and behavioural perspective, this suggestion makes sense as the adult green sea turtles must undertake enormous migration distances during breeding seasons.

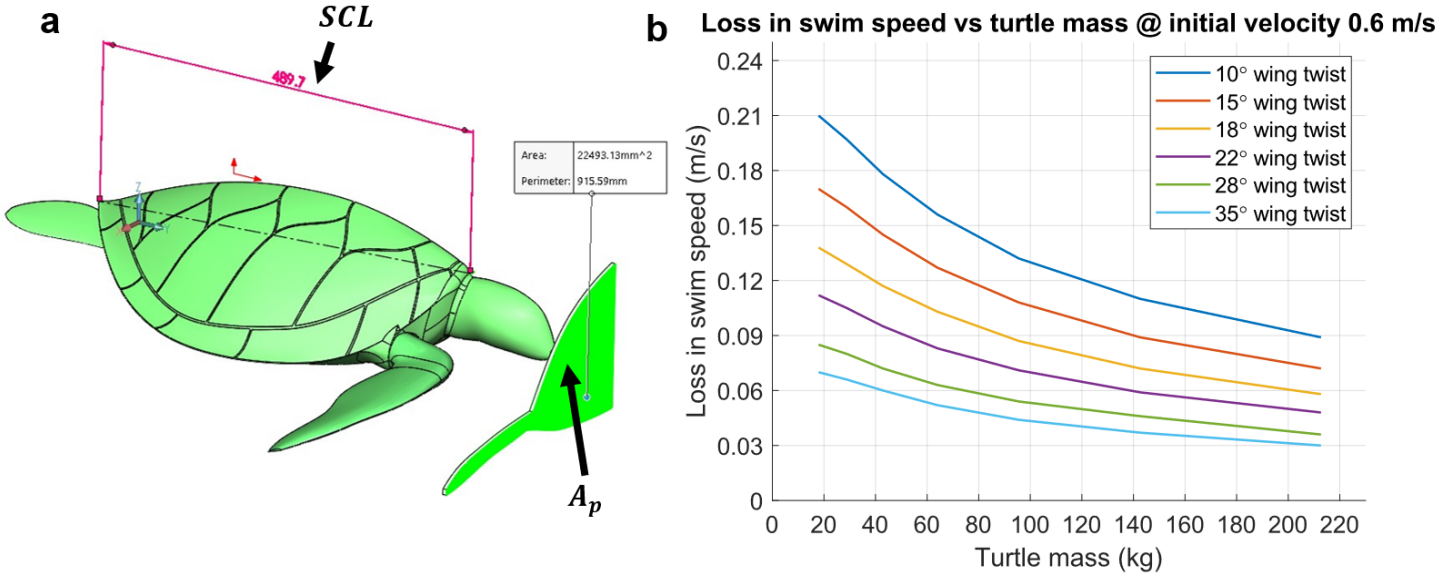

Figure 19: Turtle geometry and its effects on swim speed. a, Extraction of turtle frontal area A_p with respect to SCL from CAD. b, Loss in turtle swim speed during a passive upstroke with an initial swim speed of 0.6 m/s versus turtle mass. Based on the time required for each wing to complete upstroke displacement of 79.6˚ obtained from testing data.

4.14 Conclusion and Future work

Although in this study, a rigid body with constant wing twist is analysed, when applying a wing twist of 28˚, our model completes the turtle's upstroke in 1.25 seconds at a swim speed of 0.6 m/s. This aligns smartly with the findings of wild green sea turtles of 28˚ wing twist completing their upstroke in 1.2 seconds [84] and turtle swim speed of 0.6 m/s [76,77]. Additionally, this supports the work of van der Geest et al.[84] that the turtle's wing remains relatively constant in shape during the upstroke. Based on these findings, we suggest that sea turtles apply a drag-reducing passive upstroke to conserve energy. This makes practical sense as sea turtles have a cambered aerofoil-shaped wing that could generate inefficient thrust for the upstroke. The passive upstroke can be further justified because it occurs in approximately half the time of the turtle's downstroke [3,84]. It must be noted that sea turtles may not always apply a passive upstroke. However, the passive upstroke can substantially lower the turtle's drag coefficient to levels that cause minor changes in velocity during the upstroke period despite not generating any thrust force. This is particularly the case for larger turtles due to their increased body mass compared with their frontal area potentially helping answer how

green sea turtles (*Chelonia mydas*) migrate on such little energy intake [29,31-33]. With a passive upstroke, it is possible the turtle produces diminutive vortex shedding at the top of the upstroke this could mean the reverse von Karman vortex is unattainable. To test this hypothesis is accurate, the complete three-dimensional swimming routine will need to be reproduced. A dedicated work to produce this is currently undergoing and it will be disclosed in a future publication. Furthermore, this work provides new avenues to study animal locomotion without the need for animal interaction by utilising life-like additive manufactured testing equipment coupled with simulation. Additionally, these findings could be optimised for conserving energy in bio-inspired underwater drone technologies.

Chapter 5: Soft-robotic green sea turtle (*Chelonia mydas*) developed to replace animal experimentation provides new insight into their propulsive strategies

5.0 Preface

This research into the remarkable biomechanical prowess and physiological efficiencies of sea turtles, particularly their propulsion mechanisms in aquatic environments, continues to unveil fascinating insights. Chapter 4 focused on the sea turtle's upstroke motion during swimming. Through a model based on the green sea turtle (Chelonia mydas), we discovered that sea turtles utilise a passive upstroke, reducing drag significantly and maintaining swim speed without actively producing thrust force, presenting a possible energy-saving mechanism integral to their incredible endurance.

Building on these insights, chapter 5 dives deeper into understanding the green sea turtle's astonishing ability to accomplish expansive journeys up to 50km per day on a diet primarily composed of seagrass or microalgae. These feats not only point towards the efficacy of their swimming techniques but also stand as a powerful testament to the process of evolution.

Investigating the propulsive strategies that enable such accomplishments presents unique challenges, especially considering the ethical implications of experimenting on an endangered species and potential behavioural alterations under experimental conditions. To circumvent these issues, chapter 5 details the development a new soft-robotic sea turtle that accurately replicates the form and function of the real animal, offering crucial biomechanical insights without resorting to invasive experimentation.

5.1 Abstract

Green sea turtles (*Chelonia mydas*) can swim up to 50km per day while only consuming seagrass or microalgae. How the animal accomplishes this vast journey on such low energy intake points to the effectiveness of their swimming technique and is a testament to the power of evolution. Understanding the green sea turtle's ability to accomplish these journeys requires insight into their propulsive strategies. Conducting animal testing to uncover their propulsive strategies brings significant challenges: firstly, the ethical issues of conducting experiments on an endangered animal, and secondly, the animal may not even swim with its regular routine during the experiments. In this work, we develop a new soft-robotic sea turtle that reproduces the real animal's form and function to provide biomechanical insights without the need for invasive experimentation. We found that the green sea turtle may only produce propulsion for approximately 30% of the limb beat cycle, with the remaining 70% exploiting a power-preserving low-drag glide. Due to the animal's large mass and relatively low drag coefficient, losses in swim speed are minimal during the gliding stage. These findings may lead to the creation of a new generation of robotic systems for ocean exploration that use an optimised derivative of the sea turtle propulsive strategy.

5.2 Introduction

The migrations of green sea turtles (*Chelonia mydas*) have been shown to cover as far as 2342km in only 47 days, the equivalent of travelling 50km per day [16]. What makes this journey remarkable is the low-energy foods they consume, mainly seagrass and microalgae [32].The biology of sea turtles dominates the literature, yet, research into the animal's propulsive performance has had little investigation, with most work simplifying their analysis to a rigid body with simplified kinematics[17,18]. Understanding the sea turtle's propulsion methods could potentially lead to the development of highly efficient robots for long-term underwater missions that take inspiration from the animal's locomotor patterns. However, gaining this understanding is of enormous complexity. Firstly, studying an endangered live animal brings tremendous inconvenience in obtaining ethical approvals [84]. Additionally, the animal may not even swim with its natural locomotor pattern when in captivity [84]. To overcome these limitations, researchers have tried to design and build animal-inspired robots to help comprehend and take advantage of unique animal characteristics [49-54,94]. Developing a robotic sea turtle could be the solution to uncovering the sea turtle's secrets in propulsion and energy consumption. Some robotic sea turtles have been created in the past [55,56,58-62] however, all attempts have failed to entirely mimic the sea turtle's locomotor pattern and flexible limbs. In some cases, these attempts have only introduced two degrees of freedom systems[56,59,62]. It is well understood that sea turtles produce complex three degrees of freedom motion, demonstrating the shortfall in those studies to reproduce genuine kinematics. While other works have introduced three degrees of freedom [55,58,60,63] the main goal in their works was not to try and truly mimic the sea turtle but demonstrate a novel turtle-inspired robotic technology. In recent work, an updated sea turtle locomotor description for the animal's general swimming routine is provided by van der Geest et al. [84], which details the 3-dimensional flipper patterns, including the active twisting of the flipper. They found that wild green sea turtles had a different swimming pattern than previous studies on juveniles in capitivity[3]. Additionally, they outlined how the flipper's motion can be broken up into five stages consisting of: Downstroke (DS), Sweep stroke (SS), Recovery stroke one (RS1), Upstroke (US) and, Recovery stroke two (RS2) (Fig .20). During the green sea turtles general swimming routine it is understood green sea turtles produce an average limb beat cycle of about 0.23Hz[28,84] to swim an average speed of approximately 0.6m/s[28,76,77,95].

Developing a robotic sea turtle that can genuinely mimic a real animal brings two significant complexities: Firstly, the flippers need to be a soft robotic device that can actively change shape to achieve optimum levels of wing twist while simultaneously supporting large flexural loads from the hydrodynamic forces. This is difficult to achieve with rigid robots that require stiff and multiple mechanisms leading to intricate assemblies to realize complex movements. Hence, soft robotic devices have been developed, as they can use simple deformations to achieve natural movements mimicking biological systems [65,96,97]. Current soft wing twisting technology has, in most cases, taken two forms: the first form produces actuation via shape memory alloys (SMA) or ionic polymer-metal composite (IPMC) [60,67,68]. However, as a creative approach, these solutions fail to produce large hydrodynamic forces when used in flapping wing conditions. The second form comes in solutions that include a soft material in the rigid robot, adding compliance to the system and allowing them to generate complex movements [49,52,69,70]. These solutions can support higher hydrodynamic loading at the expense of more complex design and manufacturing requirements. The second complexity to producing a realistic robotic sea turtle is that the overall form factor of the robot should look identical to that of the actual animal, thus making packaging of the required hardware within

the robotic limbs a tedious and ambitious design challenge. In recent work by Yan et al[61]., a turtle-inspired robot with variable stiffness hydrofoils describes a design that can vary the spanwise stiffness of the flippers with an assembly of small rigid bodies. Although it shows novel elements, it fails to realise an essential aspect of the sea turtle's flippers: the spanwise twist. The continuous smooth (one single body) twisting of the pectoral flippers is essential to ensure the correct angle of attack is produced along the flipper span to achieve maximum efficiency.

To address these challenges, we reverse-engineered the natural sea turtle into a robotic form to attempt and replicate the real turtle's form and function (Fig 21 and Movie S1 available at https://www.nature.com/articles/s41598-023-37904-5#Sec17). To the best of our knowledge, this is the world's first sea turtle robot designed exclusively for replicating the natural animal locomotion. The goal of this robot is not to enhance or improve sea turtle locomotion but gain further insight into how this animal produces propulsion. This new robot design is equipped with soft robotic flippers and a rigid shell, made possible by taking advantage of modern additive manufacturing equipment. The design can reproduce the natural swimming patterns based on the natural form of the green sea turtle (*Chelonia mydas*) (Movie S1). The flipper design, consists of a variable stiffness (across the span) polyurethane rubber that is cast in situ over a central carbon fibre spar that is connected to an additively manufactured rigid flipper tip. The design can produce near perfect linear twist along its span up to the rigid zone as per the twisting motion of real green sea turtles [84] (Movie S2 available at https://www.nature.com/articles/s41598-023-37904-5#Sec17) using only a single actuator. To determine the mechanical performance and endurance of the soft flipper design, bending and fatigue tests were performed. These results indicated that the design could support large flexural loads and operate robustly throughout its intended lifespan (Movie S3 available at https://www.nature.com/articles/s41598-023-37904-5#Sec17).

To reveal the propulsion performance, testing was performed within a freshwater tow tank to measure power consumption, thrust, drag and lift forces during the animal's regular swimming routine. Our findings show that the animal only produces thrust for approximately 1.4 seconds of the animal's 4.3-second flipper oscillation to produce an average swim speed of 0.602 m/s. During the remaining 2.9 seconds, the flippers go into a remarkable energy-saving recovery glide that does not substantially reduce the swim speed due to the animal's large mass and relatively low drag coefficient.

These findings advance our understanding of how sea turtles produce propulsion during their regular swimming routine. Thus, these findings may lead to new opportunities to optimise the findings for higher propulsive performance and efficiency to enhance the next generation of ocean exploration technologies.

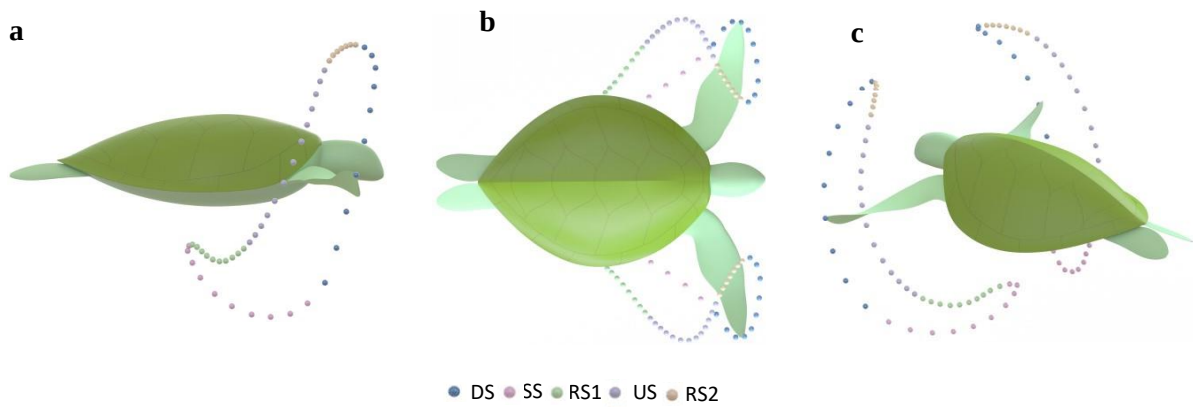

Figure 20: Five stages of the green sea turtle's swimming pattern as illustrated with coloured spheres [84]. (a) Swim pattern viewed from the sagittal plane (b) Swim pattern viewed from the Coronal plane. (c) Swim pattern viewed from a 3D viewpoint.

5.3 Results

5.4 Sea turtle robot design

Designing the robot to meet a real sea turtle's natural form and function brought with it many levels of complexity. Most of which come from packaging the required hardware into the organic surfaces that make up the turtle's form. The design process took an iterative approach by starting with a CAD model based on real sea turtles developed through multiplane extraction of video footage [84,95] and building in the necessary hardware required to have the robot meet the natural sea turtle locomotion while attempting to obtain the original form as closely as possible. To simplify the manufacturing process, the flipper geometry was simplified compared to a real turtle by removing the trailing edge serrations, scales and leading edge claw (Fig. S8a). However, the flipper cross-section remained as a turtle-inspired cambered hydro-foil profile [3,5]. Additionally, the locomotor pattern was minimised to three degrees of freedom. The locomotor patterns (Fig. 22a and Movie S1) were based on recent work by van der Geest et al. [84], with the flipper equations of motion (plotted in Fig. 22b) in roll and yaw, expressed using a Fourier series with $n = 8$, (equations 1-2) and pitch (flipper twist) expressed as a linear piecewise function (equation 3) with ($t = 0$) set at the end of the sweep stroke (SS) and beginning of Recovery stroke one (RS1):

$$\theta_{roll}(t) = a_r + \sum_{i=1}^{n} a_{ir}\, cos(iw_r t) + b_{ir}\, sin(iw_r t) \quad (1)$$

$$\theta_{yaw}(t) = a_y + \sum_{i=1}^{n} a_{iy}\, cos(iw_y t) + b_{iy}\, sin(iw_y t) \quad (2)$$

$$\theta_{Pitch}(t) = \begin{cases} a_{p1}t, & 0 \le t < t_1 \\ a_{p2}, & t_1 \le t < t_2 \\ a_{p3}t + b_{p3}, & t_2 \le t < t_3 \\ a_{p4}t + b_{p4}, & t_3 \le t < t_4 \\ a_{p5}, & t_4 \le t < t_5 \\ a_{p6}t + b_{p6}, & t_5 \le t < t_6 \end{cases} \quad (3)$$

Rotation axes were placed, considering the location of the turtle's shoulder and elbow joints based on video footage of real animals swimming in Australia's Great Barrier Reef (Fig. 22c). It is worth highlighting that despite the limb degrees of freedom being constrained to three, the robot could still perform the general patterns described by van der Geest et al.[84].

Due to the turtle body's complex surfaces, additive manufacturing was extensively used throughout the assembly, with carbon fibre and aluminium only used on highly stressed components such as drive shafts and couples. The turtle was manufactured to a straight carapace length (SCL) of 610mm from nine bonded sections to form the final geometry (Fig. S7b). Additionally, the turtle's main body was designed to fill with water to help neutralise buoyant and gravity forces. All rotation axes were supported with zirconia oxide bearings to remove unwanted wobble to the robotic limb and provide a smooth, corrosion-resistant rotation. Due to the additive manufacturing process, all cable management was done through specially printed internal channels within the turtle limbs to hide and protect the cables while allowing the necessary degree of freedom during operation. The robot's rear flippers were left static and thus uncontrolled. This was because when entering their general swimming routine, the rear flippers are almost motionless, tucked in, and pointing backwards to lower their parasitic drag [84,95] (Movie S4 available at https://www.nature.com/articles/s41598-023-37904-5#Sec17).

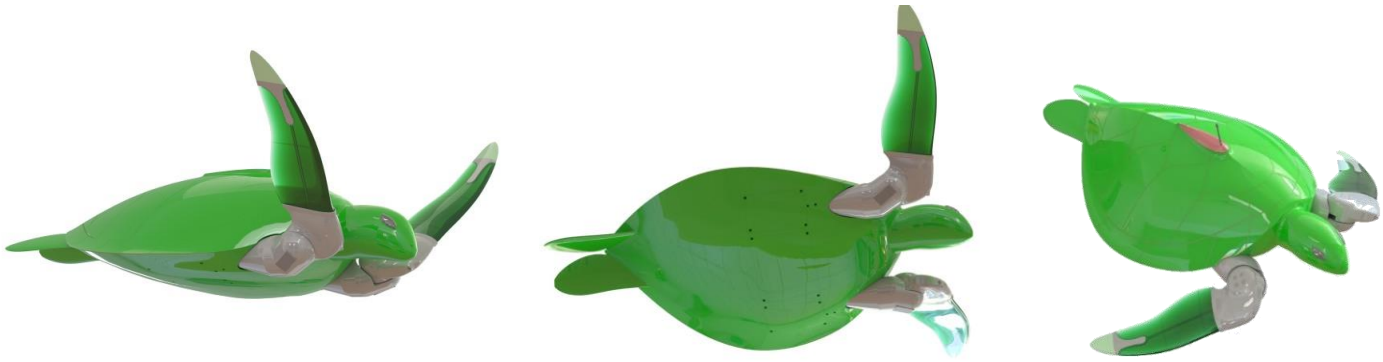

Figure 21: Final sea turtle robot design based on the green sea turtle (Chelonia mydas).

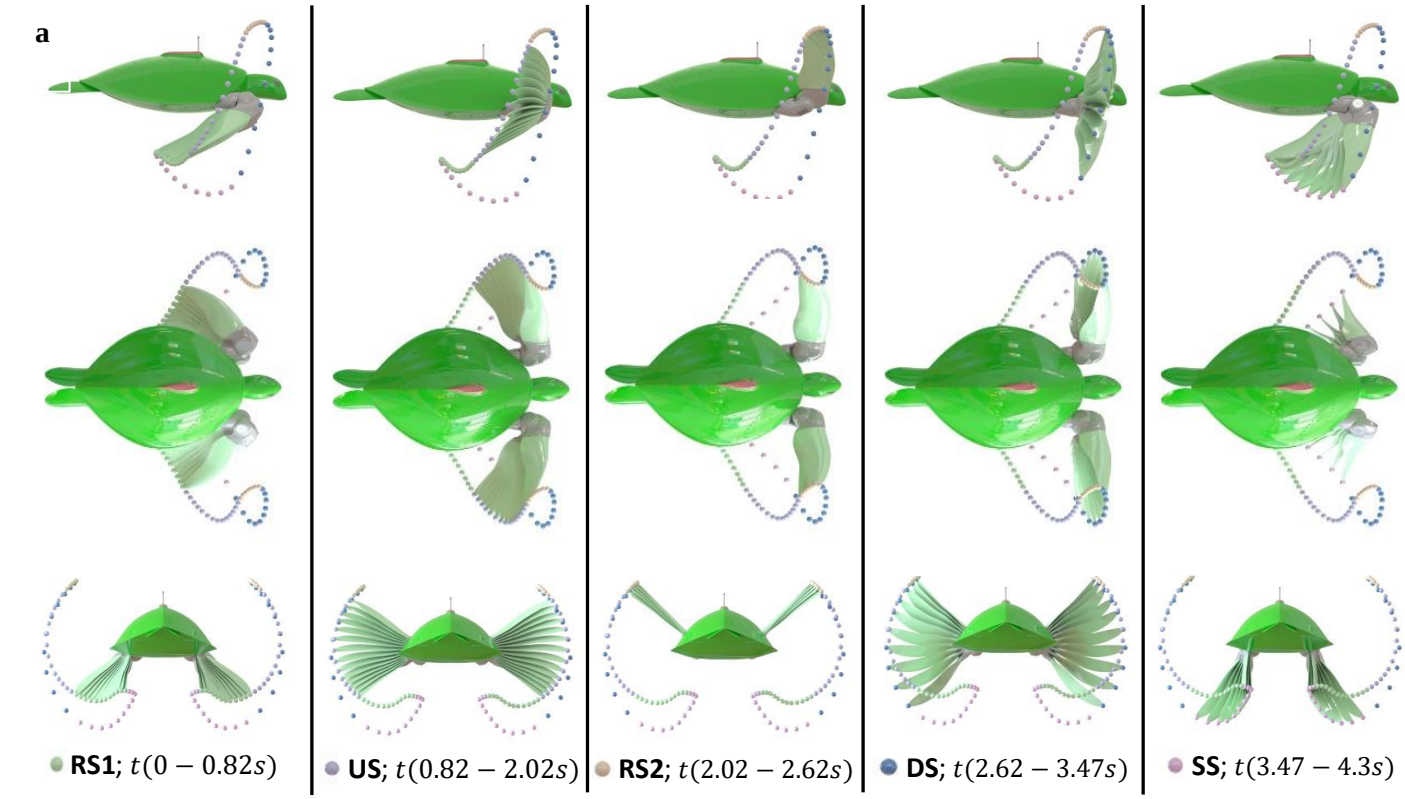

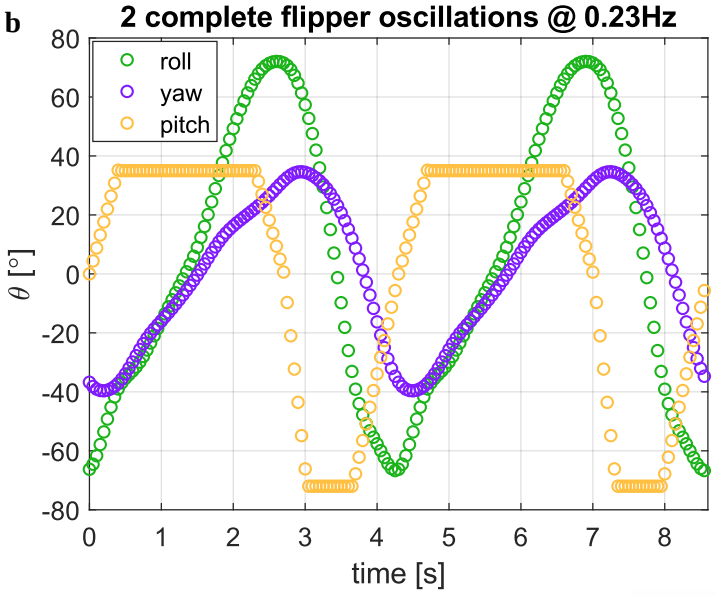

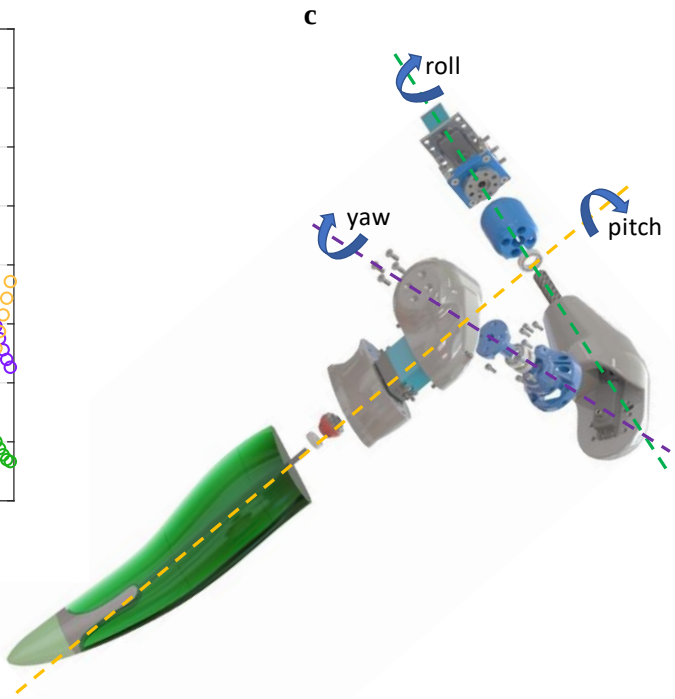

Figure 22: Sea turtle locomotion patterns. (a) Robot sea turtle assembly showing flipper position and twist @ 0.08 second time intervals in the five stages of the sea turtle locomotor pattern consisting of the downstroke (DS), Sweep stroke (SS), Recovery stroke one (RS1), Upstroke (US), and Recovery stroke two (RS2) as viewed from the Sagittal, Coronal and transverse planes. Time taken to complete each of the five stages is presented at the bottom of each column (b) Equations of motion in roll, yaw and pitch (Twist) plotted against time for two complete flipper cycles at a flapping frequency of 0.23hz. (c) Exploded parts view of the sea turtle robot limb showing the rotation axis locations and hardware.

5.5 Soft robotic flipper design

The natural twisting of the sea turtle's forearm can be illustrated with a linearly varying twisting motion from the turtle's flipper tip to the elbow [84]. The exact level of twist along the flipper span can be found with $\theta(x) = \frac{\vartheta_{pitch}(t)}{s}x$. Where $\theta_{Pitch}(t)$ is the maximum amount of twist applied by the turtle at any point in time and x the position of interest along the flipper span (s).

To physically achieve a linear twist relationship, it is understood that when torque is applied to a cylinder of constant stiffness and diameter from a solid mechanics principle, a linear twist is produced down the cylinder length. Applying such a simple principle to achieve linear twist to a soft robotic flipper of varying cross-sections required the device to be manufactured in sections of varying stiffness.

The design process to achieve this took an iterative design approach by solving simulations within FEA of various composite flipper models (see methods section for FEA setup). This process involved slicing the flipper model into various sections and applying a variety of material properties to each section until a linear twist throughout the flipper span was achieved (Fig. 23a,b and Fig. S8b).

The optimal design was composed of a rigid carbon fibre spar that transmitted torque to a rigid flipper tip through a single actuator. As the actuated flipper tip rotates, this causes the flipper body to produce the required twist. The main body of the flipper was manufactured in three sections composed of a cast polyurethane rubber of stiffness shore A harness A40, A60 and A70 (Fig. 23c), with the softest material set at the flipper root and with the stiffest close to the flipper tip. The flipper tip was manufactured with a porous structure to allow the polyurethane to bond firmly to the rigid structure. This bond area produces a semi-rigid zone between the flipper tip and the main flipper body, where the polyurethane overlaps the rigid zone. Manufacturing the flippers involved casting each layer simultaneously from the hardest to softest material, allowing the polyurethane to bond as though one single material at each interface. The mould was of a split design incorporating shrinkage risers and a holding jig for the carbon fibre spar and flipper tip in a simple single-part design (Fig. 23c and Fig. S9a).

Overall the design ensured the flipper could sustain large flexural loads while achieving the desired soft twisting actuation from $\pm 80^{\circ}$ (Movie S2) while only consuming a maximum power input of 4.5 watts per flipper at 80˚ of twist (Fig. 23d). To understand the mechanical properties of the soft robotic flipper and evaluate its ability to support flexural loading, fatigue and single-point bending tests were performed on two identical flipper assemblies. During the single-point bending test, the flipper sustained a 14.8Nm bending moment deflecting down at the wing tip 70mm before the travel in the holding tool reached its max permissible deflection (Movie S3). The flipper may have resisted higher bending moment had the tool been designed to hold the wing higher from the machine bed. Fatigue tests were performed in a custom-built acrylic tank to actuate the flipper twisting motion for one complete cycle of -73˚ to 35˚ (108˚ total) underwater (Movie S3 and Fig. S10a-d). The flipper sustained 922,154 cycles, equivalent to swimming 2395 km (refer to the methods section for additional details). At the end of fatigue testing, the leading cause of failure was the seizing of the servo transmission. The flipper showed no evidence of failure at the casting interfaces however, at the flipper trailing edge, the adhesive had begun to separate from the wing root (Fig. S10e).

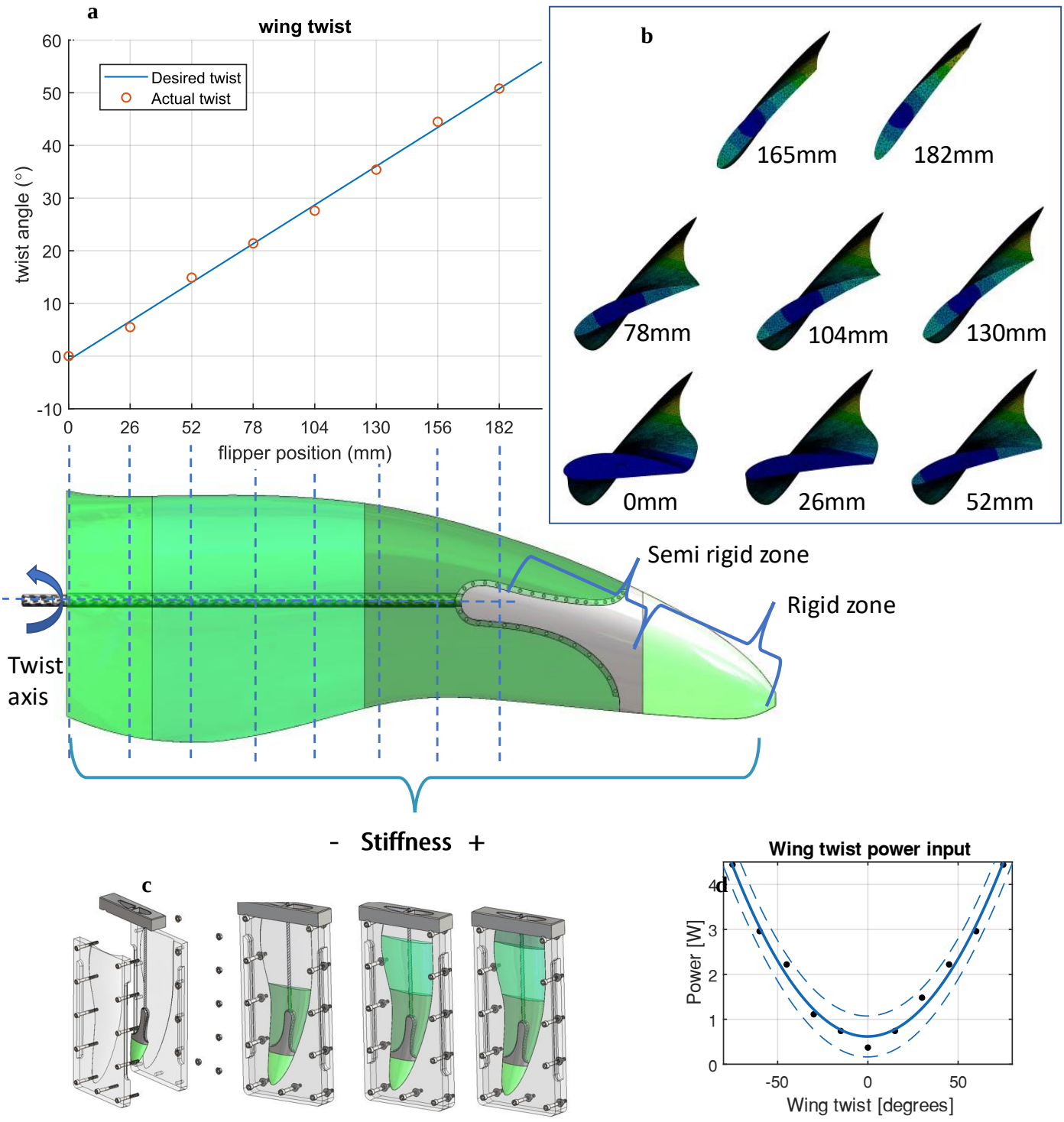

Figure 23: Twisting flipper design. (a) The plot of desired flipper twist against the actual flipper twist. The actual twist value position is projected down onto the CAD model's plan view, which also shows the twist axis's location and level of material stiffness throughout the flipper span (b) Cross sections taken from the FEA simulations that directly correspond to positions in Fig, 23a that show the level of flipper twist (c) CAD model showing split mould assembly with each of the three casting stages. (d) Power consumption to hold the flipper at each degree of twist from -80˚ to +80˚.

5.6 Robot testing overview

All swim tests conducted measured power consumption, swim speed, thrust and lift generation with the flapping frequency held constant at 0.23Hz based on freely swimming wild green sea turtles [28,84]. A total of three different testing procedures were followed, firstly constraining the robot, so it could not move. This gave insight into the turtle's propulsion from a standstill and additionally served as a benchmark for dynamic swimming tests.

The second test allowed the robot to freely swim however, the robot had to overcome a constant 2.5 N dynamic friction load within the system generated by the linear rail. This test allowed the restricted swim speed to be gathered based on the robot overcoming the friction loads and was used as a reference for calculating the possible swim speeds without friction.

Finally, the robot was towed up to speed before it could take over to propel itself. During tow testing, the robot would be towed up to 0.6 m/s based on the cruising speeds of wild sea turtles [76,77,95] until the robot began the downstroke, from where it would begin to accelerate on its own (Fig. S12b). With testing results showing propulsion was only produced during DS and SS, the loss in swim speed (without friction forces) during the remaining swim cycle was derived from Newtonian physics by integrating the acceleration term with respect to time and substituting in the hydrodynamic force with:

$$\Delta v_2 = \frac{\rho A_p c_d (v_o - \Delta v_1)^2 \Delta t}{2m}$$

Where m is the mass of the robot, ρ the fluid density, A_p is the projected frontal area of the robot and (c_d) the robot drag coefficient. This calculation was iterated with a constant time step (Δt), with the initial swim speed (v_0) defined as the maximum velocity obtained during the swim test with $\Delta v_1 = 0$ for the first iteration. For the following iterations v_0 was calculated as

$$v_0 = v_0 - \Delta v_2$$

This process was iterated to cover the time when no thrust was produced. The complete swim speed cycle was created for a freely swimming sea turtle by compiling all the velocity data from tow testing (Fig. S12b) with the loss in swim speed calculations. From this point, the swim speed was differentiated with respect to time and compared back to the original thrust values (Fig. S12a) to double check and verify that the swimming speed was possible based on the measured thrust values. To remove the need for a complex control system and make force data and power consumption easily obtainable, the robot was attached to a pylon comprised of a NACA 0024 cross-section with a varying chord. The pylon was bolted to a 40kg load cell for measuring lift forces and connected to a linear rail and cable track (Fig. 24a-b). Overall, the robot and pylon assembly weighed 30 kilograms when the cavities within the robot filled with water. Drag and constrained thrust forces were measured from the pully assembly with a built-in 20kg load cell (Fig. 24c and Fig. S11a-c). Thrust forces during free swimming were calculated based on the robot's acceleration $(\dot{v})$, friction load (F_f) and hydrodynamic drag force with:

$$F_T = m\dot{v} + \frac{\rho A_p c_d (v)^2}{2} + F_f$$

Where m is the mass of the robot, ρ the fluid density, A_p is the projected frontal area of the robot, c_d the robot drag coefficient, v the robot velocity and F_f the linear guide system friction. The robot's drag coefficient was found using both CFD with verification from tow testing by subtracting the 2.5 N dynamic friction load within the system generated by the linear rail assembly during simple tow tests. This process involved towing the robot through the pool with the limbs held stationary (Fig. S12c-e and Fig. S15).

The linear rail assembly was bolted to an aluminium extrusion truss frame that saddled a freshwater pool of dimensions 4m long, 2m wide, and 1m deep and gave a rigid foundation to the overall system, and positioned the robot centrally in the pool as shown in Fig. 24 and Fig S11d. The depth of the pool used was deemed as suitable as green sea turtles spend most of their time in the shallow fringing reefs [84] as seen in Movie S4.

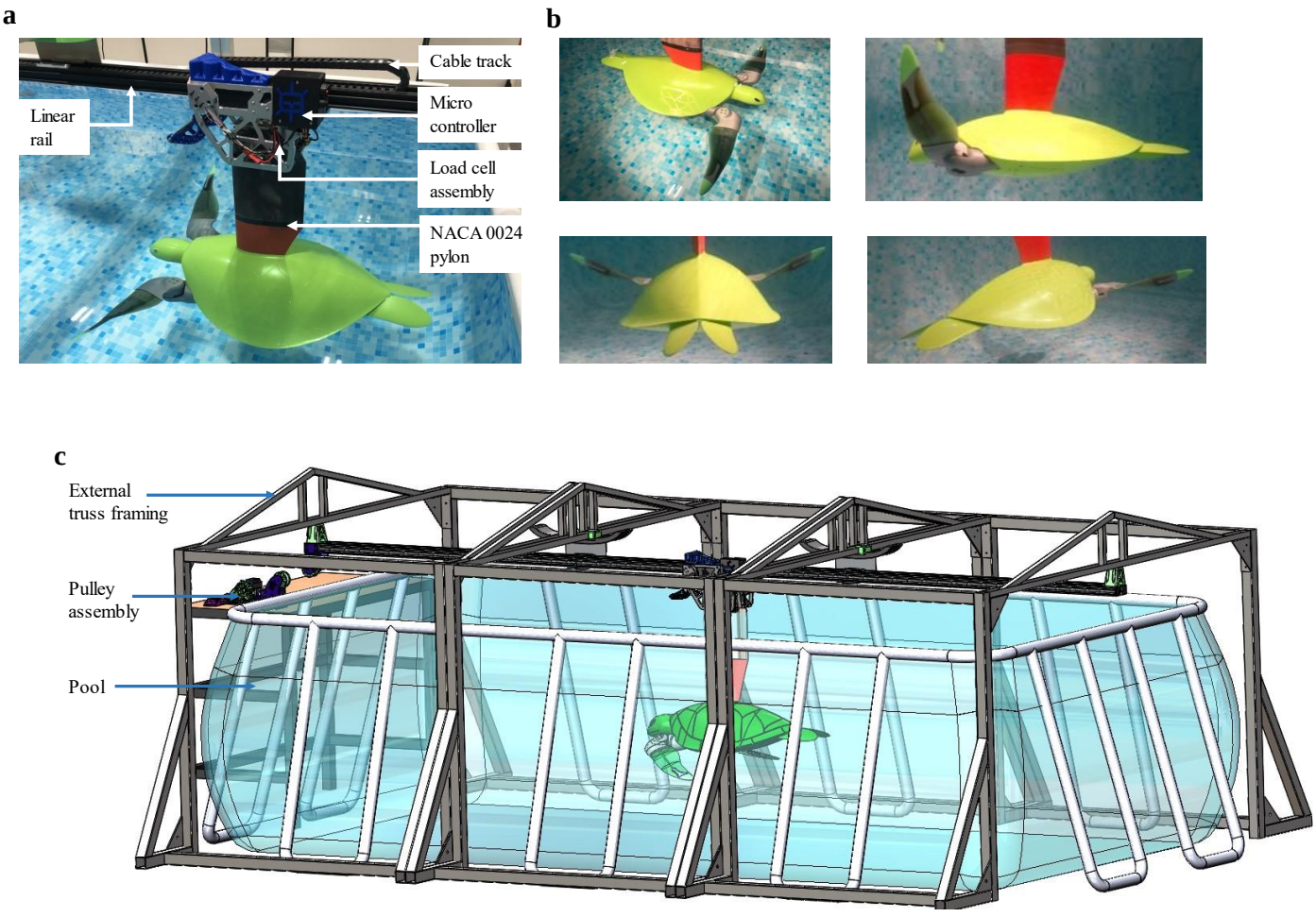

Figure 24: Robot and test rig assembly. (a) Robot, pylon and load cell assembly. (b) Footage of robot swimming from various view angles see Movie S4. (c) Complete CAD model of test rig assembly showing external truss framing to support linear rail above the pool.

5.7 Robot testing power and force

This section will continuously refer to Fig.25, where the various testing results of power consumption, thrust, lift and swim speed are detailed. All power and force plots represent constrained operation and testing with the pulley system to get the turtle up to its cruising speed. The vertical green dashed lines represent the location in time for each of the turtle's five swim stages as outlined in Fig. 22a.

Referring to Fig. 25a-b, the power consumption for both constrained and free swimming (towed up to speed) can be observed. Our findings show that the power consumption during RS1, US, and RS2 always lay below 20 watts, with the only significant energy consumption occurring during DS and SS. Additionally, the unconstrained swimming robot demonstrated a lower energy consumption, along with higher thrust values and lower lift values (Fig. 25a-f). This finding was expected as the swimming pattern is extracted from freely swimming wild green sea turtles, as demonstrated by van der Geest et al.[84]. The noticeable decrease in thrust and increase in the lift for the constrained robot is likely due to adverse pressure gradients causing excessive flow separation, making the downstroke less efficient, with the sweep stroke not being largely affected due to the relative velocity difference.

For free and constrained operation, no evidence of thrust production was detectible during the upstroke (Fig. 25c,d). However, a positive lift was generated for freely swimming, with a negative lift generated during constrained operation. This finding supports the work of van der Geest et al. [95], where green sea turtles are shown to produce a drag-reducing upstroke that utilises lift forces on the turtle's flippers to help bring the flippers up, potentially lowering energy consumption. Additionally, a non-propulsive upstroke was also discovered by David T. Booth[4] for green sea turtle hatchlings.

5.8 Robot testing swim speeds

Referring to Fig. 25g,h, the robot swim velocities are detailed for one complete wing oscillation. The velocity data in Fig. 25h represents the exact swim velocity obtained by the robot without any pulley assistance thus, the robot had to overcome the constant 2.5N friction force within the linear rail assembly. A peak swim speed of 0.45 m/s was obtained, producing an average swim speed of 0.361 m/s. As seen in Fig. 25g the swim speed for a freely swimming turtle without any friction is displayed. A peak swim speed of 0.71 m/s was obtained, with an average swim speed of 0.602 m/s, closely matching literature for freely swimming sea turtles [76-78,95]. Based on the average swim speed, the Reynolds number was calculated based on the straight carapace length (D_{SCL}) applying $Re = \frac{v\rho D_{scl}}{\mu}$, to obtain values of 220,000 and 367,000. Where v is the average swim speed ρ the fluid density and μ the fluids dynamic viscosity. At the same average swim speeds, the Strouhal number (St) of 0.24 and 0.4 was calculated by applying, $St = \frac{Df}{v}$ where D is the peak-to-peak distance of wing oscillations f the flapping fequncy and v the average swim velocity. The values of St found during testing lie in the region observed in other flying and swimming animals of 0.2 to 0.4 [98-101].

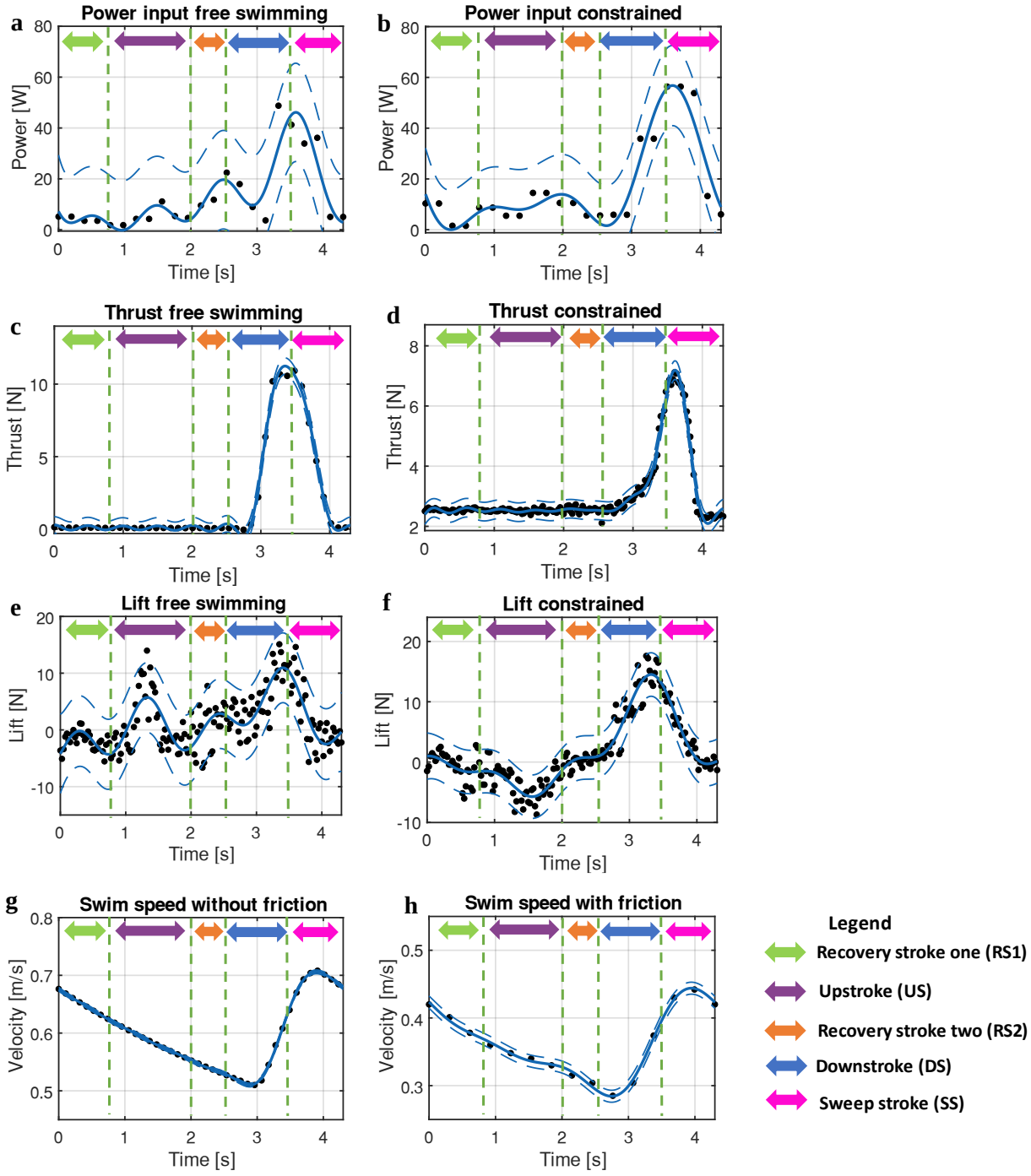

Figure 25: Testing data and results. Green arrow showing the amount of time spent during RS1, purple arrow showing the amount of time spent during the US, orange arrow showing the amount of time spent during RS2, blue arrow showing the amount of time spent during the DS and magenta arrow showing the amount of time spent during SS. (a) Power consumption against time with pulley assistance to bring robot up to speed (b) Power consumption against time for the constrained operation. (c) Thrust generation for the freely swimming robot. (d) Recorded load cell thrust generation for constrained operation. The plot includes a 2.5N vertical offset to account for the constant dynamic friction load. (e) Recorded load cell data plotted against time for the lift force with pulley assistance. (f) Recorded load cell data plotted against time for constrained operation. (g) Predicted swim speed for the robot without any friction from the test rig assembly. (h) Swim speed data for the robot without pully assistance, meaning the robot had to overcome a constant 2.5N system friction load

5.9 Discussion and Conclusion

In this work, we disclose a new soft robotic sea turtle that can closely bio-mimic the natural sea turtle's general swimming locomotor patterns as described by van der Geest et al.[84]. Developing the robot meant overcoming two significant obstacles. Firstly, designing the mechanical system to accomplish the locomotor pattern, and secondly, keeping the natural sea turtle form. The essential contribution to achieving this was our new soft twisting flipper that can replicate the natural animal's morphing ability while still being capable of supporting large flexural loads. To the best of our knowledge, this makes our robot the first attempt at producing a robotic sea turtle that can produce the general swimming patterns of a wild animal.

This work's primary purpose was to outline the design of the biomimetic robot to help better understand the sea turtle's propulsion mechanism. Gaining this understanding through conventional animal testing would have been highly challenging in our current paradigm of ethical approvals, especially when endangered animals are concerned. However, although we reverse engineer the sea turtle to take a robotic form, we demonstrate that the robot can swim at 0.6 m/s with a flapping frequency of 0.23Hz. This alone is a notable finding as previous studies on wild green sea turtles demonstrate that a swim speed of 0.6 m/s is obtained at a flapping frequency of around 0.23Hz [28]. Additionally, in our own research expedition in Australia's Great Barrier Reef [84], we also found that green sea turtles produced an average limb beat cycle of 0.234Hz, and it is understood that the average swim speed of sea turtles is 0.6 m/s [76,77,95]. We use these findings of flapping frequency and swim speed as a form of validation for the suitability of our robot as a tool for understanding sea turtle propulsion methods. Additionally, at this flapping frequency and swim speed, a Strouhal number of 0.24 is obtained, which directly lies in the region observed in other swimming and flying animals and is understood to contribute to their efficient mode of transport [98-101].

Our robot also demonstrated that during the animal's regular swimming routine, propulsion is only generated for 30% of the overall cycle, with the animal entering an energy-saving glide during the remaining 70%. This is made evident when observing the power and thrust curves, as seen in Fig. 25, with the only substantial power consumption occurring during the DS and SS, along with the thrust forces only being registered during the same period in time. During the upstroke, a positive lift force was generated, suggesting sea turtles take advantage of their flippers' hydrodynamic loading to help bring them up to the top of the stroke. This may support the findings of van der Geest et al. [95] that sea turtles produce a passive drag-reducing upstroke for conserving energy by allowing the flippers to enter a near-equilibrium state that prevents cross flows due to pressure differentials[95].

Some caveats require discussion with our findings due to the simplification of various systems, equipment and methodology. Firstly having the robot constrained in the vertical axis so lift forces could be obtained prevents the turtle from pitching up and down due to the vertical forces during swimming. The removal of the pitching motion could cause the robot to swim slightly quicker due to the body keeping a constant angle of attack to the oncoming flow. Additionally, all tests were performed and calculations made with freshwater, not typical seawater that the animal would swim in. Though both these simplifications likely affect the swim speed, they were both essential for the success of the experiments as the lift forces would have been difficult to obtain without the vertical constraint, and the amount of salt required to create the correct saltwater density was extreme at approximately 200kg.

Additionally, constraining the robot meant advanced control systems were not needed, thus allowing for a more detailed analysis of what forces are generated during the regular swimming routine. Another talking point to simplifications can be observed in the pool size. As discussed earlier in the manuscript, the depth of the pool is deemed appropriate as sea turtles spend most of their time in the fringing reefs [84], often only 1m in depth. However, the pool length of only 4 meters which resulted in limited flipper oscillations before the robot ran out of runway. This issue could be remedied in future work with the robot swimming autonomously in a large pool or even in an ocean environment.

Obviously, this work primarily takes geometric and kinematic data from video footage[84,95] rather than conventional methods that typically use a live or dead specimen. This method of data collection could potentially lead to discrepancies geometrically and kinematically. However, it must also be noted that all sea turtles vary in shape, size, mass, and flipper motion, so although video footage and photos are used when comparing the motion of our robot with natural sea turtles, there is a minimal argument that can be made regarding its ability to mimic its biological counterpart.

Also worth noting is that the turtle geometry used in this study is based on our previous work[95], where we detail the development of a turtle geometry that we compare with biological data, including the drag coefficient of the carapace (without flippers)[89], frontal area (including flippers), mass (including flippers), and SCL[34] to achieve valuable correlations and give confidence in our turtle geometry.

By removing features such as leading-edge claws and trailing-edge serrations of our turtle model could lead to hydrodynamic discrepancies from our model to its biological counterpart. However, this was, unfortunately, a necessary detail to achieve the extremely tight budget and immensely helped simplify the manufacturing process by reducing the need for complex machining of the split mould assembly, as seen in Fig.S9.

Though several caveats are evident in our work, we believe we have created what is the best understanding of the sea turtle's propulsive routine during its regular swimming pattern. Additionally, we have accomplished this without any animal testing by designing what we believe is the world's first and only robotic sea turtle that was solely developed to help understand the sea turtle's propulsion methods. We hope this work will help inspire others to develop robots as a substitute for their biological counterpart.

In future work, we plan to use this robot to identify what unique flow features, including wall effects, are responsible for the thrust generation during the DS and SS, along with how this could be optimised and developed for the next generation of robotic ocean exploration devices.

5.10 Materials and methods

5.11 Design and fabrication of Sea turtle chassis

The foundation of the robot design is based on works by van der Geest et al. [84,95], applying both the swimming locomotor patterns [84] and the green sea turtle CAD model [95] to help set the design foundation. Van der Geest et al. describe the turtle's locomotor patterns of the flipper tip, flipper elbow and flipper twist using a Fourier series as:

$$x(t) = s_f(a_x + \sum_{i=1}^{n} a_{ix}\, cos(iw_x t) + b_{ix}\, sin(iw_x t))$$

$$y(t) = s_f(a_y + \sum_{i=1}^{n} a_{iy}\, cos(iw_y t) + b_{iy}\, sin(iw_y t))$$

$$z(t) = s_f(a_z + \sum_{i=1}^{n} a_{iz}\, cos(iw_z t) + b_{iz}\, sin(iw_z t))$$

$$\theta(t) = \begin{cases} -\theta_{ds}, & 0 \le t < t_1 \\ \sum_{n=i}^{n} a_{dsi}\, sin(b_{dsi} t + c_{dsi}), & t_1 \le t < t_2 \\ \theta_{us}, & t_2 \le t < t_3 \\ \sum_{n=i}^{n} a_{usi}\, sin(b_{usi} t + c_{usi}), & t_3 \le t < t_4 \end{cases}$$

Where the position of the flipper tip and elbow can be expressed with $x(t), y(t)$ and $z(t)$ and flipper twist expressed with $\theta(t)$. The variable s_f is used to scale the equations to suit any sized turtle based on a reference straight carapace length of 610mm [84].

The green sea turtle CAD model from van der Geest et al. was inserted into a CAD (SolidWorks, Waltham, Massachusetts, USA) assembly along with the three-dimensional data points of the locomotor pattern. This was achieved by solving the equations within CAD using the "Equation Driven Curve" function to create a part consisting of only three-dimensional data points representing the turtle's locomotor pattern. Having the turtle CAD model and locomotor patterns within a CAD assembly allowed for an iterative design approach to then take place for developing the robotic limb. Once the final design was complete (Fig. S7a), a virtual clone within CAD (Movie S1) could be used to verify the locomotor patterns.

The robot's chassis was additively manufactured from PLA+ (Esun, Shenzhen, China) filament printed on an FDM 3D printer (Caribou MK3s, Remagen, Germany). As shown in Fig. S7b-f the chassis was manufactured in twelve sections (Fig.S7b), with each part sliced

(Simplify3D version 4.1, Cincinnati, Ohio, USA) with a 0.4mm nozzle at 0.2mm layer heights, 12 top and bottom layers, 6 walls, and 40% honeycomb infill. The chassis was then bonded together with methylene chloride before receiving an automotive quality paint job (Fig. S7c,d). All surface fasteners were recessed or countersunk to help lower parasitic drag. Three access hatch locations were placed under the chassis to access roll motors and electrical connections (Fig. S7e). The elbow and shoulder joints were also additively manufactured however were left as printed without paint (Fig. S7f).

5.12 Design, fabrication, FEA setup and testing of soft robotic flipper

As seen in Fig. S8, the design process to achieve the soft robotic flipper took an iterative design approach using commercial FEA software (ANSYS 2021 R2, Pennsylvania, USA). Simulations were set up to test various material layups and properties to inspect their effect on twisting motion. The first design iteration began with designing a layup that could potentially work using our mechanical design intuition coupled with the solid mechanic's principle of torsion previously mentioned in the main manuscript. From this point, the FEA results could be reviewed to see what potential layup could be applied to improve the results. This process was followed until the desired twist profile was achieved. Simulation boundary conditions consisted of a fixed support at the wing root with bonded sections between each material layup. To create the twisting motion, a frictionless contact was applied to the spar and flipper interface, with a remote angular displacement applied to the carbon fibre spar. Material properties were simplified by estimating the Young's modulus based on the shore A hardness using:

$$log_{10}E = 0.0235S_A - 0.6403$$

Where E is the elastic modulus in MPa and S_A the shore A hardness. The carbon fibre spar had mechanical properties of ultimate bending stress ($\sigma = 822MPa$) and Young's modulus of ($E = 85GPa$). Mechanical properties were found through 3-point bending tests (H10KS Universal testing machine, Tinius Olsen Ltd, Surrey, England).

The final design used a solid 5mm diameter carbon fibre spar that was lubricated just before the casting process to ensure smooth rotation between the flipper and spar interface. The flipper tip and spar were assembled into the mould assembly before casting, as seen in Fig. S3a. Each cast section was from shore A hardness polyurethane rubber (F140, F160, F170 Barnes, Moorebank, NSW, Australia). The 40 shore A section was approximately 42mm long at the flipper root, with a 60 shore A section of 121mm and finally the 70 shore A section of 71mm (Fig. S9b). Each section was directly cast one after the other to create a single casting with excellent bond strength between each material (Fig. S9c).

Fatigue testing was performed with a custom-manufactured water tank made from 18mm thick clear acrylic that would actuate the flipper through an Arduino Nano controlled (Arduino.cc, Somerville, MA, USA) servo motor (Fig. S10). The system was designed to pause the actuation if a drop or rise in current over the regular operation was detected, then save the cycle count to an SD card.

The flipper bending test was performed with a custom-manufactured holding jig, as shown in Movie S3 that was installed into a universal testing machine (H10KS, Tinius Olsen Ltd,

Surrey, England). The test was performed at 1mm/min until max permissible deflection was achieved due to design constraints.

5.13 Force and swim speed measurements

Swim speeds were found by measuring the time taken for the robot to pass markers of width 17.5mm spaced apart a distance of 30mm along the linear rail assembly (Fig. S11a). Time measurements to pass the markers were obtained by filming the robot with a camera (GoPro Hero 10, GoPro, San Mateo, California, USA) at 240 frames per second and 2K resolution. The camera was towed along with the robot down a separate linear rail that ran parallel to the robot's swim direction (Fig. S11a and Fig. S12b).

For constrained operation, thrust forces were obtained by installing an additional pulley, as seen in Fig. S11b, to allow the robot to swim against the pully load cell (Fig. S11b,c). As this setup only allowed load cell thrust measurements to be obtained while constrained, thrust for swimming operation was obtained based on the robot's acceleration, drag force and friction within the linear rail assembly as described in the main manuscript. The friction forces caused by the linear rail assembly were obtained by operating the equipment without the robot. The dynamic friction load within the system was 2.5N (Fig. S12c-d) regardless of operating speed between 0.3 to 0.6 m/s.

5.14 Electrical system robot

The simplified schematic in Fig. S13 shows the electronic system used for the control of the turtle flippers. This required a suitable power supply for the six Savöx SW1210SG servos, (SAVOX, Taichung City, Taiwan) a microcontroller (MCU) (Particle Industries Inc, San Francisco, USA) with enough timer resources to produce the PWM signals for the control of the six servos, and to generate the real time interrupts (RTI) to update the servo set positions so the flipper can follow the desired trajectory accurately. The hardware also needed to take external input to control the actions of the system for the various tasks such as starting/stopping the turtle swimming or changing the flapping frequency.

The Particle Photon MCU was chosen as it had sufficient timer resources capable of 7 independent PWM signals and a built-in WIFI module to facilitate wireless control and over-the-air (OTA) firmware updates. The main power supply was a variable 15A DC supply set to the servos recommended operating voltage of 7.4V. This power supply was external from the gantry allowing the operator of the robot to disable the supply in the event an unexpected system failure occurred. Two more on/off switches were used to separate the MCU and servos power supply control, allowing for the MCU firmware to be updated and tested without the servos operating. A buck converter was used to step down the main 7.4V supply to the 5V required by the MCU. Brownout protection was implemented to prevent voltage drop in the main power lines due to possible large changes in the servos required torque moving between set positions.

5.15 Software

The firmware for the controller was written in C++ using Particles Web IDE. The software was split into two parts: one the control of the servos for the flapping motion and moving between desired poses and two the wireless operator controls. For the control of the servos a RTI and a look-up table (LUT) containing the set positions for each step in the flapping pattern are used to control the flippers. Using equations 1-3 the LUT is generated for a 50ms interval across the 4.3s period of the motion, resulting in 86 steps. The 50ms time interval can be varied by the operator to alter the robot's flapping frequency. The firmware uses the angular set positions in the LUT to calculate the required duty cycle on period of the PWM signal 800-2200us for +/-80 degrees range of motion. To ensure the flipper will closely follow the desired trajectory and smooth motion, each step in the pattern is interpolated between taking 3 sub steps to move between steps. This means the RTI used to update the servo set positions will occur at the rate described by $T_{interrupt} = \frac{T_{step}}{n}$ where T_{step} is the period of one step, $T_{interrupt}$ is the RTI period and n is the number of interpolation steps.

For moving the robot's flippers between desired poses such as the zero position or start position of the swimming pattern, interpolation is again used. The current set position of the flippers is always stored to ensure it can be used as the starting point of the interpolation to the new pose when a command to move is received, this prevents the servos from jumping between positions. The number of steps between the two set positions and the time interval between the interpolation steps can be specified in the firmware to allow smooth control of the flippers. To prevent collisions between the flippers and the body, a set of pre-planned poses are used with the flipper's zero position always used as the first position because from any position, the flippers can reach the zero position without the possibility of collision.

The operator control of the system is facilitated by a standard state machine approach, using states such as swimming, stopped, reset, move to zero position, move to low drag position etc. The states are selected by the operator using a web-based GUI application written in HTML that communicates to the Photon MCU over WIFI using the Particle API functions.

5.16 Electrical system Testing rig

The testing rig electrical system (Fig. S14a) is composed of a graphical user interface (GUI) programmed on LabView (National Instruments, Austin, Texas, USA), two electric systems (one to control the motor and another for the data acquisition of the load cells), the pulley system and the load cell assemblies (lift and drag).

The GUI (Fig. S14c) was able to turn on and off the motor of the pulley system in a synchronous way with the load cell data acquisition system using serial communication between the computer and the microcontrollers. Furthermore, when the program starts, it records the data from the load cells into a txt file. The information on the txt file contains the data of the reading sample, the information coming from both load cells. When the system stops, it saves the file into a selected folder.

The motor control system (Fig. S14b) consisted of an electric circuit containing an A4988 stepper motor driver (Allegro Microsystems, Manchester, New Hampshire, USA), a microcontroller Arduino NANO and a variable DC power supply skyRC efuel 540w (SkyRC

Technology, Guanlan, Shenzhen, China). The Arduino controlled the angular speed of the motor in revolutions per minute (RPM) using the A4988 driver with a micro step of a 1/4 step to ensure smooth motor steps during the low initial speeds. Furthermore, to avoid high acceleration loads, linear velocity was defined as: $v = 0.2t$. Where "v" is linear velocity and "t" is time. Moreover, a pulley (r = 0.0225 m) attached to a stepper motor, "NEMA 17", was used to transform the angular speed to a linear speed. Then the linear speed could be calculated as: $v = \frac{2\pi r(RPM)}{60}$.

Finally, the data acquisition system (Fig. S14b) consisted of a second Arduino NANO connected to two SparkFun load cell amplifiers, HX711 (SparkFun Electronics, Niwot, Colorado, USA). The HX711 were connected to two load cell assemblies, one for the lift and one for the drag. To record the lift, a 20 kg load cell (YZC-1B, XIN NUO QI, China) was used, while a load cell of 40 kg (YZC-1, XIN NUO QI, China) was used for the drag force. The sampling frequency of the system was 40 Hz.

5.17 CFD Analysis and Turtle Geometry

In our previous work[95], we detail the development of a turtle geometry that we compare with biological data, including the drag coefficient of the carapace (without flippers)[89], frontal area (including flippers), mass (including flippers), and SCL[34] to achieve valuable correlations and give confidence in our turtle geometry. This geometry was used to develop our robotic sea turtle as described in the main manuscript. We use CFD as a tool to help evaluate the drag coefficient against the original more organic geometry to act as a form of validation. We found our robot produced a drag coefficient of 0.16 when the flippers/wings were held stationary, as per Fig. S15, aligning well with the values obtained in our previous work of 0.16, also obtained from CFD with the results available in the supplementary folder of that work[95]. This gave us confidence that the robot's geometry was as close as physically possible to the original geometry, given the challenging nature of creating the limbs as previously described. The simulation was set up to solve with the $k\omega\ SST$ model using commercial CFD software ANSYS Fluent (ANSYS 2021 R2, Pennsylvania, USA) with all model parameters left in their default settings. The Fluent polyhex core mesh was used, consisting of 81,001,792 nodes and 38,886,857 elements. The mesh was refined down to a y^+ of 0.75 to accurately solve the flow down to the viscous sublayer. The computational domain was modelled as per the swimming pool used and halved at the symmetry plane with the symmetry plane boundary condition applied. The pool surface of the computational domain was set as a free slip wall, with the pool walls and floor set as zero slip moving walls at the inlet velocity of 0.6 m/s. The turtle geometry was set as a smooth no-slip wall condition. Convergence reports were set up to study the standard deviation of the velocity magnitude at the outlet, the area-weighted average of the wall y^+, the lift, drag and scaled residuals.

Chapter 6: New insights into sea turtle propulsion and their cost of transport point to a potential new generation of high-efficient underwater drones for ocean exploration

6.0 Preface

The enduring mystery surrounding the Green sea turtle's (Chelonia mydas) ability to traverse up to 50 km daily, relying solely on a diet of seagrass and microalgae, has captivated the scientific community. One cannot help but wonder: How can this animal journey such vast distance, given the seemingly limited energy derived from its diet? Chapter 5 endeavoured to decode this question by focusing on the turtle's swimming technique, power consumption, and propulsion without treading the minefield of ethical and logistical challenges using robotics.

The findings illustrated that propulsion derived from the sea turtle's limbs was active for just 30% of its cycle, with the remaining 70% devoted to a power-conserving, low-drag glide. This impressive biomechanical strategy ensures the turtle sustains steady speeds while optimising energy use.

Transitioning to chapter 6, our understanding deepens further. Even though the 30:70 propulsion-to-gliding ratio was already established, a pertinent question arose: How does the sea turtle modulate the aquatic flow during its propulsive phase? Enter "Cornelia," our robotic sea turtle from the prior chaptor. For the next chapter, with the help of Cornelia's advanced mechanics, a profound exploration of turtle propulsion's hydrodynamics and cost of transport will be produced.

6.1 Abstract

Sea turtles gracefully navigate their marine environments by flapping their pectoral flippers in an elegant routine to produce the required hydrodynamic forces required for locomotion. The propulsion of sea turtles has been shown to occur for approximately 30% of the limb beat, with the remaining 70% employing a drag-reducing glide. However, what is unknown is how the sea turtle manipulates the flow during the propulsive stage. Answering this research question is a complicated process, especially when conducting laboratory tests on endangered animals, and the animal may not even swim with its regular routine while in a captive state. In this work, we take advantage of our robotic sea turtle, internally known as Cornelia, to give the first insights into the flow features during the sea turtle's propulsion cycle consisting of the downstroke and sweep stroke. Comparing the flow features to the animal's swim speed, flipper angle of attack, power consumption, thrust and lift production, we hypothesise how each of the flow features influences the animal's propulsive efforts and cost of transport (COT). Our findings show that the sea turtle can produce extremely low COT values that point to the effectiveness of the sea turtle propulsive technique. Based on our findings, we extract valuable data that can potentially lead to turtle-inspired elements for high-efficiency underwater drones for long-term/duration underwater missions.

6.2 Introduction

Sea turtles navigate their marine environments by gracefully flapping their pectoral wings/flippers to produce a visually enchanting locomotive pattern. This flapping motion allows the sea turtle to migrate thousands of kilometres to reach favourable breeding or feeding grounds [14-16,102,103]. The flapping motion has typically been described as asymmetric, with the downstroke approximately twice as fast as the upstroke[3,84,104]. In recent work by van der Geest et al.[84], the flapping motion is described three-dimensionally for the Green sea turtle (*Chelonia mydas*), including the soft twisting of the flipper. They describe the flipper motion by breaking it up into five segments consisting of the Downstroke (DS), Sweep stroke (SS), Recovery stroke one (RS1), Upstroke (US) and finally, Recover stroke two (RS2) (Fig. 26). It is understood that during the Green turtle's general flapping routine, the upstroke does not generate any thrust[4,84,95,104], however, during this time, the animal's drag coefficient is lowered to help reduce swim speed losses[95]. To quantify how the drag is reduced during the upstroke, van der Geest et al.[95] conducted dedicated work to uncover the flow features generated by the flipper during this period. Through dye visualisation of a scale turtle model in a towing tank, they found the flipper would enter a near-equilibrium state that produced near-constant pressure across the entire flipper surface [95] (Movie S1 available at https://www.mdpi.com/2077-1312/11/10/1944). The constant pressure across the surface of the flipper then cancelled out any flow mixing due to pressure differences, including the wing tip vortex. However though this work is insightful, it does not cover what flow features occur during the sea turtles (*Chelonia mydas*) propulsive cycle consisting of the downstroke and sweep stroke. The propulsion cycle in sea turtles has been previously described as only occurring during the downstroke period, with peak thrust occurring at the end of the downstroke [4,104], with the most recent works taking very different approaches to uncover the propulsive cycle. David T. Booth[4] found the propulsive cycle by studying green turtle hatchlings in a flume, while van der Geest et al.[104] developed a full-scale robotic sea turtle based on the green turtle that could reproduce the natural animals swimming patterns. Though both these works gave comparable insights into thrust production and/or energy consumption, they did not detail what flow features and fluid mechanical mechanisms were responsible for the propulsion. David T. Booth [4] hypothesised the downstroke likely produces both lift-based and drag-based propulsion depending on the flippers angle of attack however, what does lift-based or drag-based propulsion in sea turtles look like? And is this hypothesis accurate? To the best of our knowledge, no research details the flow features and fluid mechanical interactions sea turtles utilise during their downstroke using genuine sea turtle kinematics. However, work has been produced that analyses simplified 2-dimensional turtle-inspired flow features [17,18]. Though these 2-dimensional examples may give insight, they fail to reproduce 3-dimensional effects such as spanwise flow and Coriolis effects that have been shown as essential factors in biological flapping wings[21,105].

For the last 20 years, it has been well understood that the flow feature responsible for high-performance force production in biological flapping wings is the leading edge vortex (LEV)[41-43]. The LEV has been shown to occur across all categories of animal species[42-45], with insect flight first believed to be a paradox before its discovery[42]. However, although the LEV has been heavily studied in flapping wings to the best of our knowledge, no research exists for LEV generation during the downstroke in sea turtles that apply genuine and accurate sea turtle kinematics.

Recent studies into the propulsion methods of sea lions demonstrate that the sea lion's flippers create additional thrust by applying a clapping motion[50,106]. The clapping motion entrains fluid momentum on the low-pressure side of the flipper (dorsal side) that later develops into complex vortex shedding to increase thrust[50]. It is now understood that sea turtles also create a clapping motion referred to as the sweep stroke (Fig 26). However, the fluid interaction during the sea turtle's sweep stroke is entirely unknown.

Obtaining the flow features of sea turtles first requires solving two significant complications. Firstly, obtaining animal ethical approval to conduct the test on endangered species, and secondly, the animal may not even swim with its regular swim pattern while in a captive state[84,95,104]. To overcome such hurdles, we take advantage of our robotic sea turtle (Cornelia). Cornelia is the world's first and only robotic sea turtle that accurately produces the sea turtle's natural form and function, as detailed in our previous work[104]. This makes Cornelia an invaluable tool for studying the fluid-structure interactions of turtles without the need to trouble the actual animal.

In this work, with the help of Cornelia, we break down each of the observed flow features of the turtle's flippers during the propulsive cycle (Fig 27). To the best of our knowledge, this is the first study to show insight into the flow features of the sea turtle during the animal's propulsive cycle. We compare the observed flow features against the turtle's thrust and lift forces, Flipper angle of attack (AoA), Flipper velocity and power consumption to give insight into how each feature influences the animal's propulsion effort and cost of transport (COT). We compared the COT obtained by Cornelia against the current state-of-the-art swimming robotics [55,107-114], and we found Cornelia to produce extremely low values for the COT, pointing to the effectiveness of the sea turtle propulsive strategy.

Based on our findings, we hypothesise what practical aspects of the turtle's locomotive pattern could be developed and optimised to enhance the next generation of underwater drones and robotic technologies.

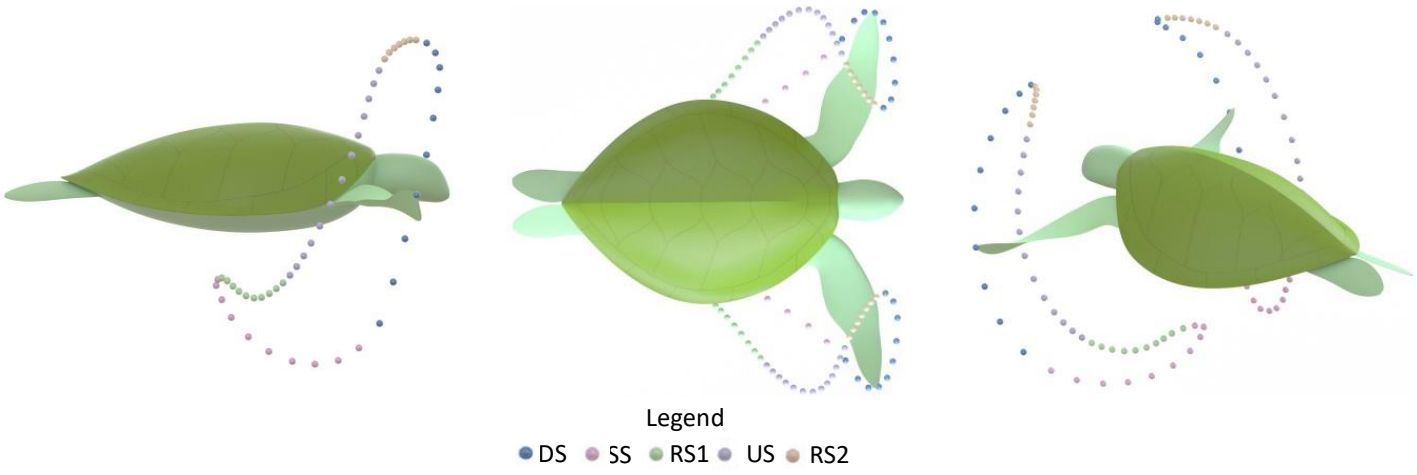

Figure 26: The wild sea turtle (Chelonia mydas) flipper pattern during the animal's regular swimming routine obtained from van der Geest et al.[84].

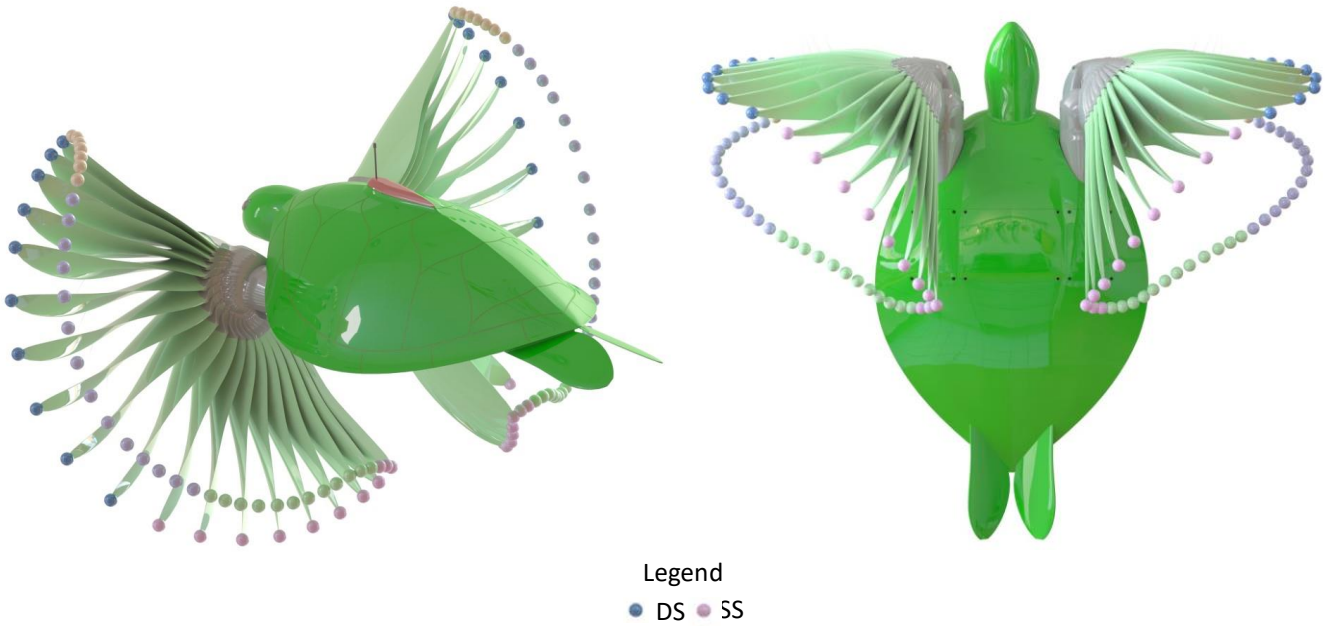

Figure 27: The robotic sea turtle (Cornelia) illustrating the propulsive cycle consisting of the downstroke and sweep stroke [104].

6.3 Methods

6.4 Methods overview

All tests were performed using our ad-hoc testing rig, internally known as the "turtle dyno", as shown in Fig. 28. Testing involved towing the robot quickly up to speed before the robot would take over to propel itself. The turtle dyno could record lift, drag, thrust, swim velocity and power consumption simultaneously during each test. The design and specification for the turtle dyno, along with a detailed analysis of the force production during the regular swimming routine, can be found in our previous work [104], so we will not cover this in detail here.

Due to its cost-effectiveness and ease of application, individual flow features were observed using dye visualisation with our in-house developed dye application tools. CFD was additionally used to help complement the field tests and provide a deeper comprehension of the flow field characteristics.

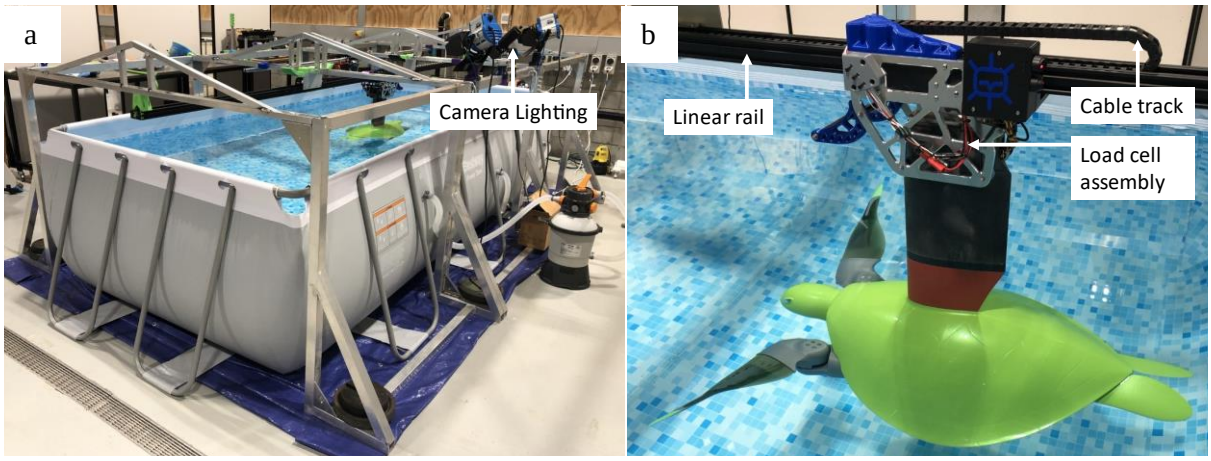

Figure 28: Turtle dyno. (a) Complete dyno assembly showing camera lighting arrangement. (b) Close-up of robot attached to load cell and linear rail assembly.

6.5 CFD calculations

In parallel with laboratory experiments, commercial CFD tools were used to help better comprehend the flow features observed during physical testing with ANSYS Fluent (ANSYS 2021 R2, Canonsburg, PA, U.S.A.). Simulations only involved studying the flow around the rear flippers and during the sea turtles downstroke. The sweep stroke was not simulated due to its complex motion coupled with the complex wing morphing during this part of the locomotive pattern, thus creating high computational expense that was not available for this study. Additionally, it must be noted that the CFD simulations from this study are not to produce highly accurate results but to help complement the results from our laboratory experiments.

Two separate simulations were set up with the $k\omega\ SST$ model used to study how the flow from the turtle's carapace travels downstream to meet the rear flippers, and the realizable $k\varepsilon$ model was used for simulating the downstroke due to its lower computational expense. The $k\omega$ model had the mesh refined down to a y^+ of 0.75, with the $k\varepsilon$ model using a y^+ of 13.15 with the addition of scalable wall functions. As the turtle's downstroke applies a relatively constant wing twist[95] and a simple rotation motion, the simulation was simplified into two separate domains: a rotating domain with the flipper using a rigid body and a sliding mesh interface paired with a static domain (Fig. S16a). The rotational domain angular velocity and velocity inlet values were established based on the values achieved by sea turtles during the downstroke period. The computational domain that used with the $k\omega$ model can be seen in Fig.S16b, with a body of influence for mesh refinement added around the turtle body and further downstream to capture the wake produced by the turtles body. A symmetry boundary condition was used to substantially lower computational expense with a constant velocity inlet defined based on the turtle's average swimming velocity.

6.6 Dye visualisation

To visualise the individual flow features during the regular swimming routines, we operated our in-house developed dye visualisation tools (Fig. 29). The tools have been successfully used in our previous studies[95], however, the streamline tool, as seen in Fig. 29a was further developed for this study in introduce up to 3 dye streamlines. The central pylon section of the tool uses a NACA 0010 cross-section with each of the three stacked bodies using a 360˚ revolution of the NACA 0010 cross-section. The tool ran on a linear rail parallel to the turtle swim path and could have the dye accurately injected when required. To ensure the tool did not generate a significant disturbance in its wake, tests were performed to inject a cloud of dye into its path and record the disturbance in the wake (Fig. 29c and Movie s3 available at https://www.mdpi.com/2077-1312/11/10/1944). Our testing suggested that the tool created insignificant disturbance compared to the disturbance an animal in the wild would likely encounter, so we deemed the tool satisfactory for use. Flow features were recorded using high-speed underwater photography (Chronos 2.1HD 32GB, Kron Technologies Inc, Burnaby, BC, Canada) at full HD 1000 FPS and an action camera (GoPro Hero 10, GoPro, San Mateo, California, USA) at full HD 240 FPS. The Chronos cameras were installed into waterproof housings (Salty surf housings, North Wollongong, NSW, Australia) and equipped with a Sigma 18-35mm lens (Sigma Corporation, Kawasaki, Kanagawa, Japan).

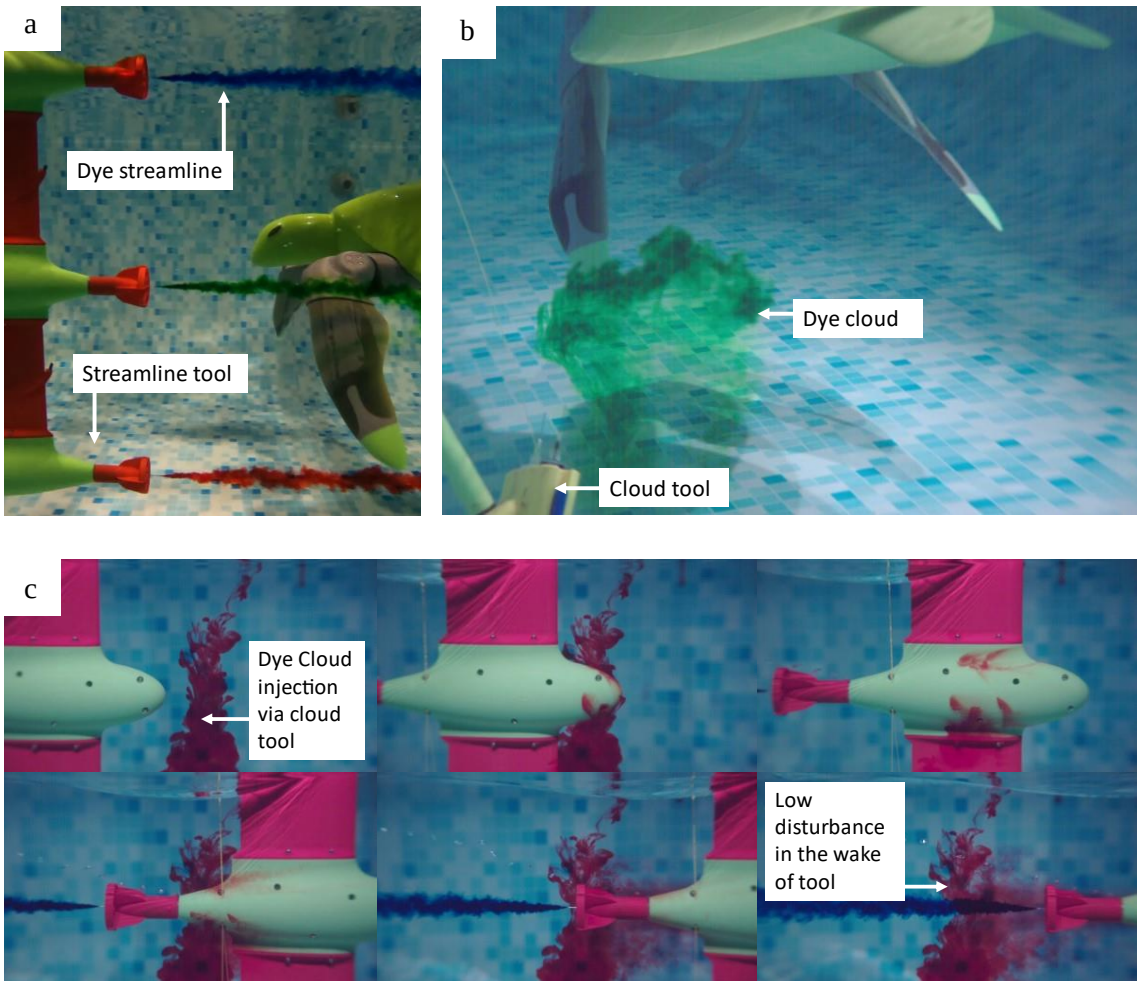

Figure 29: Dye visualisation tools. (a) Streamline tool in use. (b) Cloud tool in use. (c) Streamline tool wake disturbance testing.

6.7 Results and discussion

6.8 Results overview

As observed in Fig.30, all test results for thrust, lift, AoA, power, swim speed, and flipper tip velocity are detailed for the sea turtles DS and SS, with the corresponding flow features observed at each time interval detailed in Fig. 30g. All tests were performed with the flapping frequency remaining constant at 0.23Hz based on the average flapping observed in wild green sea turtles[28,84,104].

Testing was conducted by applying the sea turtle's regular swimming routine at a Reynolds number of 367,000, defined as:

$$Re = \frac{uD_{SCL}}{v}$$

Re was based on the average swim velocity (u) and straight carapace length (D_{SCL}). As the Reynolds number is established simply on steady, time-independent conditions[115], the Periodic Swimming Number (P) is also considerd in this study defined as:

$$P = \frac{10u}{\sqrt{4\pi f v}}$$

Where f is the flapping frequency and v the kinematics viscosity. The Periodic Swimming Number (P) was first introduced by Gurka et al. [115] as an adaptation of the Reynolds number to eliminate the need to choose a characteristic length scale and incorporate the animal's periodic motion. Applying this, we found that the sea turtle swims at a value of 3537. This puts sea turtles approximately in the same range of P as Macaroni and Adelie penguins (3729-3882), along with Harp and Ringed seals (3330-3569)[115]. Additionally, The Strouhal number (St) was calculated to be 0.24 and defined as:

$$St = \frac{D_{pp}f}{u}$$

Were D_{pp} is the sea turtle's flipper tip's peak-to-peak distance during its regular routine. This value of the Strouhal number puts sea turtles into a range observed in nature of 0.2 to 0.4, as found in other swimming and flying animals that are tuned for high power efficiency [98-100].

6.9 Flipper Angle of Attack (AoA)

To help understand the flow feature contribution based on the relative flow around the turtle flippers during the downstroke and sweep stroke, the AoA of the turtle's flipper was defined as:

$$\theta_{AoA} = \theta_p \pm \theta_f$$

Where θ_p is the spanwise twisting of the turtle's flipper given as a linear piecewise function with respect to time as:

$$\theta_p = \begin{cases} a_{p1}t, & 0 \le t < t_1 \\ a_{p2}, & t_1 \le t < t_2 \\ a_{p3}t + b_{p3}, & t_2 \le t < t_3 \\ a_{p4}t + b_{p4}, & t_3 \le t < t_4 \\ a_{p5}, & t_4 \le t < t_5 \\ a_{p6}t + b_{p6}, & t_5 \le t < t_6 \end{cases}$$

Where a_{pn} and b_{pn} are the function constants. The relative flow direction θ_f on the turtle's flipper was added or subtracted depending on what stage of motion the flipper was in (upstroke or downstroke) to provide a positive AoA for the relative flow acting on the ventral side of the flipper and negative AoA acting at the dorsal side (Fig. S17). θ_f was calculated with:

$$\theta_f = arctan\left(\frac{\sqrt{\dot{y} + \dot{z}}}{V_s + \dot{x}}\right)$$

Where V_s represents the swimming speed of the turtle, while $\dot{x}$, $\dot{y}$ and $\dot{z}$ signify the velocity components at any given point on the turtle's flipper. These velocity components are obtained by taking the time derivative of the flipper position function, which was formulated using a Fourier series with:

$$\dot{x} = V_f\left(\sum_{i=1}^{n} -iw_x a_{ix}\, sin(iw_x t) + iw_x b_{ix}\, cos(iw_x t)\right)$$

$$\dot{y} = V_f\left(\sum_{i=1}^{n} -iw_y a_{iy}\, sin(iw_y t) + iw_y b_{iy}\, cos(iw_y t)\right)$$

$$\dot{z} = V_f\left(\sum_{i=1}^{n} -iw_z a_{iz}\, sin(iw_z t) + iw_z b_{iz}\, cos(iw_z t)\right)$$

Where n was set to 8 terms, a_i and b_i are the Fourier coefficients and w the fundamental frequency. The velocity modifier (V_f) to correct the velocity for any point along the span of the turtle's flipper was represented with: $V_f = \frac{x_s}{s}$, with x_s representing any point along the flipper span (s). As the twisting of the flipper is a linear relationship [95], the exact amount of wing twist at any point along the flipper span (s) was caluculated with: $\theta(x) = \frac{\theta_p x_s}{s}$. Shown in Fig 30c the average AOA is plotted by calculating each value at various points along the flipper span.

6.10 Downstroke

During the initial stages of the DS, there was no reliable evidence of any substantial vortex formation on the turtle's flippers with relatively smooth flow conditions during this phase in time. This is predominately due to the low AoA during the early DS and low flipper tip velocity, resulting in low thrust, lift and power consumption. At approximately the 2.8-second mark, clear evidence of a LEV forming along the turtle's wing can be seen along with substantial spanwise flow from the wing root to the wing tip (Fig 31 and Movie S4 available at https://www.mdpi.com/2077-1312/11/10/1944). As the downstroke progresses, the wing tip velocity increases to reach a maximum at the end of the downstroke, where the LEV is at its most forceful stage, with thrust and lift reaching their maximum values (Movie S5 available at https://www.mdpi.com/2077-1312/11/10/1944). This finding differs from past research hypotheses that depict the large force production at the end of the sea turtles downstroke as being drag-based due to high AoA[4]. Additionally, in Fig 30c, 30f, the wings AoA begins to bleed off before the flipper reaches its maximum velocity and force production, revealing that high force production is more accurately associated with higher wing velocities and more aggressive LEV formation. Additionally, as the LEV delays wing stall[43,45,116] by forcing the flow to reattach to the low-pressure/dorsal side (Fig. 31a-d and Movie S4), this suggests the entire downstroke is completely lift-based propulsion during the sea turtle's regular swimming routine.

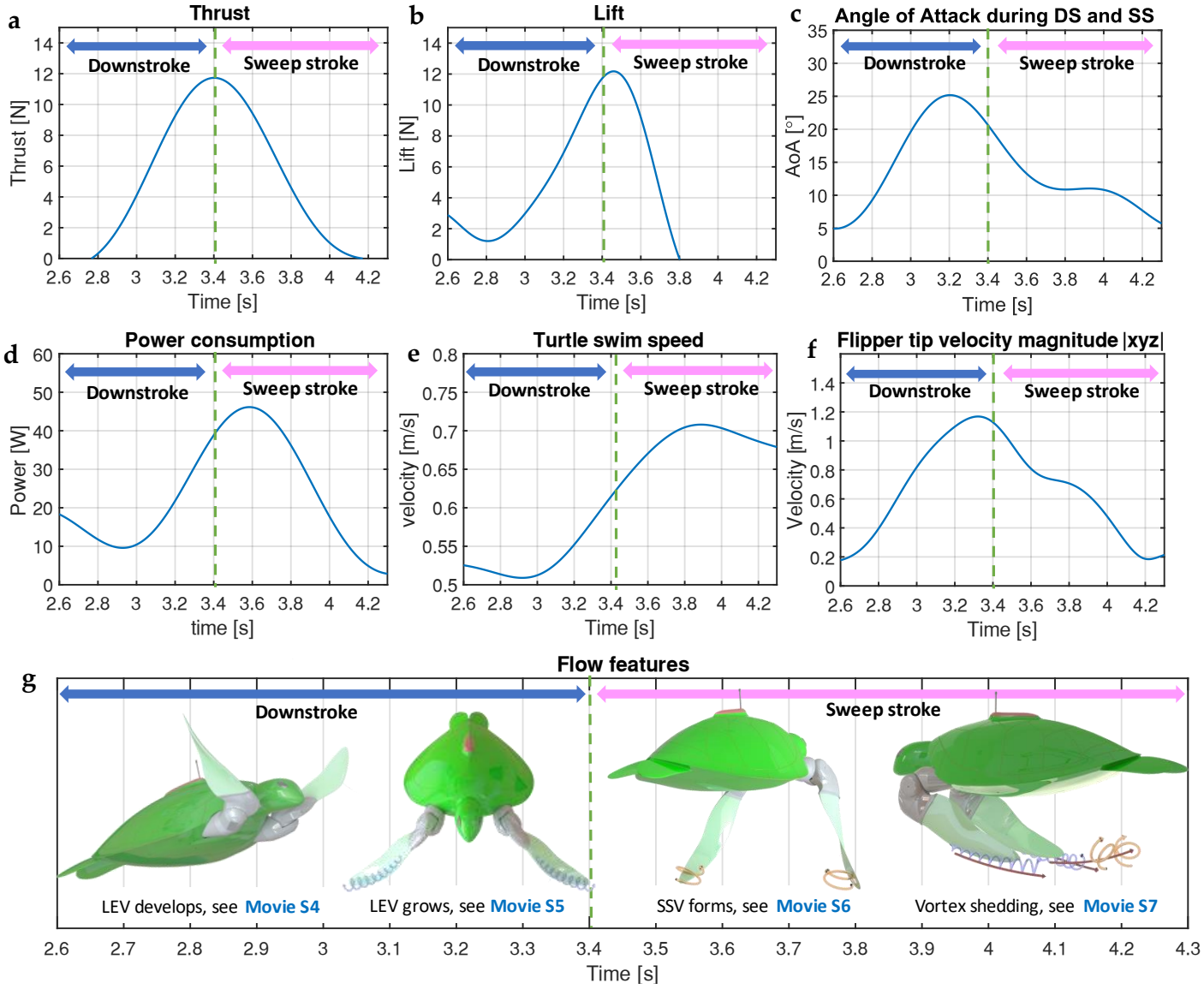

Figure 30: Swimming performance of Cornelia for the Green sea turtle's regular swimming routine. (a) Thrust production during the downstroke and sweep stroke obtained from van der Geest et al [104]. (b) Lift production during the downstroke and sweep stroke obtained from van der Geest et al [104]. (c) The average Angle of Attack across wingspan. See Fig S18 for exact AOA values across the flipper span (d) Power consumption during the downstroke and sweep stroke obtained from van der Geest et al [104]. (e) Turtle swim speed during the Downstroke and Sweep stroke obtained from van der Geest et al [104]. (f) The flipper tip velocity magnitude during the Downstroke and Sweep stroke. (g) The timing of the observed flow features during the also see Movies S4-S7 available at https://www.mdpi.com/2077-1312/11/10/1944.

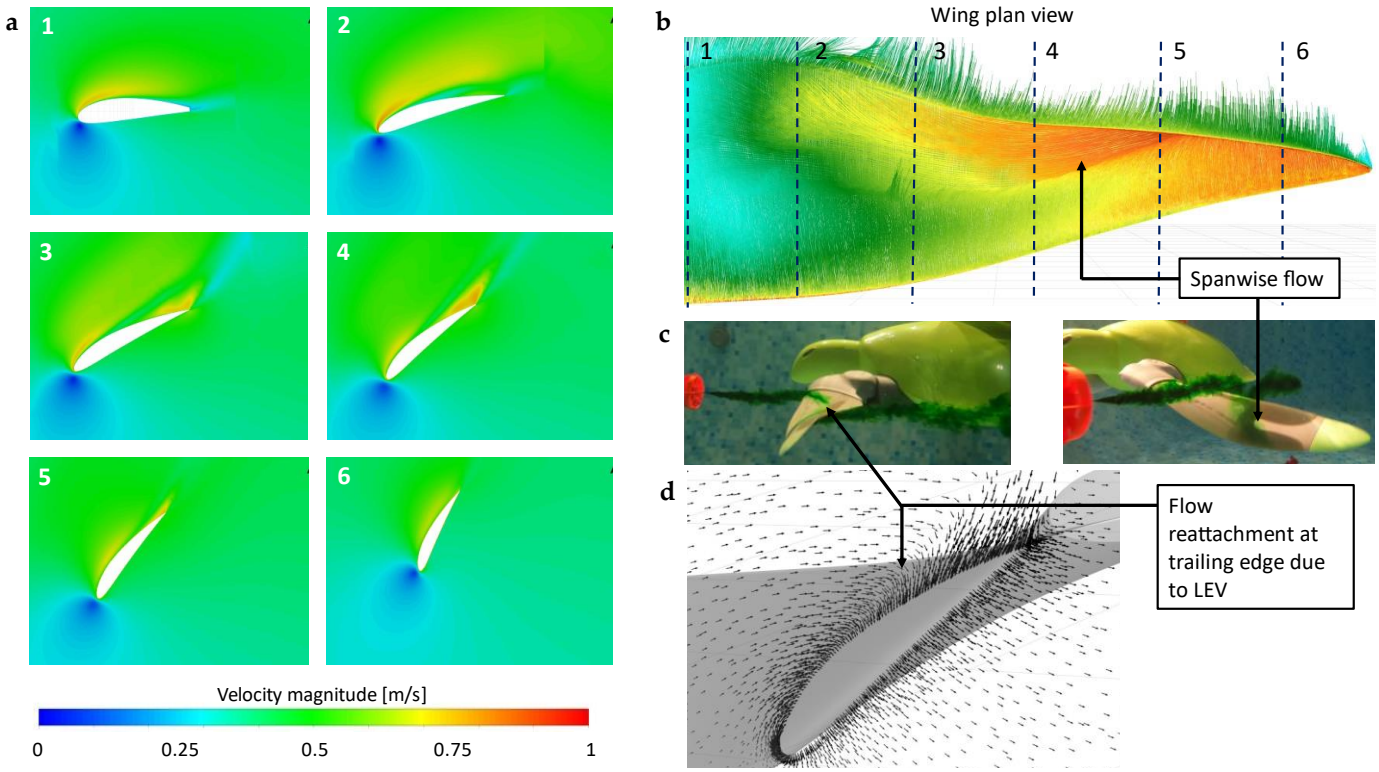

Figure 31: Downstroke flow features. (a) Velocity plots from various cross-sections along the turtle's wingspan from CFD. (b) Plan view of the turtle wing showing cross-section locations and velocity streamlines obtained from CFD. (c) Dye visualisation testing shows flow reattachment towards the wing trailing edge and the spanwise flow demonstrated by dye being transported towards the wing tip. (d) Vector plot from CFD showing flow reattachment.

6.11 Sweep stroke

The sweep stroke begins approximately 3.4 to 3.5 seconds into the turtles flapping routine, with the LEV remaining attached during the sweep strokes duration. During the entire sweep stroke, the AoA, flipper velocity, power consumption, thrust and lift begin to lower, with the turtle reaching a maximum swim speed approximately 50% into the sweep stroke stage. At roughly the 3.6 to 3.7-second mark, a vortex forms that is almost immediately shed into the turtle's wake (Fig. 30g and Movie S6). We name this vortex the sweep stroke vortex (SSV), and in contrast to the LEV, the SSV rotates in the opposite direction and is produced by the wing's ventral side (high-pressure side).

Near the end of the sweep stroke, the flippers are brought parallel beneath the carapace to create a clapping motion similar to the sealion[50,106]. At this point, the LEV is shed from the wing's dorsal side into the wake to follow behind the SSV (Fig 30g and Movie S7). Just before the LEV is shed into the wake, it entrains fluid momentum on the dorsal side of the flipper (Movie S7), similar to the sea lion[50]. In sea lions, this helps contribute to downstream momentum when the vortex structure is shed to add additional thrust[50]. Based on our observed flow features, this downstream momentum can also be assumed to happen with sea turtles, additionally, as the thrust curve towards the end of the stroke bleeds off rather than simply dropping off like the lift forces (Fig.30a-b). At this point, the sea turtle enters a glide that lasts for 70% of the overall limb beat cycle[95,104]. During the glide, the sea turtle shapes its flippers to generate a passive upstroke to recover its flippers into a position ready for the downstroke to help with energy expenditure[95,104].

6.12 Rear flippers

During the turtle's regular swimming routine van der Geest et al. [84] documented that the rear flippers would be seen to tuck in behind the carapace with the flipper tips pointing backwards and near motionless as per Fig. 32. Our CFD and field test results show that towards the rear of the carapace, the flow detaches from shell to create a low energy zone directly where the rear flippers are positioned (Fig. 32c-d and Movie S8). This volume of low energy flow will help lower both the form and friction drag the turtle experiences, thus improving the animal's drag coefficient for the gliding stage. This also helps explains why the flippers remain almost motionless, as any changes to the flipper's position within this low energy zone will not generate any significant directional control for the turtle.

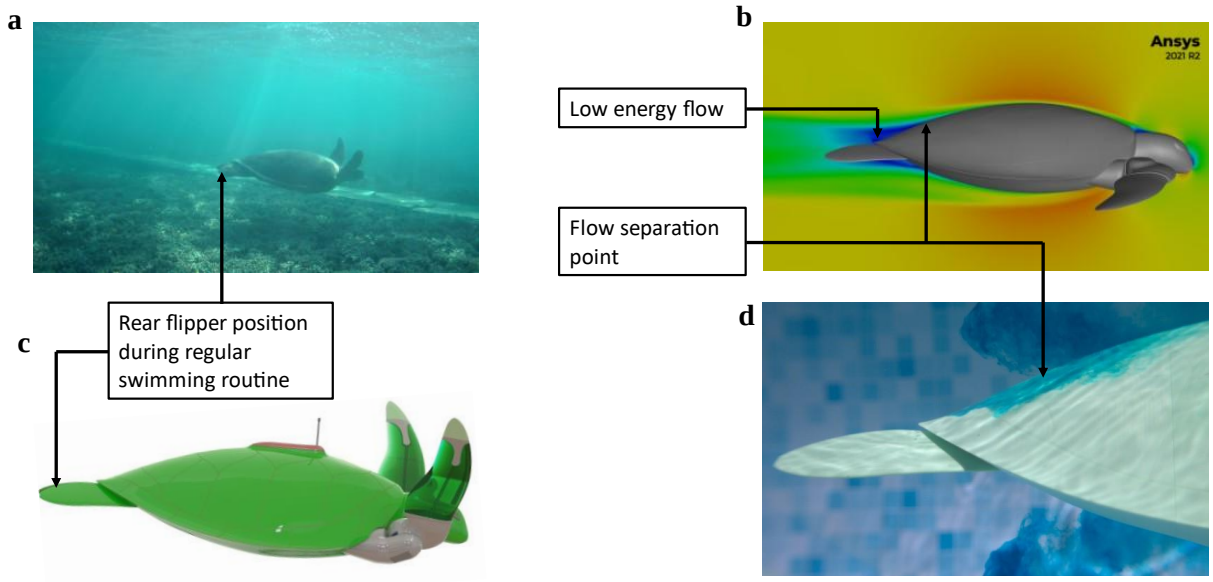

Figure 32: Flow over the sea turtle's rear flippers during its regular swimming routine. (a) A wild sea turtle producing the 5-stage locomotive cycle, demonstrating the rear flipper position. (b) Cornelia replicates the wild sea turtle in Fig. 32a. (c) CFD results showing a velocity contour of the flow around the rear the flippers. (d) Dye visualisation tests showing flow separation point. Also see Movie S8 available at https://www.mdpi.com/2077-1312/11/10/1944.

6.13 Turtle swimming efficiency and Cost of Transport

As observed in Fig. 33, the power consumption, thrust production and swim speed data are plotted from the experimental swimming tests for the complete swimming cycle. Additionally, a curve of input power (Fig. 33a) divided by output thrust (Fig. 33b) is displayed for the down and sweep strokes in Fig. 33e with the cost of transport (COT) for the complete swimming cycle detailed in Table 2 and plotted against time in Fig. 33d. The cost of transport was calculated with:

$$COT = \frac{P_{in}}{mgu}$$

Where P_{in} is the input power (Fig. 33a), m the mass of Cornelia, g acceleration due to gravity and u the swimming velocity (Fig. 33c). During the regular swimming routine, Cornelia produced an average COT for the entire swimming cycle of only 0.072 to generate one of the lowest COT values in literature for a swimming robot (Table 2). This is largely due

to the propulsion strategy, where the sea turtle produces propulsion for approximately 30% of the limb beat cycle, with the remaining 70% producing a power-saving glide that does not reduce swimming velocity substantially due to the animal's large mass and low drag coefficient[104]. This points to how effective this swimming strategy is and helps explain how sea turtles can swim such vast distances with minimal energy intake.

Cornelia demonstrated that the most energy-efficient point during the propulsion stage was at the 3.1-second mark to generate a power-to-thrust ratio of approximately 2 W/N or 7N of thrust for 14W electrical input power (Fig. 33e). At this point, the AoA is almost at its maximum value, and the sea turtle has already begun accelerating its velocity from its power-saving glide. Additionally, the LEV continues to grow, with the lift forces producing approximately 5N of upwards force.

Overall, we found the downstroke was more efficient than the sweep stroke, however, this could be due to the sweep stroke requiring all six servo motors to run simultaneously rather than the downstroke, which only required two servo motors to run heavily. Additionally, the motors used in Cornelia's robotic limbs are hobby-grade servo motors that we believe may have low mechanical efficiency.

Though the COT obtained is impressive, employing a flapping winged machine in a commercial drone or device for ocean exploration is far from practical, and the multi-degree of freedom wings produce complex maintenance procedures coupled with highly complex manufacturing. For the findings produced here to be valuable, practicable and obtainable for industry-level technology, we combine the essential variables consisting of wing twist, wingtip velocity and wing shape, to generate a CFD simulation of a continuously rotating turtle wing to continuously harness the most efficient section of the turtles locomotive cycle, as previously mentioned at the 3.1-second mark. Our results demonstrated that it was possible to achieve a maximum sustained power-to-thrust ratio of 0.5 W/N or 8N of thrust for 4W mechanical input power (Fig. 33e).

When comparing the thrust values of the continuously rotating turtle wing against the sea turtle locomotive cycle, it can be observed that the thrust values are comparable with the CFD results producing 8N and Cornelia producing 7N during the standard sea turtle locomotive cycle. However, there are variations when comparing the power values, as the CFD results do not include the overall electrical efficiency of the servo motors and electronics. Therefore, the significant difference in power consumption will likely come from two main factors: firstly, the efficiency of the electro-mechanical system and secondly, as the turtle's flipper is accelerating at this point, therefore, creating additional power consumption when compared to the constant velocity rotating model.

The continuously rotating turtle wing model could offer significant potential for enhancing propulsion technologies, especially in multi-functional applications. Beyond the clear energy-saving merits, incorporating a morphing rotating propulsor reveals an array of advantages for aquatic navigation and energy harvesting. Illustrated in Fig. 33f and further elucidated in Movie S9 available at https://www.mdpi.com/2077-1312/11/10/1944, applying a set of morphing sea turtle-inspired propulsors in a tandem orientation attached to a low-drag streamlined fuselage could facilitate a multi-purpose underwater drone. While one set of wings concentrates on propulsion, the other functions as a stabiliser. This configuration promotes consistent and controlled motion, bolstering the vessel's stability—a crucial attribute for peak performance across diverse aquatic conditions.

Furthermore, as the wings morph, they can transition into a counter-rotating setup. Such an arrangement is paramount for neutralising the rotational forces exerted on the vessel's fuselage due to the torque from a singular propellor set. This ensures that the vessel's trajectory remains unaffected by undesired rotations. Additionally, the concept of torque vectoring can be explored; by dynamically adjusting the Angle Of Attack (AOA) of each wing or flipper at precise moments, the vessel may achieve unparalleled underwater agility.

Taking cues from the biomechanics of sea turtles, the device has the potential to function as a sea glider. In certain conditions, energy can be harnessed by back-spinning the propellors. This mechanism is reminiscent of how sea turtles leverage their upstroke to optimise energy use. Thus, this could evolve beyond its foundational propulsion capabilities to also serve as a renewable energy harvester, seamlessly integrating navigation proficiency with sustainable energy solutions.

Table 2: Cost of transport of recent state-of-the-art swimming robots from literature

COT in recent state-of-the-art swimming robots	COT	Data obtained from
Cornelia	0.072	Results from this current study
ART	3	Baines et al. [55]
Eel inspired robot	10.72	Nguyen et al. [107]
Flexible swimming robot	2.5	Kwak et al. [108]
FINBOT	8.2	Berlinger et al. [109]
Squid-inspired robot	0.087	Bujard et al. [110]
Flexible robotic fish	0.293	Lu et al. [111]
Tunabot	2.83	Zhu et al. [112]
Tunabot flex	1.876	White et al. [113]
HASEL jellyfish	1.619	Wang et al. [114]

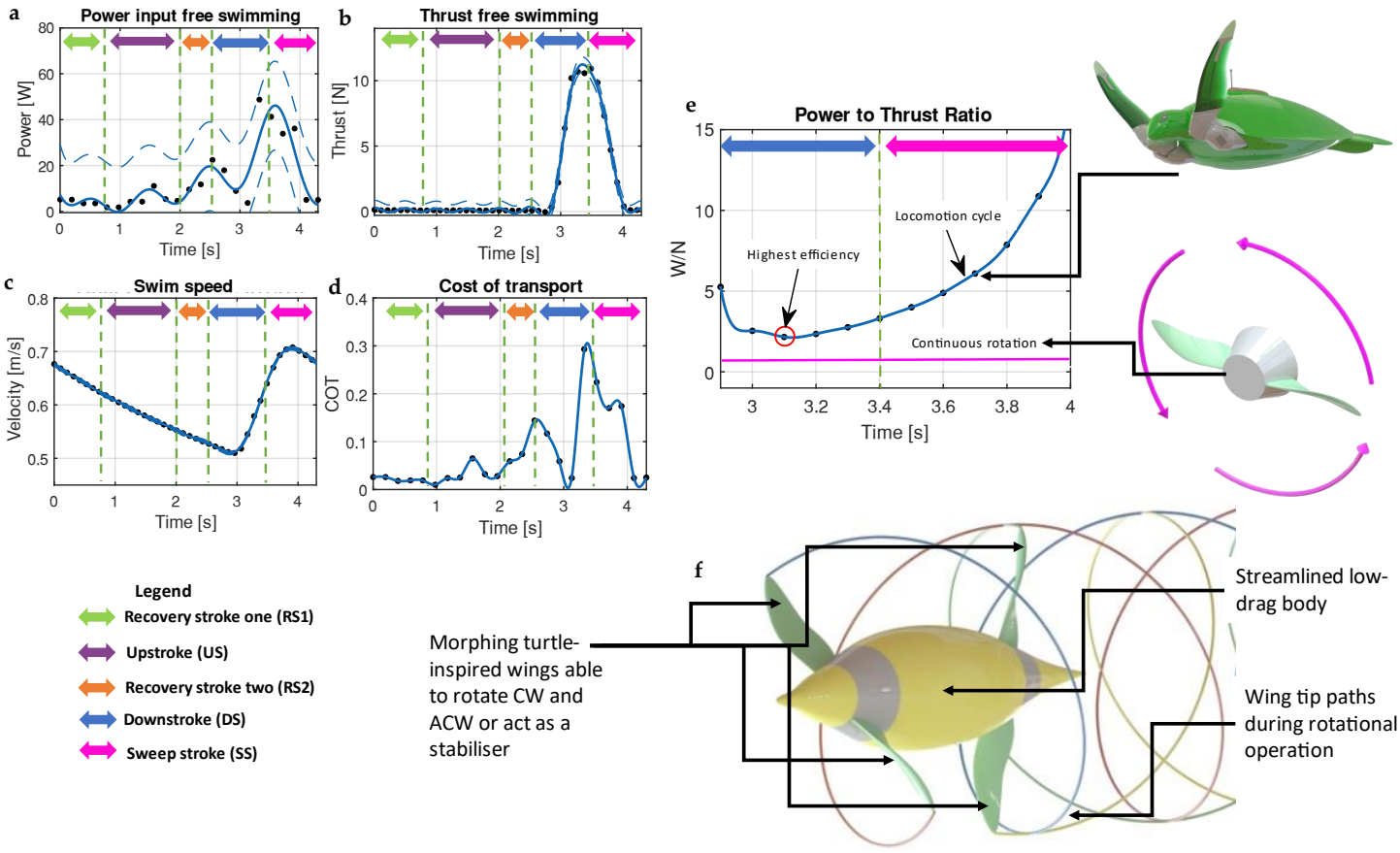

Figure 33: Turtle swimming efficiency. (a) Power input data for the complete swimming cycle obtained from van der Geest et al. [104]. (b) Thrust production for the complete swimming cycle obtained from van der Geest et al. [104]. (c) Turtle swim speed for complete swim cycle obtained from van der Geest et al. [104]. (d) Cost of transport plotted against time. (e) The power-to-thrust ratio plotted for the downstroke and sweep stroke compared to the power-to-thrust ratio of a continuous rotating turtle wing. (f) Turtle-inspired propulsion applied to a low-drag drag streamlined body. Diagram illustrating a tandem configuration with both sets of wings/flippers generating propulsion. (Also see Movie S9).

6.14 Conclusions and future work

In conclusion, this study examines the sea turtle's propulsive cycle considering the downstroke and sweep stroke during the animal's regular swimming routine. The findings reveal a critical characteristic that may account for their highly efficient swimming performance, including their capacity to generate considerable thrust and lift forces during the downstroke phase, with a continuous LEV formation during both downstroke and sweep stroke, until it is shed into the wake at the end of the sweep stroke to hypothetically contribute towards downstream momentum similarly to sea lions [50].

Additionally, the study has highlighted that the Green Sea Turtle robot, Cornelia, produces one of the lowest Cost of Transport (COT) values in literature for a swimming robot, indicating the effectiveness of the sea turtle swimming strategy for long-distance swimming with minimal energy intake. This underscores the potential for the incorporation of these principles into the design and operation of marine robots and other aquatic devices. Their low COT values are likely due to their efficient energy usage through a combination of active propulsion and passive gliding stages. This, coupled with the rear flippers' tucking motion into a zone of low energy flow, can reduce the form and friction drag the turtle experiences, thus improving its drag coefficient for the gliding stage.

Despite the energy-efficient flapping cycle exhibited by sea turtles, applying these findings to commercial drones or ocean exploration devices remains a challenge due to the complexity of their locomotion. Yet, by capturing the most efficient section of the turtle's locomotion cycle and simulating a continuously rotating turtle wing, our study offers promising avenues for developing industry-level technology.

Though this work brings new insight into the flow features during the sea turtle's propulsive cycle, it is difficult to pinpoint the exact effect of each flow feature and how these features interact with each other to generate the animal's propulsion. A deeper understanding of this can be achieved in future work with the utilisation of a high-level PIV system. Additionally, as these findings are for regular straight-line swimming, our robot Cornelia can be programmed to study how the animal creates its manoeuvring techniques by building in the required control systems.

In summary, this research provides novel insights into the flow features and COT of sea turtle locomotion and offers valuable guidance for the future development of efficient aquatic propulsion systems.

Chapter 7: Employing robotics for biomechanical validation of a prosthetic flipper for sea turtles as a substitute for animal clinical trials

7.0 Preface

In the last chapter, we gave initial insight the intricate fluid dynamics and biomechanical wonders of the Green sea turtle's propulsion. Our robotic model, "Cornelia", served as a bridge to understand the marvel of their swimming, spotlighting the power and grace of their pectoral flippers. However, it also introduced a contemplative question: What becomes of these creatures when the very essence of their mobility their flippers are compromised?

This pressing concern forms the cornerstone for chapter 7. As we know, sea turtles are a keystone species in the marine ecosystem. Alarmingly, every sea turtle species faces the looming shadow of endangerment, with human interference, mainly fishing net entanglements, being a paramount threat. Such encounters often culminate in a turtle losing its flipper, significantly hampering its survival capabilities. This is not just a tragedy on an individual scale; the ripple effects of declining sea turtle populations could upset oceanic balances, with repercussions cascading to our own way of life.

With an understanding of the magnitude of this issue, chapter 7 ventures into an innovative domain: Can robotics offer a lifeline to these injured turtles? Our study aimed to evaluate the feasibility of a prosthetic flipper tailored for sea turtles deprived of a natural flipper. Leveraging our prior experience with "Cornelia", we designed a new robotic model named Loulin, serving as a surrogate for real turtles to gauge the performance of the prosthetic without the ethical implications of live animal trials.

7.1 Abstract

Sea turtles are a keystone species for the ocean's ecosystem, with all species currently listed as endangered. Such a threat is mainly due to human factors such as fishing net entanglement. The entanglement often comes at the expense of the turtle losing a pectoral flipper. The reduction in a sea turtle's survival odds upon losing a flipper is a significant concern. This issue extends beyond individual animals, as the potential extinction of sea turtles could have detrimental effects on ocean health and subsequently disrupt our lifestyles. In this work, with the help of robotics, we test the suitability of a prosthetic flipper for sea turtles that have lost a flipper. Testing with our sea turtle-inspired robot helped to demonstrate the prosthetic flipper's performance without clinical trials in live animals. The robot showed that the prosthetic could closely mimic the sea turtle's downstroke and upstroke, allowing the animal to regain control in roll, pitch and yaw, despite the absence of anatomical joints and related muscles. Additionally, swim speed tests provided an average swim speed of 0.487 m/s while dragging 6m of cable to give a calculated maximum swim speed of 0.618 m/s coming close to the average swim speed of wild sea turtles of 0.6 m/s. Our aspiration is that the findings from this study will pave the way for an open-source implant design, empowering veterinary professionals globally to aid injured turtles. Furthermore, this research promises to inspire

additional animal-based robotic designs, advancing technologies geared towards assisting other animals in distress.

7.2 Introduction

Keystone species are recognised as playing an essential role in the form, function, and overall structural complexity of the ecosystem in which they live [117-122]." Sea turtles are known to modify their landscape through the way they feed [121]. Based on the classification, this makes the sea turtle an ecosystem engineer [123], as their feeding habits allow coral to flourish by scavenging on coral competitors [121]. Sea turtles are essential not only to the ecosystem but also for ecotourism [124], with large numbers of tourists visiting tropical locations around the world for the chance to swim with a wild sea turtle. However, not all is going well for this ecosystem engineer. All species of sea turtles are now listed under the endangered species act as threatened or endangered. The reason for this is highly complex, however, one thing that is clear is that large numbers of sea turtles every year are caught as bycatch in fishing nets [125,126]. The turtles that survive this traumatic incident frequently suffer from amputated or injured pectoral flippers [126] as a result of thrashing the flipper in a bid to release themselves. Additionally, during nesting, female sea turtles will return to land to lay approximately 50-200 eggs on the beach where they were born [127]. This enormous task could be physically impossible for a sea turtle with only one flipper. A possible solution to help these ecosystem engineers could be in the form of a prosthetic flipper. Prothesis in sea turtles has been done before, however, to the best of our knowledge, all attempts have come in the form of a flipper that straps onto the remaining limb. An example of this can be seen in the work produced by Sun et al. [128]. Although they reported promising results, their solution did not allow any rotation of the prosthetic for varying the flippers angle of attack (AOA). This is a rather important design parameter to ensure that the desired thrust forces can be achieved.

In recent work by van der Geest et al.[84], the sea turtle kinematics are detailed three-dimensionally based on the green sea turtle. They describe how the swimming pattern can be broken up into five stages consisting of the Downstroke (DS), Sweep stroke (SS), Recovery stroke one (RS1), Upstroke (US), and Recovery stroke two (RS2) (Fig. 34ab). Additionally, they detail that the sweep stroke is generated mainly by the elbow joint. Assuming the sea turtle amputation zone, as illustrated in Fig. 34c, is located just before the elbow joint, meaning if the prosthesis were required to perform the sweep stroke, it would require some form of mechanised actuation. In such a case, challenges derived from control system and signal acquisition actuation would emerge. Thus building a complex mechanised prosthesis for a wild animal is practically not feasible, meaning a simple, fully mechanical and robust solution is required for the success of such a project.

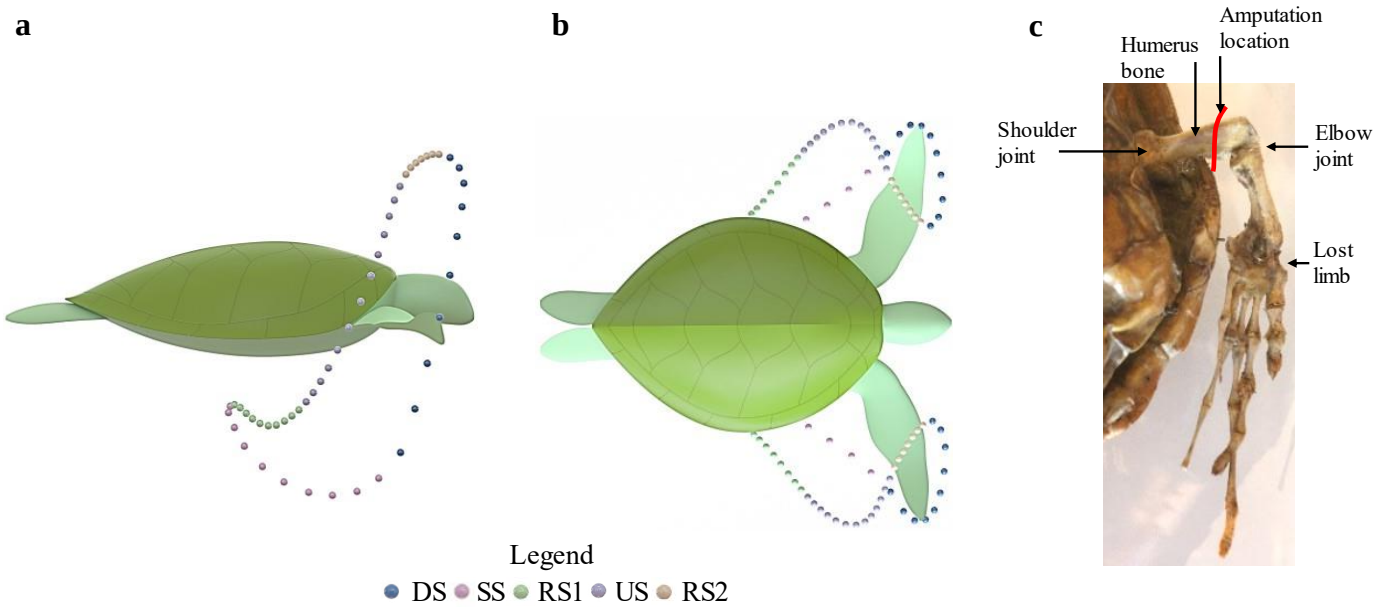

Figure 34: Sea turtle kinematics patterns obtained from van der Geest et al. [84]. Blue spheres represent the wingtip trajectory for the downstroke (D.S.), pink spheres represent the wingtip trajectory for the sweep stroke (S.S.), green spheres represent the wingtip trajectory for recovery stroke one (R.S.1), purple spheres represent the wingtip trajectory for the upstroke (U.S.), and orange spheres represent the wingtip trajectory for recovery stroke two (R.S.2). (a) kinematics as viewed from the sagittal plane, (b) kinematics as viewed from the coronal plane. (c) sea turtle flipper skeletal system sourced from [84].

In this study, we design and build a robotic sea turtle to test a fully mechanical prosthesis design. Thus, The robot and implanted animal must only actuate the prosthesis in a simple roll motion without the sweep stroke. Hence, it can only produce the sea turtle's up and down strokes without incorporating any control or electrical system. We consider only the downstroke and upstroke to simplify the prosthetic design and thus ensure a robust and simple mechanical operation. The AOA is achieved passively with a soft rubber flipper to help mimic natural locomotion. Therefore we evaluate whether a prosthetic flipper with no induced actuation mechanism at the elbow joint can be sufficient in propulsion and manoeuvrability. Although using a robot to help develop a prosthesis for sea turtles is potentially a world first, robotic test platforms have been extensively used for human prosthesis development[129-131].

Outcomes from the evaluations with our biomimetic robotic model elucidated the significant potential for an implanted turtle to recuperate the locomotive capabilities it had previously lost. Moreover, the prosthesis exhibited an impressive ability to visually replicate the natural kinetic patterns characteristic of a sea turtle's up and downstrokes. This visual mimicry underscores the successful integration of biological locomotion within the prosthetic design, suggesting a promising interface between the mechanical system and the biological organism. We hope our findings could lead to other animal-inspired robots to help develop technology to assist other animals in need.

7.3 Methods

7.4 Design overview and objective

The primary objectives for the prosthetic flippers are multifaceted, aiming to restore function and quality of life to sea turtles. Firstly, the prosthesis seeks to replicate a turtle-inspired form and function, ensuring the turtle can achieve effective aquatic locomotion. This involves producing sufficient thrust and providing the turtle with sufficient manoeuvrability for activities such as evading predators and navigating various marine environments. Secondly, the prosthetic flipper should be durable and simple, requiring minimal maintenance. The criteria for evaluating the success of these prosthetics are grounded in both quantitative and qualitative measures. Quantitatively, success can be measured by comparing the thrust and speed achieved with the prosthesis to that of a natural flipper. Additionally, manoeuvrability will be judged based on reviewing simple videography of the robot performing simple roll, pitch and yaw manoeuvres.

7.5 Prosthetic flipper design and manufacturing

The prosthesis design was modelled in CAD (SP5.0, Solidworks 2019, Dassault Système, U.S.A.). The design process followed an iterative cycle using finite element analysis (F.E.A.) (R19.1, ANSYS, Canonsburg, PA, U.S.A), simulating loading from swimming and land-based locomotion. Loads were applied to the flipper body as a uniformly distributed load acting across the entire flipper surface. Initiating with a basic design concept and geometric framework for facilitating passive flipper rotation, we honed the geometry using a cycle of refinements in F.E.A. We adhered to this procedure until we achieved the sought-after stress distribution for both terrestrial and swimming locomotion, as depicted in Fig. 35. The targeted stress was determined according to the fatigue life of Electron Beam Melting (EBM)-manufactured Ti64[132].

For swimming, the loading was obtained from the study performed by van der Geest et al. [104] (Fig. 35a-b), for freely swimming green sea turtles. As no prior literature was found for the loading case for land-based locomotion in sea turtles, some simplifications and assumptions had to be made. Given that sea turtles inherently display the behaviour of dragging their carapace across sandy terrain during terrestrial transit to and from their nesting locations, it was imperative to elucidate the potential friction coefficients existing between the carapace and sand. This critical information was gleaned using a test rig conceptually modelled to emulate the underbelly of a turtle's carapace (Fig. 35f-i).

The rig was designed with an adjustable mass component, enabling normal and frictional load data estimation for various distinct loading scenarios. This customisable setup facilitated the experimental determination of diverse friction coefficients, thus enhancing our understanding of the carapace-sand interaction dynamic.

In order to ascertain the load imposed on each flipper during terrestrial locomotion, we simplified our calculations by assuming a state of static equilibrium. This assumption was deemed appropriate due to the characteristically low velocity of sea turtles during land transit, resulting in negligible acceleration. Moreover, we postulated that the pectoral flippers would bear approximately half of the turtle's vertical load, with the rear flippers primarily

contributing to the propulsive force, rather than supporting the turtle's weight (Fig 35e). The loading for each flipper was then calculated with equations 1-3:

$$R_a = \frac{m_f.B}{(A+B)} \quad (1)$$

$$R_b = \frac{m_f.A}{(A+B)} \quad (2)$$

$$\mu.R_b = F_f \quad (3)$$

Where R_a is the total load in the vertical direction experienced by both pectoral flippers and R_b is the total vertical load acting on the turtle's shell. The turtle's mass is represented as m_f with A and B representing the distance from the turtle's centre of mass to the reaction points R_a and R_b. A friction force F_f between the sand and shell is found using an experimental coefficient of friction value μ.

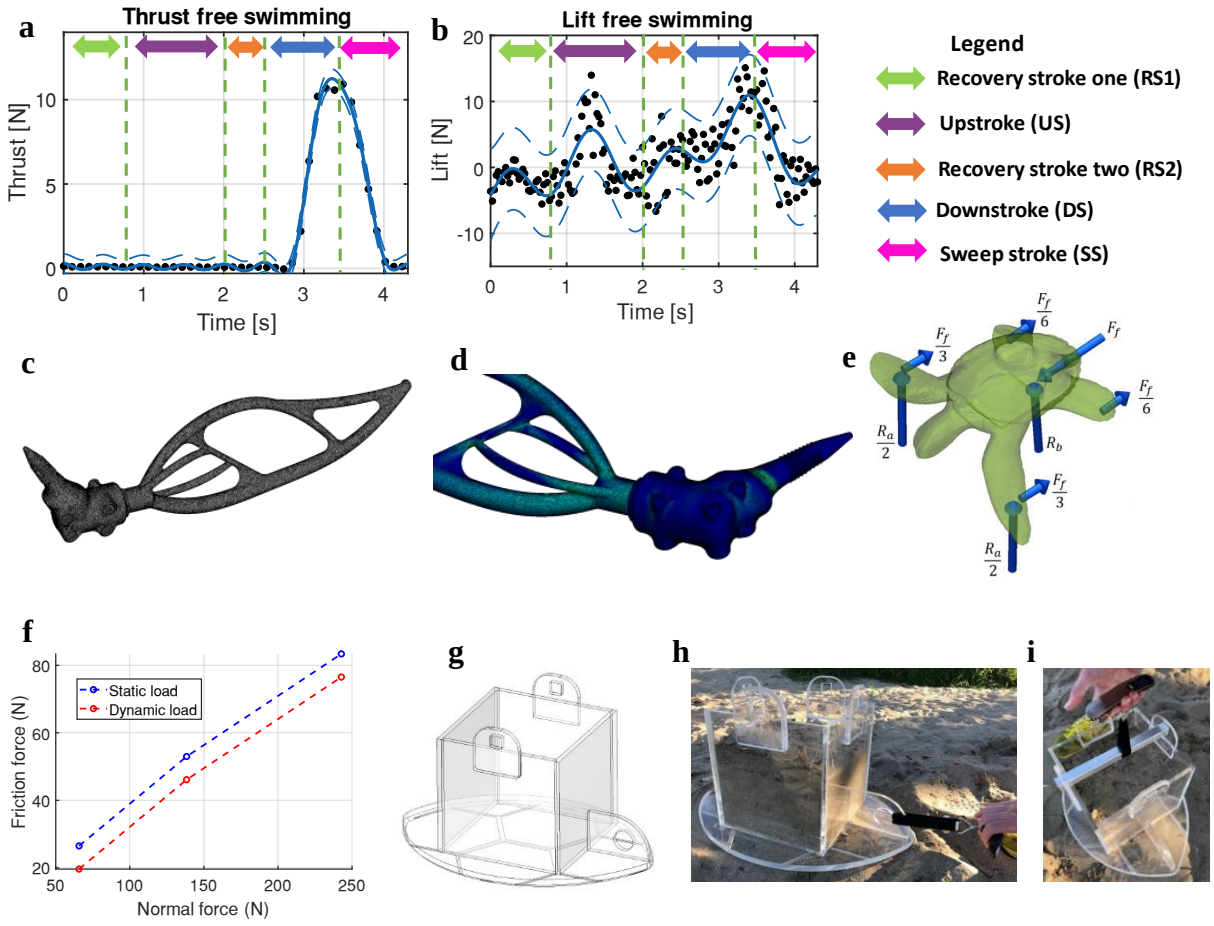

Figure 35: Prosthesis design process. (a) Sea turtle thrust production at 0.23Hz for one complete flipper oscillation obtained from van der Geest et al. Black dots signify individual data points, while the blue line illustrates the curve fit to the data. [104]. (b) Sea turtle lift production at 0.23Hz for one complete flipper oscillation obtained from van der Geest et al. Black dots signify individual data points, while the blue line illustrates the curve fit to the data. [104]. (c) F.E.A. mesh displayed without soft flipper. (d) Typical F.E.A. results showing stress distribution. (e) Free body diagram of the simplified forces during land-based locomotion. (f) Friction coefficient testing results. (g) Friction coefficient testing unit. (h) Testing for friction force. (i) Testing for normal force.

The flipper's AOA was achieved passively by designing the flipper to rotate on a transmission shaft held in place by two ceramic bearings (Fig. 36a-c). The torque (M_z) to rotate the flipper into its downstroke and upstroke positions passively can be modelled using:

$$M_z = F_{cp} * \Delta x$$

Where F_{cp} is the force acting at the centre of pressure a distance Δx from the flipper rotation axis (Fig. 36b).

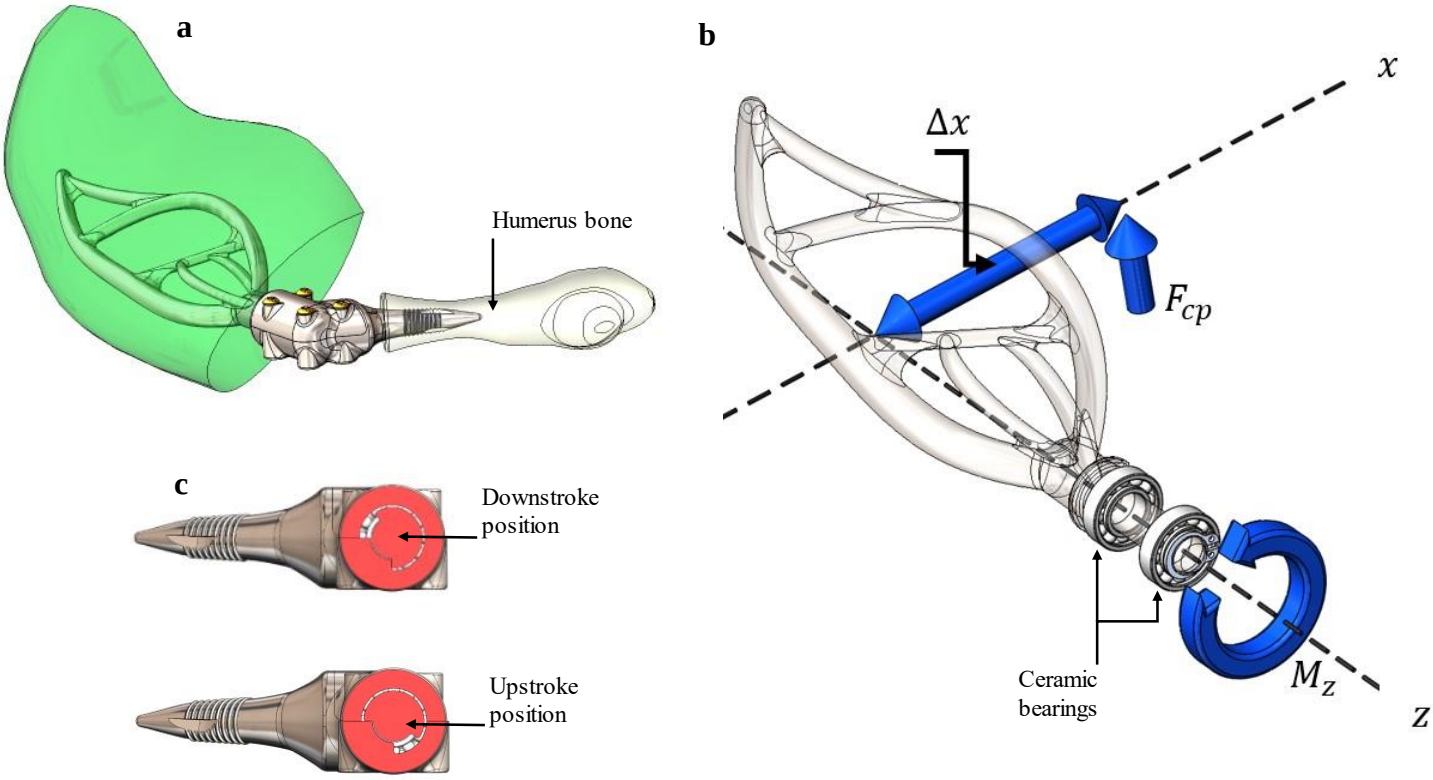

Figure 36: Prosthetic flipper design. (a) Complete CAD model showing the implant in the humerus bone along with the soft slipper that is cast over the flipper mechanism. (b) Free body diagram of flipper mechanism with F_{cp} the force acting at the flipper centre of pressure. M_z the moment applied to rotate the mechanism and Δx the distance of the centre of pressure from the mechanism's rotation axis. (c) A.O.A. generating mechanism showing the mechanical limits for the upstroke and downstroke.

The stem was designed with a porous lattice structure to promote bone ingrowth and help lower stress shielding[133-135]. The stem and internal flipper structure was additively manufactured using electron beam manufacturing (EBM) technology from titanium alloy (Ti64). CAD Models were processed using Solidworks 2019 SP5.0 and then exported to STL mesh files. The STL Mesh files were prepared in Materialize Magics 23 software. The turtle stems were built on an Arcam Q10plus EBM machine with SOP17:1 running EBMControl 5.0 software. The solid regions of the component were built using a standard process melt theme with 0.05mm layer thickness. The porous structure was generated using Materialize Magics 23, using the Structures module. This used a 0.60mm unit cell with 0.05mm overlap in x,y and z, and a 45-degree growth angle. This generated a mesh with a 0.27mm strut diameter. The porous structure was built using the standard NET process theme with 0.05mm layer thickness.

The main bearing housing is bolted together with four Ti64 fasteners, as seen in Fig. 37a-d. The two ceramic bearings were installed with 98A TPU bushings to reduce the chances of impact loads damaging the bearings. After printing, the transmission shaft and bearing races were machined to achieve the required bearing tolerances. The soft flipper was manufactured by casting 70A polyurethane rubber over the flipper's internal structure using a split mould assembly. Shore A 70 hardness polyurethane rubber was used as it gave what we feel is the best compromise between bio-mimicking the natural flipper flex and structural resistance to hydrodynamic loads. Additionally, the lid of the mould assembly acted as a holding jig to precisely position the flipper structure within the correct design location of the overall flipper geometry, as seen in Fig. 37e.

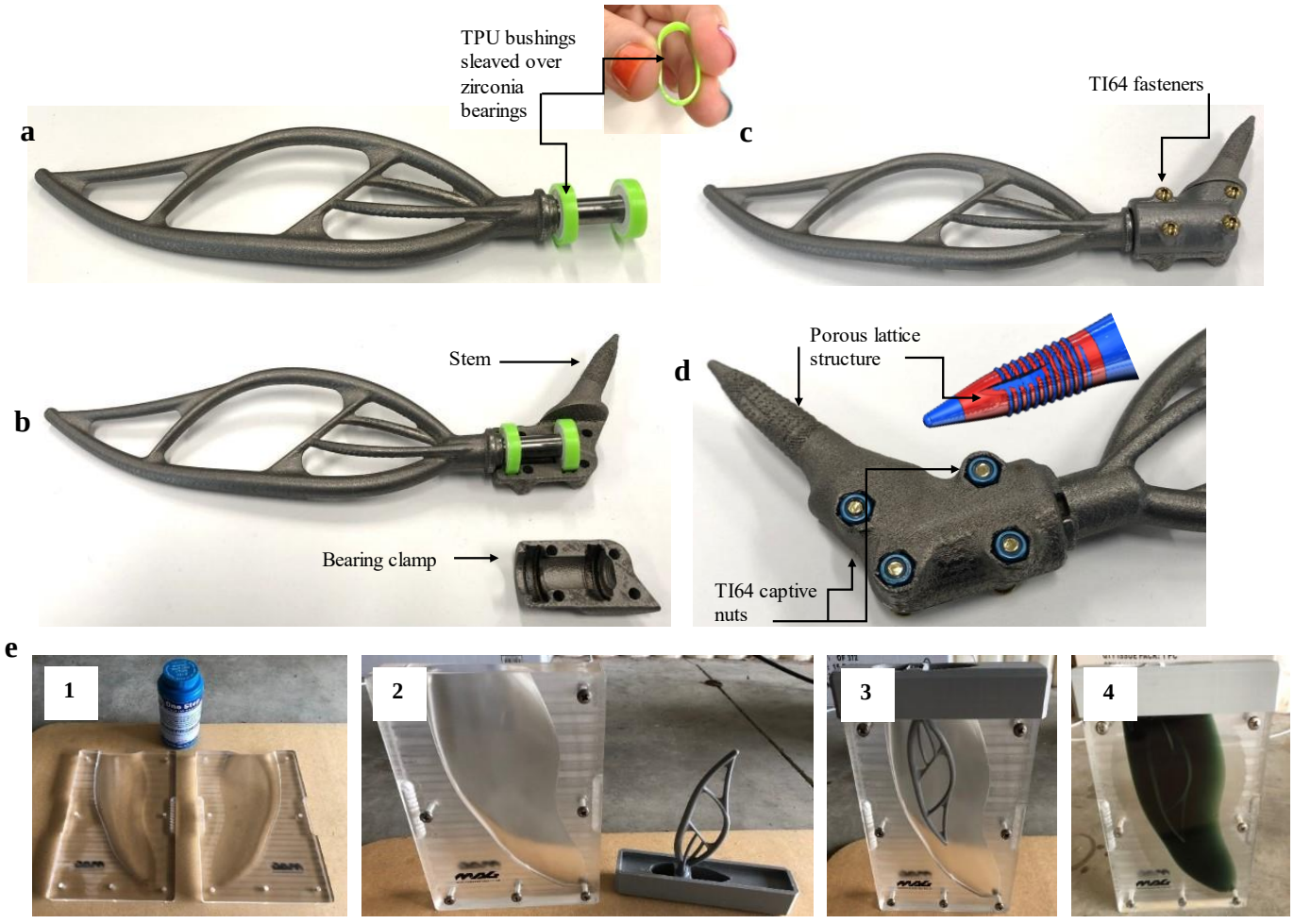

Figure 37: 3D printed titanium prosthetic assembly. (a) Flipper mechanism showing Soft TPU bearing bushings to help reduce impact loadings. (b) Flipper mechanism being assembled to stem. (c) Fully assembled prosthetic without the soft flipper. (d) close up of the porous stem structure (Red areas are the porous zones with blue areas solid zones) and captive nuts for securing stem to flipper mechanism. (e) Flipper casting process. (1) split mould preparation. (2) assembly of split mould and flipper mechanism. (3) Full mould assembly. (4) Casting of soft rubber flipper.

7.6 Sea turtle-inspired robot design and manufacture

As previously explained, the swimming cycle of sea turtles is composed of five distinct stages, namely, DS, SS, RS1, US, and RS2. The SS and RS1 phases are predominantly enabled by articulating the turtle's elbow joint. Without this joint, as the results of amputation, only the DS and US stages can be attained. This understanding aids in streamlining the design process for both the robotic model and the prosthesis, as the designs need only facilitate a simple roll motion coupled with a passive pitching rotation, as depicted in Fig. 38.

The robot's carapace, as illustrated in Fig. 38a-b, was intentionally simplified relative to the intricate form of a natural sea turtle. This was achieved by designing a body symmetrical in both sagittal and coronal planes. Moreover, the carapace's overall volume was reduced, thereby decreasing the required material volume and consequently simplifying the manufacturing process. It is worth mentioning that despite these modifications for practicality, the robotic model retains an overall form that is heavily inspired by sea turtles.

These design choices are justified by the need for technical efficiency, material economy, and manufacturing simplicity. The iterative process of developing a bio-inspired robotic system necessitates these simplifications as a practical compromise between biologically accurate representation and feasible engineering solutions. The objective is to attain a balance between biological mimicry and operational efficiency, ensuring the robotic model can adequately perform its testing role for the prosthesis.

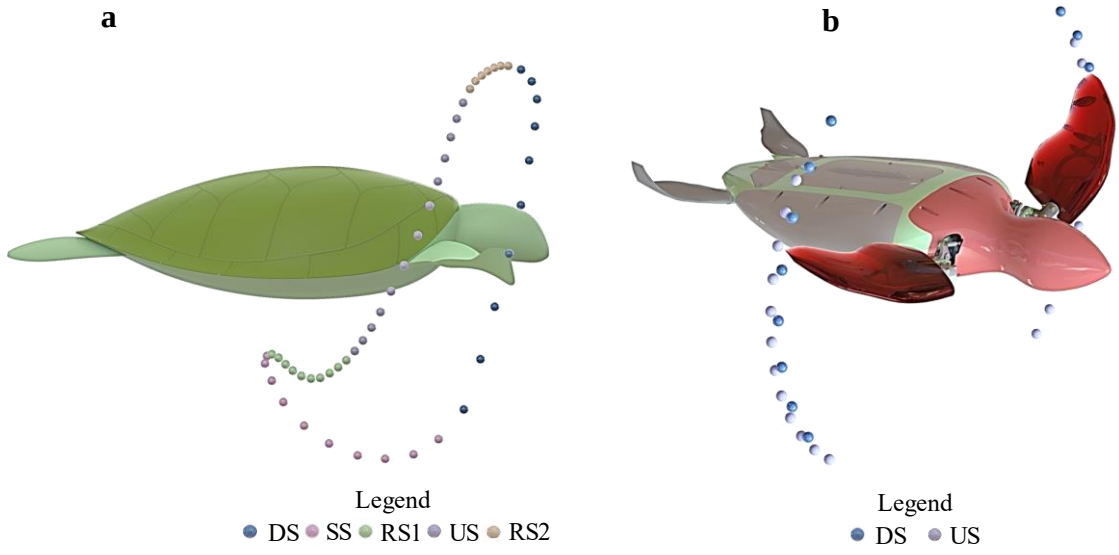

Figure 38: Robot sea turtle simplifications and comparisons to natural sea turtle locomotion. (a) Natural sea turtle locomotion displays each of the five stages. (b) Simplified robot sea turtle locomotion displaying upstroke and downstroke flipper tip path.

Using additive manufacturing equipment, the turtle-inspired robot chassis was 3d printed from PLA+ filament (Esun, Shenzhen, China). Printing was done with an FDM machine (Caribou Mk3s, Caribou, Remagen, Germany) with the model sliced into 0.16mm layer heights and printed with 40% honeycomb infill. The front transmission assembly used two Savox SW-0231MG servos (Savox, Taichung City, Taiwan). The servos were bolted to a CNC machined adaptor plate that connected the prosthetic flippers to the servo motors with two four-bar linkage mechanisms made from titanium turnbuckles (Fig. 39a-c) to produce a maximum roll amplitude of 90º (Fig. 39c). The same servo motors actuated the rear flippers however actuation went through a simple belt drive of 1:1 drive ratio (Fig. 39b). To achieve the correct buoyancy the chassis was designed to allow water ingress, except for a small acrylic box that kept the non-waterproof electronics dry (Fig. 39b). Power was sent to the four servo motors via a 6.6V, 4C, 1800mAh LiFe battery (Muchmore Racing, Seoul, Korea) that was also housed inside the watertight enclosure.

To avoid the necessity for a control system to maintain stability, the robotic model was strategically engineered to exhibit inherent stability. This was achieved by ensuring the centre of buoyancy (COB) was above the robot's centre of gravity (COG) as viewed from the y-z plane in Fig. 40a to generate a natural righting moment.

Sea turtles produce a more aggressive downstroke when compared to their upstroke[3,4,84,95,104]. To offset the powerful downstroke and help the robot swim level, the COG was designed to be frontwards of the COB seen from the x-y plane in Fig. 40b. This caused the robot to pitch noise down when stationary and level out during swimming operation. The robot operator generated the servo actuation via a handheld controller, as seen in Fig. 39a. This allowed the operator to control each servo actuation as needed to perform the desired motion underwater.

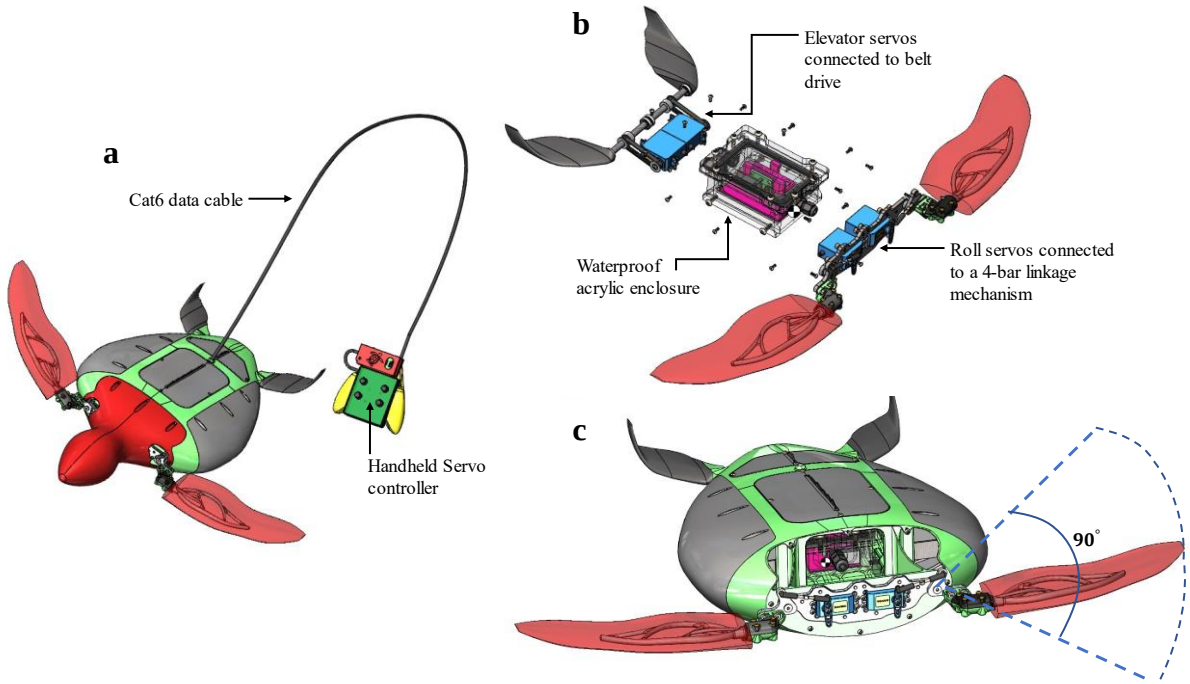

Figure 39: Robot sea turtle assembly. (a) Complete assembly showing hand controller connected to a cat6 data cable. (b) Internal hardware showing front transmission with servos and 4-bar linkage mechanism, waterproof Acrylic electrical enclosure and rear flippers/elevators with belt drive. (c) Front transmission assembly with the front flipper roll amplitude limited to the transverse plane.

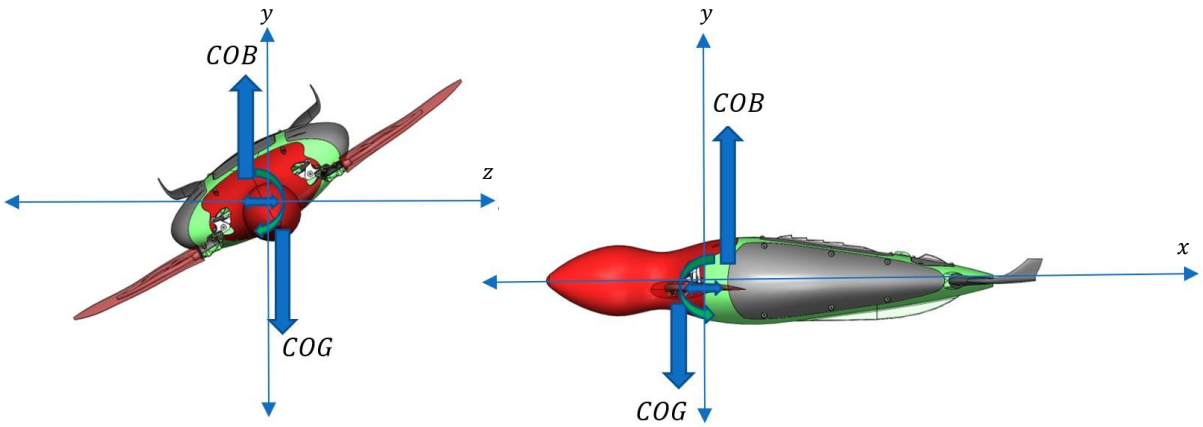

Figure 40: Free body diagram of robot turtle. (a) Centre of buoyancy vs centre of gravity as viewed from the y-z plane. (b) Centre of buoyancy vs centre of gravity as viewed from the x-y plane.

To ensure a naturally stable robot during swimming, as described before, the COG and COB needed to be precisely positioned relative to one another. To accomplish this, a complete CAD model of the robot, including every nut, bolt and circuit board, along with the correct volumes and masses, was defined within the CAD model to create a virtual clone of the robot assembly. This allowed the COG to be atomically calculated within CAD relative to the COB.

Calculating the COB required the CAD model to be converted into water by defining all the solid bodies within the entire assembly as the density of water. Additionally, the watertight enclosure had to be remodelled as a solid body (No longer hollow) to ensure the correct fluid volumes were obtained. This process was iterated in CAD by tuning the internal geometry of the robot model until the desired COB and COG positions were obtained within the CAD virtual space.

During the manufacturing process, each part and sub-assembly was weighed after manufacturing to ensure its mass properties matched the virtual part from CAD. The virtual robot's mass was 2507.2 grams, and the final completely assembled robot was 2507 grams. As a result of this design process within the CAD virtual environment, the robot achieved perfect buoyancy in the water column and required no trimming.

7.7 Results and discussion

7.8 Swim speed and average thrust generation

All swim tests were performed at the AUT Millennium Centre high-performance training facilities in Auckland, New Zealand. The centre utilises an internal system they name "Video tracking". Video tracking is used to measure the swim speed of Olympic athletes during their training sessions. It is programmed to follow red objects from multiple gigabit ethernet cameras built into the pool roof, thus allowing swim speed to be easily calculated by differentiating the position data (Fig. 41a). The robot's head and flippers were manufactured red to take advantage of Video tracking to find the swim speed of the robot. Due to the robot's low drag, the cable did produce significant interference during swimming compared with the body's drag forces. Despite this, the robot produced a maximum swim speed of 0.487±0.001 m/s at a flapping frequency of 0.9Hz while dragging 6m of cat6 data cable underwater (Fig. 41b).

An estimated theoretical max swim speed was calculated for the robot without the data cable with the help of C.F.D. ANSYS CFX (ANSYS 2019 R2, Canonsburg, P.A, USA). The CFD code used the ke model for two separate simulations, one with the robot and one with the cable (Fig. 41cd). The simulation for the robot was performed without flippers, as they are propulsion generators rather than drag generators, with the cable modelled as per the video footage in Fig. 41b. Simulations predicted a drag coefficient (c_d) of 0.205 for the robot and 0.364 for the cable. Based on the c_d of the cable and robot a total drag force (F_{total}) of 1.239N was calculated for 0.487 m/s. From this, the estimated maximum swim speed of 0.618 m/s was calculated using:

$$V_{max} = \sqrt{\frac{2F_{total}}{\rho A c_d}}$$

Where A and c_d are the frontal area and drag coefficient of the robot's body only. Given that the robot was swimming at a constant velocity, the total drag force can be mathematically equated to the average thrust generation. Through our analysis, we ascertained that the robot with the prosthesis produced an average thrust of 1.239 N, utilising a basic roll and pitch motion. Drawing comparisons from a study by van der Geest et al.[104], a wild sea turtle of comparable dimensions generates an average thrust of 2.4N during its typical swimming activities. While the prosthetic flippers recapture only approximately 50% of this native thrust, it is noteworthy to emphasise that this is a significant improvement over having no flipper at all. This demonstrates that even the rudimentary motion facilitated by the prosthesis can offer meaningful propulsion, underscoring its potential utility in locomotion.

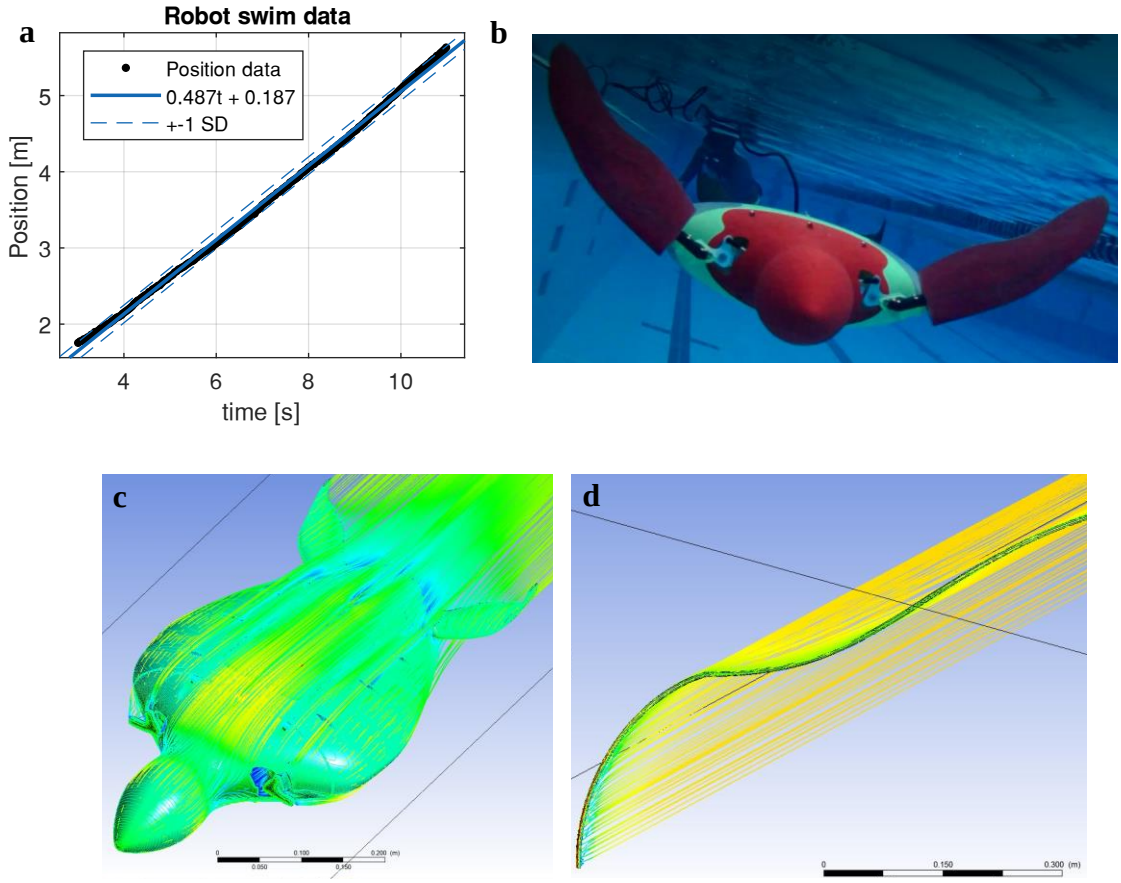

Figure 41: Robot swim speed data and tests. (a) Position vs time data from the AUT Millenium centres video tracking software. (b) The image shows the robot dragging the data cable through the water during a speed test. (c) CFD simulation of robot turtle body. (d) CFD simulation of data cable.

7.9 Manoeuvrability tests

While motion capture techniques were employed to determine swim speed, these methods proved ineffective in capturing roll, pitch, and yaw motions during swim tests. In order to support these motions, we employed underwater videography (Movie S1 available at https://www.mdpi.com/2077-1312/10/11/1770). While relying on videography data can be considered a more qualitative approach, the footage shows that the prosthesis performed admirably in executing roll, pitch, and yaw motions based on basic user inputs (Fig. 42a-e).

For instance, the yawing action to steer the robot left and right (Fig. 42d-e) was realised by having the operator modulate the speed of the left or right flipper, thereby generating the desired thrust vector. Yaw motions could be adeptly executed both during full-speed swimming and when stationary. Similarly, the robot's pitch was controlled by altering the frequency of the upward and downward strokes relative to one another while concurrently adjusting the angle of the rear flippers/elevators, as depicted in Fig. 42a-c. This adaptive strategy, wherein the simple adjustments to the flipper movements result in complex and precise manoeuvres such as yaw and pitch, underscores the efficacy and versatility of the prosthesis in mimicking authentic sea turtle locomotion. The notable aspect of this finding lies not merely in replicating these complex movements but through intuitive controls and uncomplicated modifications to flipper speed.

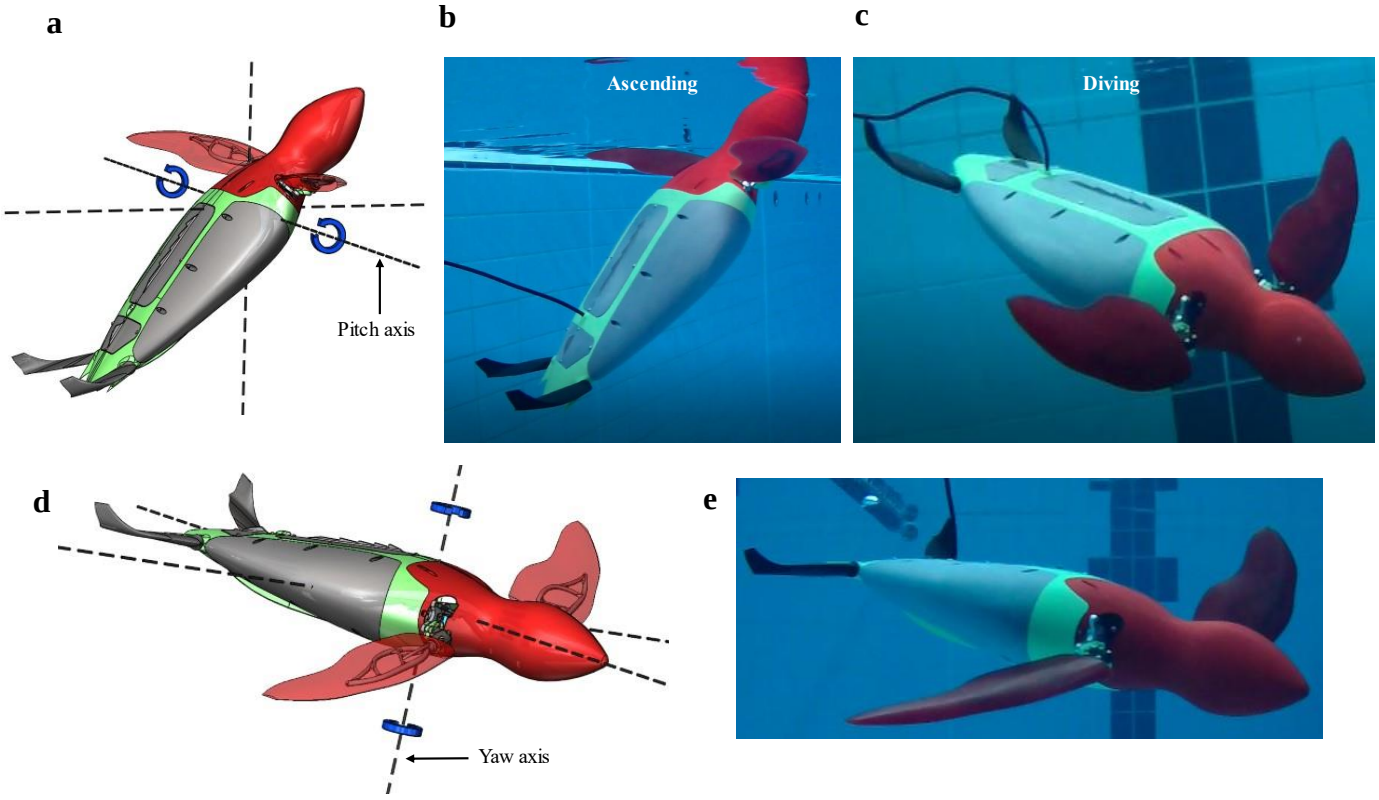

Figure 42: Manouvrability tests. (a) free body diagram showing the pitching axis. (b) Pitching up to ascend towards the surface. (c) pitching down to dive. (d) free body diagram showing the yaw axis. (e) Robot producing stationary yaw without forward swimming motion. Also see Moivie S1 available at https://www.mdpi.com/2077-1312/10/11/1770.

When evaluating the locomotion patterns of our robot fitted with the prosthetic flipper, focusing on the downstroke, upstroke, and wing rotation phases, a striking similarity is evident when compared with the green sea turtle's natural movements, as depicted in Fig. 43. These parallels offer significant insights into the biomechanical fidelity of our robotic design. However, a discernible deviation is noticeable in how the flipper articulates during each phase. The green sea turtle can morph and twist its flipper in its natural environment, providing multifaceted control over its aquatic manoeuvres. Conversely, our prosthetic design, bounded by current technological constraints, limits the flipper's movement to a rotation along a singular axis, as illustrated in Fig. 43 under the wing twist column.

This distinction, while noteworthy, is a conscious design decision rooted in prioritising mechanical durability and simplicity. As alluded to in our previous discussions about removing the sweep stroke, the design's simplification to mere rotation minimises the number of potential failure points. This decision not only ensures the longevity and reliability of the prosthesis but also streamlines the engineering challenges, offering a robust solution that, while not perfectly emulating nature, strikes a balance between biomechanical accuracy and mechanical pragmatism.

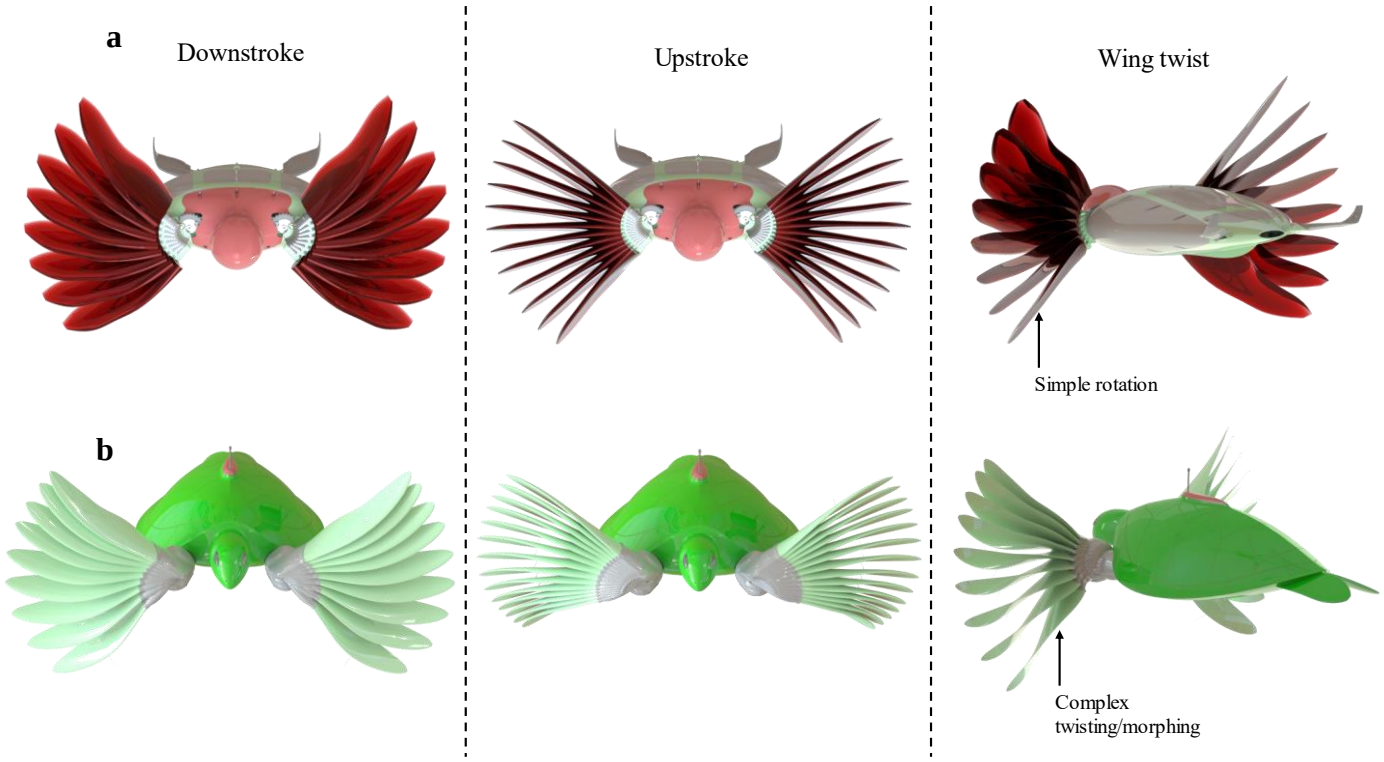

Figure 43: Prosthetic implant graphical comparison against the natural green sea turtle locomotion. (a) The turtle-inspired robot applying the downstroke, upstroke and wing rotation. (b) A computer render from van der Geest et al.[104] demonstrates the natural sea turtle downstroke, upstroke and wing morphing/twisting at 0.08 second time steps for the natural swimming routine outlined in Fig 43a-b.

7.10 Conclusion and future work

In this research, we conceptualised and constructed a robotic sea turtle to evaluate a purely mechanical prosthetic design. The robotic model, representing the prospective implanted animal, was engineered to actuate the prosthesis through a basic roll and passive pitch motion, excluding the sweep stroke. This approach allowed us to emulate the sea turtle's up and down strokes. The study has shown that the prosthesis could allow an implanted animal to regain intricate movements, such as roll, yaw and pitch, through relatively straightforward inputs.

The average thrust generated by the prosthesis, though presently amounting to roughly half of what wild sea turtles can produce, holds particular promise. This thrust enhancement, even in the absence of a complete Sweep Stroke (SS) that characterises the natural propulsion cycle of the turtles, demonstrates a marked improvement over having no flipper at all.

However, while filled with potential, some limitations require discussion. A significant limitation was the motion capture techniques' inability to accurately track stationary roll, pitch, and yaw motions during swim tests. Though invaluable, our dependence on underwater videography did not provide the quantitative precision desired, especially in capturing the nuances of thrust dynamics and the various motions.

Moving forward, the goal is not merely to optimise the design but to understand and develop the complete integration of the prosthesis with the sea turtle's body which will require animal

trials. Detailed attention must be paid to the stem and the intricacies of the implantation procedures. Every surgical step, from the initial incision to the post-surgical aftercare, plays a crucial role in ensuring that the prosthesis remains anchored and can deliver the requisite thrust without complications.

However, the challenges do not end post-surgery. The animal with an implanted limb will need comprehensive rehabilitation programs designed to familiarise them with the unique thrust dynamics of their new appendage, ensuring they can regain and, maybe, exceed their previous swimming capabilities. Through this rehabilitation, the goal is to restore physical function and bolster the turtle's confidence in navigating aquatic terrains with their new prosthetic.

Even though we currently cannot replicate the complete SS with the prosthesis, and thus, the entire swimming cycle is not 100% mimicked, the results are promising.

Collaborations with marine biologists, veterinary surgeons, and biomechanics experts will be instrumental. Their combined expertise can push the boundaries of what is possible for rehabilitating injured sea turtles and advancing the frontiers of bioinspired robotic design. Both authors of this communication welcome the international scientific community for future collaborations.

In wrapping up, the technology presented in this communication could offer a lifeline for injured sea turtles requiring prosthetic support, enabling naturalistic movement patterns crucial for survival. The ability to emulate such intricate and nuanced motions of an actual sea turtle using a relatively simple and controllable prosthetic system highlights an innovative intersection of biology, technology, and engineering that could have far-reaching impacts. Given the inherent simplicity of the prosthesis operation, it is entirely plausible that a sea turtle, renowned for its adaptability, could learn to utilise this prosthetic flipper effectively.

Chapter 8: Discussion and Conclusion

The sea turtle, a marvel of biological evolution, represents an outstanding case study in biomechanics and hydrodynamics. Over the course of this thesis, we have sought to answer four research questions spread across five sequential peer-reviewed publications serving as individual chapters that delved into swimming kinematics, propulsion methods, fluid mechanics, and the potential of using these insights for practical applications.

The research presented in this thesis was grounded in a series of five peer-reviewed published works, each meticulously contributing to the exploration and understanding of four critical research questions regarding sea turtle locomotion. These questions were:

1- What are the defining characteristics of aquatic locomotion in Sea turtles within their natural habitat, and how do these differ from locomotive behaviours observed in juvenile turtles in captive settings?
2- Which biomechanical and physiological mechanisms enable Sea turtles to generate efficient thrust for propulsion in their aquatic environments?
3- How does the morphology and movement of Sea turtle flippers affect and interact with surrounding hydrodynamic fields to influence their locomotion?
4- Can the insights derived from studying Sea turtle propulsion mechanisms be applied to practical uses, particularly in advancing marine technologies?

The progression of these peer-reviewed publications began with Chapter 3, which specifically addresses the first question to characterise the aquatic locomotion in wild sea turtles. Chapters 4, 5, and 6 collectively delve into the biomechanical and physiological aspects of sea turtle propulsion, providing answers to the second question. These chapters also revisit and further elaborate on the third question, deepening the understanding of flipper movement and hydrodynamics. Finally, Chapters 6 and 7 synthesize this knowledge, exploring how it can be applied to the development of marine technology and other practical applications, thereby addressing the fourth question. This cohesive body of peer-reviewed research ensures a robust and scholarly approach to the study of sea turtle locomotion and its broader implications.

The study's findings illuminate the extraordinary biomechanics of sea turtle locomotion. By developing non-invasive techniques to record their swimming kinematics, we have unearthed a new five-stage cycle swimming locomotion model. This model offers a comprehensive understanding of how sea turtles create propulsion, providing a more nuanced picture than previous models.

In our continuous quest to understand the intricate biomechanical strategies of sea turtles, we ventured into creating an advanced robotic model we named Cornelia that meticulously mimics the green sea turtle's form and functional attributes. Drawing from the wealth of data from this robotic surrogate, we discerned an intriguing propulsion paradigm: sea turtles allocate a mere 30% of their limb beat cycle towards active propulsion. The remaining 70% of the cycle is harnessed for a power-conservative low-drag glide.

During this hydrodynamically efficient glide, the sea turtles exhibit an astute exploitation of the ambient fluid dynamics. By harnessing the kinetic energy embedded within the surrounding aquatic medium, they ingeniously facilitate a passive elevation of their flippers

during the pivotal upstroke phase. This orchestrated motion serves a dual purpose. Firstly, it precipitates a palpable reduction in hydrodynamic drag, achieved through the creation of low-pressure differentials. This ensures the circumvention of turbulent interactions notorious for energy wastage, such as the wingtip vortices. On the flip side, the active propulsive phase is a theatre of complex vortex dynamics. Our analysis reveals the generation of a Leading Edge Vortex (LEV) that is judiciously shed at the culmination of the sweep stroke. In parallel, we identified a distinct vortex formation, we call the Sweep Stroke Vortex (SSV), which intriguingly is delivered and released almost in tandem during the sweep stroke. The synergistic shedding of the SSV and LEV into the wake appears to impart downstream momentum, possibly amplifying the turtle's hydrodynamic efficiency.

These observed hydrodynamic orchestrations converge to reveal an astonishingly low Cost of Transport (COT) for sea turtles, a testament to the evolutionary refinement of their propulsion strategies. Such propulsion intricacies, nuanced over aeons, underscore the sea turtles' remarkable prowess in traversing vast oceanic expanses, even while subsisting on a diet that offers a relatively low energetic return.

In the culmination of this PhD thesis, which sought to unravel the biomechanics of sea turtle locomotion and its potential technological extrapolations, our inquiries have illuminated several compelling facets, especially in biomechanically-inspired prosthetics.

Our meticulous examination of sea turtle propulsion mechanics inspired the exploration of a purely mechanical prosthetic design. Operated through a fundamental roll combined with passive pitch and intentionally excluding the sweep stroke, our intention was streamlined: to mirror only the turtles' essential vertical movements. The outcomes from these investigations have been particularly encouraging. The designed prosthesis promises the restoration of complex motions, such as roll, yaw, and pitch, to an implanted host and achieves this feat via a surprisingly minimalistic actuation paradigm.

It is also imperative to underscore the significance of the generated thrust. While achieving approximately half of the thrust of wild sea turtles, this is a formidable stride in biomechanical prosthetics. The fact that significant thrust can be augmented without fully emulating the Sweep Stroke (SS), a hallmark of natural turtle propulsion, signals a beacon of hope for future interventions. This relative augmentation is a testament to the prosthesis's efficacy, especially when compared to the unfortunate circumstance of a turtle without a flipper.

In the culminating phases of this thesis, we described the prospective applications of our investigative results to marine exploration technologies. Navigating the intricacies of transmuting the multifaceted biomechanics of an oscillating sea turtle flipper into a tangible mechanical prototype presented challenges. Nevertheless, our computational fluid dynamics (CFD) simulations, which focused on a constantly rotating turtle wing, demonstrated a promising energy-to-thrust output. This gives a compelling blueprint for conceptualising high-efficacy, bio-mimetic underwater drones incorporating a rotating, turtle-inspired, morphing propulsor. Our research posits that, when employed in a tandem configuration, such a propulsor can manifest a myriad of adaptive functionalities. This encompasses roles as a rudder or stabiliser, a propulsion mechanism, an energy harvester, and potentially a means of dynamic thrust vectoring. Envisioning a drone endowed with such versatility and paired with the appropriate sensor array, one can foresee profound applications in domains like

search and rescue operations, bathymetric charting, and coral reef replanting, all while operating at minimal energy expenditure.

These revelations emphasise the intricate beauty of nature's biomechanics and highlight the immense potential at the crossroads of biology and technology. The quest for bridging these two domains, albeit challenging, carries with it the promise of innovations that could revolutionise how we perceive biological interventions and their techno-inspired counterparts.

While this study provides valuable insights into sea turtle swimming mechanics, it represents an initial foray into this intricate domain. To further unravel the complexities of sea turtle biomechanics and its potential technological implications, the findings from this research present several pivotal directions for continued inquiry and development:

8.1 Future research

1 Fluid-Structure Interactions and Wake Patterns
Objective: Further comprehending the intricate fluid dynamics intrinsic to sea turtle locomotion, primarily focusing on the interactions between fluid and the biological structure, alongside the consequential wake patterns and vortices.
Methodology: Harnessing advanced Computational Fluid Dynamics (CFD) simulations in tandem with Particle Image Velocimetry (PIV) will offer high-resolution insights into the emergent wake patterns of flapping flippers. This can be complemented with experimental setups involving wind tunnels and hydrodynamic flow tanks for real-world validation.
Significance: A profound understanding of these nuanced interactions will pave the way for enhanced design and efficiency in bio-inspired marine technologies, potentially leading to innovative propulsion mechanisms that borrow from nature's evolutionary optimisation.

2 Kinematics in Navigational Dynamics
Objective: Elucidate the kinematic intricacies during yaw, roll, and pitch, particularly when sea turtles face the challenges of navigating currents. The end goal is understanding, replicating, and controlling these movements in mechanical counterparts.
Methodology: By integrating motion capture technologies with state-of-the-art telemetry tools, the movements of wild sea turtles in varied conditions, including adversarial currents, can be closely monitored and analysed. Such data can inform and calibrate robotic models to replicate similar kinematic responses.
Significance: For marine technologies, mastering navigational dynamics, especially in unpredictable conditions, is paramount. The ability to manoeuvre adeptly through yaw, roll, and pitch can dramatically augment the performance and versatility of underwater robotic systems.

3 Morphing Turtle-Inspired Propellor Development
Objective: Undertake iterative design and testing to evolve the turtle-inspired morphing propellor, aiming for efficiency, adaptability, and versatility.
Methodology: Drawing from the research findings and integrating them with iterative prototyping, simulations, and real-world testing, the propellor's design and functionality can be incrementally refined.
Significance: A morphing propellor, inspired by the biomechanics of sea turtles, can usher in a new era for marine propulsion systems, having implications not only for exploration but also for sustainable marine technologies.

These proposed avenues for future exploration represent a natural extension of the groundwork laid in this thesis. By delving deeper into these domains, the promise of merging biological insights with engineering innovations can further the frontiers of marine technology and conservation, leading to a more harmonious coexistence of nature and technology.

This study represents a significant stride towards understanding the marvel of sea turtle locomotion and how we can apply this knowledge to technological advancement. It is hoped that this novel work will inspire further research into the biomechanics of other marine creatures and contribute to the ongoing quest to develop more efficient, bioinspired technologies for ocean exploration. In this context, our work reaffirms that nature, through its millions of years of evolutionary optimisation, has much to teach us, and the sea turtle remains an effective teacher in the realm of efficient propulsion.

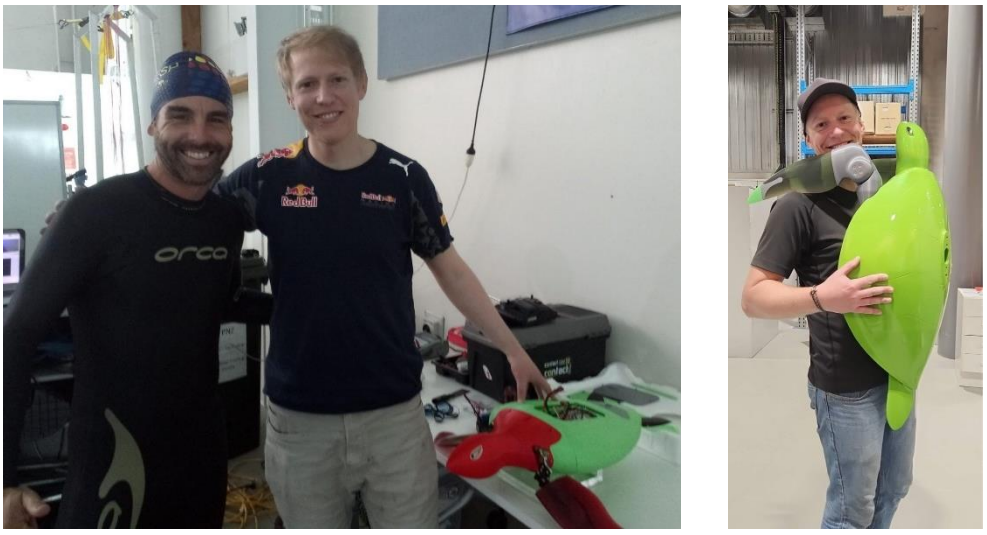

Figure 44: The synergy squad..

References

1 Chiari, Y., Cahais, V., Galtier, N. & Delsuc, F. Phylogenomic analyses support the position of turtles as the sister group of birds and crocodiles (Archosauria). *BMC Biology* **10**, 65, doi:10.1186/1741-7007-10-65 (2012).

2 Hochscheid, S., Bentivegna, F. & Speakman, J. R. The dual function of the lung in chelonian sea turtles: buoyancy control and oxygen storage. *J. Exp. Mar. Biol. Ecol.* **297**, 123-140, doi:10.1016/j.jembe.2003.07.004 (2003).

3 Davenport, J., Munks, S. A. & Oxford, P. J. A Comparison of the swimming of Marine and Freshwater Turtles. *Royal Society of London. Series B, Biological Sciences* **220**, doi:https://doi.org/10.1098/rspb.1984.0013 (1984).

4 Booth, D. T. Kinematics of swimming and thrust production during powerstroking bouts of the swim frenzy in green turtle hatchlings. *Biol Open* **3**, 887-894, doi:10.1242/bio.20149480 (2014).

5 Walker, W. F. Swimming in Sea Turtles of the Family Cheloniidae. *Copeia* **1971**, 229 (1971).

6 Font, D. *et al.* Design and implementation of a biomimetic turtle hydrofoil for an autonomous underwater vehicle. *Sensors (Basel)* **11**, 11168-11187, doi:10.3390/s111211168 (2011).

7 Xu, J., Liu, X., Chu, D., Sun, L. & Zhang, M. in *2009 IEEE International Conference on Robotics and Biomimetics (ROBIO)*.

8 Colmenares, D., Kania, R., Zhang, W. & Sitti, M. Bio-inspired Flexible Twisting Wings Increase Lift and Efficiency of a Flapping Wing Micro Air Vehicle. *ArXiv* **abs/2001.11586** (2020).

9 Kaygan, E. & Ulusoy, C. Effectiveness of Twist Morphing Wing on Aerodynamic Performance and Control of an Aircraft. *Journal of Aviation* **2**, 77-86, doi:10.30518/jav.482507 (2018).

10 Thielicke, W. & Stamhuis, E. J. The effects of wing twist in slow-speed flapping flight of birds: trading brute force against efficiency. *Bioinspir Biomim* **13**, 056015, doi:10.1088/1748-3190/aad5a3 (2018).

11 Truong, T. Q., Phan, V. H., Park, H. C. & Ko, J. H. Effect of Wing Twisting on Aerodynamic Performance of Flapping Wing System. *AIAA Journal* **51**, 1612-1620, doi:10.2514/1.J051831 (2013).

12 Vos, R., Gürdal, Z. & Abdalla, M. Mechanism for Warp-Controlled Twist of a Morphing Wing. *Journal of Aircraft* **47**, 450-457, doi:10.2514/1.39328 (2010).

13 Zheng, L., Hedrick, T. L. & Mittal, R. Time-varying wing-twist improves aerodynamic efficiency of forward flight in butterflies. *PLoS One* **8**, e53060, doi:10.1371/journal.pone.0053060 (2013).

14 Hays, G. C. & Scott, R. Global patterns for upper ceilings on migration distance in sea turtles and comparisons with fish, birds and mammals. *Functional Ecology* **27**, 748-756, doi:https://doi.org/10.1111/1365-2435.12073 (2013).

15 Eckert, S. A. High-use oceanic areas for Atlantic leatherback sea turtles (Dermochelys coriacea) as identified using satellite telemetered location and dive information. *Marine Biology* **149**, 1257-1267, doi:10.1007/s00227-006-0262-z (2006).

16 Luschi, P., Hays, G. C., Del Seppia, C., Marsh, R. & Papi, F. The navigational feats of green sea turtles migrating from Ascension Island investigated by satellite telemetry. *Proceedings of the Royal Society of London. Series B: Biological Sciences* **265**, 2279-2284, doi:doi:10.1098/rspb.1998.0571 (1998).

17 Izraelevitz, J. S. & Triantafyllou, M. S. Adding in-line motion and model-based optimization offers exceptional force control authority in flapping foils. *Journal of Fluid Mechanics* **742**, 5-34, doi:10.1017/jfm.2014.7 (2014).

18 Licht, S. C., Wibawa, M. S., Hover, F. S. & Triantafyllou, M. S. In-line motion causes high thrust and efficiency in flapping foils that use power downstroke. *J Exp Biol* **213**, 63-71, doi:10.1242/jeb.031708 (2010).

19 Zhou, K., Liu, J.-k. & Chen, W.-s. Numerical and experimental studies of hydrodynamics of flapping foils. *Journal of Hydrodynamics* **30**, 258–266, doi:10.1007/s42241-018-0028-3 (2018).

20 Chen, L., Wu, J. & Cheng, B. Leading-edge vortex formation and transient lift generation on a revolving wing at low Reynolds number. *Aerospace Science and Technology* **97**, doi:10.1016/j.ast.2019.105589 (2020).

21 Jardin, T. Coriolis effect and the attachment of the leading edge vortex. *Journal of Fluid Mechanics* **820**, 312-340, doi:10.1017/jfm.2017.222 (2017).

22 Lu, X. Y., Yang, J. M. & Yin, X. Z. Propulsive performance and vortex shedding of a foil in flapping flight. *Acta Mechanica* **165**, 189-206, doi:10.1007/s00707-003-0013-x (2003).

23 Depecker, M., Broin, F. d. L. d., Renous, S., Davenport, J. & Bels, V. in *Biology of Turtles* 97-138 (2007).

24 Renous, S. & Bels, V. Comparison between aquatic and terrestrial locomotions of the leatherback sea turle (Dermochelys coriacea). *Journal of Zoology* **230**, 357-378 (1993).

25 Renous, S., Bels, V. & Davenport, J. Locomotion in marine Chelonia: Adaptation to the aquatic habitat. *Historical Biology* **14**, 1-13, doi:10.1080/10292380009380549 (2000).

26 Rivera, A. R., Rivera, G. & Blob, R. W. Forelimb kinematics during swimming in the pig-nosed turtle, Carettochelys insculpta, compared with other turtle taxa: rowing versus flapping, convergence versus intermediacy. *J Exp Biol* **216**, 668-680, doi:10.1242/jeb.079715 (2013).
27 Rivera, A. R. V., Wyneken, J. & Blob, R. W. Forelimb kinematics and motor patterns of swimming loggerhead sea turtles (Caretta caretta): are motor patterns conserved in the evolution of new locomotor strategies? *J. Exp. Biol.* **214**, 3314-3323, doi:10.1242/jeb.057364 (2011).
28 Yasuda, T. & Arai, N. Changes in flipper beat frequency, body angle and swimming speed of female green turtles Chelonia mydas. *Marine Ecology Progress Series* **386**, 275-286, doi:10.3354/meps08084 (2009).
29 Bjorndal, K. A. Nutritional Ecology of Sea Turtles. *Copeia* **1985**, 736-751, doi:10.2307/1444767 (1985).
30 Bjorndal, K. A. in *The biology of sea turtles* 199-231 (CRC press, 2017).
31 Díaz-Abad, L. *et al.* eDNA metabarcoding for diet analyses of green sea turtles (Chelonia mydas). *Marine Biology* **169**, doi:10.1007/s00227-021-04002-x (2021).
32 Howell, L. N. & Shaver, D. J. Foraging Habits of Green Sea Turtles (Chelonia mydas) in the Northwestern Gulf of Mexico. *Frontiers in Marine Science* **8**, doi:10.3389/fmars.2021.658368 (2021).
33 McDermid, K., Stuercke, B. & Balazs, G. Nutritional composition of marine plants in the diet of the green sea turtle (Chelonia mydas) in the Hawaiian Islands. *Bulletin of Marine Science* **81**, 55-71 (2007).
34 Kinoshita, C., Fukuoka, T., Narazaki, T., Niizuma, Y. & Sato, K. Analysis of why sea turtles swim slowly: a metabolic and mechanical approach. *J Exp Biol* **224**, doi:10.1242/jeb.236216 (2021).
35 Davari, A. R. Wake structure and similar behavior of wake profiles downstream of a plunging airfoil. *Chinese Journal of Aeronautics* **30**, 1281-1293, doi:10.1016/j.cja.2017.05.007 (2017).
36 Hedenström, A. A general law for animal locomotion? *Trends in Ecology & Evolution* **19**, 217-219, doi:10.1016/j.tree.2004.02.005 (2004).
37 Khalid, M. S. U., Wang, J., Dong, H. & Liu, M. Flow transitions and mapping for undulating swimmers. *Physical Review Fluids* **5**, 063104, doi:10.1103/PhysRevFluids.5.063104 (2020).
38 Lentink, D., Muijres, F. T., Donker-Duyvis, F. J. & van Leeuwen, J. L. Vortex-wake interactions of a flapping foil that models animal swimming and flight. *J Exp Biol* **211**, 267-273, doi:10.1242/jeb.006155 (2008).
39 Rayner, J. M. Dynamics of the vortex wakes of flying and swimming vertebrates. *Symp Soc Exp Biol* **49**, 131-155 (1995).
40 Sohn, S.-I. A computational model of the swimming dynamics of a fish-like body in two dimensions. *Phys. Fluids* **33**, doi:10.1063/5.0070258 (2021).
41 Birch, J. M. & Dickinson, M. H. Spanwise flow and the attachment of the leading-edge vortex on insect wings. *Nature* **412**, 729-733, doi:10.1038/35089071 (2001).
42 Johansson, L. C., Engel, S., Kelber, A., Heerenbrink, M. K. & Hedenstrom, A. Multiple leading edge vortices of unexpected strength in freely flying hawkmoth. *Sci Rep* **3**, 3264, doi:10.1038/srep03264 (2013).
43 Nabawy, M. R. A. & Crowther, W. J. The role of the leading edge vortex in lift augmentation of steadily revolving wings: a change in perspective. *J R Soc Interface* **14**, doi:10.1098/rsif.2017.0159 (2017).
44 Menzer, A., Gong, Y., Fish, F. E. & Dong, H. Bio-Inspired Propulsion: Towards Understanding the Role of Pectoral Fin Kinematics in Manta-like Swimming. *Biomimetics (Basel)* **7**, doi:10.3390/biomimetics7020045 (2022).
45 Videler, J. J., Stamhuis, E. J. & Povel, G. D. E. Leading-Edge Vortex Lifts Swifts. *Science* **306**, 1960-1962, doi:doi:10.1126/science.1104682 (2004).
46 Bottom Ii, R. G., Borazjani, I., Blevins, E. L. & Lauder, G. V. Hydrodynamics of swimming in stingrays: numerical simulations and the role of the leading-edge vortex. *Journal of Fluid Mechanics* **788**, 407-443, doi:10.1017/jfm.2015.702 (2016).
47 Lentink, D., Dickson, W. B., van Leeuwen, J. L. & Dickinson, M. H. Leading-Edge Vortices Elevate Lift of Autorotating Plant Seeds. *Science* **324**, 1438-1440, doi:doi:10.1126/science.1174196 (2009).
48 Muijres, F. T. *et al.* Leading-Edge Vortex Improves Lift in Slow-Flying Bats. *Science* **319**, 1250-1253, doi:doi:10.1126/science.1153019 (2008).
49 Chen, L., Bi, S., Cai, Y., Cao, Y. & Pan, G. Design and Experimental Research on a Bionic Robot Fish with Tri-Dimensional Soft Pectoral Fins Inspired by Cownose Ray. *Journal of Marine Science and Engineering* **10**, doi:10.3390/jmse10040537 (2022).
50 Kashi, E., Kulkarni, A. A., Perrotta, G. & Leftwich, M. C. Flowfields produced by a robotic sea lion foreflipper starting from rest. *Bioinspir Biomim* **15**, 035002, doi:10.1088/1748-3190/ab6a62 (2020).

51 Kawamura, Y. in *2010 International Conference on Broadband, Wireless Computing, Communication and Applications.* 755-759.
52 Liu, Q. *et al.* A Manta Ray Robot with Soft Material Based Flapping Wing. *Journal of Marine Science and Engineering* **10**, doi:10.3390/jmse10070962 (2022).
53 Niikura, A. *et al.* Giraffe Neck Robot: First Step Toward a Powerful and Flexible Robot Prototyping Based on Giraffe Anatomy. *IEEE Robotics and Automation Letters* **7**, 3539-3546, doi:10.1109/LRA.2022.3146611 (2022).
54 Xie, H. *et al.* A Motion Generation Strategy of Robotic Rat Using Imitation Learning for Behavioral Interaction. *IEEE Robotics and Automation Letters* **7**, 7351-7358, doi:10.1109/LRA.2022.3182472 (2022).
55 Baines, R. *et al.* Multi-environment robotic transitions through adaptive morphogenesis. *Nature* **610**, 283-289, doi:10.1038/s41586-022-05188-w (2022).
56 Haomachai, W., Teerakittikul, P. & Ieee. *An Artificial Hormone System for Adaptable Locomotion in a Sea Turtle-Inspired Robot*. (2019).
57 Jansen, A., Luck, K. S., Campbell, J., Amor, H. B. & Aukes, D. M. in *Biomimetic and Biohybrid Systems.* (eds Michael Mangan *et al.*) 216-229 (Springer International Publishing).
58 Kim, H.-J., Song, S.-H. & Ahn, S.-H. A turtle-like swimming robot using a smart soft composite (SSC) structure. *Smart Materials and Structures* **22**, doi:10.1088/0964-1726/22/1/014007 (2013).
59 Mazouchova, N., Umbanhowar, P. B. & Goldman, D. I. Flipper-driven terrestrial locomotion of a sea turtle-inspired robot. *Bioinspiration & Biomimetics* **8**, doi:10.1088/1748-3182/8/2/026007 (2013).
60 Song, S.-H. *et al.* Turtle mimetic soft robot with two swimming gaits. *Bioinspiration & Biomimetics* **11**, doi:10.1088/1748-3190/11/3/036010 (2016).
61 Yan, Y. *et al.* in *2022 IEEE International Conference on Mechatronics and Automation (ICMA)* 493-498 (2022).
62 Jansen, A., Luck, K. S., Campbell, J., Amor, H. B. & Aukes, D. M. 216-229 (Springer International Publishing).
63 Siegenthaler, C., Pradalier, C., Gunther, F., Hitz, G. & Siegwart, R. in *2013 Ieee/Rsj International Conference on Intelligent Robots and Systems IEEE International Conference on Intelligent Robots and Systems* (ed N. Amato) 3790-3795 (2013).
64 Gorissen, B. *et al.* Elastic Inflatable Actuators for Soft Robotic Applications. *Advanced Materials* **29**, 1604977, doi:https://doi.org/10.1002/adma.201604977 (2017).
65 Yang, Y., Wu, Y., Li, C., Yang, X. & Chen, W. Flexible Actuators for Soft Robotics. *Advanced Intelligent Systems* **2**, 1900077, doi:https://doi.org/10.1002/aisy.201900077 (2020).
66 Zhou, D., Zuo, W., Tang, X., Deng, J. & Liu, Y. A multi-motion bionic soft hexapod robot driven by self-sensing controlled twisted artificial muscles. *Bioinspir Biomim* **16**, doi:10.1088/1748-3190/ac0121 (2021).
67 Kim, H. S., Heo, J. K., Choi, I. G., Ahn, S. H. & Chu, W. S. Shape memory alloy-driven undulatory locomotion of a soft biomimetic ray robot. *Bioinspir Biomim* **16**, doi:10.1088/1748-3190/ac03bc (2021).
68 Shen, Q. *et al.* Basic design of a biomimetic underwater soft robot with switchable swimming modes and programmable artificial muscles. *Smart Materials and Structures* **29**, doi:10.1088/1361-665X/ab6fe8 (2020).
69 Luo, B., Cui, W. & Li, W. Active and Robust Twisting Morphing Wings With Geometric Constraints for Flying or Swimming Robots. *IEEE ASME Trans Mechatron*, 1-6, doi:10.1109/tmech.2021.3137951 (2022).
70 Pham, N. K. & Peraza Hernandez, E. A. Modeling and Design Exploration of a Tensegrity-Based Twisting Wing. *J. Mech. Robot.* **13**, doi:10.1115/1.4050149 (2021).
71 Cieri, R. L., Hatch, S. T., Capano, J. G. & Brainerd, E. L. Locomotor rib kinematics in two species of lizards and a new hypothesis for the evolution of aspiration breathing in amniotes. *Sci Rep* **10**, 7739, doi:10.1038/s41598-020-64140-y (2020).
72 Weller, H. I. *et al.* An XROMM Study of Food Transport and Swallowing in Channel Catfish. *Integr Org Biol* **2**, obaa018, doi:10.1093/iob/obaa018 (2020).
73 Smolowitz, R. J., Patel, S. H., Haas, H. L. & Miller, S. A. Using a remotely operated vehicle (ROV) to observe loggerhead sea turtle (Caretta caretta) behavior on foraging grounds off the mid-Atlantic United States. *J. Exp. Mar. Biol. Ecol.* **471**, 84-91, doi:https://doi.org/10.1016/j.jembe.2015.05.016 (2015).
74 Maki, T., Horimoto, H., Ishihara, T. & Kofuji, K. Tracking a Sea Turtle by an AUV with a Multibeam Imaging Sonar: Toward Robotic Observation of Marine Life. *International Journal of Control, Automation and Systems* **18**, 597-604, doi:10.1007/s12555-019-0690-4 (2020).

75 Prange, H. D. Energetics of swimming of a sea turtle. *J. Exp. Biol.* **64**, 1-12, doi:10.1242/jeb.64.1.1 (1976).
76 Watanabe, Y. Y. *et al.* Scaling of swim speed in breath-hold divers. *J Anim Ecol* **80**, 57-68, doi:10.1111/j.1365-2656.2010.01760.x (2011).
77 Narazaki, T., Sato, K., Abernathy, K. J., Marshall, G. J. & Miyazaki, N. Sea turtles compensate deflection of heading at the sea surface during directional travel. *J Exp Biol* **212**, 4019-4026, doi:10.1242/jeb.034637 (2009).
78 Narazaki, T., Sato, K., Abernathy, K. J., Marshall, G. J. & Miyazaki, N. Loggerhead turtles (Caretta caretta) use vision to forage on gelatinous prey in mid-water. *PLoS One* **8**, e66043, doi:10.1371/journal.pone.0066043 (2013).
79 Hays, G. C., Metcalfe, J. D., Walne, A. W. & Wilson, R. P. First records of flipper beat frequency during sea turtle diving. *J. Exp. Mar. Biol. Ecol.* **303**, 243-260, doi:10.1016/j.jembe.2003.11.010 (2004).
80 Wilme, L., Waeber, P. O. & Ganzhorn, J. U. Marine turtles used to assist Austronesian sailors reaching new islands. *C R Biol* **339**, 78-82, doi:10.1016/j.crvi.2015.12.001 (2016).
81 Chin, D. D. & Lentink, D. Birds repurpose the role of drag and lift to take off and land. *Nat Commun* **10**, 5354, doi:10.1038/s41467-019-13347-3 (2019).
82 Henningsson, P., Hedenstrom, A. & Bomphrey, R. J. Efficiency of lift production in flapping and gliding flight of swifts. *PLoS One* **9**, e90170, doi:10.1371/journal.pone.0090170 (2014).
83 Iosilevskii, G. Centre-of-mass and minimal speed limits of the great hammerhead. *Royal Society Open Science* **7**, 200864, doi:doi:10.1098/rsos.200864 (2020).
84 van der Geest, N., Garcia, L., Nates, R. & Godoy, D. A. New insight into the swimming kinematics of wild Green sea turtles (Chelonia mydas). *Scientific Reports* **12**, 18151, doi:10.1038/s41598-022-21459-y (2022).
85 Bandyopadhyay, P. R., Beal, D. N., Hrubes, J. D. & Mangalam, A. Relationship of roll and pitch oscillations in a fin flapping at transitional to high Reynolds numbers. *Journal of Fluid Mechanics* **702**, doi:10.1017/jfm.2012.178 (2012).
86 Carr, Z. R., Chen, C. & Ringuette, M. J. Finite-span rotating wings: three-dimensional vortex formation and variations with aspect ratio. *Experiments in Fluids* **54**, doi:10.1007/s00348-012-1444-8 (2013).
87 Firat, E., Ozkan, G. M. & Akilli, H. Flow past a hollow cylinder with two spanwise rows of holes. *Experiments in Fluids* **60**, doi:10.1007/s00348-019-2814-2 (2019).
88 Kartheeswaran, A., Jothi, T. J. S. & Arackal, R. S. Visualisation studies on plane jets at low Reynolds numbers. *Sādhanā* **46**, doi:10.1007/s12046-021-01568-6 (2021).
89 Todd Jones, T. *et al.* Calculating the ecological impacts of animal-borne instruments on aquatic organisms. *Methods in Ecology and Evolution* **4**, 1178-1186, doi:10.1111/2041-210x.12109 (2013).
90 Sato, K. Body temperature stability achieved by the large body mass of sea turtles. *J Exp Biol* **217**, 3607-3614, doi:10.1242/jeb.109470 (2014).
91 Eguchi, T. *et al.* Morphology and Growth Rates of the Green Sea Turtle (Chelonia mydas) in a Northern-most Temperate Foraging Ground. *Herpetologica* **68**, 76-87, doi:10.1655/herpetologica-d-11-00050.1 (2012).
92 Chaloupka, M. & Limpus, C. Estimates of sex- and age-class-specific survival probabilities for a southern Great Barrier Reef green sea turtle population. *Marine Biology* **146**, 1251-1261, doi:10.1007/s00227-004-1512-6 (2004).
93 Goshe, L. R., Avens, L., Scharf, F. S. & Southwood, A. L. Estimation of age at maturation and growth of Atlantic green turtles (Chelonia mydas) using skeletochronology. *Marine Biology* **157**, 1725-1740, doi:10.1007/s00227-010-1446-0 (2010).
94 Hou, T. *et al.* in *2019 IEEE International Conference on Robotics and Biomimetics (ROBIO).* 1020-1026.
95 van der Geest, N., Garcia, L., Nates, R. & Gonzalez-Vazquez, A. Sea Turtles Employ Drag-Reducing Techniques to Conserve Energy. *Journal of Marine Science and Engineering* **10**, 1770, doi:https://doi.org/10.3390/jmse10111770 (2022).
96 Gorissen, B. *et al.* Elastic inflatable actuators for soft robotic applications. *Advanced Materials* **29**, 1604977 (2017).
97 Zhou, D., Zuo, W., Tang, X., Deng, J. & Liu, Y. A multi-motion bionic soft hexapod robot driven by self-sensing controlled twisted artificial muscles. *Bioinspiration & Biomimetics* **16**, 045003 (2021).
98 Eloy, C. Optimal Strouhal number for swimming animals. *Journal of Fluids and Structures* **30**, 205-218, doi:https://doi.org/10.1016/j.jfluidstructs.2012.02.008 (2012).
99 Triantafyllou, G. S., Triantafyllou, M. S. & Grosenbaugh, M. A. Optimal Thrust Development in Oscillating Foils with Application to Fish Propulsion. *Journal of Fluids and Structures* **7**, 205-224, doi:https://doi.org/10.1006/jfls.1993.1012 (1993).

100 Taylor, G. K., Nudds, R. L. & Thomas, A. L. R. Flying and swimming animals cruise at a Strouhal number tuned for high power efficiency. *Nature* **425**, 707-711, doi:10.1038/nature02000 (2003).
101 Liu, H., Kolomenskiy, D., Nakata, T. & Li, G. Unsteady bio-fluid dynamics in flying and swimming. *Acta Mechanica Sinica* **33**, 663-684, doi:10.1007/s10409-017-0677-4 (2017).
102 Heaslip, S. G., Iverson, S. J., Bowen, W. D. & James, M. C. Jellyfish Support High Energy Intake of Leatherback Sea Turtles (Dermochelys coriacea): Video Evidence from Animal-Borne Cameras. *PLOS ONE* **7**, e33259, doi:10.1371/journal.pone.0033259 (2012).
103 Alerstam, T., Hedenström, A. & Åkesson, S. Long-distance migration: evolution and determinants. *Oikos* **103**, 247-260, doi:https://doi.org/10.1034/j.1600-0706.2003.12559.x (2003).
104 van der Geest, N., Garcia, L., Borret, F., Nates, R. & Gonzalez, A. Soft-robotic green sea turtle (Chelonia mydas) developed to replace animal experimentation provides new insight into their propulsive strategies. *Sci Rep* **13**, 11983, doi:10.1038/s41598-023-37904-5 (2023).
105 Birch, J. M. & Dickinson, M. H. in *Macmillan Magazines Ltd* (2001).
106 Liu, Y. *et al.* Biomimetic Robotic Sea Lion Foreflippers: Design, Modeling, and Experimentation. *IEEE ASME Trans Mechatron* **27**, 5679-5689, doi:10.1109/tmech.2022.3187014 (2022).
107 Nguyen, D. Q. & Ho, V. A. Anguilliform Swimming Performance of an Eel-Inspired Soft Robot. *Soft Robot* **9**, 425-439, doi:10.1089/soro.2020.0093 (2022).
108 Kwak, B., Choi, S. & Bae, J. Development of a Stiffness-Adjustable Articulated Paddle and its Application to a Swimming Robot. *Advanced Intelligent Systems* **5**, doi:10.1002/aisy.202200348 (2023).
109 Berlinger, F., Saadat, M., Haj-Hariri, H., Lauder, G. V. & Nagpal, R. Fish-like three-dimensional swimming with an autonomous, multi-fin, and biomimetic robot. *Bioinspiration & Biomimetics* **16**, 026018, doi:10.1088/1748-3190/abd013 (2021).
110 Bujard, T., Giorgio-Serchi, F. & Weymouth, G. D. A resonant squid-inspired robot unlocks biological propulsive efficiency. *Science Robotics* **6**, eabd2971, doi:doi:10.1126/scirobotics.abd2971 (2021).
111 Lu, B., Zhou, C., Wang, J., Zhang, Z. & Tan, M. Toward Swimming Speed Optimization of a Multi-Flexible Robotic Fish With Low Cost of Transport. *IEEE Transactions on Automation Science and Engineering*, 1-12, doi:10.1109/tase.2023.3269775 (2023).
112 Zhu, J. *et al.* Tuna robotics: A high-frequency experimental platform exploring the performance space of swimming fishes. *Science Robotics* **4**, eaax4615, doi:doi:10.1126/scirobotics.aax4615 (2019).
113 White, C. H., Lauder, G. V. & Bart-Smith, H. Tunabot Flex: a tuna-inspired robot with body flexibility improves high-performance swimming. *Bioinspir Biomim* **16**, doi:10.1088/1748-3190/abb86d (2021).
114 Wang, T. *et al.* A versatile jellyfish-like robotic platform for effective underwater propulsion and manipulation. *Sci Adv* **9**, eadg0292, doi:10.1126/sciadv.adg0292 (2023).
115 Gurka, R., Nafi, A. S. & Weihs, D. On an adaptation of the Reynolds number, applicable to body-caudal-fin aquatic locomotion. *Frontiers in Marine Science* **9**, doi:10.3389/fmars.2022.914214 (2022).
116 Carr, L. W. & Chandrasekhara, M. S. Compressibility effects on dynamic stall. *Progress in Aerospace Sciences* **32**, 523-573, doi:https://doi.org/10.1016/0376-0421(95)00009-7 (1996).
117 Garibaldi, A. & Turner, N. Cultural Keystone Species
Implications for Ecological Conservation and Restoration. *Ecology and Society* **9** (2004).
118 Coleman, F. C. & Williams, S. L. Overexploiting marine ecosystem engineers: potential consequences for biodiversity. *Trends in Ecology & Evolution* **17**, 40-44, doi:https://doi.org/10.1016/S0169-5347(01)02330-8 (2002).
119 Hannan, L. B., Roth, J. D., Ehrhart, L. M. & Weishampel, J. F. DUNE VEGETATION FERTILIZATION BY NESTING SEA TURTLES. *Ecology* **88**, 1053-1058, doi:https://doi.org/10.1890/06-0629 (2007).
120 Houghton, J. D. R., Doyle, T. K., Wilson, M. W., Davenport, J. & Hays, G. C. JELLYFISH AGGREGATIONS AND LEATHERBACK TURTLE FORAGING PATTERNS IN A TEMPERATE COASTAL ENVIRONMENT. *Ecology* **87**, 1967-1972, doi:https://doi.org/10.1890/0012-9658(2006)87[1967:JAALTF]2.0.CO;2 (2006).
121 Martins, R. F. *et al.* Niche partitioning between sea turtles in waters of a protected tropical island. *Regional Studies in Marine Science* **39**, doi:10.1016/j.rsma.2020.101439 (2020).
122 Davic, R. D. Linking Keystone Species and Functional Groups
A New Operational Definition of the Keystone Species Concept. *Conservation Ecology* **7** (2003).
123 Lawton, J. H. & Jones, C. G. in *Linking Species & Ecosystems* (eds Clive G. Jones & John H. Lawton) 141-150 (Springer US, 1995).
124 Tisdell, C. & Wilson, C. Ecotourism for the survival of sea turtles and other wildlife. *Biodiversity & Conservation* **11**, 1521-1538, doi:10.1023/A:1016833300425 (2002).

125 Lewison, R. L. & Crowder, L. B. Putting longline bycatch of sea turtles into perspective. *Conserv Biol* **21**, 79-86, doi:10.1111/j.1523-1739.2006.00592.x (2007).
126 Stelfox, M., Bulling, M. & Sweet, M. Untangling the origin of ghost gear within the Maldivian archipelago and its impact on olive ridley (Lepidochelys olivacea) populations. *Endangered Species Research* **40**, 309-320, doi:10.3354/esr00990 (2019).
127 Davenport, J. Temperature and the life-history strategies of sea turtles. *Journal of Thermal Biology* **22**, 479-488, doi:https://doi.org/10.1016/S0306-4565(97)00066-1 (1997).
128 Sun, X. *et al.* Three-dimensional Hydrodynamic Analysis of Forelimb Propulsion of Sea Turtle With Prosthetic Flippers. *Journal of Aero Aqua Bio-mechanisms* **3**, 36-44, doi:10.5226/jabmech.3.36 (2013).
129 Ayub, R., Villarreal, D., Gregg, R. D. & Gao, F. Evaluation of transradial body-powered prostheses using a robotic simulator. *Prosthet Orthot Int* **41**, 194-200, doi:10.1177/0309364616650077 (2017).
130 Caputo, J. M. & Collins, S. H. in *2013 IEEE International Conference on Robotics and Automation.* 2645-2650.
131 Kashef, S. R., Amini, S. & Akbarzadeh, A. Robotic hand: A review on linkage-driven finger mechanisms of prosthetic hands and evaluation of the performance criteria. *Mechanism and Machine Theory* **145**, doi:10.1016/j.mechmachtheory.2019.103677 (2020).
132 Vayssette, B., Saintier, N., Brugger, C., Elmay, M. & Pessard, E. Surface roughness of Ti-6Al-4V parts obtained by SLM and EBM: Effect on the High Cycle Fatigue life. *Procedia Engineering* **213**, 89-97, doi:https://doi.org/10.1016/j.proeng.2018.02.010 (2018).
133 Pilliar, R. M., Cameron, H. U., Binnington, A. G., Szivek, J. & Macnab, I. Bone ingrowth and stress shielding with a porous surface coated fracture fixation plate. *Journal of Biomedical Materials Research* **13**, 799-810, doi:https://doi.org/10.1002/jbm.820130510 (1979).
134 Jafari Chashmi, M. *et al.* Design and Analysis of Porous Functionally Graded Femoral Prostheses with Improved Stress Shielding. *Designs* **4**, doi:10.3390/designs4020012 (2020).
135 Arabnejad, S., Johnston, B., Tanzer, M. & Pasini, D. Fully porous 3D printed titanium femoral stem to reduce stress-shielding following total hip arthroplasty. *Journal of Orthopaedic Research* **35**, 1774-1783, doi:https://doi.org/10.1002/jor.23445 (2017).

Appendices

Appendix A: New insights into the swimming kinematics of wild Green sea turtles (*Chelonia mydas*)

Supplementary Figure S1, Swimming patterns from observed turtles, showing the five flipper stages

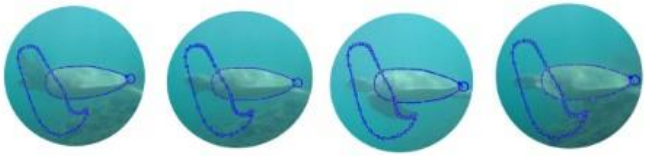

FLAP DURATION (s)	DS (s)	SS (s)	RS1 (s)	US (s)	RS2 (s)
4.3	0.9	0.8	0.9	1.1	0.6

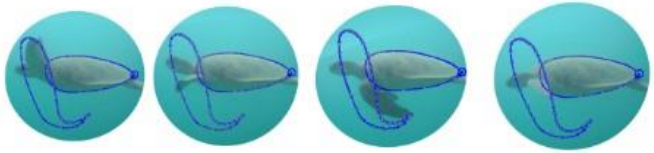

FLAP DURATION (s)	DS (s)	SS (s)	RS1 (s)	US (s)	RS2 (s)
4.2	0.9	0.7	0.8	1.2	0.6

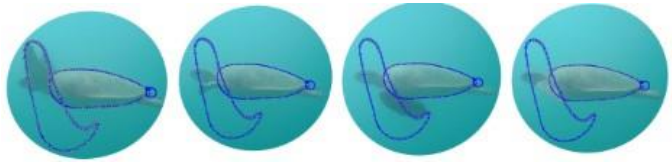

FLAP DURATION (s)	DS (s)	SS (s)	RS1 (s)	US (s)	RS2 (s)
5	1	1	1	1.3	0.7

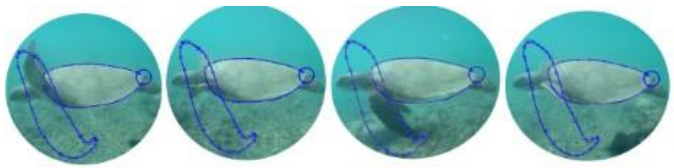

FLAP DURATION (s)	DS (s)	SS (s)	RS1 (s)	US (s)	RS2 (s)
3.9	0.8	0.8	0.7	1.1	0.5

FLAP DURATION (s)	DS (s)	SS (s)	RS1 (s)	US (s)	RS2 (s)
3.7	0.7	0.7	0.8	1.1	0.4

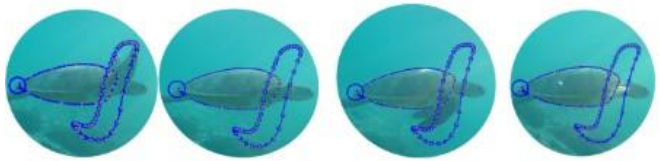

FLAP DURATION (s)	DS (s)	SS (s)	RS1 (s)	US (s)	RS2 (s)
4.4	0.7	0.9	0.7	1.2	0.9

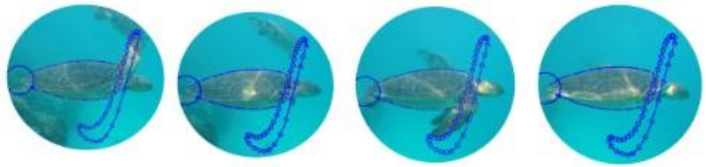

FLAP DURATION (s)	DS (s)	SS (s)	RS1 (s)	US (s)	RS2 (s)
3.9	0.8	0.7	0.7	1.2	0.5

Matlab code to generate swimming kinematic models and animations.

```
clear all
%constants for wing tip

a0x =       117.1;  %Coefficients (with 95% confidence
bounds) (116.9, 117.4)
a1x =      -182.9;  %Coefficients (with 95% confidence
bounds) (-183.3, -182.6)
b1x =       42.63;  %Coefficients (with 95% confidence
bounds) (42.04, 43.23)
a2x =       -13.3; %Coefficients (with 95% confidence
bounds) (-13.72, -12.88)
b2x =      -54.58;  %Coefficients (with 95% confidence
bounds) (-54.93, -54.23)
a3x =       17.38;  %Coefficients (with 95% confidence
bounds) (17.04, 17.73)
b3x =       -8.86;  %Coefficients (with 95% confidence
bounds) (-9.22, -8.5)
a4x =      -5.189;  %Coefficients (with 95% confidence
bounds) (-5.53, -4.848)
b4x =       1.512;  %Coefficients (with 95% confidence
bounds) (1.158, 1.867)
a5x =      -2.687;  %Coefficients (with 95% confidence
bounds) (-3.029, -2.345)
b5x =      -2.955;  %Coefficients (with 95% confidence
bounds) (-3.302, -2.607)
a6x =       2.653;  %Coefficients (with 95% confidence
bounds) (2.31, 2.996)
b6x =      -2.801;  %Coefficients (with 95% confidence
bounds) 3.146, -2.455)
a7x =     -0.3433;  %Coefficients (with 95% confidence
bounds) (-0.6859, -0.0006559)
b7x =       -1.62;  %Coefficients (with 95% confidence
bounds) (-1.965, -1.275)
a8x =    -0.08304;  %Coefficients (with 95% confidence
bounds) (-0.425, 0.2589)
b8x =      -1.225; %Coefficients (with 95% confidence
bounds)  (-1.57, -0.8805)
wx =       1.496;  %Coefficients (with 95% confidence
bounds) (1.495, 1.497)

 a0y =         303;%Coefficients (with 95% confidence
bounds)  (302.6, 303.3)
 a1y =       219.6;%Coefficients (with 95% confidence
bounds)  (219.1, 220.1)
 b1y =      -164.3; %Coefficients (with 95% confidence
bounds)(-165, -163.7)
```

```
 a2y =       84.45; %Coefficients (with 95% confidence
bounds) (83.9, 85)
 b2y =      -65.54; %Coefficients (with 95% confidence
bounds) (-66.06, -65.02)
 a3y =       26.33; %Coefficients (with 95% confidence
bounds) (25.82, 26.83)
 b3y =       45.71; %Coefficients (with 95% confidence
bounds) (45.25, 46.17)
 a4y =      -11.23; %Coefficients (with 95% confidence
bounds)(-11.7, -10.76)
 b4y =       20.05; %Coefficients (with 95% confidence
bounds) (19.58, 20.51)
 a5y =     -0.5956;  %Coefficients (with 95% confidence
bounds)(-1.049, -0.1426)
 b5y =      -2.631;  %Coefficients (with 95% confidence
bounds)(-3.086, -2.177)
 a6y =      -2.667;  %Coefficients (with 95% confidence
bounds)(-3.118, -2.217)
 b6y =      0.6726;  %Coefficients (with 95% confidence
bounds)(0.2169, 1.128)
 a7y =       0.678; %Coefficients (with 95% confidence
bounds) (0.2276, 1.128)
 b7y =     -0.7038; %Coefficients (with 95% confidence
bounds) (-1.158, -0.2495)
 a8y =       2.542; %Coefficients (with 95% confidence
bounds) (2.091, 2.993)
 b8y =     -0.9941; %Coefficients (with 95% confidence
bounds) (-1.45, -0.5381)
 wy =       1.496; %Coefficients (with 95% confidence
bounds) (1.495, 1.497)

a0z =       262.7; %Coefficients (with 95% confidence
bounds) (262.2, 263.2)
a1z =       11.65; %Coefficients (with 95% confidence
bounds) (10.84, 12.46)
b1z =      -63.16; %Coefficients (with 95% confidence
bounds) (-63.81, -62.51)
a2z =      -33.56; %Coefficients (with 95% confidence
bounds) (-34.47, -32.65)
b2z =       82.36; %Coefficients (with 95% confidence
bounds) (81.6, 83.12)
a3z =      -38.04;  %Coefficients (with 95% confidence
bounds)(-38.75, -37.33)
b3z =        23.7;  %Coefficients (with 95% confidence
bounds)(22.93, 24.46)
a4z =      -14.84;  %Coefficients (with 95% confidence
bounds)(-15.5, -14.19)
```

```
b4z =      -8.802;  %Coefficients (with 95% confidence
bounds)(-9.464, -8.14)
a5z =      -7.894; %Coefficients (with 95% confidence
bounds) (-8.537, -7.251)
b5z =       -4.65; %Coefficients (with 95% confidence
bounds) (-5.307, -3.993)
a6z =      -6.884; %Coefficients (with 95% confidence
bounds) (-7.532, -6.236)
b6z =      -6.088; %Coefficients (with 95% confidence
bounds) (-6.757, -5.419)
a7z =       2.615; %Coefficients (with 95% confidence
bounds)(1.972, 3.258)
b7z =      -3.547; %Coefficients (with 95% confidence
bounds) (-4.197, -2.897)
a8z =      -1.716;  %Coefficients (with 95% confidence
bounds)(-2.362, -1.069)
b8z =       1.293; %Coefficients (with 95% confidence
bounds) (0.6416, 1.945)
wz =       1.496; %Coefficients (with 95% confidence
bounds) (1.495, 1.497)

%constants for elbow
a0xe =       54.06; %Coefficients (with 95% confidence
bounds) (53.98, 54.14)
a1xe =      -5.371; %Coefficients (with 95% confidence
bounds) (-5.497, -5.246)
b1xe =      -2.415;  %Coefficients (with 95% confidence
bounds)(-2.539, -2.29)
a2xe =      -3.954;  %Coefficients (with 95% confidence
bounds)(-4.108, -3.8)
b2xe =       -4.81; %Coefficients (with 95% confidence
bounds) (-4.951, -4.67)
a3xe =       -0.15; %Coefficients (with 95% confidence
bounds) (-0.3219, 0.02195)
b3xe =      -4.306; %Coefficients (with 95% confidence
bounds) (-4.428, -4.183)
a4xe =     -0.3527; %Coefficients (with 95% confidence
bounds) (-0.4713, -0.2341)
b4xe =      0.5996;%Coefficients (with 95% confidence
bounds)(0.4677, 0.7315)
a5xe =     -0.3945; %Coefficients (with 95% confidence
bounds) (-0.5205, -0.2685)
b5xe =      0.8514; %Coefficients (with 95% confidence
bounds) (0.7257, 0.9772)
a6xe =       0.203; %Coefficients (with 95% confidence
bounds)(0.06776, 0.3383)
```

```
b6xe =       1.067; %Coefficients (with 95% confidence
bounds) (0.9507, 1.184)
a7xe =     -0.2762; %Coefficients (with 95% confidence
bounds) (-0.3959, -0.1564)
b7xe =      0.4133; %Coefficients (with 95% confidence
bounds) (0.2967, 0.5299)
a8xe =   0.0009741; %Coefficients (with 95% confidence
bounds) (-0.1218, 0.1238)
b8xe =      -0.565; %Coefficients (with 95% confidence
bounds) (-0.6814, -0.4487)
wxe =       1.496; %Coefficients (with 95% confidence
bounds) (1.493, 1.498)

a0ye =       318.1; %Coefficients (with 95% confidence
bounds) (318, 318.2)
a1ye =       30.55; %Coefficients (with 95% confidence
bounds)(30.36, 30.74)
b1ye =      -44.92; %Coefficients (with 95% confidence
bounds) (-45.08, -44.76)
a2ye =       10.14; %Coefficients (with 95% confidence
bounds) (10.01, 10.27)
b2ye =      -5.333; %Coefficients (with 95% confidence
bounds) (-5.458, -5.208)
a3ye =       1.414; %Coefficients (with 95% confidence
bounds) (1.293, 1.534)
b3ye =       2.968;  %Coefficients (with 95% confidence
bounds)(2.847, 3.09)
a4ye =     -0.2397;  %Coefficients (with 95% confidence
bounds)(-0.3597, -0.1196)
b4ye =        1.66;  %Coefficients (with 95% confidence
bounds)(1.538, 1.782)
a5ye =      -0.499;  %Coefficients (with 95% confidence
bounds)(-0.6186, -0.3795)
b5ye =      0.7714; %Coefficients (with 95% confidence
bounds) (0.6502, 0.8926)
a6ye =      -1.155;  %Coefficients (with 95% confidence
bounds)(-1.274, -1.035)
b6ye =    -0.02553;  %Coefficients (with 95% confidence
bounds)(-0.1491, 0.09802)
a7ye =      0.2741; %Coefficients (with 95% confidence
bounds)(0.1543, 0.394)
b7ye =     -0.5696;  %Coefficients (with 95% confidence
bounds)(-0.69, -0.4492)
a8ye =      0.3139;  %Coefficients (with 95% confidence
bounds)(0.1945, 0.4334)
b8ye =     -0.1613; %Coefficients (with 95% confidence
bounds) (-0.2817, -0.04093)
```

```
wye =       1.496;  %Coefficients (with 95% confidence
bounds)(1.495, 1.497)

a0ze =       83.11;%Coefficients (with 95% confidence
bounds)  (83.03, 83.19)
a1ze =      -17.35;%Coefficients (with 95% confidence
bounds)  (-17.46, -17.24)
b1ze =       7.056;%Coefficients (with 95% confidence
bounds)  (6.894, 7.217)
a2ze =     -0.8165; %Coefficients (with 95% confidence
bounds)(-0.9859, -0.6471)
b2ze =       9.892; %Coefficients (with 95% confidence
bounds) (9.787, 9.997)
a3ze =     0.05326; %Coefficients (with 95% confidence
bounds) (-0.0635, 0.17)
b3ze =       2.799;%Coefficients (with 95% confidence
bounds) (2.691, 2.908)
a4ze =     -0.8515;%Coefficients (with 95% confidence
bounds) (-0.9561, -0.7468)
b4ze =      0.5612;%Coefficients (with 95% confidence
bounds) (0.4565, 0.6659)
a5ze =     -0.4952; %Coefficients (with 95% confidence
bounds) (-0.5999, -0.3906)
b5ze =      0.3133;%Coefficients (with 95% confidence
bounds) (0.2086, 0.418)
a6ze =     -0.1586; %Coefficients (with 95% confidence
bounds) (-0.264, -0.05326)
b6ze =      0.3581; %Coefficients (with 95% confidence
bounds) (0.2529, 0.4633)
a7ze =     -0.1013; %Coefficients (with 95% confidence
bounds) (-0.2051, 0.002457)
b7ze =    -0.05005; %Coefficients (with 95% confidence
bounds) (-0.1552, 0.05508)
a8ze =       0.13; %Coefficients (with 95% confidence
bounds) (0.02614, 0.2339)
b8ze =     0.03394; %Coefficients (with 95% confidence
bounds) (-0.07221, 0.1401)
wze =       1.495; %Coefficients (with 95% confidence
bounds) (1.494, 1.497)

%function only defined for time = 0 to 8.4 seconds
time=4.2;
fidelity=1e3;
t=linspace(0,time,fidelity)';

%flipper tip eqautions of motion
```

```
xt =  a0x + a1x*cos(t*wx) + b1x*sin(t*wx) +
a2x*cos(2*t*wx) + b2x*sin(2*t*wx) + a3x*cos(3*t*wx) +
b3x*sin(3*t*wx) + a4x*cos(4*t*wx) + b4x*sin(4*t*wx) +
a5x*cos(5*t*wx) + b5x*sin(5*t*wx) + a6x*cos(6*t*wx) +
b6x*sin(6*t*wx) + a7x*cos(7*t*wx) + b7x*sin(7*t*wx) +
a8x*cos(8*t*wx) + b8x*sin(8*t*wx);
yt =  a0y + a1y*cos(t*wy) + b1y*sin(t*wy) +
a2y*cos(2*t*wy) + b2y*sin(2*t*wy) + a3y*cos(3*t*wy) +
b3y*sin(3*t*wy) + a4y*cos(4*t*wy) + b4y*sin(4*t*wy) +
a5y*cos(5*t*wy) + b5y*sin(5*t*wy) + a6y*cos(6*t*wy) +
b6y*sin(6*t*wy) + a7y*cos(7*t*wy) + b7y*sin(7*t*wy) +
a8y*cos(8*t*wy) + b8y*sin(8*t*wy);
zt =  a0z + a1z*cos(t*wz) + b1z*sin(t*wz) +
a2z*cos(2*t*wz) + b2z*sin(2*t*wz) + a3z*cos(3*t*wz) +
b3z*sin(3*t*wz) + a4z*cos(4*t*wz) + b4z*sin(4*t*wz) +
a5z*cos(5*t*wz) + b5z*sin(5*t*wz) + a6z*cos(6*t*wz) +
b6z*sin(6*t*wz) + a7z*cos(7*t*wz) + b7z*sin(7*t*wz) +
a8z*cos(8*t*wz) + b8z*sin(8*t*wz);

%elbow eqautions of motion
xte =  a0xe + a1xe*cos(t*wxe) + b1xe*sin(t*wxe) +
a2xe*cos(2*t*wxe) + b2xe*sin(2*t*wxe) + a3xe*cos(3*t*wxe)
+ b3xe*sin(3*t*wxe) + a4xe*cos(4*t*wxe) +
b4xe*sin(4*t*wxe) + a5xe*cos(5*t*wxe) + b5xe*sin(5*t*wxe)
+ a6xe*cos(6*t*wxe) + b6xe*sin(6*t*wxe) +
a7xe*cos(7*t*wxe) + b7xe*sin(7*t*wxe) + a8xe*cos(8*t*wxe)
+ b8xe*sin(8*t*wxe);
yte =  a0ye + a1ye*cos(t*wye) + b1ye*sin(t*wye) +
a2ye*cos(2*t*wye) + b2ye*sin(2*t*wye) + a3ye*cos(3*t*wye)
+ b3ye*sin(3*t*wye) + a4ye*cos(4*t*wye) +
b4ye*sin(4*t*wye) + a5ye*cos(5*t*wye) + b5ye*sin(5*t*wye)
+ a6ye*cos(6*t*wye) + b6ye*sin(6*t*wye) +
a7ye*cos(7*t*wye) + b7ye*sin(7*t*wye) + a8ye*cos(8*t*wye)
+ b8ye*sin(8*t*wye);
zte =  a0ze + a1ze*cos(t*wze) + b1ze*sin(t*wze) +
a2ze*cos(2*t*wze) + b2ze*sin(2*t*wze) + a3ze*cos(3*t*wze)
+ b3ze*sin(3*t*wze) + a4ze*cos(4*t*wze) +
b4ze*sin(4*t*wze) + a5ze*cos(5*t*wze) + b5ze*sin(5*t*wze)
+ a6ze*cos(6*t*wze) + b6ze*sin(6*t*wze) +
a7ze*cos(7*t*wze) + b7ze*sin(7*t*wze) + a8ze*cos(8*t*wze)
+ b8ze*sin(8*t*wze);

%origin
Ox=92.518247572;
Oy=305.148699736;
Oz=27.556599226;
```

```
%plot flipper tip path
plot3(xt,yt,zt,'LineWidth',2)
axis square
axis equal
grid on
xlabel('x(t) (mm)')
ylabel('y(t) (mm)')
zlabel('z(t) (mm)')
xlim([-150 350])
ylim([-50 700])
zlim([0 400])
hold on

%plot elbow path
plot3(xte,yte,zte,'LineWidth',2)
axis square
axis equal
grid on
xlabel('x(t) (mm)')
ylabel('y(t) (mm)')
zlabel('z(t) (mm)')
title('turtle motion')

%create point
[sX,sY,sZ] = sphere(10);
r=10;
surf(sX*r+Ox,sY*r+Oy,sZ*r+Oz,'FaceColor',[0.4660 0.6740
0.1880]);

%run flipper animation
loops=5
timedelay=time/fidelity;
for loop=1:loops

for s=1:length(xt)
  p2=plot3([xt(s) xte(s)],[yt(s) yte(s)],[zt(s)
zte(s)],'g','LineWidth',5);
  p1=plot3([Ox xte(s)],[Oy yte(s)],[Oz
zte(s)],'g','LineWidth',5);

h1=surf(sX*r+xt(s),sY*r+yt(s),sZ*r+zt(s),'FaceColor',[0.4
660 0.6740 0.1880]);

h2=surf(sX*r+xte(s),sY*r+yte(s),sZ*r+zte(s),'FaceColor',[
0.4660 0.6740 0.1880]);
  xlim([-150 350]);
  ylim([-50 700]);
```

```
  zlim([0 400]);
  pause(timedelay);
  delete(p1);
  delete(p2);
  delete(h1);
  delete(h2);
end
end
```

Appendix B: Sea Turtles Employ Drag-Reducing Techniques to Conserve Energy.

Supplementary Figure S2 3d printed sea turtle sections.

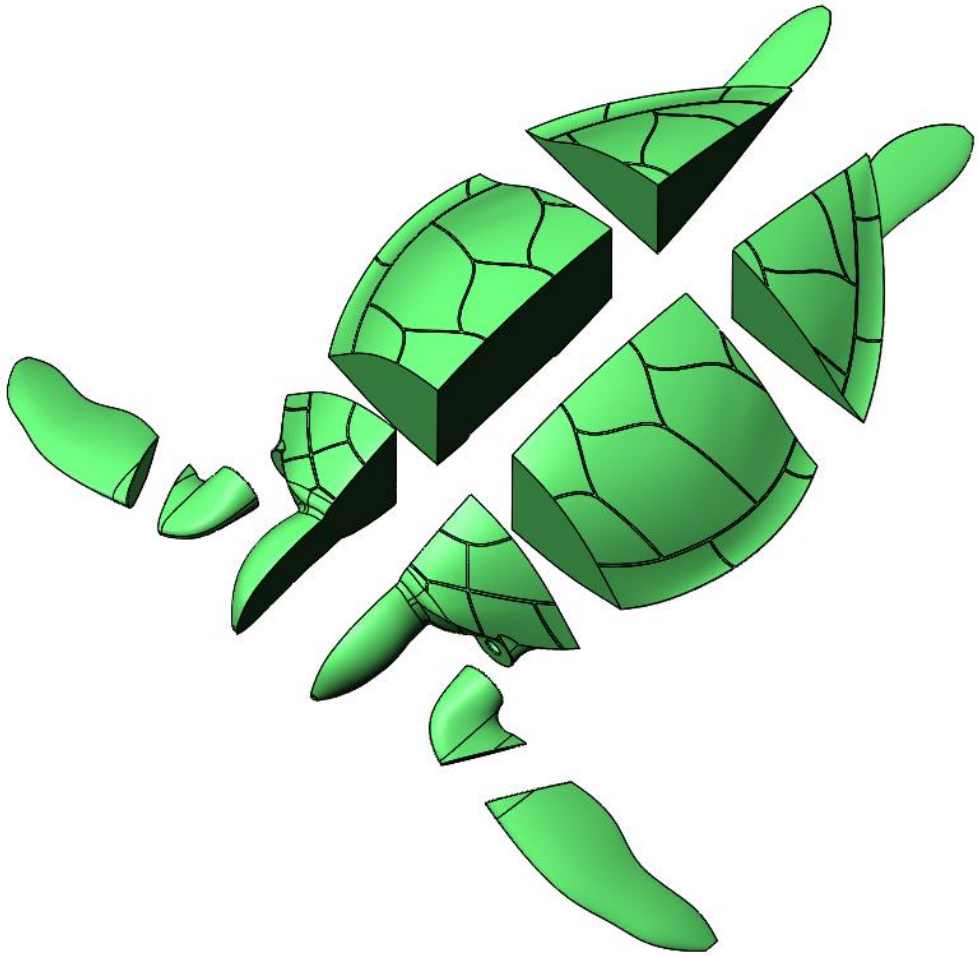

Supplementary Figure S3 3D printed parts surface quality testing. a, testing parallel to flow direction. b, testing perpendicular to flow direction.

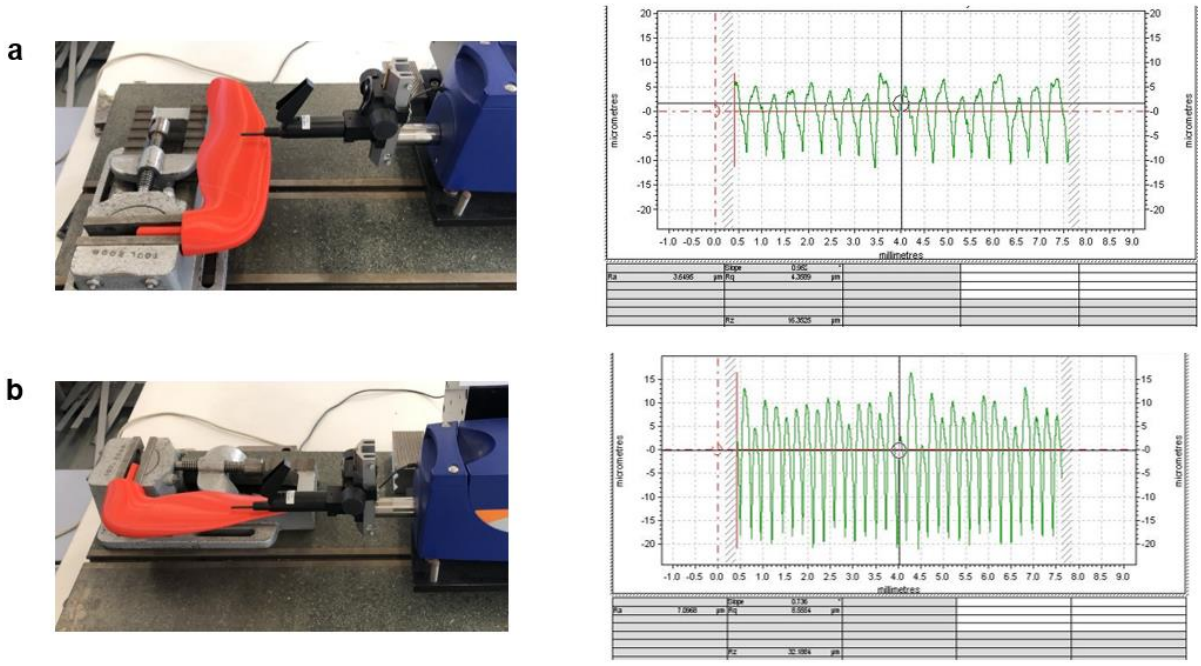

Supplementary Figure S4 lift force Sensitivity study results.

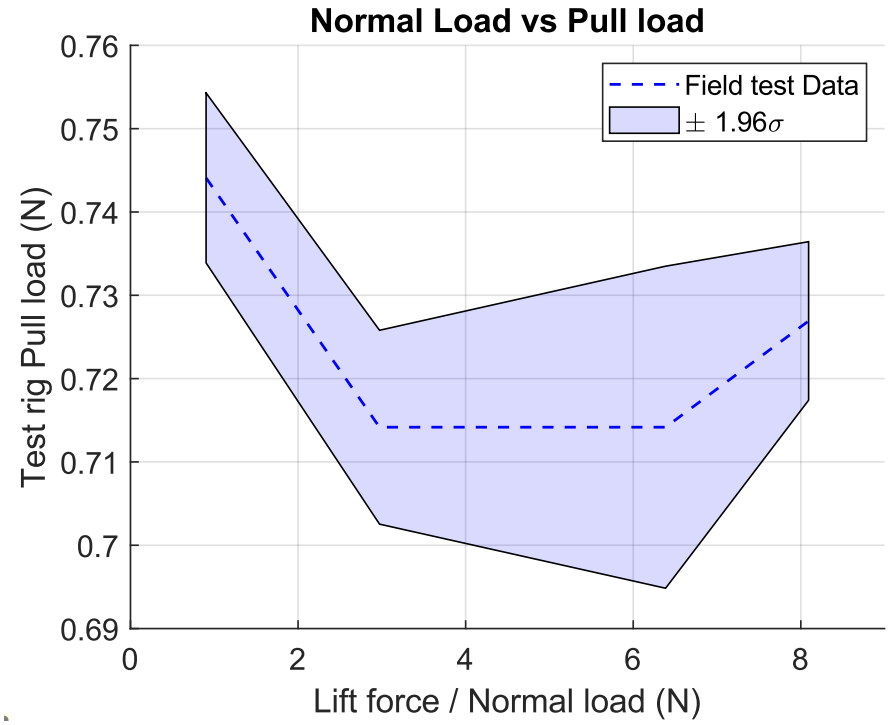

Supplementary Figure S5a Rigid mounted wings demonstrating excessive flow separation.

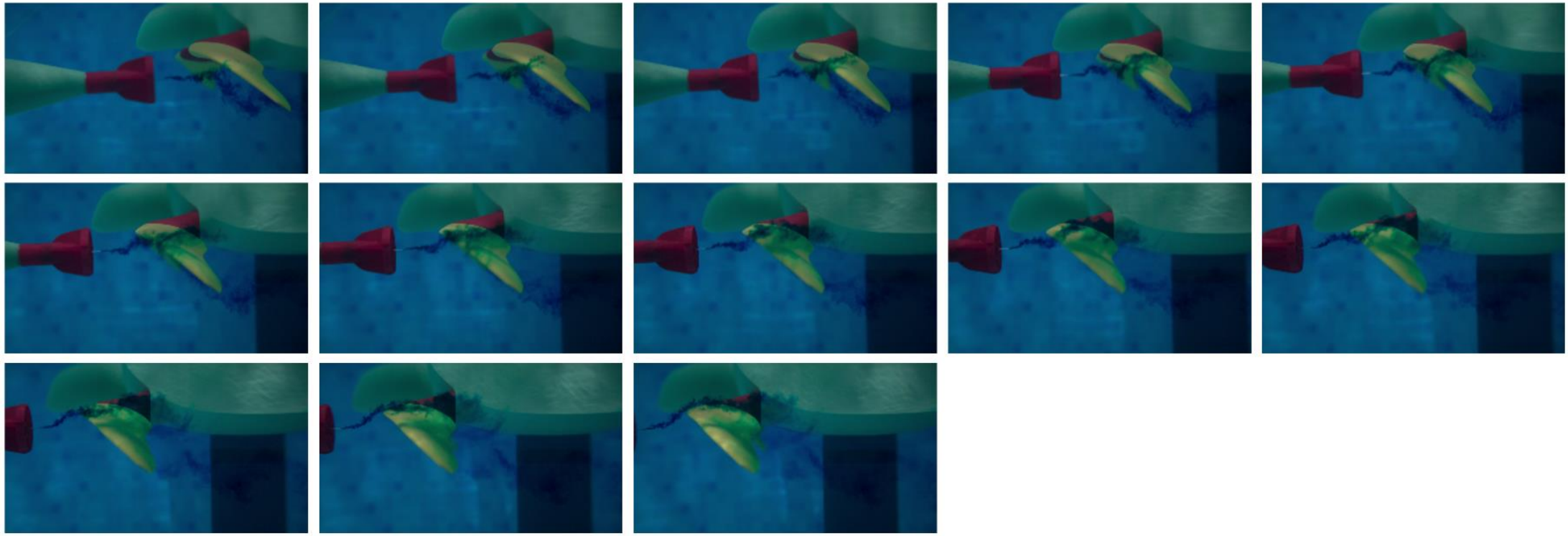

Supplementary Figure S5b Passive mounted wings demonstrating flow attachment across low pressure side.

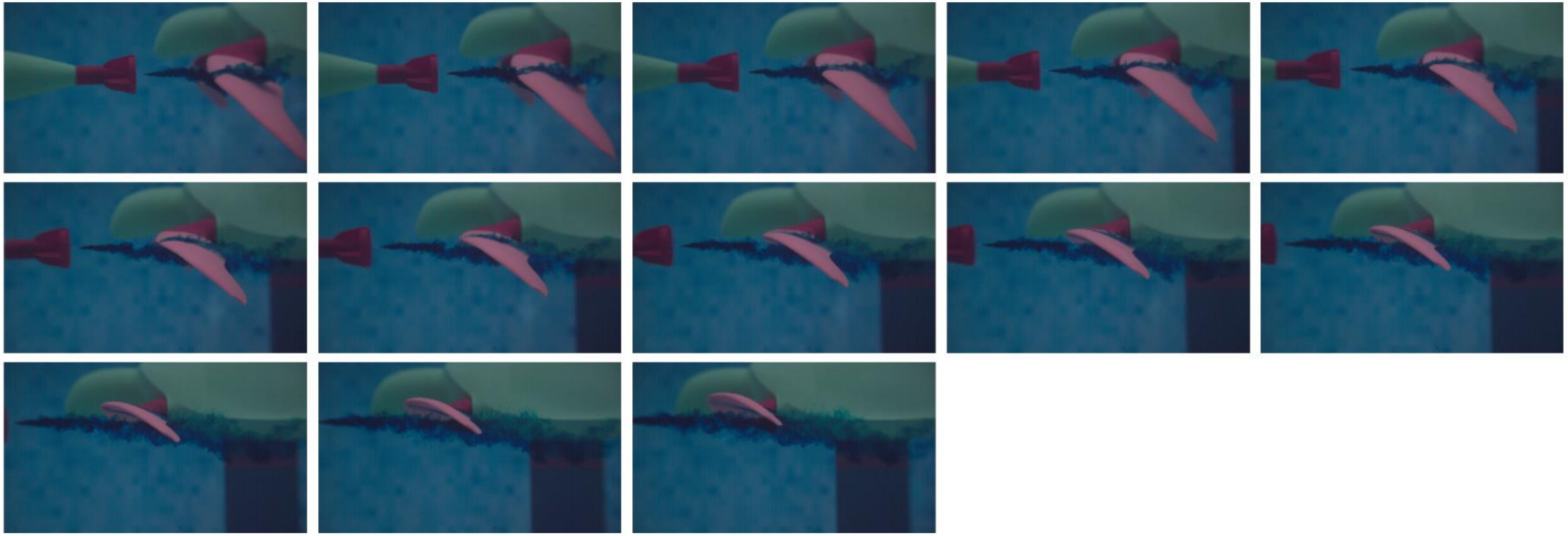

Supplementary Figure S5c Rigid mounted wing demonstrating development of wing tip vortex.

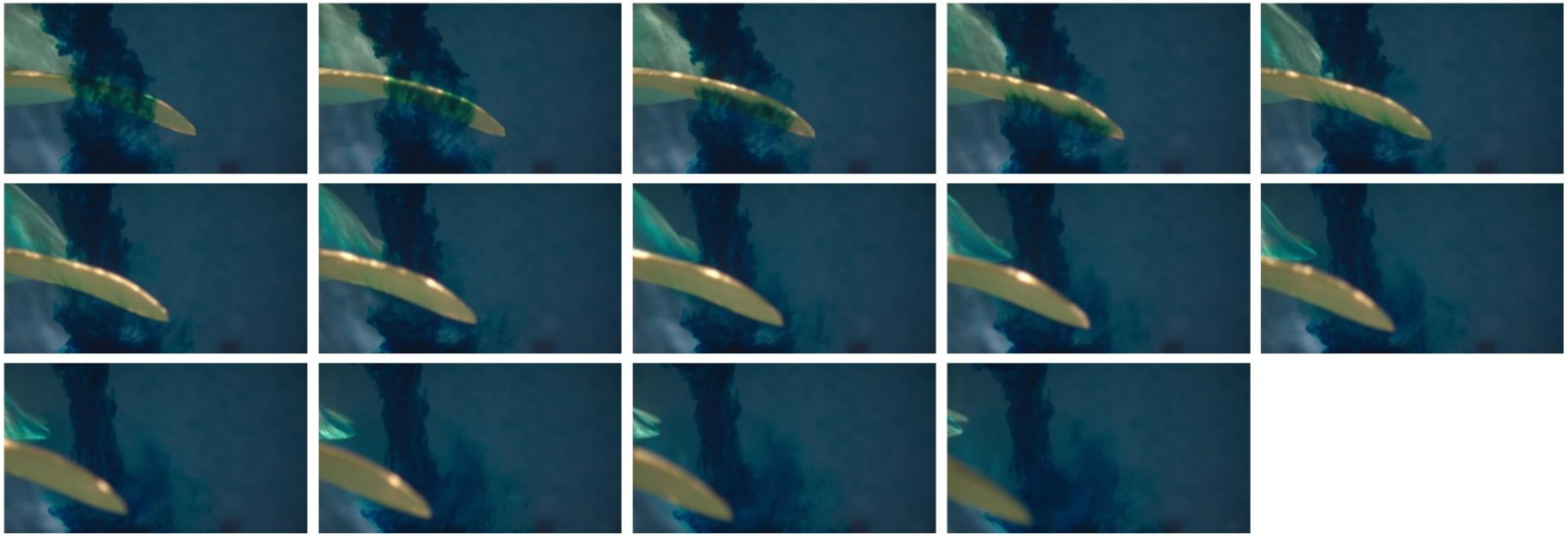

Supplementary Figure S5d Passive wing demonstrating no evidence of wingtip vortex formation.

Supplementary Figure S6 a, computational domain. b, CFD results compared with fielding tests for a rigid mounted wing.

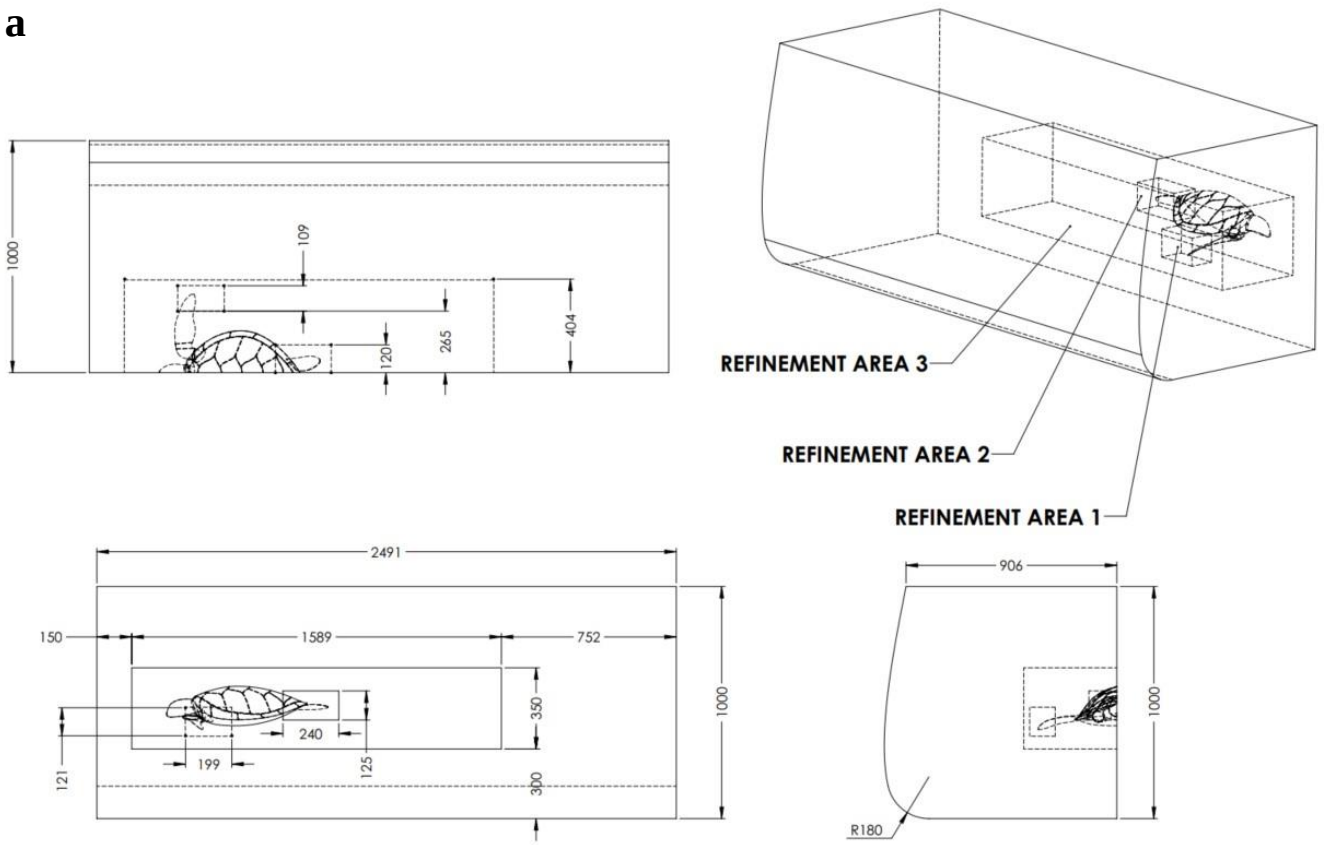

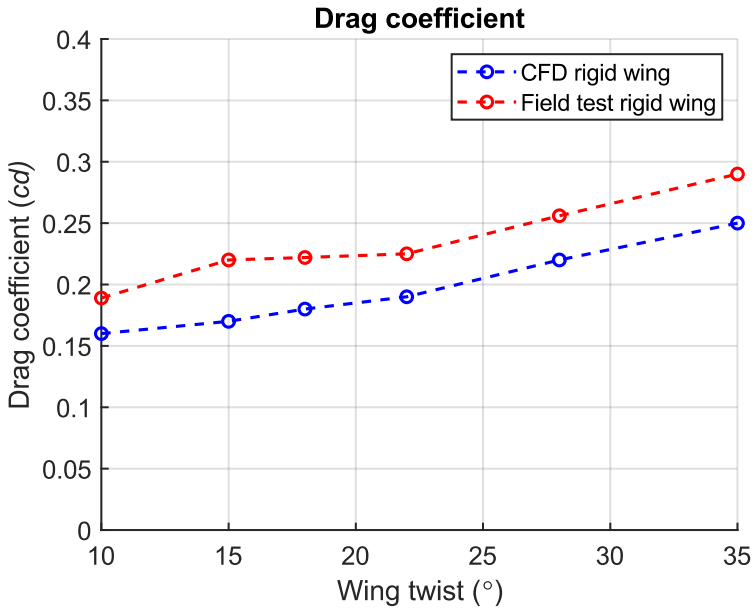

Arduino code to control pully system.

```
/* Program: Variable Stepper Motor
#include <SoftwareSerial.h>
#include <math.h>
const int dirPin = 9;
const int stepPin = 8;
const int steps = 3200;
float rpm = 250.00;
int labview = 0;
char newData;
int microPause = 0;
int turns = 0;
float countSteps = 0;
float radious = 0.0225;
float RPMn = 0;
//float RpmMax;
//float coeff;
//Main Speeds
//Flippers only
float RpmMax=450,coeff=1;
//speed 0.3 m/s @ 127.3rpm
//float RpmMax = 127.3, coeff = 2.52;
//speed 0.45 m/s & 191rpm
//float RpmMax = 191, coeff = 2.91;
//speed 0.6 m/s @ 254.6rpm
//float RpmMax = 254.6, coeff = 3.41;
//speed 0.75 m/s @ 318.25rpm
```

```
//float RpmMax = 318.25, coeff = 4.2;
void setup()
{
  pinMode(dirPin, OUTPUT);
  pinMode(stepPin, OUTPUT);
  Serial.begin(9600); //115200
  // Change Direction of Motor
  digitalWrite(dirPin, LOW); // Away from us
  //digitalWrite(dirPin, HIGH); // Towards us
  //Serial.println("Input s to Turn Motor on, p to off, c to cycle");
  microPause = int(((1.8 / 4) * 60.0) / (rpm * 360.0) * 1000000);
}
void loop()
{
  swimSpeed(); // Function to change the swimming speed of turtle via LABVIEW
  motorSequence(); // Function to provide stepper motor with instructions
}
void swimSpeed()
{
  if (Serial.available())
  {
    labview = Serial.read();
    if (labview == '1')
      digitalWrite(dirPin, LOW);
    if (labview == '0')
      digitalWrite(dirPin, HIGH);
    if (labview == 'p')
      newData = 'p';
```

```
if (labview == 's')
  newData = 's';
if (labview == 'r')
  newData = 'r';
if (labview == 'c')
  newData = 'c';
if (labview == 'x')
{
  long int num = Serial.parseInt();
  switch (num)
  {
    case 1:
      //RpmMax = 63;
      //coeff = 2.26;
      RpmMax = 750;
      coeff = 7.8;
      break;

    case 2:
      RpmMax = 127.3;
      coeff = 2.52;
      break;
    case 3:
      RpmMax = 191;
      coeff = 2.87;
      break;
    case 4:
      RpmMax = 254.6;
```

```
          coeff = 3.365;
          break;
        default:
          // statements
          break;
      }
    }
    if (labview == 'y')
    {
      turns = 0;
      countSteps = 0;
    }
  }
}
void motorSequence()
{
  if (newData == 'p')
  {
    //delay(1000);
    turns = 0;
    countSteps = 0;
  }
  if (newData == 's')
  {
    //Cuadratic
    //RPMn=(6*countSteps*countSteps)/(2*PI*radious);
    //Linear
    RPMn = (60 * 0.8 * countSteps) / (2 * PI * radious);
```

```
  if (RPMn > (RpmMax * coeff))
    RPMn = RpmMax * coeff;
  microPause = int(((1.8 / 4) * 60.0) / (RPMn * 360.0) * 1000000);
  digitalWrite(stepPin, HIGH);
  delayMicroseconds(microPause);
  digitalWrite(stepPin, LOW);
  delayMicroseconds(microPause);
  countSteps = (countSteps + 0.001);
 }
 if (newData == 'r')
 {
  digitalWrite(dirPin, HIGH);
  for (int x = 0; x < steps; x++)
  {
    digitalWrite(stepPin, HIGH);
    delayMicroseconds(microPause);
    digitalWrite(stepPin, LOW);
    delayMicroseconds(microPause);
  }
  turns++;
  Serial.println(turns);
 }
 if (newData == 'c')
 { //twist phase
 }
}
```

Arduino code to control load cells.

```
/* Program: Mutiple Load Cells 2.0
 * Rewritten 06/2022 */
#include "HX711.h"
//HX711 Global Constants (Circuit Wiring)
const int LOADCELL_DOUT_PIN = 3;
const int LOADCELL_SCK_PIN = 2;
const int scale2_DOUT = 11;
const int scale2_SCK = 10;
int labview = 0;
int resultCounter = 0;

HX711 scale, scale2;
void setup()
{
  Serial.begin(9600);
  scale.begin(LOADCELL_DOUT_PIN, LOADCELL_SCK_PIN);
  scale2.begin(scale2_DOUT,scale2_SCK);
  // Calibrate the load cell using a known weight.
  //** DRAG FORCE LOADCELL **
  float calibration = (41900)/(400); // Change calibration value here depending on environment
  scale.set_scale(calibration);
  scale.tare();
  //101.345
  // Calibrate the load cell using a known weight. [approx: 42611 @300g]
  //** LIFT FORCE LOADCELL **
  float calibration2 = (78478)/(700); //22366
```

```
  scale2.set_scale(calibration2);
  scale2.tare();
  // Average of 5 readings from the ADC minus the tare weight, set with tare()
  Serial.println("Setup Values: \t\t");
  Serial.println(scale.get_value(5));
  Serial.println(scale2.get_value(5));
  Serial.println("");
  // Average of 5 readings from the ADC minus tare weight, divided by the SCALE parameter set with set_scale
  Serial.println("Setup Units: \t\t");
  Serial.println(scale.get_units(5), 1);
  Serial.println(scale2.get_units(5), 1);
  Serial.println("");
  Serial.println("Load Cell Readings: ");
  Serial.println("Reading Num, Load Cell 1, Load Cell 2");
}
void loop()
{
  if(Serial.available())
  {
    labview = Serial.read();
    if(labview == '1')
    {
      resultCounter++;
      Serial.print(resultCounter); //Number of Results
      Serial.print(", ");
      Serial.print(scale.get_units(2), 2); // Takes the Average of 2 readings
      Serial.print(", ");
```

```
    Serial.println(scale2.get_units(2), 2); // Takes the Average of 2 readings
   }
   if(labview == '0')
   {
   }
  }
}
```

Arduino code to calibrate load cells.

```
// Program: Load Cell Calibraiton
#include "HX711.h"
// HX711 circuit wiring
const int LOADCELL_DOUT_PIN = 3;
const int LOADCELL_SCK_PIN = 2;
const int scale2_DOUT = 11;
const int scale2_SCK = 10;
HX711 scale, scale2;
void setup()
{
  Serial.begin(57600);
  scale.begin(LOADCELL_DOUT_PIN, LOADCELL_SCK_PIN);
  scale2.begin(scale2_DOUT, scale2_SCK);
}
void loop()
{
  scale.set_scale();
  scale2.set_scale();
  Serial.println("You have 4 seconds to empty the scale");
  delay(4000);
```

```
  scale.tare();
  scale2.tare();
  Serial.println("Now you have 6 seconds to place a known weight on the scale");
  delay(6000);
  long reading = scale.get_units(10);
  long reading2 = scale2.get_units(10);
  Serial.println("Result: ");
  Serial.println(reading);
  Serial.println(reading2);
  Serial.println("Calibration Factor = (reading)/(known weight)");
  Serial.println("");
  delay(1000);
}
```

Appendix C: Soft-robotic Green sea turtle (Chelonia mydas) developed to replace animal experimentation provides new insight into their propulsive strategies.

Supplementary figure S7 Sea turtle robot chassis.

(a) Rendered CAD model of final robot design **(b)** 3D printed sections **(c)** Bonding of each section to form complete chassis. **(d)** Painting of chassis. **(e)** Access hatch locations to access electrical components. **(f)** Assembly of 3D printed limb onto chassis.

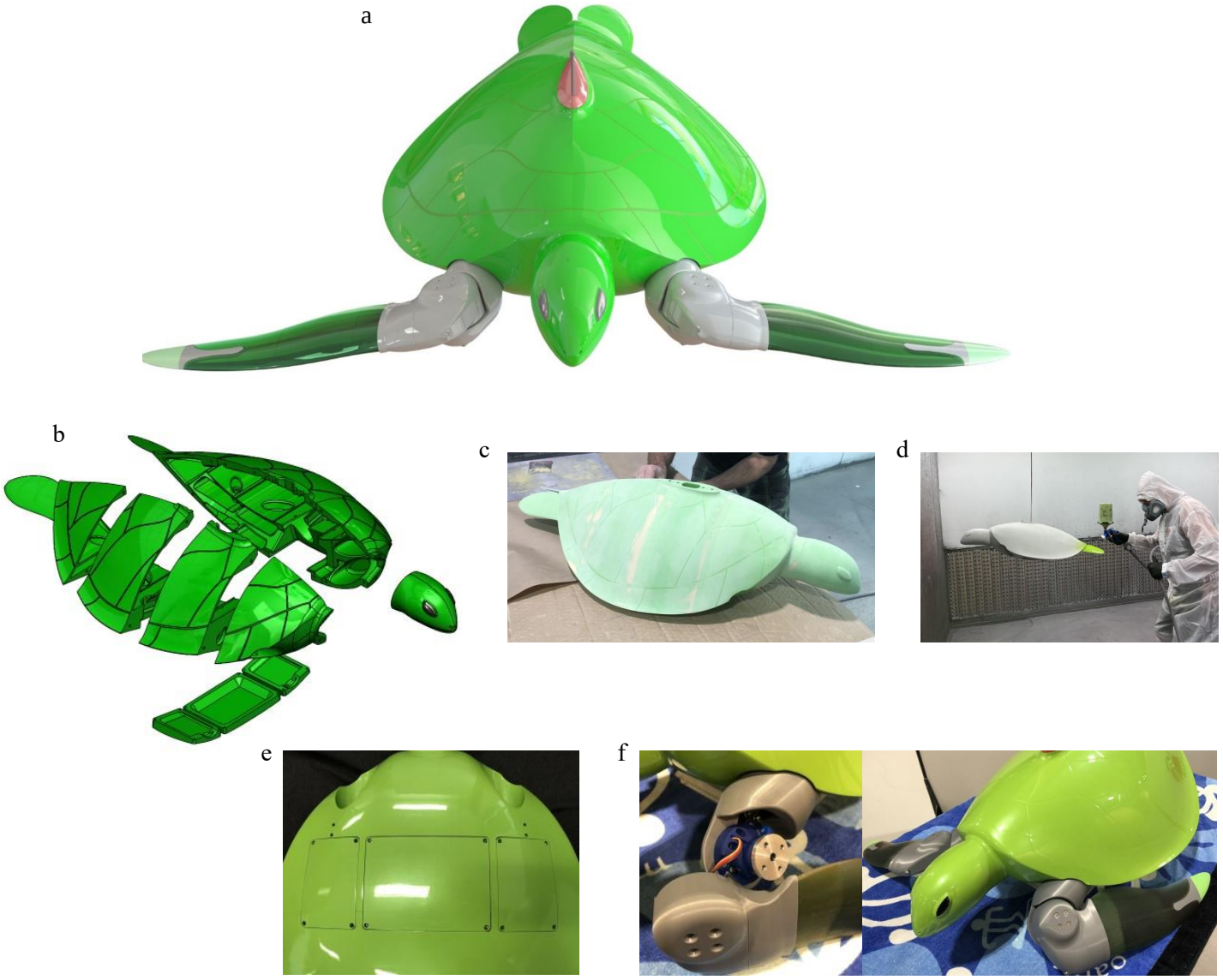

Supplementary figure S8 Soft robotic flipper design

(a) Three different green sea turtle flipper geometries showing leading edge claw and trailing edge serrations. It can be observed that each flipper has a slightly different shape. Additionally, the image on the right shows the final geometry and cross-section profile that was derived for the robot. **(b)** Design iterations starting from the top left image showing the first design iteration. The larger geometries shown below are the final iteration, with the left image showing the typical mesh used for FEA simulations

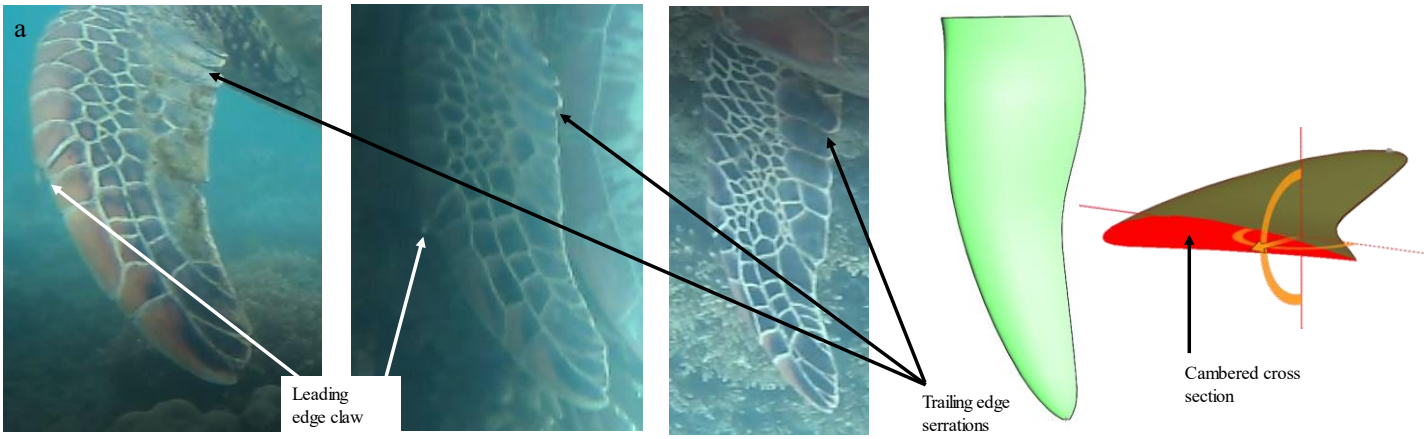

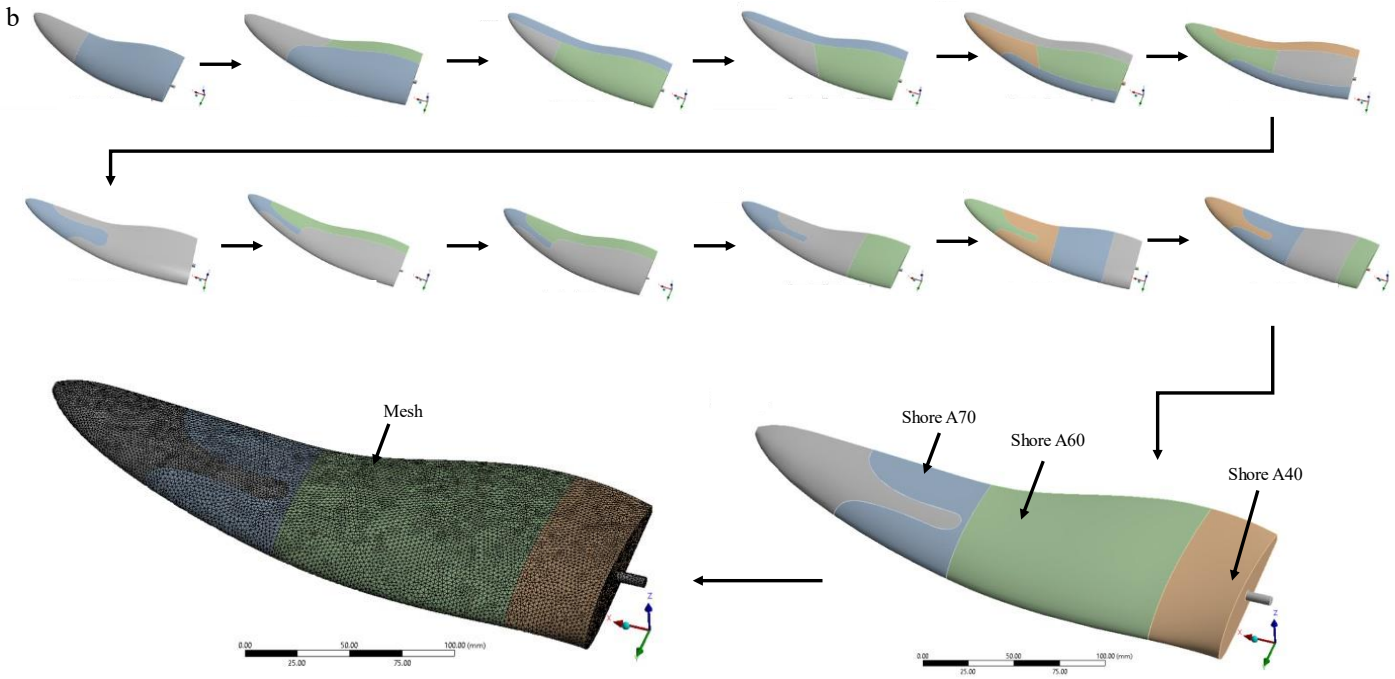

Supplementary figure S9 Flipper manufacturing

(a) Split mould assembly showing flipper tip and carbon fibre spar installed ready for casting **(b)** Casting levels for each compound. **(c)** Pair of newly manufactured flippers. At the trailing edge, the material has lifted slightly above the desired level due to capillary effects.

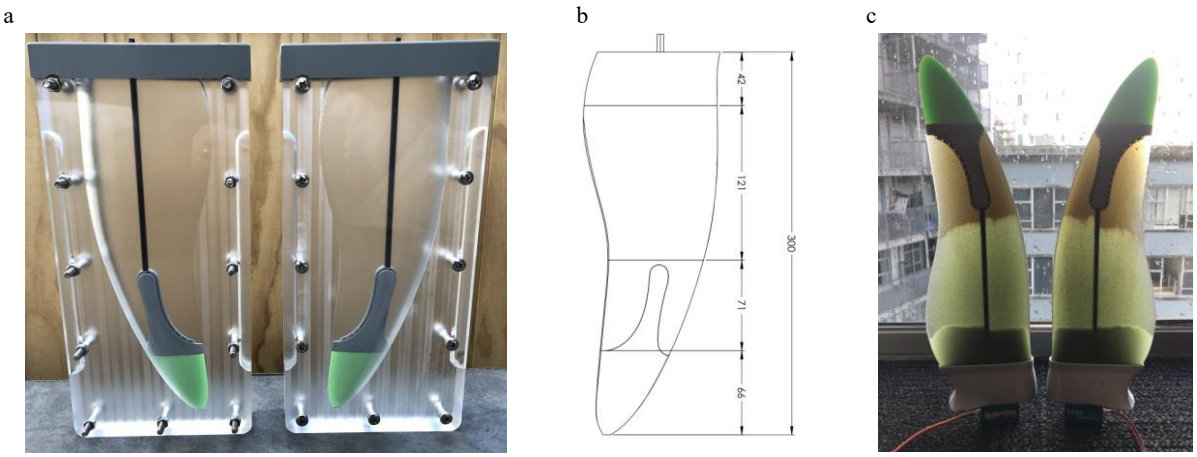

Supplementary figure S10 Fatigue test machine

(a) Fatigue testing machine showing flipper in position **(b)** Controller showing cycle counter. **(c)** max cycle count of 922,154 cycles. **(d)** Showing twisting motion after 922,154 cycles and small trailing edge failure. **(e)** Close up of the trailing edge failure.

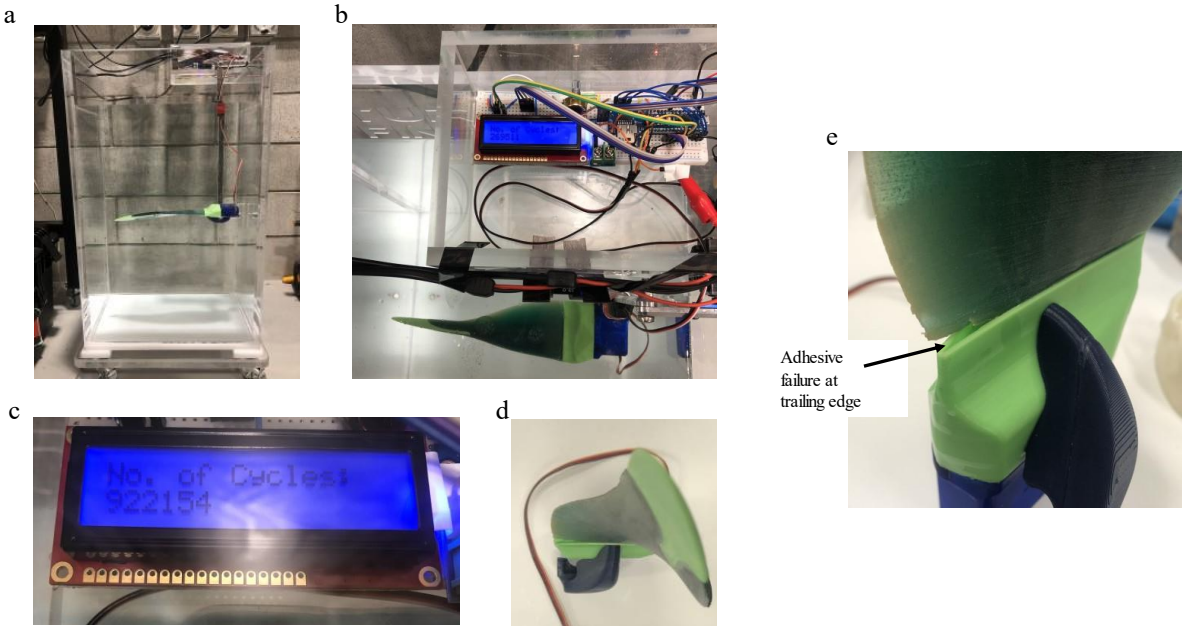

Supplementary figure S11 Test rig setup

(a) Robot swimming past markers on a linear rail for obtaining swim speed data, followed by a camera on a linear rail running parallel with robot swim path **(b)** (1) Test rig setup for constrained operation (2) test rig setup for towing operation. **(c)** Pulley assembly. **(d)** Complete test rig assembly

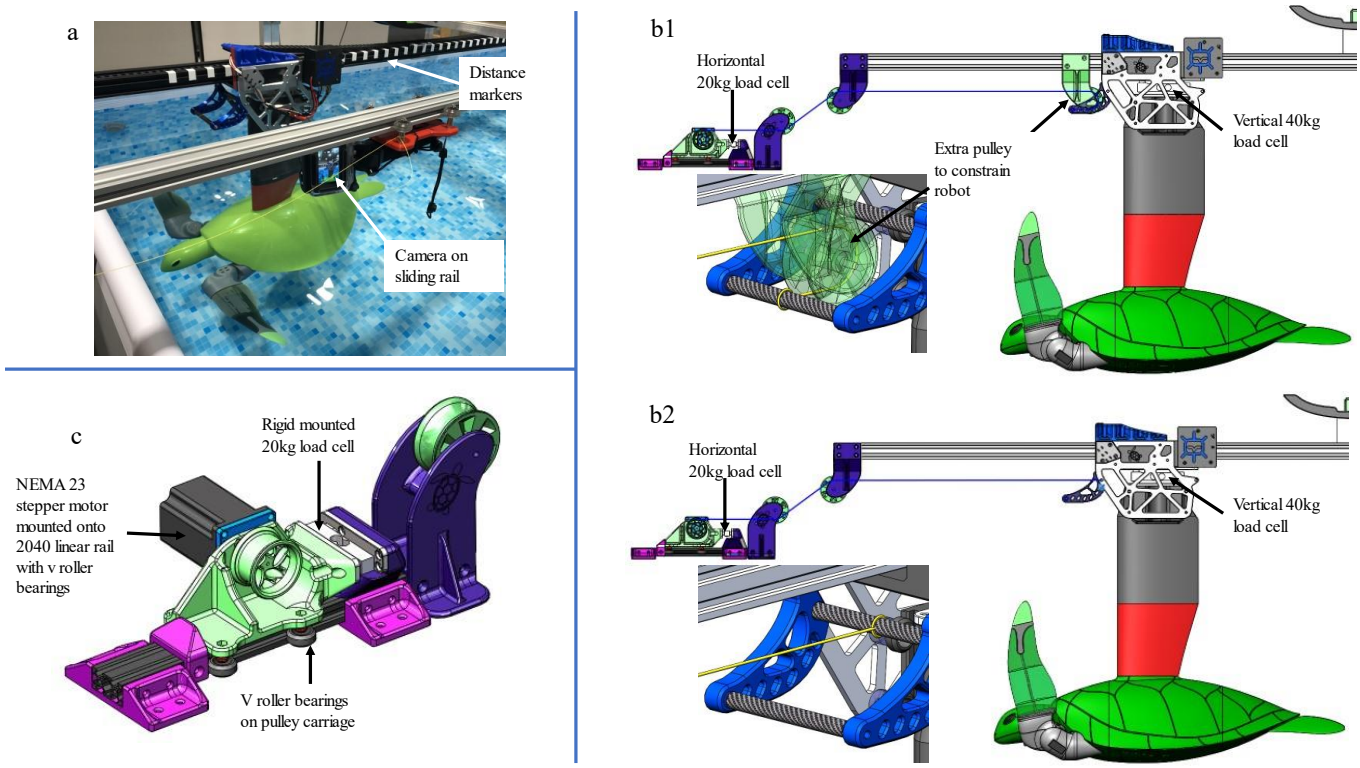

d

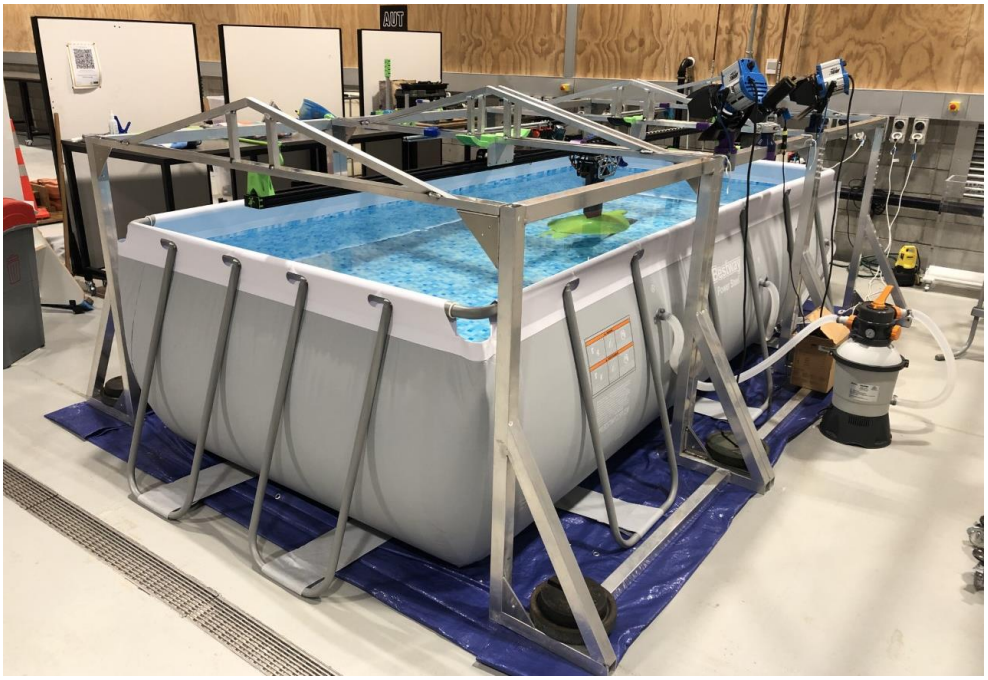

Supplementary figure S12 data from towing tests

(a) The thrust produced by the turtle during tow testing **(b)** Swim speed data from tow test with an initial velocity of 0.6 m/s. **(c)** Drag produced by the turtle. The blue line represents the hydrodynamic drag force created by the turtle itself. The orange line shows the hydrodynamic drag forces with the addition of the friction forces from the test rig linear rail assembly. **(d)** Data plot showing friction produced by linear rail assembly. Test produced without the robot attached **(e)** Drag produced by towing robot at 0.45 m/s. Plot includes friction from linear rail assembly. Test produced with robot limbs held stationary.

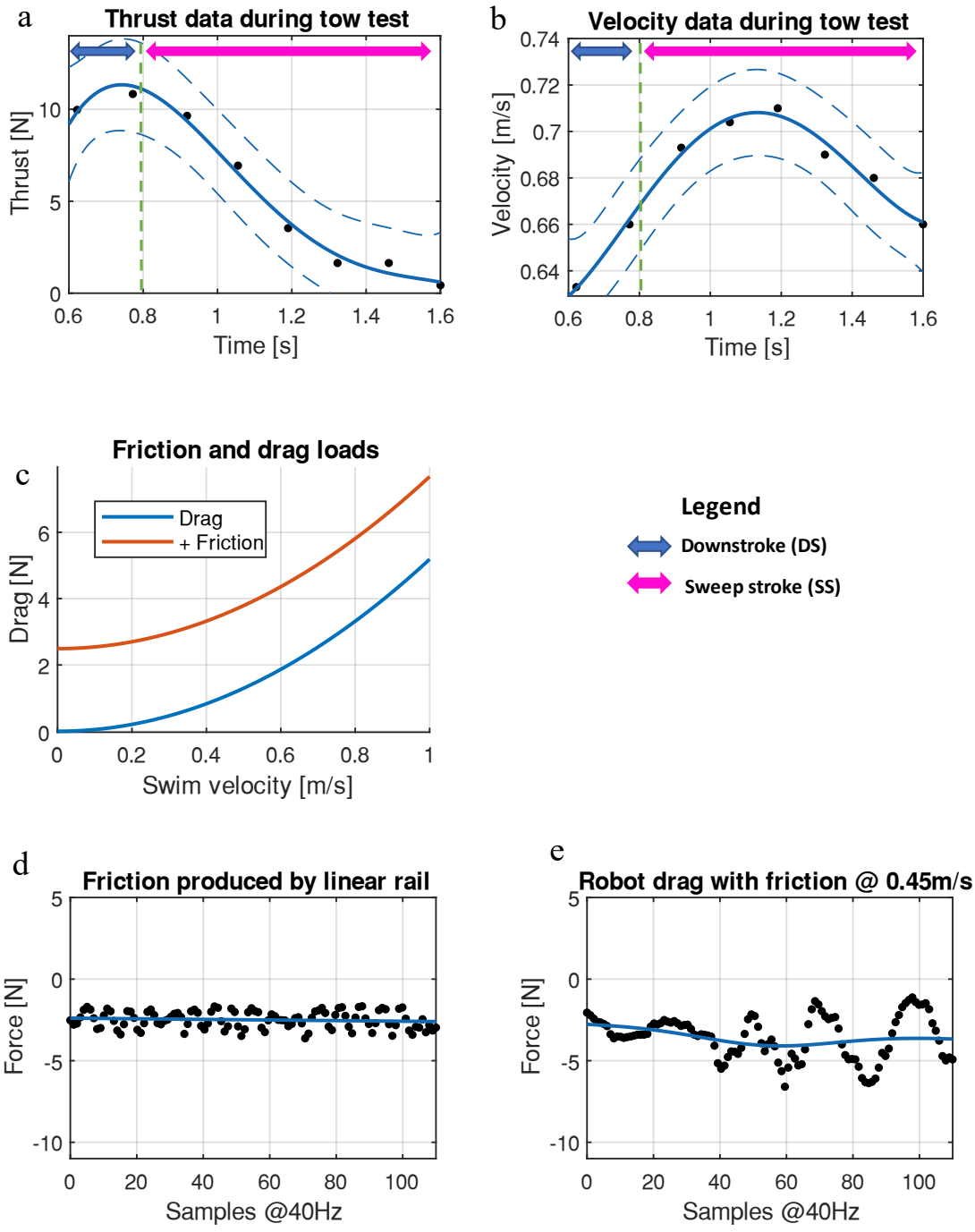

Supplementary figure S13 Simplified hardware schematic for turtle controller

Contains Particle Photon MCU, power regulator for MCU, servo signal and power headers with brownout protection.

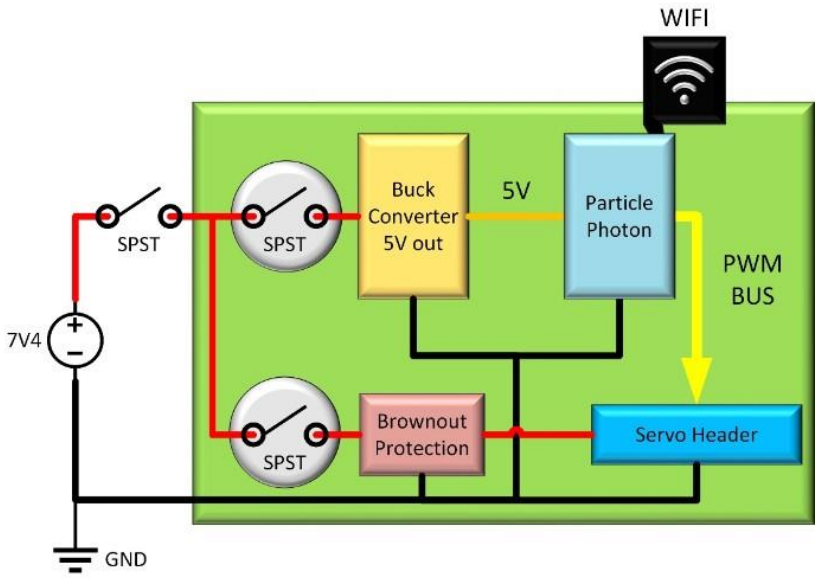

Supplementary figure S14 Test rig eletrical system

(a) Electrical system block diagram. **(b)** Electrical system test rig workstation setup, where 1 is the motor control system, 2 data acquisition system, 3 stepper motor and pulley assembly, 4 load cell assembly (drag). **(c)** Electrical system GUI.

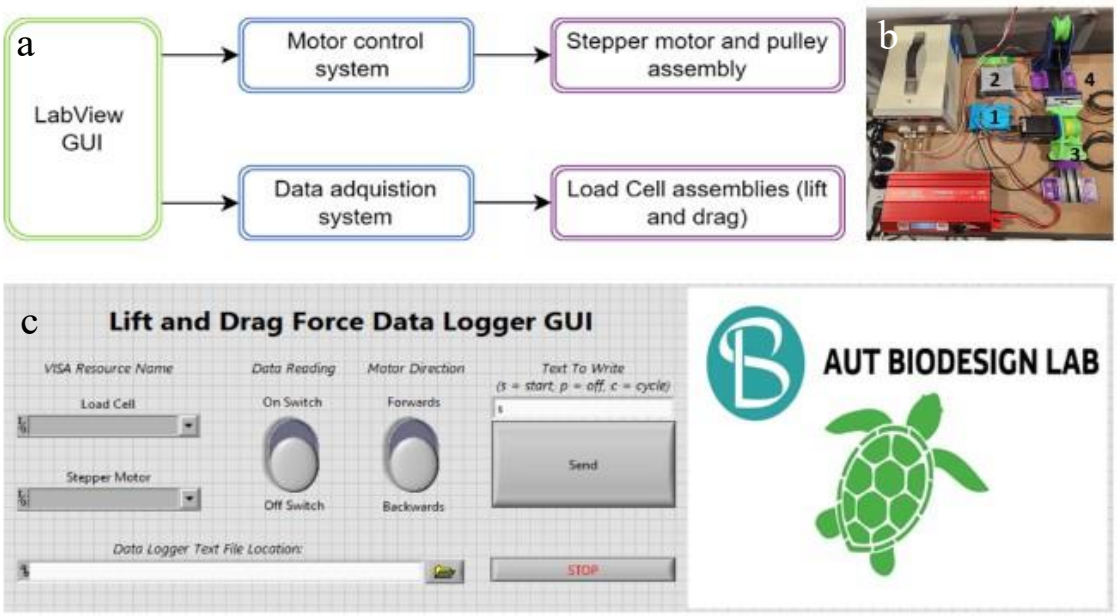

Supplementary figure S15 CFD results showing pressure contour plots on the robot with a focus around the robotic limb area

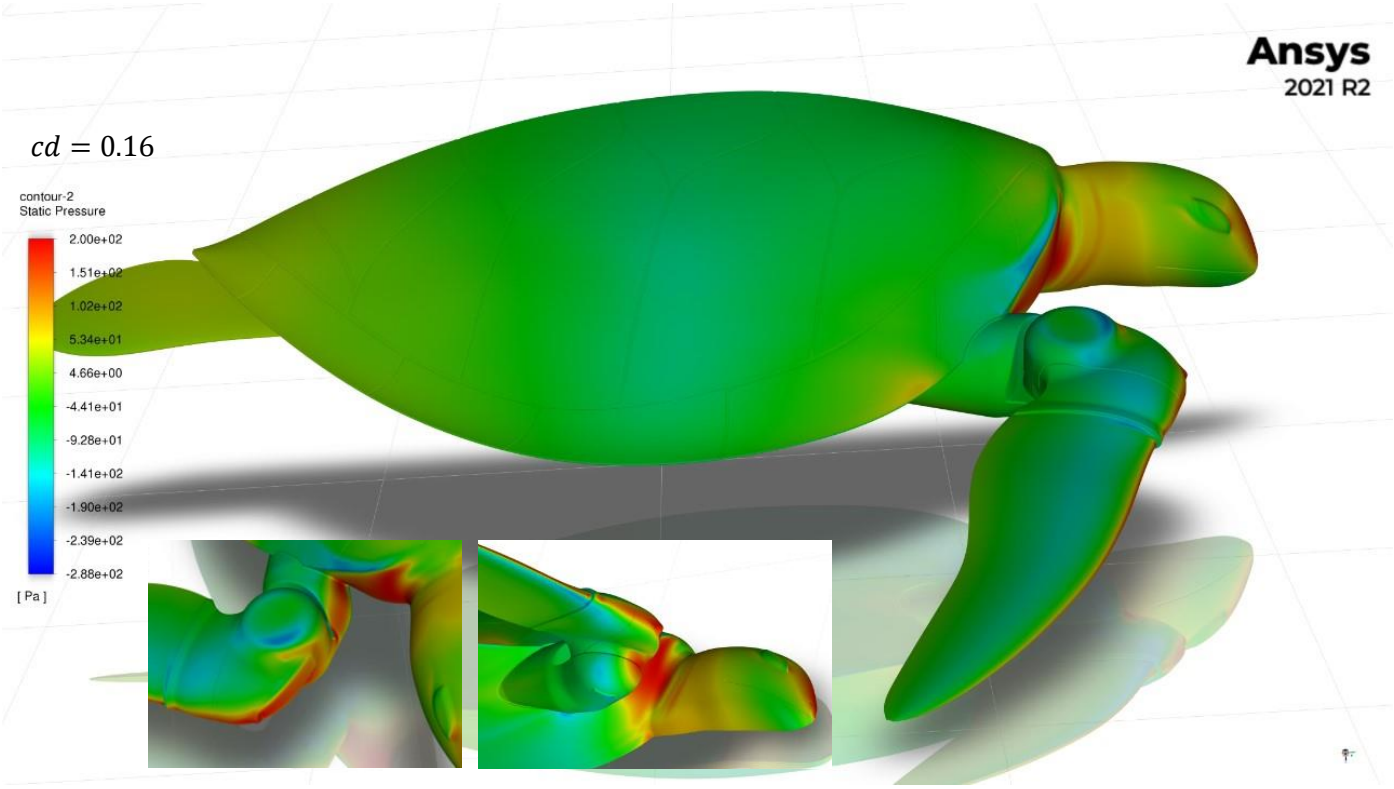

Code to control robot turtle

```
#define LEFT true

#define RIGHT false

#define LEFT_SIGN -1

#define RIGHT_SIGN 1

#define ROLL_SIGN -1

#define STATE_MOVING 0

#define STATE_STOPPED 1

#define STATE_RESET 2

#define STATE_CALIBRATE 3

#define STATE_ZERO 4

#define STATE_BRAKE 5

#define STATE_ROLL_MOUNT 6

#define STATE_LOW_DRAG_1 7

#define STATE_LOW_DRAG_2 8

#define CMD_MOVING "on"

#define CMD_STOPPED "off"

#define CMD_RESET "reset"

#define CMD_CALIBRATE "calibrate"

#define CMD_ZERO "zero"

#define CMD_BRAKE "brake"

#define CMD_ROLL_MOUNT "roll_mount"

#define CMD_LOW_DRAG_1 "low_drag_1"

#define CMD_LOW_DRAG_2 "low_drag_2"

#define SERVO_ROLL 0

#define SERVO_YAW 1

#define SERVO_PITCH 2
```

```
#define MAX_SERVO_ANGLE 80
#define MIN_SERVO_ANGLE -80
#define ROLL_MOUNT_SERVO_ANGLE -64.6
#define PITCH_BRAKE_ANGLE 70
#define SIZE_OF_SEQUENCE 86
#define INCREMENTS 10
//TX, WKP, A4, D2, D0, D1
// 1,   2,  3,  4,  5,  6

// function dec ////////////////////////////////////////////////////////////////////////////////
int my_map(float value, int fromStart, int fromEnd, int toStart, int toEnd);
void setServoPosition(float angle,bool left,int joint);
float interpolateServoAngle(float high_val, float low_val,int inc, int max_inc);
void updatePosition();
int startStopRobot(String command);
int updateFrequency(String command);

// photon onboard led //////////////////////////////////////////////////////////////////////////
int led_board = D7;
int led_state=0;

// turtle seq //////////////////////////////////////////////////////////////////////////////////
// postive right, needs negative sign for left flipper
float roll[]={-66.25,-64.54,-61.66,-57.87,-53.58,-49.22,-45.19,-41.74,-39.02,-36.97,-35.43,-34.16,-
32.94,-31.57,-29.93,-28.00,-25.82,-23.45,-20.98,-18.49,-16.01,-13.56,-11.15,-8.77,-6.41,-4.06,-
1.70,0.72,3.25,5.99,9.00,12.35,16.07,20.13,24.44,28.90,33.36,37.70,41.83,45.68,49.27,52.61,55.72,58
.65,61.37,63.85,66.06,67.94,69.45,70.60,71.39,71.87,72.06,71.95,71.51,70.67,69.31,67.34,64.70,61.3
6,57.35,52.73,47.59,41.99,35.95,29.47,22.50,15.03,7.07,-1.27,-9.77,-18.13,-26.01,-33.08,-39.10,-
43.99,-47.81,-50.78,-53.20,-55.40,-57.62,-59.93,-62.28,-64.42,-66.01,-66.71};
```

```
float
pitch[]={0.00,4.40,8.79,13.19,17.59,21.98,26.38,30.78,35.18,35.00,35.00,35.00,35.00,35.00,35.00,35.
00,35.00,35.00,35.00,35.00,35.00,35.00,35.00,35.00,35.00,35.00,35.00,35.00,35.00,35.00,35.00,35.00
,35.00,35.00,35.00,35.00,35.00,35.00,35.00,35.00,35.00,35.00,35.00,35.00,35.00,35.00,35.00,31.39,2
7.00,22.60,18.20,13.81,9.41,5.01,0.62,-9.70,-20.99,-32.28,-43.56,-54.85,-66.13,-72.00,-72.00,-72.00,-
72.00,-72.00,-72.00,-72.00,-72.00,-72.00,-72.00,-72.00,-72.00,-73.47,-67.82,-62.17,-56.51,-50.86,-
45.21,-39.56,-33.91,-28.26,-22.61,-16.95,-11.30,-5.65};

float yaw[]={-36.76,-38.18,-39.08,-39.55,-39.65,-39.45,-38.95,-38.15,-37.05,-35.64,-33.93,-31.99,-
29.89,-27.73,-25.62,-23.63,-21.80,-20.16,-18.66,-17.27,-15.91,-14.56,-13.16,-11.72,-10.23,-8.70,-
7.14,-5.54,-3.90,-2.20,-
0.42,1.44,3.37,5.34,7.28,9.14,10.89,12.47,13.89,15.15,16.28,17.32,18.30,19.26,20.21,21.17,22.14,23.
15,24.21,25.33,26.51,27.76,29.05,30.33,31.56,32.66,33.55,34.20,34.56,34.64,34.45,34.03,33.39,32.56
,31.55,30.35,28.92,27.26,25.34,23.16,20.73,18.06,15.17,12.07,8.73,5.15,1.30,-2.82,-7.17,-11.70,-
16.27,-20.76,-24.98,-28.79,-32.06,-34.71};


// servo config ////////////////////////////////////////////////////////////////////////////

Servo left_servos[3];

Servo right_servos[3];

int left_servo_pins[]={TX,WKP,A4};

int right_servo_pins[]={D2,D0,D1};

int left_servo_min_us[]={800,800,800};

int right_servo_min_us[]={800,800,800};

int left_servo_max_us[]={2200,2200,2200};

int right_servo_max_us[]={2200,2200,2200};


// state control params ////////////////////////////////////////////////////////////////////////////

int move_counter=0;

int calibrate_counter=0;

int robot_state=STATE_STOPPED;

float robot_interval=50;

float robot_interval_buf=50;
```

```
int state_update=0;
int freq_update=0;
float move_increment_counter=0;
float current_position_left[]={roll[0],yaw[0],pitch[0]};
float current_position_right[]={roll[0],yaw[0],pitch[0]};

// cal angles
float zero_angles[]={0,0,0};
float cal_roll_pos_angles[]={60,0,0};
float cal_roll_neg_angles[]={-60,0,0};
float cal_yaw_pos_angles[]={0,35,0};
float cal_yaw_neg_angles[]={0,-35,0};
float cal_pitch_pos_angles[]={0,0,60};
float cal_pitch_neg_angles[]={0,0,-60};

//low drag positions
float ldr_1_pos_final={0,-35,0};

float ldr_2_pos_int={61.6,0,0};
float ldr_2_pos_final={61.6,-34,0};

// position seq timer ////////////////////////////////////////////////////////////////////////////////
Timer timer(robot_interval/(float)INCREMENTS, updatePosition);

void moveWingsFromCurrentToSet(float new_angles_left[],float new_angles_right[],float steps,int
delay_time){
```

```
        float inc_l_roll=(new_angles_left[SERVO_ROLL]-
current_position_left[SERVO_ROLL])/steps;
        float inc_l_pitch=(new_angles_left[SERVO_PITCH]-
current_position_left[SERVO_PITCH])/steps;
        float inc_l_yaw=(new_angles_left[SERVO_YAW]-
current_position_left[SERVO_YAW])/steps;

        float inc_r_roll=(new_angles_right[SERVO_ROLL]-
current_position_right[SERVO_ROLL])/steps;
        float inc_r_pitch=(new_angles_right[SERVO_PITCH]-
current_position_right[SERVO_PITCH])/steps;
        float inc_r_yaw=(new_angles_right[SERVO_YAW]-
current_position_right[SERVO_YAW])/steps;

        for(int step=0; step<steps; step++){
            setServoPosition(current_position_left[SERVO_ROLL]+inc_l_roll,LEFT,SERVO_ROLL);
            setServoPosition(current_position_left[SERVO_PITCH]+inc_l_pitch,LEFT,SERVO_PITCH);
            setServoPosition(current_position_left[SERVO_YAW]+inc_l_yaw,LEFT,SERVO_YAW);
           setServoPosition(current_position_right[SERVO_ROLL]+inc_r_roll,RIGHT,SERVO_ROLL);
         etServoPosition(current_position_right[SERVO_PITCH]+inc_r_pitch,RIGHT,SERVO_PITCH);
            setServoPosition(current_position_right[SERVO_YAW]+inc_r_yaw,RIGHT,SERVO_YAW);
            delay(delay_time);
        }
}
// setup ////////////////////////////////////////////////////////////////////////////
void setup()
{
   // servo setup
   Serial.end();
```

```
    Serial1.end();
    pinMode(TX, OUTPUT);
    for(int i=0;i<3;i++){
        if(i==SERVO_ROLL)
            left_servos[i].attach(left_servo_pins[i],500,20000);
        else
            left_servos[i].attach(left_servo_pins[i]);
        right_servos[i].attach(right_servo_pins[i]);
    }
        // particle func setup
    Particle.function("updateFrequency",updateFrequency);
    Particle.function("startStopRobot",startStopRobot);
            // util setup
    pinMode(led_board, OUTPUT);
    digitalWrite(led_board, LOW);
    timer.start();
}
// main loop ////////////////////////////////////////////////////////////////////////////////
void loop()
{
    if(state_update){
        state_update=0;
        if (robot_state==STATE_MOVING) {
            if (!timer.isActive())
                timer.STATE_RESET();
                }else if (robot_state==STATE_STOPPED) {
            if (timer.isActive())
                timer.stop();
```

```
}else if (robot_state==STATE_RESET) {
   if (timer.isActive())
      timer.stop();
   move_counter=0;
   calibrate_counter=0;
   move_increment_counter=0;
            robot_interval=50;
   robot_interval_buf=50;
             float new_angles[]={roll[0],yaw[0],pitch[0]};
   moveWingsFromCurrentToSet(new_angles,new_angles,400,5);
   robot_state=STATE_STOPPED;
   state_update=0;
   freq_update=0;
    }else if (robot_state==STATE_ZERO) {
   if (timer.isActive())
      timer.stop();
   move_counter=0;
   calibrate_counter=0;
   move_increment_counter=0;
            float new_angles[]={0,0,0};
   moveWingsFromCurrentToSet(new_angles,new_angles,400,5) ;
   robot_state=STATE_STOPPED;
}else if (robot_state==STATE_BRAKE) {
   if (timer.isActive())
      timer.stop();
   move_counter=0;
   calibrate_counter=0;
   move_increment_counter=0;
```

```
            float new_angles[]={0,0,PITCH_BRAKE_ANGLE};
    moveWingsFromCurrentToSet(new_angles,new_angles,400,5);
    robot_state=STATE_STOPPED;
  }else if (robot_state==STATE_ROLL_MOUNT) {
    if (timer.isActive())
      timer.stop();
    move_counter=0;
    calibrate_counter=0;
    move_increment_counter=0;
            float new_angles[]={ROLL_MOUNT_SERVO_ANGLE,0,0};
    moveWingsFromCurrentToSet(zero_angles,zero_angles,400,5);
    moveWingsFromCurrentToSet(new_angles,new_angles,400,5);
    robot_state=STATE_STOPPED;
  }else if (robot_state==STATE_LOW_DRAG_1) {
    if (timer.isActive())
      timer.stop();
    move_counter=0;
    calibrate_counter=0;
    move_increment_counter=0;
            moveWingsFromCurrentToSet(zero_angles,zero_angles,400,5);
    moveWingsFromCurrentToSet(ldr_1_pos_final,ldr_1_pos_final,400,5);
    robot_state=STATE_STOPPED;
  }else if (robot_state==STATE_LOW_DRAG_2) {
    if (timer.isActive())
      timer.stop();
    move_counter=0;
    calibrate_counter=0;
    move_increment_counter=0;
```

```
            moveWingsFromCurrentToSet(zero_angles,zero_angles,400,5);
    moveWingsFromCurrentToSet(ldr_2_pos_int,ldr_2_pos_int,400,5);
                        moveWingsFromCurrentToSet(ldr_2_pos_final,ldr_2_pos_final,400,5);

    robot_state=STATE_STOPPED;
  }else if (robot_state==STATE_CALIBRATE) {
    if (!timer.isActive())
      timer.STATE_RESET();

    calibrate_counter+=1;
    moveWingsFromCurrentToSet(zero_angles,zero_angles,400,5);
    moveWingsFromCurrentToSet(cal_roll_pos_angles,cal_roll_pos_angles,400,5);
    moveWingsFromCurrentToSet(cal_roll_neg_angles,cal_roll_neg_angles,400,5);
    moveWingsFromCurrentToSet(zero_angles,zero_angles,400,5);
    moveWingsFromCurrentToSet(cal_yaw_pos_angles,cal_yaw_pos_angles,400,5);
    moveWingsFromCurrentToSet(cal_yaw_neg_angles,cal_yaw_neg_angles,400,5);
    moveWingsFromCurrentToSet(zero_angles,zero_angles,400,5);
    moveWingsFromCurrentToSet(cal_pitch_pos_angles,cal_pitch_pos_angles,400,5);
    moveWingsFromCurrentToSet(cal_pitch_neg_angles,cal_pitch_neg_angles,400,5);
    moveWingsFromCurrentToSet(zero_angles,zero_angles,400,5);
    robot_state=STATE_STOPPED;

  }
   }
if(freq_update){
  freq_update=0;
  robot_interval=robot_interval_buf;
  timer.changePeriod(robot_interval/(float)INCREMENTS);
```

```
    }
    }
// state & control methods ////////////////////////////////////////////////////////////////////////////
int startStopRobot(String command) {
    state_update=1;
    if (command==CMD_MOVING) {
        robot_state=STATE_MOVING;
    }else if (command==CMD_STOPPED) {
        robot_state=STATE_STOPPED;
    }else if (command==CMD_RESET) {
        robot_state=STATE_RESET;
    }else if (command==CMD_CALIBRATE) {
        robot_state=STATE_CALIBRATE;
      }else if (command==CMD_ZERO) {
        robot_state=STATE_ZERO;
           }else if (command==CMD_BRAKE) {
        robot_state=STATE_BRAKE;
            }else if (command==CMD_ROLL_MOUNT) {
        robot_state=STATE_ROLL_MOUNT;
    }else if (command==CMD_LOW_DRAG_1) {
        robot_state=STATE_LOW_DRAG_1;
    }else if (command==CMD_LOW_DRAG_2) {
        robot_state=STATE_LOW_DRAG_2;
                }else{
        state_update=0;
        return -1;
    }
            return robot_state;
```

```
    }
int updateFrequency(String command) {
   //put in bounds
   robot_interval_buf=command.toFloat();
   freq_update=1;
   return 42;
}
// servo methods ////////////////////////////////////////////////////////////////////////////////
void setServoPosition(float angle,bool left,int joint){
   if (robot_state!=STATE_STOPPED){
      int max_us,min_us=0;
      int sign=0;
           if(left){
         max_us=(int)left_servo_max_us[joint];
         min_us=(int)left_servo_min_us[joint];
         sign=LEFT_SIGN;
         current_position_left[joint]=angle;
      }else{
         max_us=(int)right_servo_max_us[joint];
         min_us=(int)right_servo_min_us[joint];
         sign=RIGHT_SIGN;
         current_position_right[joint]=angle;
      }
           if(joint==SERVO_ROLL){
         sign=sign*ROLL_SIGN;
      }
```

```
            int val = (int)my_map(angle*sign, MIN_SERVO_ANGLE, MAX_SERVO_ANGLE,
min_us, max_us);
                    if(left && joint==SERVO_ROLL)
          left_servos[SERVO_ROLL].writeMicroseconds(20000-val);
       else if(left)
          left_servos[joint].writeMicroseconds(val);
       else
          right_servos[joint].writeMicroseconds(val);
   }
     }
float interpolateServoAngle(float high_val, float low_val,int inc, int max_inc){
   float angle_delta=(high_val- low_val)*(inc/max_inc);
   float angle=(angle_delta*inc) + low_val;
    return angle;
}
// timer function to control sequence
void updatePosition(){
   if(robot_state==STATE_MOVING){
            int low_index=move_counter;
       int high_index=move_counter+1;
       if(high_index>=SIZE_OF_SEQUENCE)
          high_index=0;
               // float roll_angle_delta=(roll[high_index]-
roll[low_index])*(increment_counter/INCREMENTS);
       // float roll_angle=(roll_angle_delta*increment_counter) + roll[low_index];
       float roll_angle=interpolateServoAngle(roll[high_index],
roll[low_index],move_increment_counter, INCREMENTS);
       setServoPosition(roll_angle,LEFT,SERVO_ROLL);
       setServoPosition(roll_angle,RIGHT,SERVO_ROLL);
```

```
            float pitch_angle=interpolateServoAngle(pitch[high_index],
pitch[low_index],move_increment_counter, INCREMENTS);
        setServoPosition(pitch_angle,LEFT,SERVO_PITCH);
        setServoPosition(pitch_angle,RIGHT,SERVO_PITCH);
            float yaw_angle=interpolateServoAngle(yaw[high_index],
yaw[low_index],move_increment_counter, INCREMENTS);
        setServoPosition(yaw_angle,LEFT,SERVO_YAW);
        setServoPosition(yaw_angle,RIGHT,SERVO_YAW);
            move_increment_counter+=1;
        if(move_increment_counter>=INCREMENTS){
          move_counter++;
          move_increment_counter=0;
        }
        if(move_counter>=SIZE_OF_SEQUENCE)
          move_counter=0;
    }
    }
// util methods ////////////////////////////////////////////////////////////////////////////
int my_map(float value, int fromStart, int fromEnd, int toStart, int toEnd)
{
    if (fromEnd == fromStart) {
        return value;
    }
    return ((value - fromStart) * (toEnd - toStart) / (fromEnd - fromStart)) + toStart;
}
```

Appendix D: New insights into sea turtle propulsion methods and cost of transport point to the effectiveness of the animal's swimming technique.

Supplementary Figure S16 CFD computational domains

(a) $k\varepsilon$ rotational domain for downstroke simulations. (b) $k\omega$ domain for simulating flow over the rear flippers

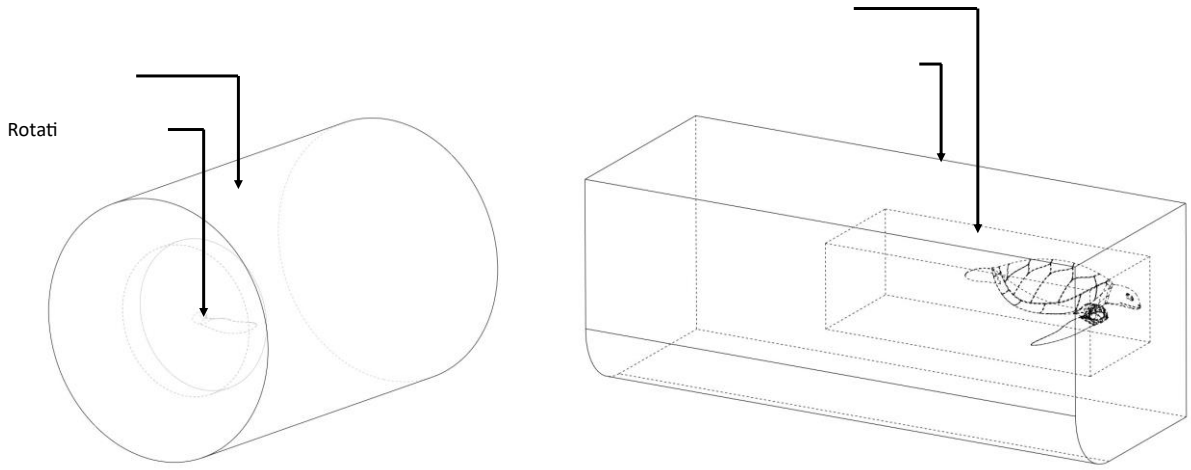

Supplementary Figure S17 free body diagram of the twisted turtle flipper illustrating Dorsal and ventral sides

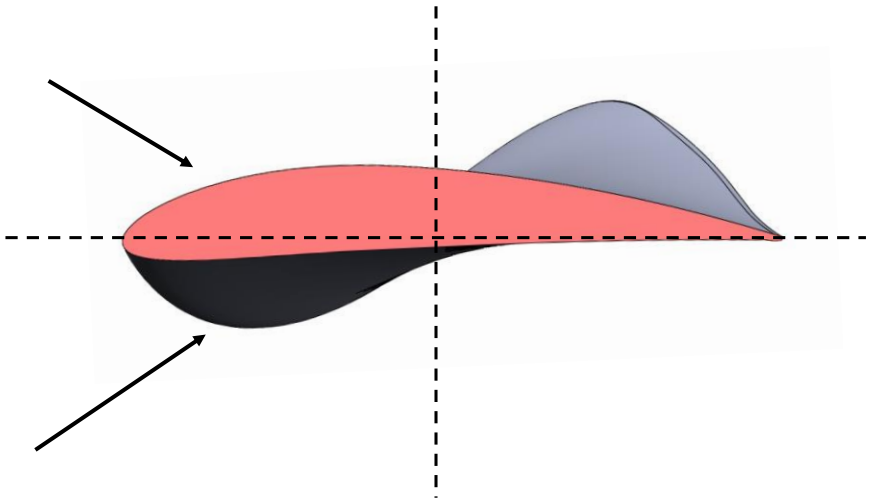

Supplementary Figure S18 AOA values at various points along the turtle's flipper, L represents the complete wing span (flipper tip position)

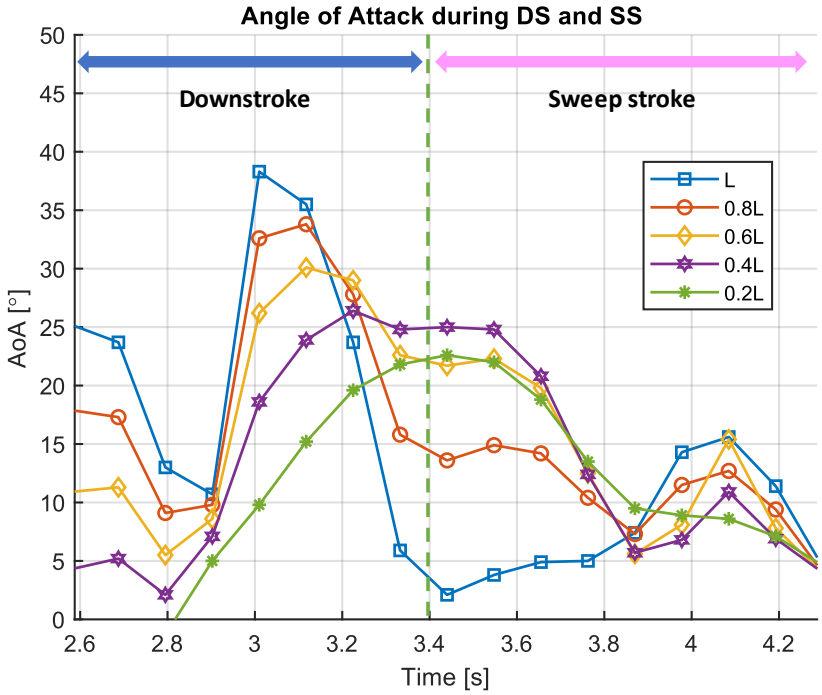

Appendix E: Research Permit

Marine Parks — Australian Government, Great Barrier Reef Marine Park Authority — Queensland Government

PERMIT

Great Barrier Reef Marine Park Regulations 2019 (Commonwealth)
Marine Parks Regulation 2017 (Queensland)

G21/45637.1

CORE MATTERS

These permissions remain in force, unless sooner surrendered or revoked for the following period:

26-MAY-2021 TO **30-JUN-2022**

Permission is granted to:

PERMIT HOLDER: **Dr Lorenzo GARCIA**
School of Engineering, Computer and Mathematical Science
ADDRESS: **Auckland University of Technology**
31 Symonds Street
AUCKLAND 1010 NEW ZEALAND

for use of and entry to zones in the **Amalgamated Great Barrier Reef Marine Park Section** (as established by the *Great Barrier Reef Marine Park Act 1975* (Cth)) and the **Great Barrier Reef Coast Marine Park** (as established by the *Marine Parks Act 2004* (Qld)) in accordance with the details set out herein.

Date 25-May-2021
Delegate for the
Great Barrier Reef Marine Park Authority

Date 26-May-2021
Delegate for the Chief Executive of the
Department of Environment and Science

THE PURPOSE/S OF USE AND ENTRY MAY ONLY BE UNDERTAKEN IN THE ZONE/S AND LOCATION/S DESCRIBED BELOW.

ZONE/S AND LOCATION/S TO WHICH THE PERMISSION APPLIES:

- GENERAL USE ZONE – Lady Musgrave Reef (23-082a)
- HABITAT PROTECTION ZONES – Boult Reef (23-079), Lady Musgrave Island Reef (23-082) Habitat Protection Zone; Lamont Reef (23-076) and Fitzroy Reef (23-077) Habitat Protection Zone; Lady Elliot Reef (18-050); and Lady Musgrave Reef (23-082a).
- CONSERVATION PARK ZONES – Fitzroy and Little Fitzroy Islands Conservation Park Zone; and Heron Reef (23-052a).
- SCIENTIFIC RESEARCH ZONE – Heron Island Reef east (23-052) Scientific Research Zone; and One Tree Island Reef (23-055) Scientific Research Zone.
- MARINE NATIONAL PARK ZONES – Wistari Reef (23-053), Heron Island Reef (23-052) and inter-reefal areas adjacent to One Tree Island Marine National Park Zone; Lady Elliot Island Reef (24-008) Marine National Park Zone; Llewellyn Reef (23-078), Hoskyn Reef (23-080), Fairfax Reef (23-081) and northern Side of Lady Musgrave Reef (23-082) Marine National Park Zone.
- COMMONWEALTH ISLAND ZONE – Lady Elliot Island (24-008) and Little Fitzroy Island (16-055a).

PURPOSE/S OF USE AND ENTRY AUTHORISED BY THE PERMISSION:

CONDUCT OF A RESEARCH PROGRAM – Kinematics analysis of sea turtles.

CONDITIONS OF PERMISSIONS

COMPLIANCE WITH ALL LAWS

1 All activities conducted under this permission must be undertaken in accordance with the provisions of the laws in force from time to time in the State of Queensland and the Commonwealth of Australia.

2 To the extent applicable and unless written endorsement to the contrary appears in this permit, the Permit Holder must:
- (i) comply with the enforcement provisions contained in Part 2 of the Plans of Management gazetted under Part VB of the *Great Barrier Reef Marine Park Act 1975*; and
- (ii) may only operate to an intertidal area adjacent to a location within the Planning Areas with access consistent with that provided in the Plans of Management for that adjacent location.

3 The Permit Holder must ensure:
- (i) the Restricted Access Special Management Areas are not used or entered at any time unless otherwise permitted in the core matters; and
- (ii) the Maritime Cultural Heritage Special Management Areas are only used or entered for the purpose of transiting; and
- (iii) all other Special Management Areas are used and entered in accordance with the restrictions specified in the Great Barrier Reef Marine Park Regulations 2019 and the Great Barrier Reef Marine Park Zoning Plan 2003.

4 The Permit Holder must ensure that when operations are conducted in the Marine Parks under this permit, a copy of this permit is held at the site or sites of operation and on the vessel or aircraft or ship during transit to and from that site or sites.

5 The Permit Holder must inform staff and participants in the program of relevant restrictions applying under any zoning plans, plans of management, Marine Parks regulations and this permit.

RESEARCH PROGRAM CONDITIONS

6 This permit allows for the use of small, passive items that support data collection, provided they are carried continuously on a person's body or are attended at all times.

7 This permit allows for the use of small non-fixed still and video cameras, which must be attended at all times.

8 This permit allows for the use of an underwater remotely operated vehicle (no larger than 5 kg including equipment), which must be operated in accordance with the following:
- (i) units must not approach closer than:
  - (a) 5 metre radius from marine turtles;
  - (b) 30 metre radius from crocodiles;
  - (c) 30 metre radius from dugongs; and
  - (d) 75 metre radius from seabirds; and
- (ii) units must be operated by appropriately trained persons only.

REPORTING AND NOTIFICATION CONDITIONS

9 When undertaking research in the vicinity of those locations listed below, the Permit Holder must discuss the study sites with the appropriate person as specified, and abide by resulting guidelines for location of the manipulative work:

LOCATION	APPROPRIATE PERSON
Heron Island	Station Manager of Heron Island Research Station
Wistari Reef	Station Manager of Heron Island Research Station
One Tree Island	Resident Officer of One Tree Island Research Station

10 The Permit Holder must ensure that all vessels used in connection with the activities permitted herein are clearly marked "Research Vessel" while being used for those activities.

11 The Permit Holder must submit a Marine Wildlife Stranding and Mortality Report (Attachment A) to the Great Barrier Reef Marine Park Authority within 72 hours if a protected species is injured or killed during the conduct of this research program. If a protected species is injured or killed, the Permit Holder must ensure that:
(i) all use of the equipment that injured or killed the protected species ceases;
(ii) an assessment is made of the cause of the incident;
(iii) review measures are implemented to minimise the risks identified; and
(iv) the activity does not resume without the written permission of the Great Barrier Reef Marine Park Authority.

12 The Permit Holder must ensure that all equipment placed in the Marine Parks in connection with this permit is clearly marked with the name of the Permit Holder and permit number condition G21/45637.1 and removed from the Marine Parks prior to the expiry of the permit.

13 The Permit Holder must submit a research report annually from the date of issue of the permit and at any other time within 21 days of request. Report submission must be done through the Great Barrier Reef Marine Park Authority's Permits Online Portal, unless otherwise approved.

INTERPRETATION AND DEFINITIONS

INTERPRETATION

This permit extends to all employees of the Permit Holder, or other persons, who are acting on behalf of, or at the direction of, the Permit Holder for the purposes specified in this permit.

This permit is not intended to extinguish any native title.

A law shall be taken to be a law in force in the State of Queensland notwithstanding that it applies to only part of the State.

A word or phrase in this permit has the same meaning as the word or phrase has in the *Great Barrier Reef Marine Park Act 1975* (Cth), the Great Barrier Reef Marine Park Regulations 2019 (Cth), the Marine Parks Act 2004 (Qld), the Marine Parks Regulation 2017 (Qld), Zoning Plans or Plans of Management, unless the contrary intention appears.

A note or heading may be used to give assistance in interpreting conditions in case of ambiguity.

A reference to a date includes that date.

DEFINITIONS

'appropriately trained person' means any person trained in accordance with best-practice techniques and methods covered in a current Animal Ethics Approval.

'attended at all times' means the Permit Holder must actively monitor the equipment (including keeping it within sight) and remain close enough to be able to take control of it within a few minutes.

'Boult Reef (23-079), Lady Musgrave Island Reef (23-082) Habitat Protection Zone' means that area defined as HP-23-5366 in Item 2.343 of Schedule 1 to the Great Barrier Reef Marine Park Zoning Plan 2003 (Cth) and the intertidal area adjacent to HP-23-5366.

'Fitzroy and Little Fitzroy Islands Conservation Park Zone' means that area defined as CP-16-4039 in Item 3.36 of Schedule 1 to the Great Barrier Reef Marine Park Zoning Plan 2003 (Cth) and the intertidal area adjacent to CP-16-4039.

'Heron Island Reef east (23-062) Scientific Research Zone' means that area defined as SR-23-2009 in Item 5.09 of Schedule 1 to the Great Barrier Reef Marine Park Zoning Plan 2003 (Cth) and the intertidal area adjacent to SR-23-2009.

'incident' means an event involving actual or potential harm to the ecosystem, including but not limited to:

(a) coral damage; or
(b) a cyclone; or
(c) any shipping event that requires notification to a relevant authority under the Queensland Marine Act 1958 or the Navigation Act 2012; or
(d) any aircraft event that requires notification to the relevant Authority under the Civil Aviation Act 1988; or
(e) any discharge of more than five (5) litres of untreated sewage effluent; or
(f) any discharge of more than five (5) litres of hazardous chemicals, fuel or biotoxic products.

'Lady Elliot Island Reef (24-008) Marine National Park Zone' means that area defined as MNPZ-23-1169 in Item 2.343 of Schedule 1 to the Great Barrier Reef Marine Park Zoning Plan 2003 (Cth) and the intertidal area adjacent to MNPZ-23-11690.

'Lamont Reef (23-076) and Fitzroy Reef (23-077) Habitat Protection Zone' means that area defined as HP-23-5364 in Item 2.341 of Schedule 1 to the Great Barrier Reef Marine Park Zoning Plan 2003 (Cth) and the intertidal area adjacent to HP-23-5364.

'Llewellyn Reef (23-078), Hoskyn Reef (23-080), Fairfax Reef (23-081) and northern side of Lady Musgrave Reef (23-082) Marine National Park Zone' means that area defined as MNPZ-23-1168 in Item 6.156 of Schedule 1 to the Great Barrier Reef Marine Park Zoning Plan 2003 (Cth) and the intertidal area adjacent to MNPZ-23-1168.

'location' means a discrete, identified reef, or a continuous non-reef area of up to 10 square kilometres.

'Marine Parks' means:

(a) the Great Barrier Reef Marine Park established by the *Great Barrier Reef Marine Park Act 1975* (Cth); and
(b) the Great Barrier Reef Coast Marine Park established pursuant to the *Marine Parks Act 2004* (Qld).

'Marine Parks regulations' means:

(a) in relation to the Great Barrier Reef Marine Park, the Great Barrier Reef Marine Park Regulations 2019 (Cth); and
(b) in relation to the Great Barrier Reef Coast Marine Park, the Marine Parks Regulation 2017 (Qld).

'One Tree Island Reef (23-066) Scientific Research Zone' means that area defined as SR-23-2010 in Item 5.10 of Schedule 1 to the Great Barrier Reef Marine Park Zoning Plan 2003 (Cth) and the intertidal area adjacent to SR-23-2010.

'permit' means the permissions the subject of Permit Number G21/45637.1 granted to the Permit Holder pursuant to the Great Barrier Reef Marine Park Regulations 2019 (Cth) and the Marine Parks Regulation 2017 (Qld).

'per year' means each 12 month period starting from the commencement date of the permit.

'protected species' means any individual from any species that meets one of the following criteria:

(a) is a listed threatened species, a listed migratory species or a listed marine species under the *Environment Protection and Biodiversity Conservation Act 1999* (Cth);
(b) is prescribed as endangered, vulnerable, near-threatened or least concern under the *Nature Conservation Act 1992* of Queensland;
(c) is mentioned in Section 30 Protected species table of the Great Barrier Reef Marine Park Regulations 2019 (Cth); or
(d) is from the genus *Epinephelus* (cods and groupers other than *E. tukula* or *E. lanceolatus*) and is more than 1000 millimetres in length.

'Remotely operated vehicle (ROV)' means a vessel, aircraft or other vehicle which is directly controlled by a human operator who is not located in or on the vehicle; may or may not be physically connected to the operator by a cable or tether; most commonly used to refer to underwater vehicles, but also includes remotely piloted aircraft.

'site' means an area of 3,000 square metres within a location.

'small, passive items' means items of the following: underwater slates and pencils, taxa ID cards, watches and timers, global positioning devices, data loggers (which are not greater than 500 millimetres in their longest dimension), sensors that do not emit significant electrical signals, sound, or light into the environment (e.g. secchi discs, digital thermometers, light meters and pH, dissolved oxygen and salinity meters), integrated transponder tag readers, transect tapes, quadrats, portable hydrophones, towboards, and standard, low power, recreational fish-finders and depth sounders when affixed to research boats.

'Wistari Reef (23-063) – Heron Island Reef (23-062) and inter-reefal areas adjacent to One Tree Island Marine National Park Zone' means that area defined as MNP-23-1164 in Item 6.152 of Schedule 1 to the Great Barrier Reef Marine Park Zoning Plan 2003 (Cth) and the intertidal area adjacent to MNP-23-1164.

'visit' in relation to a vessel (including the use of an ancillary vessel) means accessing a permitted location, without departure, for a period not exceeding 24 hours.

'Zoning Plan' means:

(a) in relation to the Great Barrier Reef Marine Park, the Great Barrier Reef Marine Park Zoning Plan 2003 (Cth); and
(b) in relation to the Great Barrier Reef Coast Marine Park, the Marine Parks (Great Barrier Reef Coast) Zoning Plan 2004 (Qld).

ATTACHMENT A

Marine Wildlife Stranding and Mortality Report

Turtles, dolphins, whales, dugong, sharks, seals, groupers

Australian Government Great Barrier Reef Marine Park Authority — Queensland Government

Date: ____/____/____	Time: ____:____	Tag Number/s:

SPECIES

☐ Turtle	☐ Mammal	☐ Other
☐ Green ☐ Loggerhead ☐ Hawksbill ☐ Flatback ☐ Olive ridley ☐ Leatherback ☐ Unidentified	☐ Dugong ☐ Dolphin *Species:* _____ ☐ Whale *Species:* _____ ☐ Unidentified	☐ Shark *Species:* _____ ☐ Seal *Species:* _____ ☐ Other *Species:* _____

MEASUREMENTS

TURTLE	MAMMAL	SEA SNAKE	OTHER
Curved carapace length: _____ cm Tail length: _____ cm Head width: _____ cm	Body length: _____ cm Fluke / tail width: _____ cm	Total length: _____ cm	*Specify:* _____ Body length: _____ cm

SEX AND MATURITY

Sex: ☐ Female ☐ Male ☐ Unknown	Maturity: ☐ Immature ☐ Adult ☐ Unknown

LOCATION

Coordinates: *(in decimal degrees)* Latitude _____ S Longitude _____ E	Dugong Protection Area? ☐ Yes ☐ No
Location Accuracy: ☐ Estimated ☐ Exact location +/– 10m ☐ General area +/– 1km ☐ Map reference +/– 1nm	
Location Description:	

PRIMARY ACTIVITY

☐ Beach washed (dead or sick on beach or coast) ☐ Floating offshore (dead, sick, unable to dive) ☐ Attacked by predator *Predator species:* _____	☐ Released ☐ Swimming, sleeping, feeding, etc. ☐ Other – *Specify:* _____

SECONDARY ACTIVITY *Leave blank if not applicable*

☐ Trapped inside crab pot *Complete crab pot section on page 2* ☐ Tangled in float line to crab pot, anchor line, etc. ☐ Fishing: captured by net/gill net ☐ Fishing: hooked by fishing line, including SCP shark-hooks	☐ Tangled in fishing line ☐ Fishing: trawling ☐ Fishing: speared ☐ Trapped in ghost net *Identify net from WWF Net Kit* ☐ Other – *Specify:* _____

CONDITION

UNKNOWN	ALIVE	DEAD	
☐ Unknown if dead or alive	☐ Alive and left to natural process, not rescued (DL) ☐ Alive and rescued (DZ)	☐ Live but subsequently died (D1) ☐ Carcass in good condition (fresh) (D2) ☐ Carcass fair (decomposing but organs intact) (D3)	☐ Carcass poor (advanced decomposition with internal organs falling apart) (D4) ☐ Mummified carcass (skin holding bones) (D5) ☐ Disarticulated bones (no soft tissue remaining) (D6) ☐ Unknown (D)

ASSESSMENT OF BODY CONDITION ☐ Good ☐ Poor ☐ Very poor ☐ Unknown

FATE / DISPOSAL

☐ Released	☐ Buried onsite *Buried by:* _____
☐ Left in situ	☐ Buried offsite *Buried by:* _____
☐ Animal sent for rehabilitation/euthanasia	☐ Carcass sent for necropsy *Facility:* _____
Facility: _____	☐ Other *Please specify:* _____

ATTACHMENT A

DAMAGE AND INJURIES

☐ Damage or injuries observed (photos required)
☐ No damage or injuries observed

FRESHNESS OF INJURY:
☐ Very fresh, no healing evident
☐ A recent wound, partly healed
☐ Scar only, healed

NOTES

Sketch damage and distinguishing marks or attach photos. If photos are available, replace sketches below with photos.

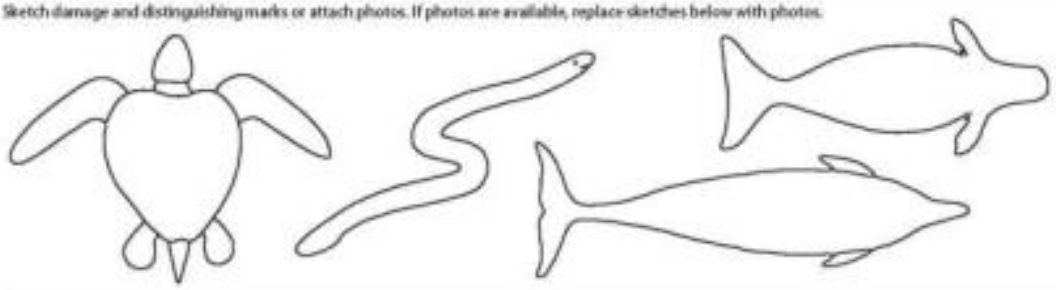

ADDITIONAL NOTES

CONTACT DETAILS

CONTACTS *Persons involved in the marine stranding response*

Name: _____
Address: _____
Email: _____
Organisation: _____
Phone: _____

EXPERT ASSESSOR *Person experienced in species identification of marine animals*

Name: _____
Address: _____
Email: _____
Organisation: _____
Phone: _____

CHECKLIST

Samples taken: ☐ Yes ☐ No Details of samples:

Photos taken: ☐ Yes ☐ No
☐ Photos attached to or received with form

Compliance notified:
☐ Yes ☐ No, not required

Reporting:
☐ Stranding report entered into StrandNet database

INSTRUCTIONS FOR COMPLETING THE DATA SHEET

- **DATE and TIME:** record as day / month / year and hours / minutes.
- **SPECIES:** Identify the species using the identification keys. If the species not already listed on the form, list it under 'Other species'. State the species name and submit the form to strand.data@ehp.qld.gov.au.
- **SEX and MATURITY:** Where possible, identify sex (see key illustration for mammals) and maturity.
- **TAGS:** Record any tag number/s. Tags may be attached to the rear edge of the front flipper of turtles.
- **LOCATION ACCURACY and DESCRIPTION:** Be precise and use more than one line if necessary; e.g. North Stradbroke Island, eastern ocean beach, 5km south of Pt Lookout.
- **CONDITION:** Record the health/condition of the animal using the fields provided.
- **FATE:** Describe the steps taken to secure the animal to ensure it is not lost with currents or tides.
- **DISPOSAL:** Summarise how the carcass has been disposed of.
- **DAMAGE and INJURIES:** Describe any damage or injuries observed and their freshness. If you cannot take photos, use the diagrams on the form to sketch any damage or distinguishing marks.
- **EXPERT ASSESSORS:** Identify the veterinary and/or biological experts who examined the animal.
- **NOTES:** Address the full range of your observations. Attach extra pages if required.
- **CRAB POT STRANDINGS:** Complete this page if the marine stranding relates to being trapped inside a crab pot or tangled in the float-line to a crab pot.
- **PHOTOS:** Forward all photos along with this report to the contacts listed at the bottom of this page.

In the GBR Region, return immediately to:
GBR Marine Animal Strandings Coordinator
Telephone (07) 4047 9616, Email: GBRR-Strandings@npsr.qld.gov.au and GBRMPA Assessments
Telephone (07) 4750 0700 Email: assessments@gbrmpa.gov.au

Outside the GBR Region, return immediately to:
EHP Marine Wildlife Stranding Coordinator
Telephone (07) 3170 5618, Email: strand.data@ehp.qld.gov.au

ATTACHMENT A

CRAB POT STRANDINGS *Only complete if applicable*

Position of entanglement on turtle or dugong *(e.g. right front flipper)*: _____

Is the turtle/dugong: ☐ trapped inside the pot or ☐ entangled in the rope/frame on the outside of the pot?

TYPE OF CRAB POT

- ☐ Commercial
- ☐ Recreational
- ☐ Unidentified type or condition
- ☐ Large circular
- ☐ Collapsible rectangular
- ☐ Opera house
- ☐ Dilly – blue swimmer crab gear
- ☐ Dilly with barrier – spanner crab gear
- ☐ Inverted dilly (illegal 2010)

CONDITION

- ☐ Working crab pot
- ☐ Lost or discarded (ghost fishing)

ROPE TO CRAB POT ☐ Weighted ☐ Unweighted Rope type and length: _____

OTHER DETAILS Type of float: _____ Type of weights: _____ Size of pot entrance: _____ cm

CRAB POT OWNERSHIP Registration details: _____ Date crab pot was set: __ __/__ __/__ __

Location crab pot was set: _____

ADDITIONAL INFORMATION:

REFERENCE DIAGRAMS